Universitat Autònoma de Barcelona

"PLATINUM-BASED NANOSTRUCTURED POLYMERS FOR GLIOBLASTOMA TREATMENT"

Xiaoman Mao

Universitat Autònoma de Barcelona

Departament de Química

Facultat de Ciències

“PLATINUM-BASED NANOSTRUCTURED POLYMERS FOR GLIOBLASTOMA TREATMENT”

Xiaoman Mao

Ph.D. Thesis

Ph.D. in Materials Science

2021

Supervisors:

Dr. Daniel Ruiz Molina

Dr. Fernando Novio Vázquez

Tutor:

Jordi Hernando Campos

Memòria presentada per aspirar al Grau de Doctor per Xiaoman Mao.

Xiaoman Mao

Vist i plau,

Dr. Daniel Ruiz Molina

Dr. Fernando Novio Vázquez

Bellaterra, 28 de Febrer del 2021

Acknowledgments

I would like to express my deep and sincere gratitude to everyone who played a role in the accomplishment of this thesis.

First and foremost, praises and thanks to my research supervisors, Dr. Daniel Ruiz-Molina and Dr. Fernando Novio, the group leader and senior researcher in Nanostructured Functional (NanosFun) group at Institut Català de Nanociència i Nanotecnologia (ICN2). They gave me enormous guide, valuable advice, extended help, and constant encouragement during my whole PhD period. Their strict academic spirit, open-minded personality, and inclusive while positive attitude towards life inspired me so much, which will keep influencing me in future.

Besides, my biological advisors, Dr. Julia Lorenzo from Institut de Biotecnologia I de Biomedicina (IBB), and Dr. Ana Paula Candiota from Dept. Bioquímica i Biologia Molecular at UAB, also helped me a lot during the latter part of my work, especially the biological experiments. Without their guidance and help, this thesis could not have been completed.

Also, special thanks to my comrade, Ms. Shuang Wu, my collaborator of *in vivo* experiments who worked extremely hard and just obtained her PhD degree. And thanks to Ms. Pilar Calero, who took over Shuang's position to finish the work.

In addition, I would like to thank my colleagues from NanosFun group. To Salvio and Miguel, who helped me a lot at the beginning of my study. To David, Eddy, both Sergi, and Rafa who supported my work at IBB with the *in vitro* experiments. To Carolina, Noe, Junda, Sergio, Hector, Bea, Claudio, Jaume and all other fellows at ICN2 and CM3, for your kindness, sympathy, and joy when we were together.

I also want to especially thank the directors of all the groups where I stayed during my research: thanks to Prof. Zhuang Liu for supporting my work at Soochow University, China; and to Prof. Stefan Jurga and Dr. Radosław Mrówczyński for helping me at NanoBioMedical Centre at Adam Michiewicz University in Poznan, Poland.

And thanks to La Caixa Foundation, who financed my PhD study here.

Finally, I would like to express my deep thanks to my families and friends, who are always behind me and support all my decisions and work.

Abstract

Nanostructured Coordination polymers (NCPs) have emerged as a new family of nanoparticles with interesting properties due to the versatility of coordination chemistry. The multiple combinations between metal ions and organic ligands as precursors of self-assembled materials have attracted scientists for decades. The potential multifunctionality of these nanosystems and the facility for the modification of their physicochemical properties open new perspectives in different fields, including medicine. The recent advances have showed the potentiality of NCPs as smart drug delivery systems, bioimaging probes or a combination of both. The application of coordination chemistry at the nanoscale is considered one of the most versatile approaches for the development of new nanostructured materials with unprecedented properties.

This Thesis has been focused in the design, synthesis and characterization of platinum-based NCPs for exploring the possibilities of these nanosystems in the treatment of cancer, and in particular in the treatment of glioblastoma. Different platinum-based coordination polymers have been obtained and evaluated for the biomedical use based on different studies in silico, *in vitro* and *in vivo*. The synthetic methodology, the proper selection of precursors and reaction conditions, and the study of the final physicochemical and biological properties has centered the work carried out. A big effort has been put in the obtaining of chemical and colloidal stable nanoparticles in physiological conditions and in the evaluation of their therapeutic activity against glioblastoma *in vitro* and *in vivo*. For that, a multidisciplinary work has been carried out with the collaboration of specialized research groups in different areas (i.e., materials chemistry, biology, medicine). Achieving this objective was possible thanks to a proper design of the strategy followed together with a complete characterization of the prepared nanostructures and evaluation of their potentiality as anticancer nanoparticles.

In the first part of this Thesis, the nanostructuration of Pt(IV)-based coordination polymers was achieved by the coordination of a Pt(IV)-prodrug with iron(III) ions (Pt-Fe NCPs). The resulting nanoparticles were evaluated in terms of chemical and water-colloidal stability, cytotoxicity, biocompatibility and controlled drug delivery profile. Moreover, it has been evaluated their anticancer activity *in vitro* and *in vivo*, and also their potentiality for being used as MRI contrast agents. Specifically, these nanoparticles were validated by preclinical *in vivo* tests using GB murine models and using the intranasal administration as administration

route. The nanoparticles showed interesting performance as potential anticancer agents for glioblastoma disease. On the one hand, a chemical polymerization of a catechol-based Pt(IV) prodrug was carried out to obtain a robust and colloidal stable nanoparticles. In this case, the resulting nanoparticles showed low cytotoxicity, good biocompatibility and interesting controlled drug delivery profile. These nanoparticles were evaluated for their anticancer activity against GB *in vitro* as alternative nanosystems to the Pt-Fe NCPs. The characteristic of this new nanosystem make it an interesting candidate to future developments.

List of abbreviations

ABC ATP-binding cassette

AFM Atomic force microscopy

BBB Blood-brain barrier

BBTB Blood-brain tumour barrier

BSA Bovine serum albumin

CAs Contrast agents

Calcd Calculated

CDDP Cisplatin

CED convection enhanced delivery

CK2 Protein kinase CK2

CNS Central nervous system

CT Computed tomography

CTLs Cytotoxic T-lymphocytes

DCs Dendritic cells

DCC N,N'-dicyclohex ylcarbodiimide

DLS Dynamic light scattering

DMEM Dulbecco's modified eagle medium

DMF Dimethylformamide

DMSO Dimethyl sulfoxide

DNA Deoxyribonucleic acid

DSB Double-strand break

DSC Differential scanning calorimetry

DSCP Disuccinic cisplatin

DTT Dithiothreitol

ECM Extracellular matrix

EDTA Ethylenediaminetetraacetic acid

EDX Elemental energy dispersive X-ray

EE Enriched environment

EGFR Epidermal growth factor receptor

EPR Enhanced permeability and retention

ERK Extracellular signal-regulated kinases

EtOH Ethanol

FBS Fetal bovine serum

FDA Food and Drug Administration

GAMs Glioma-associated microglia/macrophages

GB Glioblastoma

GSCs Glioma stem cells

GSH Glutathione

HGGs High-grade gliomas

HIF Hypoxia-inducible factor

HMDA Hexamethylenediamine

HMGB-1 High-mobility group protein box-1

HRMS High-resolution mass spectrometry

IC_{50} Half maximal inhibitory concentration

ICD Immunogenic cell death

ICPs Infinite coordination polymers

ICP-MS Inductively coupled plasma-Mass spectrometry

ID Injected/initial dose

IMS Immune-enhancing metronomic schedule

IL Interleukin

IV Intravenous

IN Intranasal

JAK Janus kinases

LGGs Low-grade gliomas

mAbs Monoclonal antibodies

MDR Multidrug resistance

MEM Minimum essential medium

MeOH Methanol

MMR Mismatch repair

MR Magnetic resonance

MRI Magnetic resonance imaging

MW Molecular weight

NADPH Nicotinamide adenine dinucleotide phosphate hydrogen

NCPs Nanoscale coordination polymers

NK Natural killer

NMM N-methylmorpholine

NMR Nuclear magnetic resonance

NP Nanoparticle

PB Phosphate buffer

PBS Phosphate buffer saline

PCL Poly(ε-caprolactone)

PD-1 Programmed cell death protein 1

PD-L1 Programmed death-ligand 1

PDA Polydopamine

PDI polydispersity index

PEG Poly(ethylene glycol)

p.i. post-implantation

PLGA Poly(lactic-*co*-glycolic acid)

ppm Part per million

ppb Part per billion

PtBC Pt(IV)-biscatechol prodrug

PVA Poly(vinyl alcohol)

PVP Polyvinylpyrrolidone

PXRD Powder X-ray diffraction

r_1 Longitudinal relaxivity value

r_2 Transversal relaxivity value

RES Reticuloendothelial system

RNA Ribonucleic acid

ROI Region of interest

ROS Reactive oxygen species

RPMI Roswell Park Memorial Institute

rt Room temperature

SEM Scanning electron microscopy

SPIONs Superparamagnetic iron oxide nanoparticles

STAT Signal transducer and activator of transcription

T_1 Longitudinal relaxation time

T_2 Transversal relaxation time

TAMs Tumour-associated macrophages

TEM Transmission electron microscopy

TGA Thermogravimetric analysis

THF Tetrahydrofuran

TILs Tumour-infiltrating lymphocytes

TLC Thin layer chromatography

TME Tumor microenvironment

TMZ Temozolomide

TNF-α Tumor necrosis factor-α

TP53 Tumor protein p53

Treg Regulatory T cells

T_{1w} T_1-weighted MRI

T_{2w} T_2-weighted MRI

VEGF Vascular endothelial growth factor

WHO World health organization

XRD X-ray diffraction

Table of contents

Chapter 1

General introduction

1.1 Glioblastoma: Definition, Characteristics and Clinical Treatment

1.1.1 Overview on glioblastoma

Glioblastoma, also called Glioblastoma Multiforme (GB), is the most common and devastating tumor of the central nervous system (CNS) in adults, accounting for about 15% of all brain tumors, > 48% of malignant CNS tumors, and > 57% of gliomas (glial tumors). The average annual incidence rate of GB is the highest in brain tumors as 3.22 per 100 000 population (Figure 1.1), while 5-year relative survival is the lowest less than 7%.[1] With extremely poor prognosis and low median survival, it is classified as the highest Grade IV in brain tumors by the World Health Organization (WHO).[2-3] The poor clinical outcome of GB is usually attributed to its heterogeneity, complicated tumor microenvironment, and acquisition of resistance,[4-6], aggressive infiltration, and rapid growth.[7] Due to the fast development, most patients with GB are diagnosed at stage IV, especially magnetic resonance imaging (MRI).[8]

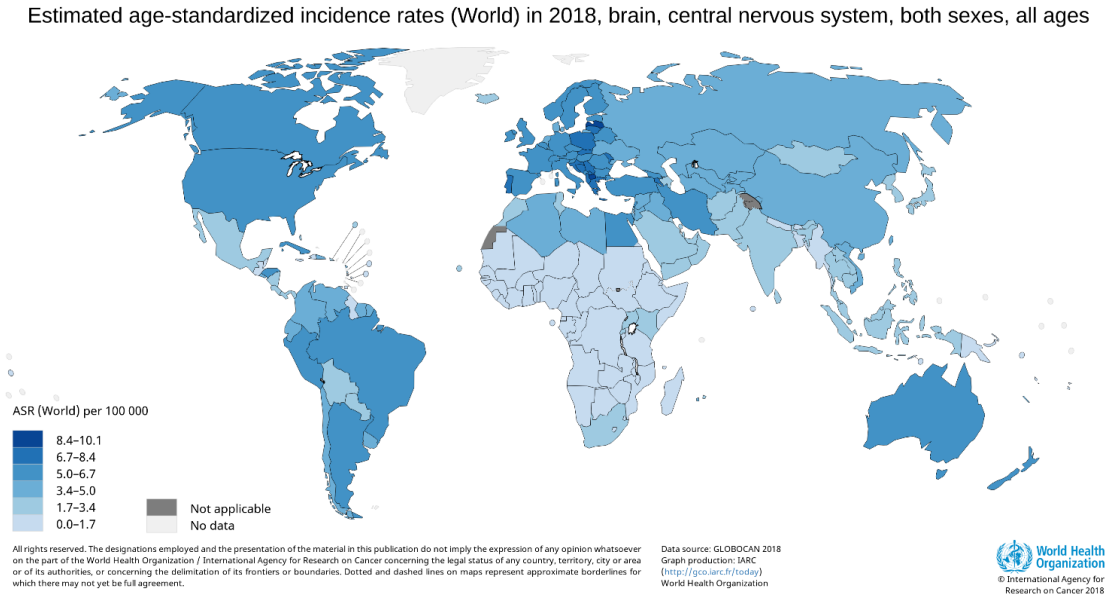

Figure 1.1 Global incidence of brain/CNS tumors in 2018 in estimated age-standardized incidence rates (ASR), extracted from Global Cancer Observatory https://gco.iarc.fr/.

The complex tumor microenvironment (TME) plays a pivotal role in the growth, proliferation, and invasion of GB and other brain tumors.[9] GB TME consists of GB cells,

GB stem cells (GSC), extracellular matrix (ECM), interstitial fluid, and stromal cells including resident glial cells (astrocytes, microglia, endothelial cells, etc.) and infiltrating immune cells like monocytes, macrophages and lymphocytes (Figure 1.2).[10-11] As showed in Figure 1.2, TME components contribute to the growth, invasion, suppression of antitumor immunity and metastasis of GB. [11-12]

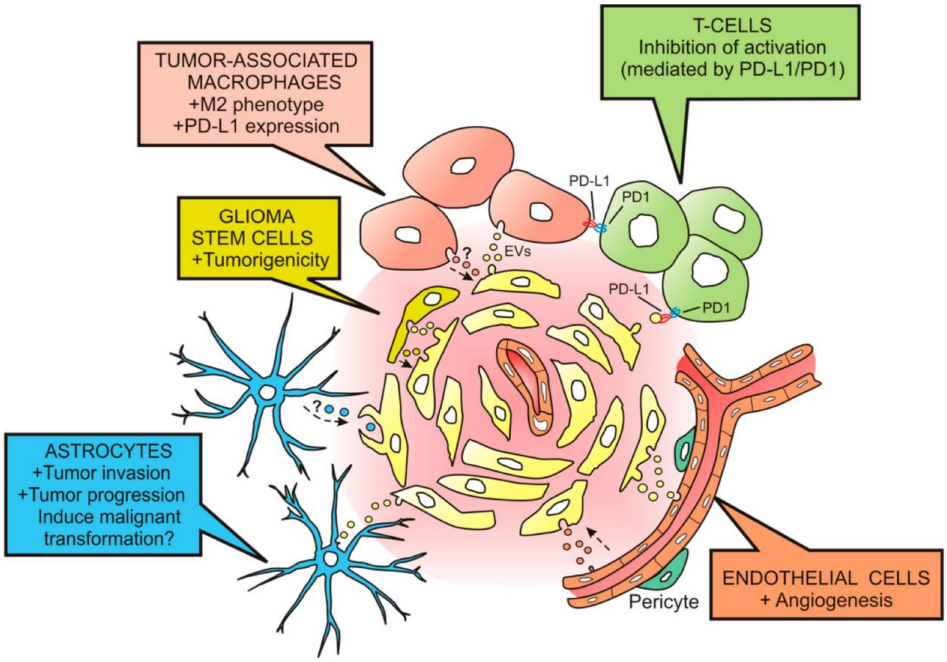

Figure 1.2 Communication between GB cells and cells from the TME, mainly the effects via GB-derived extracellular vesicles (EVs) on TME cells, which promote the GB growth in turn.[11]

Besides, the unique location of GB into the brain poses more challenges for its treatment, especially the presence of blood-brain barrier (BBB).[9,13] The BBB is a physical barrier formed by specialized neurovascular units between the CNS and blood circulation, responsible for blocking harmful substances from entering the brain and maintaining the cerebral ion homeostasis. It is estimated that all macromolecules, and over 98% of small molecules, are normally excluded from the CNS by the BBB, leading to an extremely low effective drug concentration and availability of chemotherapeutic agents at the desired target sites in the treatment for all CNS diseases, including GB.[14] Although the integrity of the BBB might be compromised by developed GB and form so-called blood-brain tumor barrier (BBTB), the permeability of BBTB may increase

compared to BBB but it still remains a formidable obstacle to the transport of therapeutics.[15-16]

Additionally, GB is of highly intrinsic and highly adaptive resistance, which is considered as a highly immunologically “cold” tumor, with limited clinical response to the therapy and high recurrence.[17] Commonly, the existence of GSCs is considered as the dominant driver accountable for the resistance of GB, due to their robust DNA-repair mechanisms imparting resistance to chemotherapy and radiation, and strong capacity to differentiate into stromal and vascular structures supporting tumor regrowth.[18] Besides, other changes in the GB also promote the tumor cell survival and adaptation, thus reinforce the development of resistance, for example, the hypoxia microenvironment, induced autophagy for cytoprotection, overexpressed vascular endothelial growth factor (VEGF) and other functional proteins, etc.[19] Apart from the factors originating in the tumor cells, new evidence substantiates that the TME also plays a critical role in the GB resistance.[5,20]

1.1.2 Glioblastoma therapy

In 2004, phase III trials of temozolomide (TMZ) demonstrated its superior outcome for GB treatment with significantly improved overall survival. Since then standard clinical treatment for GB includes maximal surgical resection, followed by radiotherapy and concurrent chemotherapy, typically with temozolomide (TMZ),[3,21-22] a standard care drug for GB for almost the last two decades.[23] First synthesized in the early 60s from reaction of diazonium and methyl isocyanate,[24] this lipophilic compound showed effective activity against various tumors,[25] ability to cross the BBB and stability in acidic pH of the stomach suitable for oral administration.[26] The anticancer action of TMZ is due to the formation of diazomethane after TMZ hydrolysis, which alkylates DNA and therefore triggers further apoptosis (Figure 1.3).[27-28]

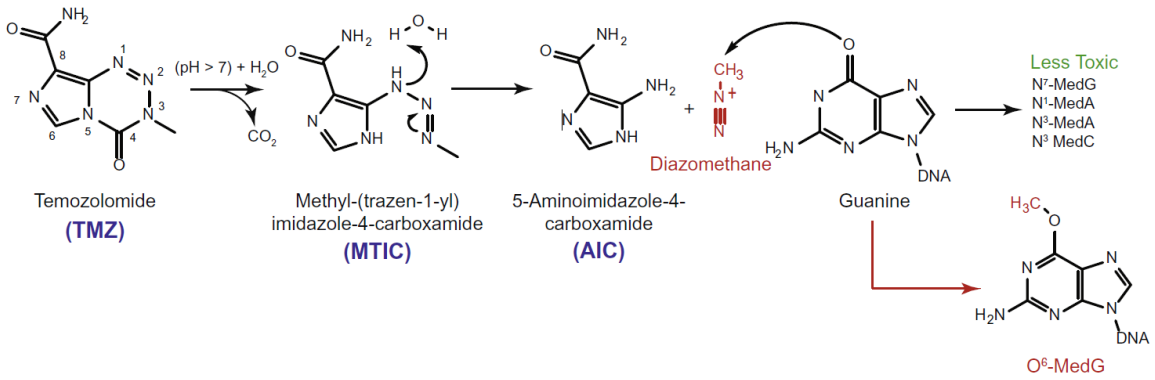

Figure 1.3 Mechanism of action of TMZ, illustrating the release of diazomethane, which alkylates DNA and therefore triggers further apoptosis.[27]

However, although it is beneficial to the survival of patients, the therapeutic outcome of TMZ treatment is still limited and unsatisfying, and the clinical responses lacks robust predictive markers.[28] The compound is not soluble under physiologic conditions, easily inactivated via hydrolysis in the cells, and causes harmful side effects because of off-target DNA damage.[29] Moreover, the failure of clinically adjuvant chemotherapy is often attributed to the heterogeneity nature of GB and the emergence of resistance to TMZ.[30-31] Indeed, the chemoresistance of GB to TMZ is commonly attributed to the DNA repair mechanisms including direct repair by O6-methylguanine-DNA methyltransferase (MGMT), which are activated to eliminate the DNA damage and reduce apoptosis.[32] Despite the specific TMZ chemoresistance, the presence of cancer stem cells, GSCs in GB, is a major contributor to the resistance and recurrence of GB.[33-34] Additionally, multidrug resistance based on overexpressed drug efflux transporters like ATP-binding cassette (ABC) family difficult that therapeutic agents reach the brain.[35] Thus, the unsatisfactory clinical outcome of TMZ treatment and the development of TMZ resistance urge for novel chemotherapeutic drugs or alternative therapeutic strategies. However, this is not an easy task as brain location and characteristics of GB challenge the effectivity of drug delivery, including the crossing of BBB and the BBTB, the GB nature like its heterogeneity and the presence of glioma stem cells (GSCs), and the intra-brain transport, among others (see Figure 1.4).[36]

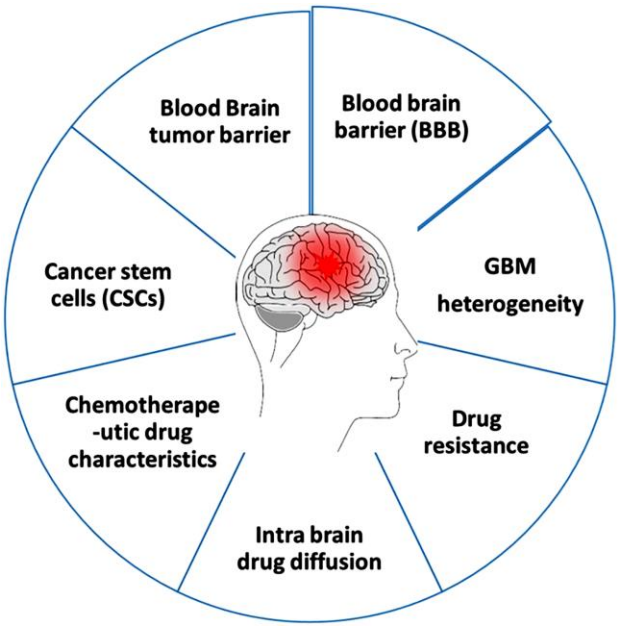

Figure 1.4 Major challenges in GB chemotherapy.[36]

1.1.3 Nanoparticles as platforms for drug delivery

Despite the pursuit of progress in necessary technologies assisting diagnosis, surgery, and radiotherapy, multiple therapeutic strategies were explored and investigated by researchers to tackle the challenges faced by GB treatment, including chemical modification of therapeutics, combined therapies, BBB-penetrating strategies (though modifications normally affect target binding or decrease compound effectivity), efflux transporter inhibition, GB microenvironment targeting, and phenotype polarization of tumor associated microglia/macrophage (TAM).[37-40] Among them, nanotechnology offer a novel and potential opportunity for the treatment of GB, due to its size effects, multifunctional versatility, and other advantages.

Compared to conventional therapeutic agents, nanodrug delivery systems demonstrate enormous advantages, including stability, feasibility of incorporation of both hydrophilic and hydrophobic substances, improved bioavailability, prolonged blood circulation, and enhanced accumulation in tumor sites. Indeed, based on the enhanced permeability and retention (EPR) effect, NPs with long circulation can passively target and accumulate into the tumor sites due to the intrinsic leaky vasculature and poor lymphatic drainage in tumor.[41] Moreover, the BBB was compromised and disrupted because of the progressed GB, which allows passive

accumulation of chemotherapeutic agents, especially NPs, in the vicinity of the disruption.[42] These features are key factors to increase the therapeutic efficiency, reducing dose and side effects, and improving patient compliance.[43]

However, the extent of BBB disruption varies due to the heterogeneity of GB tumor, and it can be negligible at some point/region or remain intact in some extreme cases.[44] Thus, relying solely on the passive targeting may be insufficient for the nanodrug delivery systems to effectively deliver the therapeutic drugs, especially if we also consider the heterogeneous BBTB, dense brain matrix impeding diffusion and elevated interstitial fluid pressure.[45] To increase the targeting effect, targeting molecules are integrated such as antibodies, peptides or proteins, aptamers, or small molecules, that can bind to antigens or receptors on the target tumor cells to increase cellular uptake and accumulation thus improve the therapeutic efficacy.[46]

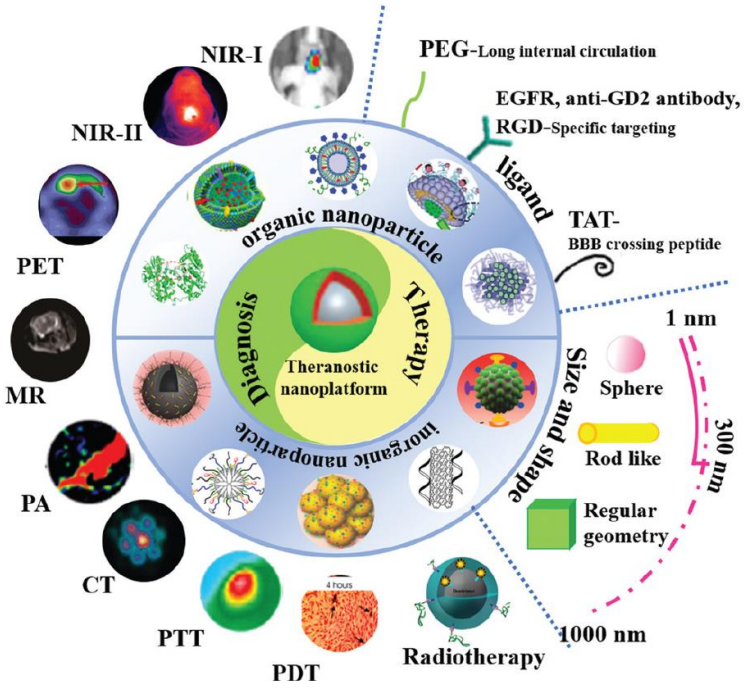

Figure 1.5 Schematic illustration of theranostic applications and key features of nanodrug delivery systems for brain tumors.[47] The nanocarriers can vary with different types of NPs; The geometry, size, surface charge, and surface modifications are among key features of theranostic NPs for brain tumors.

The integration of a specific drug on the nanostructure could be performed through physical encapsulation methods, absorption procedures, or generating covalent bonds

between the drug and the nanoparticle body.[46] According to the structure of the nanocarriers, they can be classified into different types, liposomes, micelles, dendrimers, solid lipid nanoparticles (NPs), nanorods, inorganic NPs, etc.[46] Besides, the diversity of the biomaterials for nanodrug delivery systems can enable the loading of various therapeutic and/or diagnostic agents simultaneously, which makes the delivery system a multifunctional "n-in-one" platform. There are many reports where nanodrug delivery systems serve as theranostic (Figure 1.5) or combinational therapeutic platforms.[48] Besides, the nanocarriers can be designed or modified to enable controlled drug release and selective targeting to desired location.

Overall, the surge in nanomedicine research in past few decades has witnessed the translation from bench to bed, with many products available and a growing number in the pipeline, among which, applications as drug delivery systems account for more 75% of the total sales of nanoformulations.[46,49]

1.1.4. Nanoparticles for Glioblastoma

The most investigated NP delivery systems for the CNS (Figure 1.6) include vesicles (lipidic, micellar or exosomes),[50-52] organic polymers,[53] mesoporous silica,[54] metal NPs,[55] dendrimers,[56] and quantum dots[57]. In most of the studies the size of the NPs is determinant in the BBB crossing; several studies indicated an inverse correlation between the size and BBB penetration.[58-59] The influence of NP surface charge/modification on the brain permeability was also well studied; a moderate or high positive zeta potential (> 15 mV) was reported to enable the NPs to cross the BBB and result in efficient brain delivery.[60-62] Also the geometry and shape of the NPs also greatly affected the clearance and biodistribution of the NPs.[63-65] In addition, the decoration of NPs with targeting molecules is another important strategy to increase the BBB penetration and drug accumulation in GB.[66-67] The critical influence of all these factors is important and they should be taken into account when designing NP drug delivery systems for GB treatment.

Some excellent reviews have detailed different NPs used for GB treatment.[68-69] A selection of the most representative examples are showed in this section.

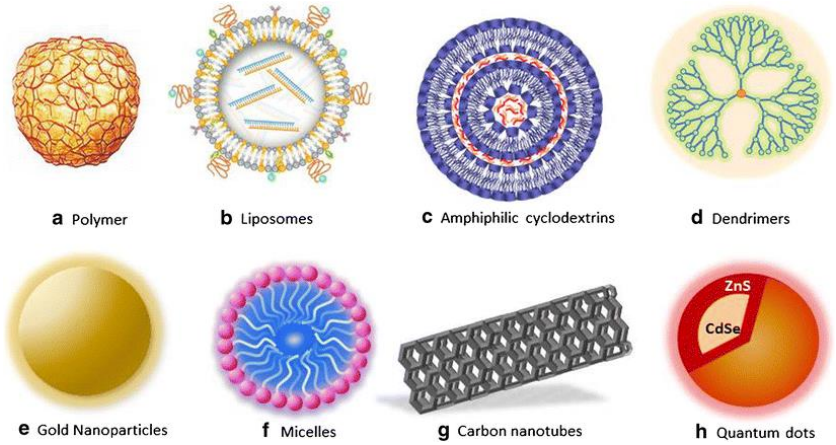

Figure 1.6 Schematic of different nanocarriers commonly used for BBB crossing.[70]

Polymeric NPs. Polymeric NPs are a typical and main family used for the drug delivery, rapidly biodegradable *in vivo*. Chitosan-based NPs have been used to encapsulate TMZ, leading to significant increased half-life activity from 1.8 h to 13.4 h.[29] PLGA is a copolymer approved by US FDA owing to its biodegradability and biocompatibility, which is also widely used in a host of NP drug delivery systems against GB. Paclitaxel (PTX)-loaded PLGA NPs were reported to reach tumor tissue when administered by CED in a intracranial glioma rat model, resulting in a longer median survival compared to treatments with free PTX or PTX-loaded PLGA NPs without CED delivery.[71-72] In another work, DOX-conjugated PEG-poly(aspartic acid) micelles were delivered into the brain parenchyma of L9 GB-bearing rats using CED, showing prolonged median survival compared to CED liposomal or free DOX, indicating its potential for improved treatment for GB.[73]

Liposomes. The use of liposomes for brain delivery has been broadly explored for many years. Camptothecin (CPT)-encapsulated liposomes were reported back in 2006, co-delivering topoisomerase I inhibitor (irinotecan) using CED to obtain higher chemotherapeutic dose to the brain with lower systemic toxicity.[74] Later on the targeted delivery of liposomal nanocontainers to the peritumoral regions of GB was reported,[75] and since then more successful examples emerged. For instance, cationic liposomes were used to load different therapeutic agents (siRNA and small molecules) targeting GB and functionalized with an antibody targeting transferrin receptor, which allowed

transport across the BBB and entrance into tumor cells, obtaining a more efficient effect compared to free TMZ.[76]

Metallic NPs. The surface of metallic NPs is usually modified with specific moieties or biomolecules or imaging contrast agents to fabricate multifunctional nanoplatforms in addition to deliver therapeutic drugs into tumor sites.[77] With the innate properties of the metallic NPs, combined therapies could also be realized. For example, iron oxide NPs (IONPs) can used as MRI imaging agents except as delivery nanocarriers. After coating with a copolymer of chitosan, PEG, and poly(ethylenimine) (PEI), IONPs provided T_2 contrast in MRI while delivering siRNA against apurinic endonuclease 1 (Ape1), an enzyme crucial in base excision repair pathway. The penetration in GB resulted in successful knockdown of the Ape1 expression and increased radiosensitivity in GB cells and tumors.[78] Besides, IONPs decorated with gemcitabine, chlorotoxin and hyaluronic acid showed targeting ability to GB tumor cells probably through a glioma-specific chloride ion channel. It also inhibited the infiltration of GB probably through interaction with MMP-2 receptor.[79-80]

Others. Other nanoplatforms are based on nanocomposites able to encapsulate different chemotherapeutics and reach the brain with BBB-crossing designs. For instance, a CPT prodrug linked to tetraethylene glycol and α-lipoic acid was encapsulated in nanoemulsions which can be enzymatically degraded by oxidation to act as a ROS scavenger and to finally release CPT in its active form.[81] Within U87 GB cell model, it showed notable intracellular uptake via direct cell membrane penetration instead of endocytosis, and the *in vivo* study demonstrated a higher accumulation of the nanodrug in brain tumor tissue compared with other organs, leading to beneficial and significant effects in tumor growth rate and survival rate in U87 xenograft models.

1.2 Platinum anticancer drugs as alternative treatment for GB

1.2.1 Platinum complexes as anticancer drugs

cis-diamminedichloroplatinum(II), cisplatin (CDDP), is also known as Peyrone's chloride at the end of nineteenth century named after Michele Peyrone who first

synthesized it.[82] The antibacterial effect was first discovered by Barnett Rosenberg while doing experiments to assess the effect of electric field on bacterial growth in the late 1960s.[83] Subsequent investigations testing it in a sarcoma mouse model showed the capacity of cisplatin to block cell division in tumors.[84] Clinical trials of cisplatin started in 1971, and became the first platinum complex introduced to the market since 1979 by the US Food and Administration (FDA) and several European countries.[85] From then on, cisplatin and subsequent expansion of platinum-based drug family remains the most widely used anticancer chemotherapeutics, accounting for almost 50% of clinically used anticancer therapeutic agents.[86] Up to date, there are still a large number of clinical trials undertaking with cisplatin, as shown in Figure 1.7.

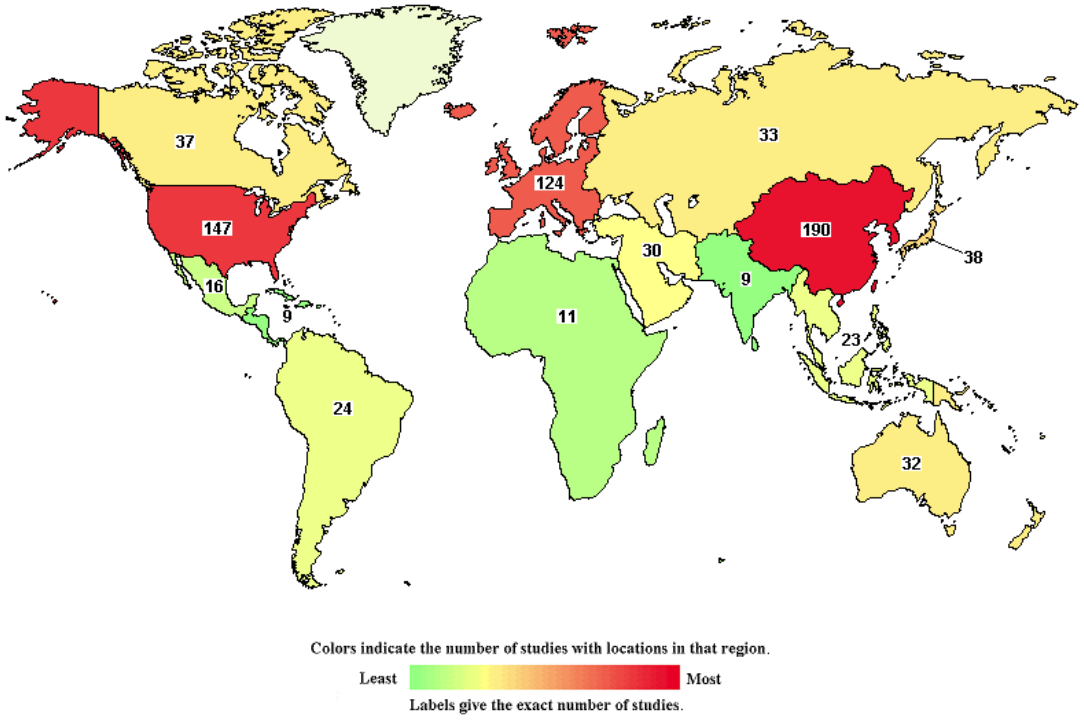

Figure 1.7 NIH-registered clinical trials involving cisplatin globally in last two years till the end of 2019. The numbers reflect only those open and verified by the NIH. Graphic generated using search tools from www.clinicaltrials.org.

Beyond CDDP, other platinum-based drugs are approved worldwide for combating cancer in humans, carboplatin, and oxaliplatin. In specific countries, other three Pt(II) compounds (nedaplatin, lobaplatin, and heptaplatin) are approved for clinical use.[87] Figure 1.8 depicts the chemical structures of the related Pt drugs. The discovery of

cisplatin and subsequent expansion of the platinum-based anticancer family witnessed its revolutionizing worldwide use against a wide spectrum of cancers, including testicular, cervical, ovarian, bladder, lung, colorectal, and head and neck cancers.[88-89] The enlisting fact of cisplatin, carboplatin and oxaliplatin in *Model List of Essential Medicines* by the WHO implies that the clinical potential of these drugs might be further underscored.[90] Moreover, the use frequency of platinum complex family in the medical charts of the US patients was only surpassed by five other anticancer agents (methotrexate, raloxifene, medroxyprogesterone, tamoxifen, and leuprolide), according to the 2009 Ambulatory Care Drug Database maintained by the US Centers for Disease Control and Prevention.[91] Cisplatin remains more active in clinical trials than any other anticancer drug,[92] with more than 343.000 trails in USA[93] and over 25 000 trials in Europe.[94]

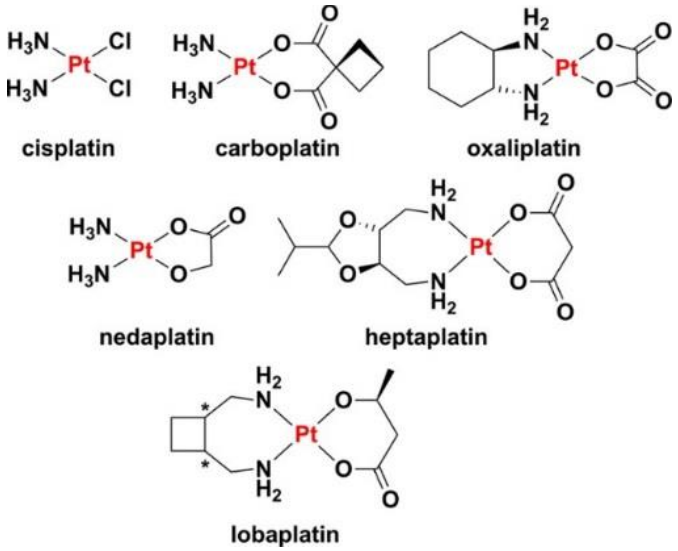

Figure 1.8 Chemical structures of approved platinum drugs.[87]

The anticancer effect of these drugs has been researched comprehensively which generally arises from the formation of Pt-DNA adducts and interfering with transcription, thus leading to the death of cancer cells.[87,95] More in detail, classical Pt(II) complexes are neutral and square-planar, bearing similar structure as cis-$[PtX_2A_2]$, like cisplatin, where A_2 represents two monodentate or one bidentate ligand(s) with nitrogen donor atoms, referred to as “non-leaving group ligands” because they remain bound to the metal centre throughout the intracellular transformation. In contrast, X_2

refers to the "leaving group", usually two anionic ligands, which leave the Pt coordination intracellularly.[96] Due to their similar structure, these classical complexes also share similar mechanisms of action even side effects. Commonly, four steps are involved in the mechanism of action of Pt(II) compounds (Figure 1.9): cellular uptake of the Pt complex, intracellular aquation/activation, DNA binding, and cellular processing of DNA lesions leading to apoptosis.[87]

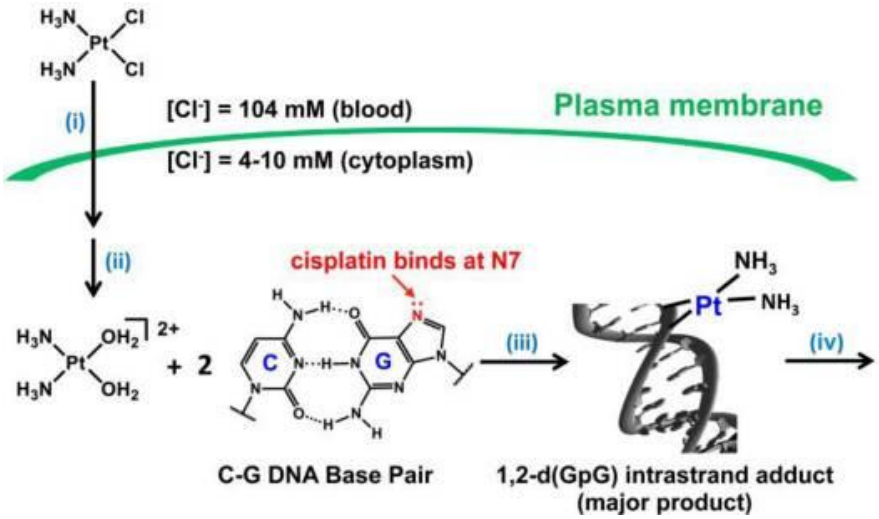

Figure 1.9 Four steps of mechanism of cisplatin: i) cellular uptake, ii) aquation/activation, iii) DNA binding, and iv) cellular processing of DNA lesions leading to apoptosis.[87]

Passive diffusion through the plasma membrane has long been considered as the major cellular internalization pathway of cisplatin.[97] Conversely, recent studies suggest that it is taken up by cells predominantly via active transport mediated by membrane proteins, like copper transporters (CTRs) and organic cation transporters (OCTs).[98-99] Once cisplatin enters the cells, it is activated via the aquation of one chloride leaving group due to the drastic decrease of chloride level. The monoaquated cisplatin can enter the nucleus and bind to DNA base and form monofunctional DNA adducts. Crosslinks can also form after the remaining chloride ligand is replaced for a second purine base, giving rise to intrastrand and interstrand DNA crosslinks.[100] Without repair these adducts distort the DNA structure and arrest the cell circle, leading to apoptotic cell death.[101] New evidence proves that the targets and mechanisms of action of Pt drugs are increasingly complex. Despite the well-known DNA binding mechanism, other targets

are also involved in their anticancer efficacy such as RNA binding, protein binding and damage, as well as immunogenic effects.[102-105] Interestingly, lower sustained dose of Pt drug may be required over a relatively long term to achieve the immunogenic effects and permit extended cell viability. These immunomodulation effects induced by Pt agents encourage the repurposing of Pt drugs for GB treatment.[106]

1.2.2 Pt(II) drugs for GB treatment

The potential of Pt compounds were long explored since 1990s in clinical studies against recurrent gliomas,[107] and CDDP was reported to show synergistic antitumor effect with TMZ.[108-109] The combination of CDDP and TMZ showed partial responses with a 6-month progression free survival of 35% in a phase II trial in pretreated recurrent GB patients.[110] In the preclinical studies, CDDP enhanced the antiangiogenic effects of an octamer peptide and the combination inhibited GB growth in both *in vitro* and *in vivo* assays.[111] Favorable and synergistic effects were also reported when CDDP combined with an inhibitor of tyrosine kinase.[112] On the other hand, *in vitro* studies reported that non-conventional Pt complexes were synthesized and exhibited toxicities superior to CDDP or TMZ,[113-114] and CDDP in combination with p(65)+Be neutron irradiation showed marked reinforcement of cytotoxicity against U87 GB cells.[115]

Since then, Pt complexes have been increasingly investigated alone[114] or in combined therapies with other agents, including dose-intense TMZ,[116-117] bee venom,[118] β-elemene extracted from curcuma wenyujin,[119] nitrosoureas,[120-121] targeting peptide,[122] various functional inhibitors,[123-127] and immunotherapy[128-132]. Convection enhanced delivery (CED) was adopted to deliver Pt complexes in combination with photon irradiation, leading to augmented survival of GB-bearing animals.[133-135] The relative success of Pt drugs implied their considerable anti-GB potential when effectively delivered to the targeting tumor sites.

However, the clinical responses of Pt therapeutical agents were still very limited with GB, nor in combination with radiotherapy or other chemotherapies like carmustine or TMZ[136]. For example, single-agent of Pt complexes was used as “rescue” treatment recently in patients with HGG pretreated with nitrosoureas or TMZ, showing modest activity, and resulting in partial responses and slightly improved median survival.[137]

Nowadays, Pt agents have been considered fourth-line chemotherapeutics for GB treatment, for instance, only used after all the standard protocols failed.

The limited delivery into the brain tumor has long been considered as one of the main reasons for the unsatisfactory efficacy of Pt chemotherapy for GB. The concentrations of Pt complexes in cerebrospinal fluid were reported < 5% of plasma counterparts via intravenous administration due to the poor penetration across the BBB into the brain tissue.[138] No significant improvements were detected even if the BBB was disrupted by the progress of GB, and the BBTB/neovasculature in GB was more permeable than intact BBB. Current strategies to improve the delivery of Pt agents include: 1) increasing BBB permeability,[139] 2) delivering with biodegradable implants in the tumor bed of patients,[140] and 3) bypassing the BBB via CED delivery[141]. The second reason considered for the failure is the limited half-life in most tissues, which can be only a few hours in rodent brains.[142] These factors often requires high doses of Pt agents, which may increase their extensive off-target toxicities[143], contribute to the emergence of chemoresistance and immunosuppression like lymphodepletion to further hinder the antitumor efficacy[144]. One of the possible approaches to decrease the toxicity is the use of Pt(IV) complexes.

1.2.3 Pt(IV) drugs for GB treatment

Pt(IV) complexes feature with two additional ligands in the axial positions based on the structure of Pt(II) agents, which turn to six-coordinate octahedral geometries. The saturated coordination sphere of Pt (IV) is more substitution inert than four-coordinate Pt(II) centers, thus minimizing unwanted side reactions with biomolecules prior to DNA binding.[87] The two extra ligands allow further impartment of desired properties such as lipopholicity, redox stability, cancer cell-targeting, and bioactivity. Thus, the advantages of Pt(IV) prodrugs over their Pt(II) counterparts include: (1) increased stability before reaching targeting sites; (2) diminished side effects due to less side reactions; (3) improved pharmacological properties gained with the axial ligands, e.g., cancer cell targeting, modified lipophilicity, improved cellular uptake, and attachment to NPs or other carrier systems.[88] There are some excellent reviews focused on Pt(IV) prodrugs;[87-88] however, we will mainly summarize Pt(IV) prodrugs specifically used for GB treatment.

Very recently, a cisplatin prodrug MP-Pt(IV) targeting mitochondria of GB was synthesized and showed high cytotoxicity against GB cells potentiated by elevating mitochondrial ascorbate, exhibited potent chemotherapeutic effect in intracranial GB patient-derived xenograft mouse models, and potentiated both TMZ and TMZ-chemoradiation therapies.[145-146] Another prodrug Pt(IV)Ac-POA was synthesized and evaluated against rat C6 GB cells, showing promising improvement chemotherapy *in vitro* via inducing cell death through different pathways.[123] Sabo et. cl. synthesized novel Pt(IV) complexes containing cyclohexyl ethylenediamine-N,N′-diacetate ligands, and modified them with methylene recently. [147-148] The biological activities were evaluated in a panel of cells including U251 GB cells, showing significantly increased cytotoxicity compared to the ligands and cisplatin. In an earlier report from Sabo, the cytotoxicity of the Pt(IV) prodrug was not affected by aloe emodin, while anticancer activity of cisplatin was eliminated by abolishing extracellular signal-regulated kinase (ERK) in tumor cells induced by cisplatin, implying ERK-independent toxicity of the Pt(IV) prodrug.[149] Back in 1999, a Pt(IV)-bis(monoglutarate) complex was synthesized and evaluated against glioma cells, showing significantly higher cytotoxic effect than cisplatin, probably inducing apoptosis in glioma cells through a p53-dependent pathway.[150]

1.2.4 Pt-based NPs for GB treatment

Although the large number of examples described in the previous sections and the fact that Pt agents accounts for a large proportion as anticancer drugs against a wide range of tumors, they stumbled over the treatment in GB in clinical trials with patients. Like other chemotherapeutics for GB, the most fundamental hurdle to the unsuccessful treatment of Pt agents lies in the difficulty for crossing the BBB and the requirement of relatively high doses to reach effective concentration in tumor sites thus resulting in dose-related toxicities. NPs may improve the therapeutic effects of the Pt agents, attributable to the advantages brought by nanoscale platforms to overcome such drug delivery challenges. NP formulations may also possess advantages to address the off-target toxicities over free drugs by their targeting capability. Representative examples so far described with this aim are described next and listed in Table 1.1.

To decrease the opsonization in bloodstream and prolong circulation time while increasing accumulation in tumor sites, PEG/PEO was used.[151-152] In fact, PEG itself is already used to stabilize solid lipid NPs loading Pt(IV) prodrugs to enhance BBB penetration, resulting in significantly enhanced cellular uptake and cytotoxicity in U87 GB cells.[151] PEO-triblock polymer was incorporated into hybrid Gd(III)-cisplatin NPs, showing hypersignal on T_2-weighted MR images *in vivo*, and significantly enhanced Pt accumulation and subsequent Pt-DNA adduct formation in GB cells.[152] The cisplatin-loaded poly(aspartic acid)-PEG NPs were delivered by local injection or CED into F98 glioma-bearing rats, exhibiting reduced cisplatin-induced toxicities, and significantly enhanced median survival time compared to free cisplatin or cisplatin-loaded non-PEGylated NPs.[153]

Alternatively, PCL/PLGA polymeric NPs also functioned as safe and effective carriers, providing sustained and controlled release of Pt drugs. Carboplatin-loaded PCL NPs can enhance the uptake in U87 glioma cells and reduce the carboplatin-induced hemolysis *in vivo*.[154] Another report showed that carboplatin-loaded PCL NPs can enhance the cytotoxicity compared to free drug, gain controlled release *in vitro* and *ex vivo*, and significantly enhance the in situ nasal absorption than the free drug.[155] In addition, carboplatin/PLGA NPs showed enhanced cytotoxicity compared to the free drug; after delivered to rat and pig brain using CED, the NPs resulted in prolonged tissue half-life, and reduced neuronal toxicity.[156] The authors presented for the first time the possible application of carboplatin/PLGA NPs as a potential treatment for GB by CED.

On the other hand, other polymeric NPs were coated with surfactant or small protein to facilitate the transport across the BBB. PBCA NPs were coated with polysorbate 80 (Tween® 80) as endocytosis receptor via endothelial cells. Polysorbate 80 was reported to have high affinity to apolipoprotein E in plasma, with corona of which the NPs are identified as low-density lipoprotein (LDL) and are absorbed into the brain.[157] Unfortunately, it failed to transport the PBCA NPs passing BBB *in vivo* in this case.[158] PLGA NPs were coated with a small protein, namely protamine, to facilitate the penetration of the NPs across the BBB via adsorptive-mediated transcytosis and augment the brain delivery of NPs and cisplatin loaded. The *in vitro* results showed that

protamine-coated PLGA NPs significantly increased the cellular uptake and cytotoxicity compared to uncoated NPs or cisplatin.[159]

Inorganic NP delivery systems without surface modifications showed relatively limited advantage over the free prodrugs. Still, they demonstrated the versatility of nanocarrier platforms. For instance, a hybrid nanocomposite composed of γ-Fe_2O_3 NPs and nanographene oxide showed high affinity to cisplatin, which exhibited superparamagnetic-like behavior and comparative anticancer activity to cisplatin.[160] Pt-NPs and cisplatin were compared against U87 glioma cells or tumor tissue, finding that the Pt-NPs showed antiproliferative activity but significantly lower than cisplatin.[161] Coiled nanotubes were also employed to associate with a Pt(IV) compound, showing selective cytotoxicity against GB cancer cells but not human astrocytes probable via activation of caspase 3/7.[162]

Pt agent	Form	Cells/Animal models	Effect/Mechanism of action	Reference
Pt(IV) prodrugs	Solid lipid NPs (SLNs)	U87 human glioblastoma cells, hCMEC/D3 endothelial cells	Enhanced permeability, improved cell uptake compared to free drug	[151]
Pt(IV) prodrug	Coil nanotubes	U87, U251 and patient GB cells, human astrocytes, U87 xenografts	Enhanced *in vitro* and *in vivo* toxicity than free prodrug, activating multiple cell death pathways in GB cells without affecting astrocytes *in vitro* or causing damage to normal mouse brain	[162]
Cisplatin	Liposomes functionalized with antibodies against the native form of VEGF or VEGFR2 receptor	C6, U87 cells	Prolonged blood circulation time in glioma C6-bearing rats. *In vitro* data confirmed that conjugation of specific antibodies increased the intracellular concentration of the liposomes and improved cytotoxicity	[163]
Cisplatin	PBCA NPs	C6 cells, C6 xenografts	Very slow release for encapsulated cisplatin, comparative cytotoxicity as cisplatin, slightly longer mean survival time than cisplatin, reduced side effect	[158]

Cisplatin	Protamine-functionalized PLGA NPs	U87 cells	Significantly higher cytotoxicity than cisplatin, enhanced cellular uptake, able to cross *in vitro* BBB model, improved therapeutic index	[159]
Cisplatin	γ-Fe_2O_3 NPs and nanographene oxide hybrid NPs	U87 cells	superparamagnetic-like behavior, but showed little cytotoxicity at 10 μM	[160]
Cisplatin	Gd grafted PEO micelles	U87 and U251 cells, Nude female mice	Hypersignal on T2-weighted MRI, 50-fold increased cellular accumulation and 32-fold Pt-DNA adduct compared to free cisplatin	[152]
Cisplatin	Poly(aspartic acid)-PEG NPs	9L, F98 cells, and F98 glioma-bearing Fischer rat	Controlled release, reduced cisplatin-induced toxicities, and significantly enhanced median survival time	[153]
Carboplatin	PLGA NPs	UPAN and SNB19 cells, rat and pig	enhanced cytotoxicity prolonged tissue half-life, and reduced neuronal toxicity	[156]
Carboplatin	PCL NPs	U87 cells	Enhanced cellular uptake and profound cytotoxicity, reduced carboplatin-induced hemolysis	[154]
Carboplatin	PCL NPs	LN229 cells, sheep nasal mucosa for ex vivo permeation, Wistar rats for in situ nasal perfusion	Controlled release *in vitro* and ex vivo, enhanced cytotoxicity *in vitro*, significantly increased nasal absorption *in vivo*	[155]
Pt^0 NPs	Pt NPs	U87 cells	Inhibition on viability, decreased tumor tissue and causing pathomorphological changes, upregulated p53 and caspase-3 mRNA expression	[161]
Pt^0 NPs	FePt NPs	U251, U87, and H4 cells	High cytotoxicity observed in lipophilic coated FePt NPs and low cytotoxicity in the case of hydrophilic FePt NPs	[164]

Table 1.1 Preclinical studies using Pt-containing NPs for GB monotherapy

1.2.5 Combined therapies for GB treatment using Pt-containing NPs

To make the encapsulation more efficient due to the complexity of GB itself, researchers has stepped up much effort to combine various therapeutic strategies, mainly chemotherapy and radiotherapy. Representative examples are described next.

Ruiz etc. developed a novel dendritic silver-platinum NPs which showed selective anticancer efficacy in glioblastoma and melanoma cell lines but no side effect in fibroblast cells at lower concentration, and higher bactericidal effect than silver NPs.[165] In another example, cisplatin-tethered Au nanospheres (Figure 1.10) sensitized the patient-derived resistant GB cells, resulting in enhanced synergy between cisplatin and radiotherapy. As a consequence, significant enhancement in DNA DSB, increased apoptosis rate, and photo/Auger electron mediated radiosensitization, leading to complete ablation of the tumor cells *in vitro*. These results highlighted the potential of Pt agents to abrogate treatment resistance in GB cells, opening the way for possible Pt-radiation combined therapies in the future.[166]

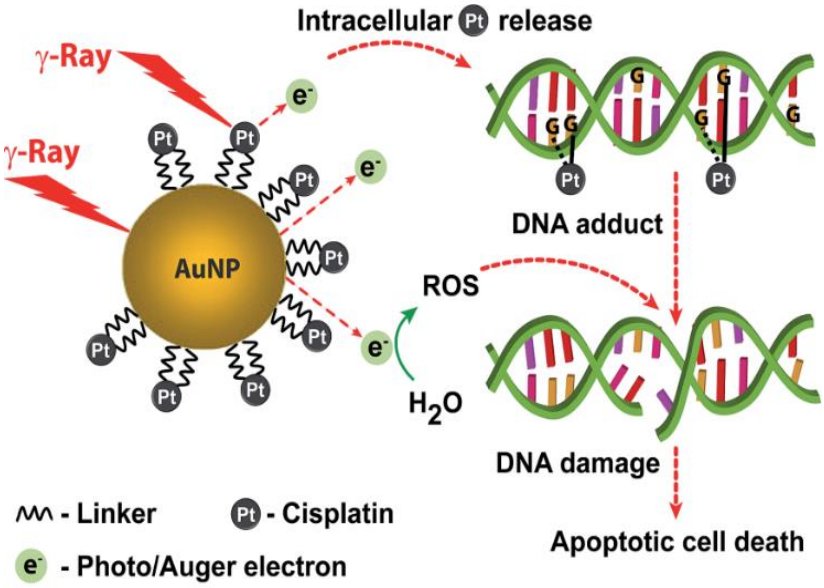

Figure 1.10 Cisplatin-tethered gold NPs combining radiotherapy for glioblastoma treatment.[166]

Coluccia et al. developed cisplatin conjugated gold NPs combining MR-guided focused ultrasound as well as targeting peptide to intensify GB treatment. It greatly inhibited the GB cell growth compared to free cisplatin and showed marked synergy with radiotherapy *in vitro*. Furthermore, this system reduced the growth of GB tumors *in vivo* and the MR-guided focused ultrasound enhanced BBB permeability and cisplatin delivery in brain.[167] The work led by M. De Waard evaluated the anti-glioma efficacy of a novel Pt-maurocalcine conjugate and explored its working mechanism. They proved

this conjugate of Pt with cell-penetrating peptide had enhanced anticancer effect than cisplatin, working by targeting the intracellular redox system, inducing apoptosis through modulation of PI3K/AKT/FoxO3a signaling pathway.[122,168] In another work, cyclic Arg-Gly-Asp (cRGD) was incorporated into the polymeric micelles loading Pt(II) complex for targeted delivery into U87 GB (Figure 1.11). cRGD is able to target $\alpha_v\beta_3/\alpha_v\beta_5$ integrins, which are overexpressed in angiogenic sites and tumors, as well as intractable human glioblastoma (U87MG). The results showed rapid and high accumulation of drug from vessels to tumor parenchyma compared with non-targeted micelles, suggesting cRGD may target via active internalization pathway.[169]

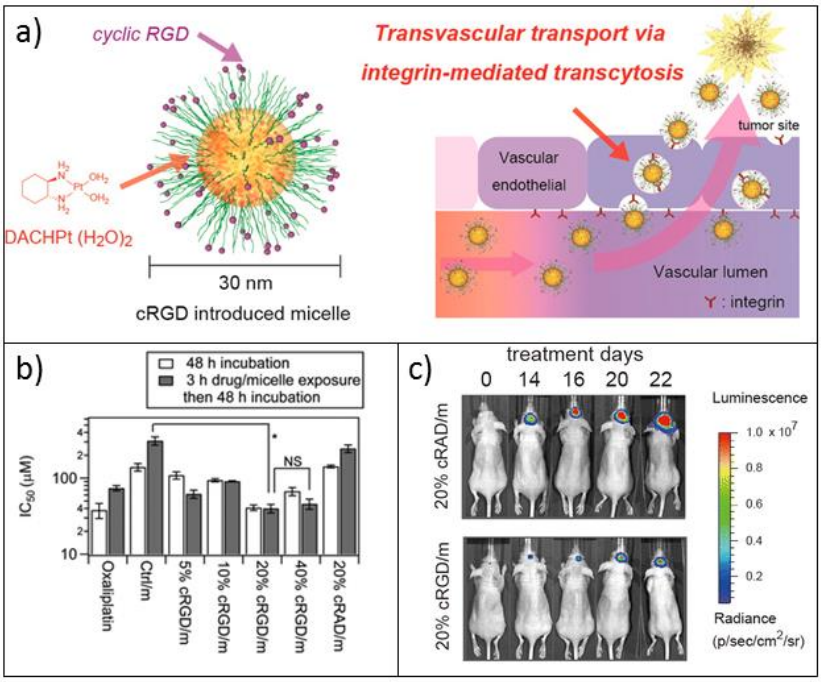

Figure 1.11 a) Schematic of cRGD-Pt-micelles (cRGD/m) and description of the mechanism of transport through BBB; b) *In vitro* cytotoxicities of cRGD-Pt-micelles in the U87MG cells; c) Effects of cRGD-Pt-micelles in orthotopic U87MG glioblastoma in comparison with the non-targeted ligand bearing micelles (cRAD/m).[169]

Finally, the research group led by Benoit Paquette published a series of papers concerning the combination of Pt drugs with concomitant radiotherapy, optimizing the formulation and administration routes to achieve the best therapeutic outcome.[133,170-171] Step by step, they optimized the combinational therapies, from the comparison of free drugs and liposomal formulations of Pt compounds to the optimization of

administration routes. Recently, these researchers optimized the combined therapies, and adopted CED to deliver the Pt drugs or their liposomal formulations, following radiation treatment. The local delivery considerably increased the drug retention in tumor compared to intravenous or intra-arterial administration, reduced the side effects, and resulted in a higher median survival time when combined with radiotherapy. When tested in F98 glioma-bearing Fischer rats, the liposomal formulations enhanced the tumor uptake, and improved specificity *in vivo*.[172]

1.3. Administration routes for nanoparticles to reach the brain

As previously mentioned, one of the biggest challenges is to design drug carriers able to cross the highly selective BBB. Even after the integrity of BBB is disrupted and so-called BBTB forms, the permeability of BBTB is heterogeneous and still remains quite low (Figure 1.12).[173]

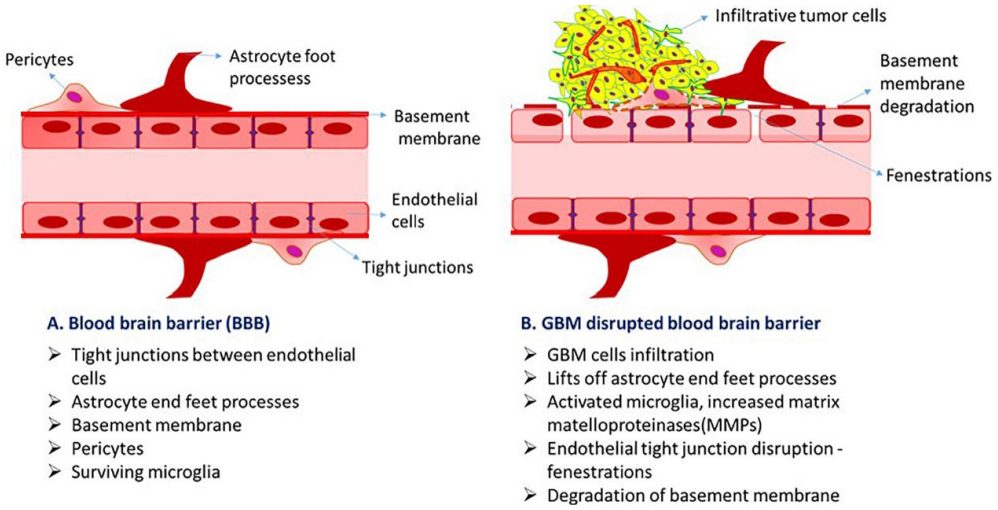

Figure 1.12 Features of the BBB (A) and disrupted BBTB (B). A) Normal BBB constitutes endothelial cells, tight junctions between endothelial cells, pericytes, basement membrane and astrocyte end foot together functioning as complex network which is impermeable to large macromolecule, excessive CNS fluids and other blood components. B) The disruption of BBB in GB condition is due to infiltrative glioma cells that lifts off the astrocytic end foot process and also glioma cells secrete factors that downregulates tight junction proteins which leads to dysfunctional blood brain barrier.[36]

Like conventional chemotherapeutic agents, nanoparticles for GB treatment were administered via various routes, including intravenous (IV) injection, intracranial delivery or oral route.[174] Depending on the delivery sites, the main administration routes

can be divided into three types for nanoparticles treating brain tumors like GB: 1) direct delivery to the brain, 2) direct systemic delivery to the brain, and 3) indirect systemic delivery to the brain.[68] In general, the choice of a particular administration route largely depends on the characteristics of the therapeutic formulations, the required time of onset of action, the required site of action, among other factors.

- *Direct delivery*. This type of administration is usually invasive, including intracerebroventricular administration, intracerebral administration, convection enhanced delivery (CED), intrathecal administration, etc.[175-176] Among them, CED is an invasive administration way where catheters are placed inside the interstitial space in parenchyma, drugs driven into the brain by positive pressure gradient using a pump. CED has been utilized to deliver paclitaxel-loaded lipid nanocapsules directly into the brain of mice, leading to significantly increased overall survival compared with mice treated with free paclitaxel.[177-178] TMZ-loaded micelles embedded in hydrogel were injected directly through an incision drilled in the skull of mice, which was well tolerated and leaded to improved drug release profile.[179] However, the direct delivery to the brain is limited to its invasive nature, the risk of infection, the need to control critical parameters to avoid brain damage, and difficulty in intracerebral diffusion.[180]

- *Direct systemic delivery*. This approach involves nanoparticles administered directly into blood stream through carotid artery and transported to the brain avoiding the rest of the systemic circulation. This administration technique showed improved survival with reduced risk of brain damage compared to CED.[181] For example, ferrociphekunol-loaded nanoparticles were administered into the brain of GB-bearing rats using both direct systemic delivery and CED. Direct systemic delivery to brain exhibited a modest increase in survival compared to CED.[180,182]

- *Indirect systemic delivery*. This approach aims to deliver nanoparticles into the systemic circulation via routes requiring indirect absorption of the brain, including intravenous (IV) injection or intraperitoneal injection and oral administration. Among these indirect brain delivery routes, IV administration is most frequently used in many preclinical studies for GB treatment.[183-185] The main advantages of IV injection set root in its rapid and accurate delivery into the systemic circulation, avoiding first-

pass metabolism, leading to relatively fast response and high bioavailability. It is extremely suitable for drugs which cannot absorbed by the gastrointestinal tract or cannot be injected into muscles or other tissues.[174] Similarly, intraperitoneal injection is commonly used when administering large doses into peritoneal tissues or when it is difficult to locate a vein for direct systemic delivery, which can avoid anaphylactic shock after IV injection and was also used in the battle against GB.[186] In addition, oral administration features with convenience, non-invasiveness, and patient compliance, which has also been applied to the research on nanoparticles for GB treatment.[187] However, the efficiency of these routes of indirect systemic delivery is highly challenging and considerably compromised due to the RES clearance of nanoparticles from the systemic circulation and the presence of the BBB blocking the transport into the brain.

However, in practice, the local delivery augment the therapeutic concentration in tumor sites while the clinical outcome was still unsatisfactory in treating GB, and the low intra-brain drug diffusion rate may cause undesired high local toxicity.[188] Fortunately, intranasal (IN) administration has been proposed as a non-invasive alternative route to enable the nose-to-brain delivery of therapeutic agents and showed promising results against GB.[189] Intranasal route provides the possibility to bypass the BBB and deliver drugs into the brain directly. The pathways of drugs delivered by IN route from nasal mucosa to the brain (Figure 1.13) have been extensively researched and reviewed in recent years. The nasal cavity can be simply divided into the respiratory and the olfactory regions. In the respiratory region, after the drugs escape from mucociliary clearance, they can either directly enter the brain through the trigeminal nerve pathway or enter the systemic circulation. On the other hand, drugs can be transported or diffuse directly into the brain through the olfactory mucosa pathway in the olfactory region.[190] Existing preclinical and clinical studies support the idea that IN delivery of nanosized therapeutic agents may become a breakthrough in the fight against GB.[191]

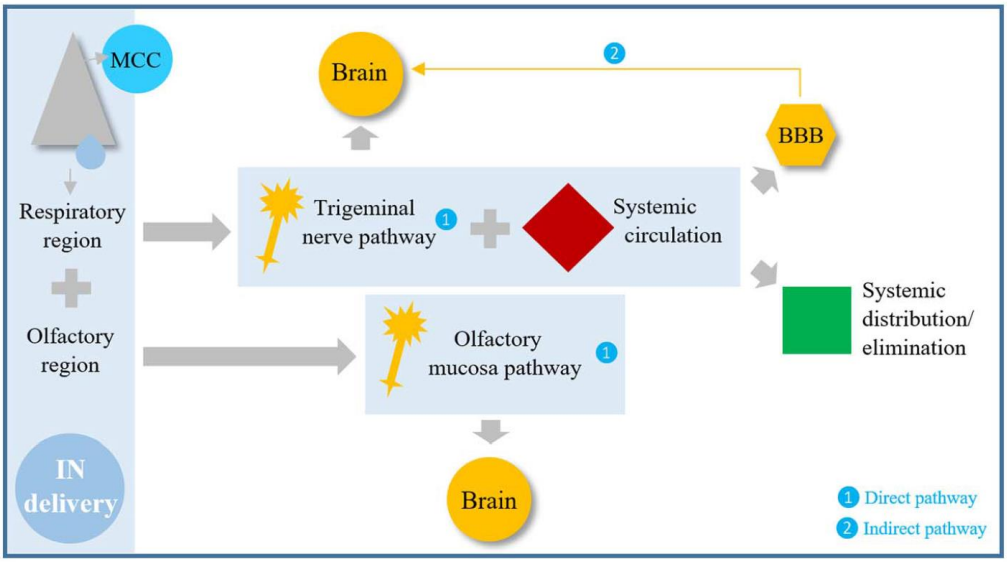

Figure 1.13 Schematic representation of IN delivery's direct and indirect pathways. After instillation, the drug can either: a) suffer mucociliary clearance (MCC); b) reach the respiratory region, where it will either enter the systemic circulation or be directly transported to the brain through the trigeminal nerve pathway (direct pathway); or c) reach the olfactory region, where it will be transported to the brain through the olfactory mucosa pathway (direct pathway). The drugs that reach systemic circulation can be distributed to nontarget tissues, followed by elimination, or still reach the brain across the blood-brain-barrier (BBB) (indirect pathway).[190]

The versatility of nanocarriers provides various approaches to overcome the problems related to IN administration such as fast mucociliary clearance, penetration through the nasal mucosa, and enzymatic degradation. Nanocarriers can be tuned with size, surface properties, targeting ligands and other factors to gain optimal conditions to effectively transport therapeutic drugs into the brain. So far, liposomes, chitosan NPs, polymeric NPs, solid lipid NPs, nanoemulsions, micelles, and nanoplexes have been mainly studied for the nose-to-brain delivery.[191] However, the application of IN delivery may also be limited due to the restriction of dosing volume, non-desired drug accumulation in off-target brain areas, and possible pulmonary risks.[190]

1.4 Our approach

As aforementioned, although the reevaluation and repurposing of platinum-based chemotherapy has aroused the attention of researchers, the current Pt-based chemotherapy has been still limited and at the early stages for GB treatment. Therefore, the development of novel chemotherapeutic strategies based on Pt agents is urgently

required to pave the way for possible improvement for the dismayed GB therapy. To take advantage of Pt(IV) prodrug and nanodrug delivery systems, a novel Pt(IV) prodrug functionalized with catechol moieties (PtBC) has been synthesized in this thesis, and used as building block for the fabrication of nanoparticle delivery systems (Figure 1.14) able to be addressed to the current challenges faced in GB chemotherapy. The chemical versatility brought by the catechol moiety present in the Pt(IV) prodrug allows different approaches to form two types of NPs, termed Pt-Fe NCPs obtained by the coordination of the Pt(IV) prodrug with iron ions (nanostructured coordination polymers) and pPtBC NPs obtained by chemical polymerization using an oxidizing agent (nanostructured polymers).

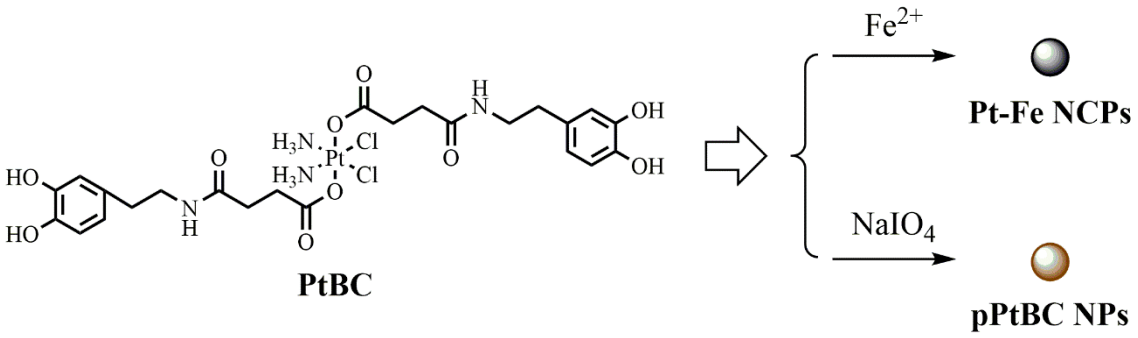

Figure 1.14 Nanodrug delivery systems formed by two different approaches using the Pt(IV) prodrug PtBC.

Both NPs has been evaluated for their potential as GB chemotherapeutic agents. Specific *in vitro* and *in vivo* studies using GB models have been stablished to determine the potentiality of the developed nanoformulated species for GB therapy. Taken the unique location and features of GB into consideration, intranasal administration has been adopted as an alternative to conventional systemic routes in the *in vivo* studies, aiming to deliver both NPs into the brain and GB tumors more effectively, thus achieving optimal responses while reducing side effects.

1.5 References

(1) Ostrom, Q. T.; Cioffi, G.; Gittleman, H.; Patil, N.; Waite, K.; Kruchko, C.; Barnholtz-Sloan, J. S. Cbtrus Statistical Report: Primary Brain and Other Central Nervous System Tumors Diagnosed in the United States in 2012–2016. *Neuro Oncol.* **2019,** *21* (Supplement_5), v1-v100. DOI: 10.1093/neuonc/noz150.
(2) Louis, D. N.; Perry, A.; Reifenberger, G.; von Deimling, A.; Figarella-Branger, D.; Cavenee, W. K.; Ohgaki, H.; Wiestler, O. D.; Kleihues, P.; Ellison, D. W. The 2016 World Health Organization Classification of Tumors of the Central Nervous System: A Summary. *Acta Neuropathol.* **2016,** *131* (6), 803-820. DOI: 10.1007/s00401-016-1545-1.
(3) Stupp, R.; Mason, W. P.; van den Bent, M. J.; Weller, M.; Fisher, B.; Taphoorn, M. J. B.; Belanger, K.; Brandes, A. A.; Marosi, C.; Bogdahn, U.; Curschmann, J.; Janzer, R. C.; Ludwin, S. K.; Gorlia, T.; Allgeier, A.; Lacombe, D.; Cairncross, J. G.; Eisenhauer, E.; Mirimanoff, R. O.; Van Den Weyngaert, D., et al. Radiotherapy Plus Concomitant and Adjuvant Temozolomide for Glioblastoma. *N. Engl. J. Med.* **2005,** *352* (10), 987-996. DOI: 10.1056/NEJMoa043330.
(4) Schiffer, D.; Annovazzi, L.; Casalone, C.; Corona, C.; Mellai, M. Glioblastoma: Microenvironment and Niche Concept. *Cancers (Basel)* **2018,** *11* (1), 5. DOI: 10.3390/cancers11010005.
(5) Zhang, X.; Ding, K.; Wang, J.; Li, X.; Zhao, P. Chemoresistance Caused by the Microenvironment of Glioblastoma and the Corresponding Solutions. *Biomed. Pharmacother.* **2019,** *109,* 39-46. DOI: 10.1016/j.biopha.2018.10.063.
(6) Yadavalli, S.; Yenugonda, V. M.; Kesari, S. Repurposed Drugs in Treating Glioblastoma Multiforme: Clinical Trials Update. *Cancer J.* **2019,** *25* (2), 139-146. DOI: 10.1097/ppo.0000000000000365.
(7) Tabatabai, G.; Wakimoto, H. Glioblastoma: State of the Art and Future Perspectives. *Cancers (Basel)* **2019,** *11* (8), 1091. DOI: 10.3390/cancers11081091.
(8) Omuro, A.; DeAngelis, L. M. Glioblastoma and Other Malignant Gliomas: A Clinical Review. *JAMA* **2013,** *310* (17), 1842-1850. DOI: 10.1001/jama.2013.280319.
(9) Quail, D. F.; Joyce, J. A. The Microenvironmental Landscape of Brain Tumors. *Cancer Cell* **2017,** *31* (3), 326-341. DOI: 10.1016/j.ccell.2017.02.009.
(10) Broekman, M. L.; Maas, S. L. N.; Abels, E. R.; Mempel, T. R.; Krichevsky, A. M.; Breakefield, X. O. Multidimensional Communication in the Microenvirons of Glioblastoma. *Nat. Rev. Neurol.* **2018,** *14* (8), 482-495. DOI: 10.1038/s41582-018-0025-8.
(11) Matarredona, E. R.; Pastor, A. M. Extracellular Vesicle-Mediated Communication between the Glioblastoma and Its Microenvironment. *Cells* **2019,** *9* (1). DOI: 10.3390/cells9010096.
(12) Nieland, L.; Morsett, L. M.; Broekman, M. L. D.; Breakefield, X. O.; Abels, E. R. Extracellular Vesicle-Mediated Bilateral Communication between Glioblastoma and Astrocytes. *Trends Neurosci.* **2020**. DOI: 10.1016/j.tins.2020.10.014.
(13) Wolf, K. J.; Chen, J.; Coombes, J. D.; Aghi, M. K.; Kumar, S. Dissecting and Rebuilding the Glioblastoma Microenvironment with Engineered Materials. *Nature Reviews Materials* **2019,** *4* (10), 651-668. DOI: 10.1038/s41578-019-0135-y.
(14) Fricker, G.; Ott, M.; Mahringer, A., The Blood Brain Barrier (Bbb). 2014.
(15) Wolburg, H.; Noell, S.; Fallier-Becker, P.; Mack, A. F.; Wolburg-Buchholz, K. The Disturbed Blood–Brain Barrier in Human Glioblastoma. *Mol. Aspects Med.* **2012,** *33* (5), 579-589. DOI: 10.1016/j.mam.2012.02.003.
(16) Watkins, S.; Robel, S.; Kimbrough, I. F.; Robert, S. M.; Ellis-Davies, G.; Sontheimer, H. Disruption of Astrocyte–Vascular Coupling and the Blood–Brain Barrier by Invading Glioma Cells. *Nat. Commun.* **2014,** *5* (1), 4196. DOI: 10.1038/ncomms5196.
(17) Jackson, C. M.; Choi, J.; Lim, M. Mechanisms of Immunotherapy Resistance: Lessons from Glioblastoma. *Nat. Immunol.* **2019,** *20* (9), 1100-1109. DOI: 10.1038/s41590-019-0433-y.

(18) Balça-Silva, J.; Matias, D.; Carmo, A. d.; Sarmento-Ribeiro, A. B.; Lopes, M. C.; Moura-Neto, V. Cellular and Molecular Mechanisms of Glioblastoma Malignancy: Implications in Resistance and Therapeutic Strategies. *Semin. Cancer Biol.* **2019,** *58*, 130-141. DOI: 10.1016/j.semcancer.2018.09.007.
(19) Hu, Y.-L.; DeLay, M.; Jahangiri, A.; Molinaro, A. M.; Rose, S. D.; Carbonell, W. S.; Aghi, M. K. Hypoxia-Induced Autophagy Promotes Tumor Cell Survival and Adaptation to Antiangiogenic Treatment in Glioblastoma. *Cancer Res.* **2012,** *72* (7), 1773. DOI: 10.1158/0008-5472.CAN-11-3831.
(20) Brandao, M.; Simon, T.; Critchley, G.; Giamas, G. Astrocytes, the Rising Stars of the Glioblastoma Microenvironment. *Glia* **2019,** *67* (5), 779-790. DOI: 10.1002/glia.23520.
(21) Han, S. J.; Englot, D. J.; Birk, H.; Molinaro, A. M.; Chang, S. M.; Clarke, J. L.; Prados, M. D.; Taylor, J. W.; Berger, M. S.; Butowski, N. A. Impact of Timing of Concurrent Chemoradiation for Newly Diagnosed Glioblastoma: A Critical Review of Current Evidence. *Neurosurgery* **2015,** *62* (CN_suppl_1), 160-165. DOI: 10.1227/NEU.0000000000000801.
(22) Wang, H.; Cai, S.; Ernstberger, A.; Bailey, B. J.; Wang, M. Z.; Cai, W.; Goebel, W. S.; Czader, M. B.; Crean, C.; Suvannasankha, A.; Shokolenkoc, I.; Wilson, G. L.; Baluyut, A. R.; Mayo, L. D.; Pollok, K. E. Temozolomide-Mediated DNA Methylation in Human Myeloid Precursor Cells: Differential Involvement of Intrinsic and Extrinsic Apoptotic Pathways. *Clin. Cancer Res.* **2013,** *19* (10), 2699. DOI: 10.1158/1078-0432.CCR-12-2671.
(23) Stupp, R.; Mason, W. P.; van den Bent, M. J.; Weller, M.; Fisher, B.; Taphoorn, M. J. B.; Belanger, K.; Brandes, A. A.; Marosi, C.; Bogdahn, U.; Curschmann, J.; Janzer, R. C.; Ludwin, S. K.; Gorlia, T.; Allgeier, A.; Lacombe, D.; Cairncross, J. G.; Eisenhauer, E.; Mirimanoff, R. O. Radiotherapy Plus Concomitant and Adjuvant Temozolomide for Glioblastoma. *N. Engl. J. Med.* **2005,** *352* (10), 987-996. DOI: 10.1056/NEJMoa043330.
(24) Stevens, M. F. G.; Newlands, E. S. From Triazines and Triazenes to Temozolomide. *Eur. J. Cancer* **1993,** *29* (7), 1045-1047. DOI: 10.1016/S0959-8049(05)80221-7.
(25) Tatar, Z.; Thivat, E.; Planchat, E.; Gimbergues, P.; Gadea, E.; Abrial, C.; Durando, X. Temozolomide and Unusual Indications: Review of Literature. *Cancer Treat. Rev.* **2013,** *39* (2), 125-135. DOI: 10.1016/j.ctrv.2012.06.002.
(26) Newlands, E. S.; Stevens, M. F.; Wedge, S. R.; Wheelhouse, R. T.; Brock, C. Temozolomide: A Review of Its Discovery, Chemical Properties, Pre-Clinical Development and Clinical Trials. *Cancer Treat. Rev.* **1997,** *23* (1), 35-61. DOI: 10.1016/s0305-7372(97)90019-0.
(27) Rai, R.; Banerjee, M.; Wong, D. H.; McCullagh, E.; Gupta, A.; Tripathi, S.; Riquelme, E.; Jangir, R.; Yadav, S.; Raja, M.; Melkani, P.; Dixit, V.; Patil, U.; Shrivastava, R.; Middya, S.; Olivares, F.; Guerrero, J.; Surya, A.; Pham, S. M.; Bernales, S., et al. Temozolomide Analogs with Improved Brain/Plasma Ratios - Exploring the Possibility of Enhancing the Therapeutic Index of Temozolomide. *Bioorg. Med. Chem. Lett.* **2016,** *26* (20), 5103-5109. DOI: 10.1016/j.bmcl.2016.08.064.
(28) Arora, A.; Somasundaram, K. Glioblastoma Vs Temozolomide: Can the Red Queen Race Be Won? *Cancer Biol. Ther.* **2019,** *20* (8), 1083-1090. DOI: 10.1080/15384047.2019.1599662.
(29) Fang, C.; Wang, K.; Stephen, Z. R.; Mu, Q.; Kievit, F. M.; Chiu, D. T.; Press, O. W.; Zhang, M. Temozolomide Nanoparticles for Targeted Glioblastoma Therapy. *ACS Appl. Mater. Interfaces* **2015,** *7* (12), 6674-6682. DOI: 10.1021/am5092165.
(30) Patel, A. P.; Tirosh, I.; Trombetta, J. J.; Shalek, A. K.; Gillespie, S. M.; Wakimoto, H.; Cahill, D. P.; Nahed, B. V.; Curry, W. T.; Martuza, R. L.; Louis, D. N.; Rozenblatt-Rosen, O.; Suvà, M. L.; Regev, A.; Bernstein, B. E. Single-Cell Rna-Seq Highlights Intratumoral Heterogeneity in Primary Glioblastoma. *Science* **2014,** *344* (6190), 1396-1401. DOI: 10.1126/science.1254257.
(31) Osuka, S.; Van Meir, E. G. Overcoming Therapeutic Resistance in Glioblastoma: The Way Forward. *J. Clin. Invest.* **2017,** *127* (2), 415-426. DOI: 10.1172/jci89587.
(32) Hombach-Klonisch, S.; Mehrpour, M.; Shojaei, S.; Harlos, C.; Pitz, M.; Hamai, A.; Siemianowicz, K.; Likus, W.; Wiechec, E.; Toyota, B. D.; Hoshyar, R.; Seyfoori, A.; Sepehri, Z.; Ande, S. R.; Khadem, F.; Akbari, M.; Gorman, A. M.; Samali, A.; Klonisch, T.; Ghavami, S.

Glioblastoma and Chemoresistance to Alkylating Agents: Involvement of Apoptosis, Autophagy, and Unfolded Protein Response. *Pharmacol. Ther.* **2018,** *184*, 13-41. DOI: 10.1016/j.pharmthera.2017.10.017.
(33) Piccirillo, S. G.; Combi, R.; Cajola, L.; Patrizi, A.; Redaelli, S.; Bentivegna, A.; Baronchelli, S.; Maira, G.; Pollo, B.; Mangiola, A.; DiMeco, F.; Dalprà, L.; Vescovi, A. L. Distinct Pools of Cancer Stem-Like Cells Coexist within Human Glioblastomas and Display Different Tumorigenicity and Independent Genomic Evolution. *Oncogene* **2009,** *28* (15), 1807-1811. DOI: 10.1038/onc.2009.27.
(34) Pistollato, F.; Abbadi, S.; Rampazzo, E.; Persano, L.; Della Puppa, A.; Frasson, C.; Sarto, E.; Scienza, R.; D'Avella, D.; Basso, G. Intratumoral Hypoxic Gradient Drives Stem Cells Distribution and Mgmt Expression in Glioblastoma. *Stem Cells* **2010,** *28* (5), 851-862. DOI: 10.1002/stem.415.
(35) Dréan, A.; Rosenberg, S.; Lejeune, F. X.; Goli, L.; Nadaradjane, A. A.; Guehennec, J.; Schmitt, C.; Verreault, M.; Bielle, F.; Mokhtari, K.; Sanson, M.; Carpentier, A.; Delattre, J. Y.; Idbaih, A. Atp Binding Cassette (Abc) Transporters: Expression and Clinical Value in Glioblastoma. *J. Neurooncol.* **2018,** *138* (3), 479-486. DOI: 10.1007/s11060-018-2819-3.
(36) Ganipineni, L. P.; Danhier, F.; Préat, V. Drug Delivery Challenges and Future of Chemotherapeutic Nanomedicine for Glioblastoma Treatment. *J. Control. Release* **2018,** *281*, 42-57. DOI: 10.1016/j.jconrel.2018.05.008.
(37) Li, M.; Luo, Z.; Xia, Z.; Shen, X.; Cai, K. Time-Sequenced Drug Delivery Approaches Towards Effective Chemotherapeutic Treatment of Glioma. *Materials Horizons* **2017,** *4* (6), 977-996. DOI: 10.1039/C7MH00342K.
(38) Le Rhun, E.; Preusser, M.; Roth, P.; Reardon, D. A.; van den Bent, M.; Wen, P.; Reifenberger, G.; Weller, M. Molecular Targeted Therapy of Glioblastoma. *Cancer Treat. Rev.* **2019,** *80*, 101896. DOI: 10.1016/j.ctrv.2019.101896.
(39) Lu, C. T.; Zhao, Y. Z.; Wong, H. L.; Cai, J.; Peng, L.; Tian, X. Q. Current Approaches to Enhance Cns Delivery of Drugs across the Brain Barriers. *Int J Nanomedicine* **2014,** *9*, 2241-2257. DOI: 10.2147/ijn.s61288.
(40) Liu, D. Z.; Cheng, Y.; Cai, R. Q.; Wang Bd, W. W.; Cui, H.; Liu, M.; Zhang, B. L.; Mei, Q. B.; Zhou, S. Y. The Enhancement of Siplk1 Penetration across Bbb and Its Anti Glioblastoma Activity *in Vivo* by Magnet and Transferrin Co-Modified Nanoparticle. *Nanomedicine* **2018,** *14* (3), 991-1003. DOI: 10.1016/j.nano.2018.01.004.
(41) Maeda, H. The Enhanced Permeability and Retention (Epr) Effect in Tumor Vasculature: The Key Role of Tumor-Selective Macromolecular Drug Targeting. *Adv. Enzyme Regul.* **2001,** *41*, 189-207. DOI: 10.1016/s0065-2571(00)00013-3.
(42) Bhowmik, A.; Khan, R.; Ghosh, M. K. Blood Brain Barrier: A Challenge for Effectual Therapy of Brain Tumors. *BioMed Research International* **2015,** *2015*, 320941. DOI: 10.1155/2015/320941.
(43) Attia, M. F.; Anton, N.; Wallyn, J.; Omran, Z.; Vandamme, T. F. An Overview of Active and Passive Targeting Strategies to Improve the Nanocarriers Efficiency to Tumour Sites. *J. Pharm. Pharmacol.* **2019,** *71* (8), 1185-1198. DOI: 10.1111/jphp.13098.
(44) Sarkaria, J. N.; Hu, L. S.; Parney, I. F.; Pafundi, D. H.; Brinkmann, D. H.; Laack, N. N.; Giannini, C.; Burns, T. C.; Kizilbash, S. H.; Laramy, J. K.; Swanson, K. R.; Kaufmann, T. J.; Brown, P. D.; Agar, N. Y. R.; Galanis, E.; Buckner, J. C.; Elmquist, W. F. Is the Blood-Brain Barrier Really Disrupted in All Glioblastomas? A Critical Assessment of Existing Clinical Data. *Neuro Oncol.* **2018,** *20* (2), 184-191. DOI: 10.1093/neuonc/nox175.
(45) Zhao, M.; van Straten, D.; Broekman, M. L. D.; Préat, V.; Schiffelers, R. M. Nanocarrier-Based Drug Combination Therapy for Glioblastoma. *Theranostics* **2020,** *10* (3), 1355-1372. DOI: 10.7150/thno.38147.
(46) Bamrungsap, S.; Zhao, Z.; Chen, T.; Wang, L.; Li, C.; Fu, T.; Tan, W. Nanotechnology in Therapeutics: A Focus on Nanoparticles as a Drug Delivery System. *Nanomedicine (London, England)* **2012,** *7* (8), 1253-1271. DOI: 10.2217/nnm.12.87.

(47) Wu, X.; Yang, H.; Yang, W.; Chen, X.; Gao, J.; Gong, X.; Wang, H.; Duan, Y.; Wei, D.; Chang, J. Nanoparticle-Based Diagnostic and Therapeutic Systems for Brain Tumors. *Journal of Materials Chemistry B* **2019,** *7* (31), 4734-4750. DOI: 10.1039/C9TB00860H.
(48) Yang, J.; Shi, Z.; Liu, R.; Wu, Y.; Zhang, X. Combined-Therapeutic Strategies Synergistically Potentiate Glioblastoma Multiforme Treatment <I>Via</I> Nanotechnology. *Theranostics* **2020,** *10* (7), 3223-3239. DOI: 10.7150/thno.40298.
(49) Havel, H. A. Where Are the Nanodrugs? An Industry Perspective on Development of Drug Products Containing Nanomaterials. *The AAPS journal* **2016,** *18* (6), 1351-1353. DOI: 10.1208/s12248-016-9970-6.
(50) Rehman, M.; Madni, A.; Shi, D.; Ihsan, A.; Tahir, N.; Chang, K. R.; Javed, I.; Webster, T. J. Enhanced Blood Brain Barrier Permeability and Glioblastoma Cell Targeting Via Thermoresponsive Lipid Nanoparticles. *Nanoscale* **2017,** *9* (40), 15434-15440. DOI: 10.1039/c7nr05216b.
(51) Ying, X.; Wang, Y.; Xu, H.; Li, X.; Yan, H.; Tang, H.; Wen, C.; Li, Y. The Construction of the Multifunctional Targeting Ursolic Acids Liposomes and Its Apoptosis Effects to C6 Glioma Stem Cells. *Oncotarget* **2017,** *8* (38), 64129-64142. DOI: 10.18632/oncotarget.19784.
(52) Singleton, W. G.; Collins, A. M.; Bienemann, A. S.; Killick-Cole, C. L.; Haynes, H. R.; Asby, D. J.; Butts, C. P.; Wyatt, M. J.; Barua, N. U.; Gill, S. S. Convection Enhanced Delivery of Panobinostat (Lbh589)-Loaded Pluronic Nano-Micelles Prolongs Survival in the F98 Rat Glioma Model. *Int J Nanomedicine* **2017,** *12*, 1385-1399. DOI: 10.2147/ijn.s125300.
(53) Lin, T.; Zhao, P.; Jiang, Y.; Tang, Y.; Jin, H.; Pan, Z.; He, H.; Yang, V. C.; Huang, Y. Blood-Brain-Barrier-Penetrating Albumin Nanoparticles for Biomimetic Drug Delivery Via Albumin-Binding Protein Pathways for Antiglioma Therapy. *ACS Nano* **2016,** *10* (11), 9999-10012. DOI: 10.1021/acsnano.6b04268.
(54) Hu, J.; Zhang, X.; Wen, Z.; Tan, Y.; Huang, N.; Cheng, S.; Zheng, H.; Cheng, Y. Asn-Gly-Arg-Modified Polydopamine-Coated Nanoparticles for Dual-Targeting Therapy of Brain Glioma in Rats. *Oncotarget* **2016,** *7* (45), 73681-73696. DOI: 10.18632/oncotarget.12047.
(55) Shen, Z.; Liu, T.; Li, Y.; Lau, J.; Yang, Z.; Fan, W.; Zhou, Z.; Shi, C.; Ke, C.; Bregadze, V. I.; Mandal, S. K.; Liu, Y.; Li, Z.; Xue, T.; Zhu, G.; Munasinghe, J.; Niu, G.; Wu, A.; Chen, X. Fenton-Reaction-Acceleratable Magnetic Nanoparticles for Ferroptosis Therapy of Orthotopic Brain Tumors. *ACS Nano* **2018,** *12* (11), 11355-11365. DOI: 10.1021/acsnano.8b06201.
(56) Lu, Y.; Han, S.; Zheng, H.; Ma, R.; Ping, Y.; Zou, J.; Tang, H.; Zhang, Y.; Xu, X.; Li, F. A Novel Rgdyc/Peg Co-Modified Pamam Dendrimer-Loaded Arsenic Trioxide of Glioma Targeting Delivery System. *Int J Nanomedicine* **2018,** *13*, 5937-5952. DOI: 10.2147/IJN.S175418.
(57) Qian, M.; Du, Y.; Wang, S.; Li, C.; Jiang, H.; Shi, W.; Chen, J.; Wang, Y.; Wagner, E.; Huang, R. Highly Crystalline Multicolor Carbon Nanodots for Dual-Modal Imaging-Guided Photothermal Therapy of Glioma. *ACS Appl. Mater. Interfaces* **2018,** *10* (4), 4031-4040. DOI: 10.1021/acsami.7b19716.
(58) Etame, A. B.; Smith, C. A.; Chan, W. C.; Rutka, J. T. Design and Potential Application of Pegylated Gold Nanoparticles with Size-Dependent Permeation through Brain Microvasculature. *Nanomedicine* **2011,** *7* (6), 992-1000. DOI: 10.1016/j.nano.2011.04.004.
(59) Shilo, M.; Sharon, A.; Baranes, K.; Motiei, M.; Lellouche, J. P.; Popovtzer, R. The Effect of Nanoparticle Size on the Probability to Cross the Blood-Brain Barrier: An in-Vitro Endothelial Cell Model. *Journal of nanobiotechnology* **2015,** *13*, 19. DOI: 10.1186/s12951-015-0075-7.
(60) Hanada, S.; Fujioka, K.; Inoue, Y.; Kanaya, F.; Manome, Y.; Yamamoto, K. Cell-Based *in Vitro* Blood-Brain Barrier Model Can Rapidly Evaluate Nanoparticles' Brain Permeability in Association with Particle Size and Surface Modification. *Int J Mol Sci* **2014,** *15* (2), 1812-1825. DOI: 10.3390/ijms15021812.
(61) Lockman, P. R.; Koziara, J. M.; Mumper, R. J.; Allen, D. D. Nanoparticle Surface Charges Alter Blood-Brain Barrier Integrity and Permeability. *J. Drug Target.* **2004,** *12* (9-10), 635-641. DOI: 10.1080/10611860400015936.

(62) Jallouli, Y.; Paillard, A.; Chang, J.; Sevin, E.; Betbeder, D. Influence of Surface Charge and Inner Composition of Porous Nanoparticles to Cross Blood-Brain Barrier *in Vitro*. *Int. J. Pharm.* **2007,** *344* (1-2), 103-109. DOI: 10.1016/j.ijpharm.2007.06.023.
(63) Sonavane, G.; Tomoda, K.; Makino, K. Biodistribution of Colloidal Gold Nanoparticles after Intravenous Administration: Effect of Particle Size. *Colloids Surf. B. Biointerfaces* **2008,** *66* (2), 274-280. DOI: 10.1016/j.colsurfb.2008.07.004.
(64) Kolhar, P.; Anselmo, A. C.; Gupta, V.; Pant, K.; Prabhakarpandian, B.; Ruoslahti, E.; Mitragotri, S. Using Shape Effects to Target Antibody-Coated Nanoparticles to Lung and Brain Endothelium. *Proceedings of the National Academy of Sciences* **2013,** *110* (26), 10753. DOI: 10.1073/pnas.1308345110.
(65) Huang, X.; Li, L.; Liu, T.; Hao, N.; Liu, H.; Chen, D.; Tang, F. The Shape Effect of Mesoporous Silica Nanoparticles on Biodistribution, Clearance, and Biocompatibility *in Vivo*. *ACS Nano* **2011,** *5* (7), 5390-5399. DOI: 10.1021/nn200365a.
(66) Zhan, C.; Gu, B.; Xie, C.; Li, J.; Liu, Y.; Lu, W. Cyclic Rgd Conjugated Poly(Ethylene Glycol)-Co-Poly(Lactic Acid) Micelle Enhances Paclitaxel Anti-Glioblastoma Effect. *J. Control. Release* **2010,** *143* (1), 136-142. DOI: 10.1016/j.jconrel.2009.12.020.
(67) Zhou, J.-e.; Yu, J.; Gao, L.; Sun, L.; Peng, T.; Wang, J.; Zhu, J.; Lu, W.; Zhang, L.; Yan, Z.; Yu, L. Ingr-Modified Liposomes for Tumor Vascular Targeting and Tumor Tissue Penetrating Delivery in the Treatment of Glioblastoma. *Mol. Pharm.* **2017,** *14* (5), 1811-1820. DOI: 10.1021/acs.molpharmaceut.7b00101.
(68) Mahmoud, B. S.; AlAmri, A. H.; McConville, C. Polymeric Nanoparticles for the Treatment of Malignant Gliomas. *Cancers (Basel)* **2020,** *12* (1), 175. DOI: 10.3390/cancers12010175.
(69) Ortiz, R.; Cabeza, L.; Perazzoli, G.; Jimenez-Lopez, J.; García-Pinel, B.; Melguizo, C.; Prados, J. Nanoformulations for Glioblastoma Multiforme: A New Hope for Treatment. *Future Med. Chem.* **2019,** *11* (18), 2459-2480. DOI: 10.4155/fmc-2018-0521.
(70) Mc Carthy, D. J.; Malhotra, M.; O'Mahony, A. M.; Cryan, J. F.; O'Driscoll, C. M. Nanoparticles and the Blood-Brain Barrier: Advancing from in-Vitro Models Towards Therapeutic Significance. *Pharm. Res.* **2015,** *32* (4), 1161-1185. DOI: 10.1007/s11095-014-1545-6.
(71) Zhou, J.; Patel, T. R.; Sirianni, R. W.; Strohbehn, G.; Zheng, M.-Q.; Duong, N.; Schafbauer, T.; Huttner, A. J.; Huang, Y.; Carson, R. E.; Zhang, Y.; Sullivan, D. J., Jr.; Piepmeier, J. M.; Saltzman, W. M. Highly Penetrative, Drug-Loaded Nanocarriers Improve Treatment of Glioblastoma. *Proc. Natl. Acad. Sci. U. S. A.* **2013,** *110* (29), 11751-11756. DOI: 10.1073/pnas.1304504110.
(72) Li, Y.; Wu, M.; Zhang, N.; Tang, C.; Jiang, P.; Liu, X.; Yan, F.; Zheng, H. Mechanisms of Enhanced Antiglioma Efficacy of Polysorbate 80-Modified Paclitaxel-Loaded Plga Nanoparticles by Focused Ultrasound. *J. Cell. Mol. Med.* **2018,** *22* (9), 4171-4182. DOI: 10.1111/jcmm.13695.
(73) Inoue, T.; Yamashita, Y.; Nishihara, M.; Sugiyama, S.; Sonoda, Y.; Kumabe, T.; Yokoyama, M.; Tominaga, T. Therapeutic Efficacy of a Polymeric Micellar Doxorubicin Infused by Convection-Enhanced Delivery against Intracranial 9l Brain Tumor Models. *Neuro Oncol.* **2009,** *11* (2), 151-157. DOI: 10.1215/15228517-2008-068.
(74) Noble, C. O.; Krauze, M. T.; Drummond, D. C.; Yamashita, Y.; Saito, R.; Berger, M. S.; Kirpotin, D. B.; Bankiewicz, K. S.; Park, J. W. Novel Nanoliposomal Cpt-11 Infused by Convection-Enhanced Delivery in Intracranial Tumors: Pharmacology and Efficacy. *Cancer Res.* **2006,** *66* (5), 2801-2806. DOI: 10.1158/0008-5472.can-05-3535.
(75) Chekhonin, V. P.; Baklaushev, V. P.; Yusubalieva, G. M.; Belorusova, A. E.; Gulyaev, M. V.; Tsitrin, E. B.; Grinenko, N. F.; Gurina, O. I.; Pirogov, Y. A. Targeted Delivery of Liposomal Nanocontainers to the Peritumoral Zone of Glioma by Means of Monoclonal Antibodies against Gfap and the Extracellular Loop of Cx43. *Nanomedicine* **2012,** *8* (1), 63-70. DOI: 10.1016/j.nano.2011.05.011.
(76) Kim, S. S.; Rait, A.; Kim, E.; DeMarco, J.; Pirollo, K. F.; Chang, E. H. Encapsulation of Temozolomide in a Tumor-Targeting Nanocomplex Enhances Anti-Cancer Efficacy and Reduces Toxicity in a Mouse Model of Glioblastoma. *Cancer Lett.* **2015,** *369* (1), 250-258. DOI: 10.1016/j.canlet.2015.08.022.

(77) Cheng, Y.; Dai, Q.; Morshed, R. A.; Fan, X.; Wegscheid, M. L.; Wainwright, D. A.; Han, Y.; Zhang, L.; Auffinger, B.; Tobias, A. L.; Rincón, E.; Thaci, B.; Ahmed, A. U.; Warnke, P. C.; He, C.; Lesniak, M. S. Blood-Brain Barrier Permeable Gold Nanoparticles: An Efficient Delivery Platform for Enhanced Malignant Glioma Therapy and Imaging. *Small* **2014,** *10* (24), 5137-5150. DOI: 10.1002/smll.201400654.
(78) Kievit, F. M.; Wang, K.; Ozawa, T.; Tarudji, A. W.; Silber, J. R.; Holland, E. C.; Ellenbogen, R. G.; Zhang, M. Nanoparticle-Mediated Knockdown of DNA Repair Sensitizes Cells to Radiotherapy and Extends Survival in a Genetic Mouse Model of Glioblastoma. *Nanomedicine* **2017,** *13* (7), 2131-2139. DOI: 10.1016/j.nano.2017.06.004.
(79) Mu, Q.; Lin, G.; Patton, V. K.; Wang, K.; Press, O. W.; Zhang, M. Gemcitabine and Chlorotoxin Conjugated Iron Oxide Nanoparticles for Glioblastoma Therapy. *Journal of materials chemistry. B* **2016,** *4* (1), 32-36. DOI: 10.1039/c5tb02123e.
(80) Deshane, J.; Garner, C. C.; Sontheimer, H. Chlorotoxin Inhibits Glioma Cell Invasion Via Matrix Metalloproteinase-2. *J. Biol. Chem.* **2003,** *278* (6), 4135-4144. DOI: 10.1074/jbc.M205662200.
(81) Lee, B. S.; Amano, T.; Wang, H. Q.; Pantoja, J. L.; Yoon, C. W.; Hanson, C. J.; Amatya, R.; Yen, A.; Black, K. L.; Yu, J. S. Reactive Oxygen Species Responsive Nanoprodrug to Treat Intracranial Glioblastoma. *ACS Nano* **2013,** *7* (4), 3061-3077. DOI: 10.1021/nn400347j.
(82) Peyrone, M. Ueber Die Einwirkung Des Ammoniaks Auf Platinchlorür. *Justus Liebigs Ann. Chem.* **1844,** *51* (1), 1-29. DOI: 10.1002/jlac.18440510102.
(83) Rosenberg, B.; Vancamp, L.; Krigas, T. Inhibition of Cell Division in Escherichia Coli by Electrolysis Products from a Platinum Eletrode *Nature* **1965,** *205*, 698-699. DOI: 10.1038/205698a0.
(84) Rosenberg, B.; Vancamp, L.; Trosko, J. E.; Mansour, V. H. Platinum Compounds: A New Class of Potent Antitumour Agents. *Nature* **1969,** *222* (5191), 385-386. DOI: 10.1038/222385a0.
(85) Wiltshaw, E. Cisplatin in the Treatment of Cancer. *Platinum Met. Rev.* **1979,** *23* (3), 90-98. DOI: N/A.
(86) Browning, R. J.; Reardon, P. J. T.; Parhizkar, M.; Pedley, R. B.; Edirisinghe, M.; Knowles, J. C.; Stride, E. Drug Delivery Strategies for Platinum-Based Chemotherapy. *ACS Nano* **2017,** *11* (9), 8560-8578. DOI: 10.1021/acsnano.7b04092.
(87) Johnstone, T. C.; Suntharalingam, K.; Lippard, S. J. The Next Generation of Platinum Drugs: Targeted Pt(Ii) Agents, Nanoparticle Delivery, and Pt(Iv) Prodrugs. *Chem. Rev.* **2016,** *116* (5), 3436-3486. DOI: 10.1021/acs.chemrev.5b00597.
(88) Dilruba, S.; Kalayda, G. V. Platinum-Based Drugs: Past, Present and Future. *Cancer Chemother. Pharmacol.* **2016,** *77* (6), 1103-1124. DOI: 10.1007/s00280-016-2976-z.
(89) Galanski, M. Recent Developments in the Field of Anticancer Platinum Complexes. *Recent Pat. Anticancer Drug Discov.* **2006,** *1* (2), 285-295. DOI: 10.2174/157489206777442287.
(90) *Who Model List of Essential Medicines*; World Health Organization: 2019.
(91) Centers for Disease Control and Prevention Ambulatory Care Drug Database System. http://www.cdc.gov/nchs/ahcd/ahcd_database.htm (accessed: 2015).
(92) World Health Organization. International Clinical Trials Registry Platform (Ictrp). http://www.who.int/ictrp/en/ (accessed: 2020).
(93) National Institutes of Health. Clinical Trials Database. http://www.clinicaltrials.gov/ (accessed: 2020).
(94) Haug, C.; Gøtzsche, P. C.; Schroeder, T. V. Registries and Registration of Clinical Trials. *N. Engl. J. Med.* **2005,** *353* (26), 2811-2812. DOI: 10.1056/NEJMe058280.
(95) Oberoi, H. S.; Nukolova, N. V.; Kabanov, A. V.; Bronich, T. K. Nanocarriers for Delivery of Platinum Anticancer Drugs. *Adv Drug Deliv Rev* **2013,** *65* (13-14), 1667-1685. DOI: 10.1016/j.addr.2013.09.014.
(96) Xiao, H.; Yan, L.; Dempsey, E. M.; Song, W.; Qi, R.; Li, W.; Huang, Y.; Jing, X.; Zhou, D.; Ding, J.; Chen, X. Recent Progress in Polymer-Based Platinum Drug Delivery Systems. *Prog. Polym. Sci.* **2018,** *87*, 70-106. DOI: 10.1016/j.progpolymsci.2018.07.004.

(97) Gately, D. P.; Howell, S. B. Cellular Accumulation of the Anticancer Agent Cisplatin: A Review. *Br. J. Cancer* **1993,** *67* (6), 1171-1176. DOI: 10.1038/bjc.1993.221.
(98) Howell, S. B.; Safaei, R.; Larson, C. A.; Sailor, M. J. Copper Transporters and the Cellular Pharmacology of the Platinum-Containing Cancer Drugs. *Mol. Pharmacol.* **2010,** *77* (6), 887-894. DOI: 10.1124/mol.109.063172.
(99) Yonezawa, A.; Masuda, S.; Yokoo, S.; Katsura, T.; Inui, K. Cisplatin and Oxaliplatin, but Not Carboplatin and Nedaplatin, Are Substrates for Human Organic Cation Transporters (Slc22a1-3 and Multidrug and Toxin Extrusion Family). *J. Pharmacol. Exp. Ther.* **2006,** *319* (2), 879-886. DOI: 10.1124/jpet.106.110346.
(100) Fichtinger-Schepman, A. M.; van der Veer, J. L.; den Hartog, J. H.; Lohman, P. H.; Reedijk, J. Adducts of the Antitumor Drug Cis-Diamminedichloroplatinum(Ii) with DNA: Formation, Identification, and Quantitation. *Biochemistry* **1985,** *24* (3), 707-713. DOI: 10.1021/bi00324a025.
(101) Wang, D.; Lippard, S. J. Cellular Processing of Platinum Anticancer Drugs. *Nat. Rev. Drug Discov.* **2005,** *4* (4), 307-320. DOI: 10.1038/nrd1691.
(102) Chapman, E. G.; DeRose, V. J. Enzymatic Processing of Platinated Rnas. *J. Am. Chem. Soc.* **2010,** *132* (6), 1946-1952. DOI: 10.1021/ja908419j.
(103) Akaboshi, M.; Kawai, K.; Maki, H.; Akuta, K.; Ujeno, Y.; Miyahara, T. The Number of Platinum Atoms Binding to DNA, Rna and Protein Molecules of Hela Cells Treated with Cisplatin at Its Mean Lethal Concentration. *Jpn. J. Cancer Res.* **1992,** *83* (5), 522-526. DOI: 10.1111/j.1349-7006.1992.tb01959.x.
(104) Tesniere, A.; Schlemmer, F.; Boige, V.; Kepp, O.; Martins, I.; Ghiringhelli, F.; Aymeric, L.; Michaud, M.; Apetoh, L.; Barault, L.; Mendiboure, J.; Pignon, J. P.; Jooste, V.; van Endert, P.; Ducreux, M.; Zitvogel, L.; Piard, F.; Kroemer, G. Immunogenic Death of Colon Cancer Cells Treated with Oxaliplatin. *Oncogene* **2010,** *29* (4), 482-491. DOI: 10.1038/onc.2009.356.
(105) Hato, S. V.; Khong, A.; de Vries, I. J.; Lesterhuis, W. J. Molecular Pathways: The Immunogenic Effects of Platinum-Based Chemotherapeutics. *Clin. Cancer Res.* **2014,** *20* (11), 2831-2837. DOI: 10.1158/1078-0432.ccr-13-3141.
(106) Roberts, N. B.; Wadajkar, A. S.; Winkles, J. A.; Davila, E.; Kim, A. J.; Woodworth, G. F. Repurposing Platinum-Based Chemotherapies for Multi-Modal Treatment of Glioblastoma. *Oncoimmunology* **2016,** *5* (9), e1208876. DOI: 10.1080/2162402x.2016.1208876.
(107) Yung, W. K.; Mechtler, L.; Gleason, M. J. Intravenous Carboplatin for Recurrent Malignant Glioma: A Phase Ii Study. *J. Clin. Oncol.* **1991,** *9* (5), 860-864. DOI: 10.1200/jco.1991.9.5.860.
(108) Piccioni, D.; D'Atri, S.; Papa, G.; Caravita, T.; Franchi, A.; Bonmassar, E.; Graziani, G. Cisplatin Increases Sensitivity of Human Leukemic Blasts to Triazene Compounds. *J. Chemother.* **1995,** *7* (3), 224-229. DOI: 10.1179/joc.1995.7.3.224.
(109) Britten, C. D.; Rowinsky, E. K.; Baker, S. D.; Agarwala, S. S.; Eckardt, J. R.; Barrington, R.; Diab, S. G.; Hammond, L. A.; Johnson, T.; Villalona-Calero, M.; Fraass, U.; Statkevich, P.; Von Hoff, D. D.; Eckhardt, S. G. A Phase I and Pharmacokinetic Study of Temozolomide and Cisplatin in Patients with Advanced Solid Malignancies. *Clin. Cancer Res.* **1999,** *5* (7), 1629-1637. DOI: N/A.
(110) Silvani, A.; Eoli, M.; Salmaggi, A.; Lamperti, E.; Maccagnano, E.; Broggi, G.; Boiardi, A. Phase Ii Trial of Cisplatin Plus Temozolomide, in Recurrent and Progressive Malignant Glioma Patients. *J. Neurooncol.* **2004,** *66* (1-2), 203-208. DOI: 10.1023/b:neon.0000013479.64348.69.
(111) Mishima, K.; Mazar, A. P.; Gown, A.; Skelly, M.; Ji, X. D.; Wang, X. D.; Jones, T. R.; Cavenee, W. K.; Huang, H. J. A Peptide Derived from the Non-Receptor-Binding Region of Urokinase Plasminogen Activator Inhibits Glioblastoma Growth and Angiogenesis *in Vivo* in Combination with Cisplatin. *Proc. Natl. Acad. Sci. U. S. A.* **2000,** *97* (15), 8484-8489. DOI: 10.1073/pnas.150239497.
(112) Nagane, M.; Narita, Y.; Mishima, K.; Levitzki, A.; Burgess, A. W.; Cavenee, W. K.; Huang, H. J. Human Glioblastoma Xenografts Overexpressing a Tumor-Specific Mutant Epidermal Growth Factor Receptor Sensitized to Cisplatin by the Ag1478 Tyrosine Kinase Inhibitor. *J. Neurosurg.* **2001,** *95* (3), 472-479. DOI: 10.3171/jns.2001.95.3.0472.

(113) Hess, S. M.; Anderson, J. G.; Bierbach, U. A Non-Crosslinking Platinum-Acridine Hybrid Agent Shows Enhanced Cytotoxicity Compared to Clinical Bcnu and Cisplatin in Glioblastoma Cells. *Bioorg. Med. Chem. Lett.* **2005,** *15* (2), 443-446. DOI: 10.1016/j.bmcl.2004.10.049.
(114) Posadas, I.; Alonso-Moreno, C.; Bravo, I.; Carrillo-Hermosilla, F.; Garzon, A.; Villaseca, N.; Lopez-Solera, I.; Albaladejo, J.; Cena, V. Synthesis, Characterization, DNA Interactions and Antiproliferative Activity on Glioblastoma of Iminopyridine Platinum(Ii) Chelate Complexes. *J. Inorg. Biochem.* **2017,** *168*, 46-54. DOI: 10.1016/j.jinorgbio.2016.11.032.
(115) Benzina, S.; Fischer, B.; Miternique-Grosse, A.; Dufour, P.; Denis, J. M.; Bergerat, J. P.; Gueulette, J.; Bischoff, P. Cell Death Induced in a Human Glioblastoma Cell Line by P(65)+Be Neutrons Combined with Cisplatin. *Life Sci.* **2006,** *79* (6), 513-518. DOI: 10.1016/j.lfs.2006.01.037.
(116) Brandes, A. A.; Basso, U.; Reni, M.; Vastola, F.; Tosoni, A.; Cavallo, G.; Scopece, L.; Ferreri, A. J.; Panucci, M. G.; Monfardini, S.; Ermani, M. First-Line Chemotherapy with Cisplatin Plus Fractionated Temozolomide in Recurrent Glioblastoma Multiforme: A Phase Ii Study of the Gruppo Italiano Cooperativo Di Neuro-Oncologia. *J. Clin. Oncol.* **2004,** *22* (9), 1598-1604. DOI: 10.1200/jco.2004.11.019.
(117) Wang, Y.; Kong, X.; Guo, Y.; Wang, R.; Ma, W. Continuous Dose-Intense Temozolomide and Cisplatin in Recurrent Glioblastoma Patients. *Medicine (Baltimore)* **2017,** *96* (10), e6261. DOI: 10.1097/md.0000000000006261.
(118) Gajski, G.; Čimbora-Zovko, T.; Rak, S.; Osmak, M.; Garaj-Vrhovac, V. Antitumour Action on Human Glioblastoma A1235 Cells through Cooperation of Bee Venom and Cisplatin. *Cytotechnology* **2016,** *68* (4), 1197-1205. DOI: 10.1007/s10616-015-9879-4.
(119) Zhu, T.; Xu, Y.; Dong, B.; Zhang, J.; Wei, Z.; Xu, Y.; Yao, Y. B-Elemene Inhibits Proliferation of Human Glioblastoma Cells through the Activation of Glia Maturation Factor B and Induces Sensitization to Cisplatin. *Oncol. Rep.* **2011,** *26* (2), 405-413. DOI: 10.3892/or.2011.1276.
(120) Park, C. K.; Park, S. H.; Lee, S. H.; Kim, C. Y.; Kim, D. W.; Paek, S. H.; Kim, D. G.; Heo, D. S.; Kim, I. H.; Jung, H. W. Methylation Status of the Mgmt Gene Promoter Fails to Predict the Clinical Outcome of Glioblastoma Patients Treated with Acnu Plus Cisplatin. *Neuropathology* **2009,** *29* (4), 443-449. DOI: 10.1111/j.1440-1789.2008.00998.x.
(121) Buckner, J. C.; Ballman, K. V.; Michalak, J. C.; Burton, G. V.; Cascino, T. L.; Schomberg, P. J.; Hawkins, R. B.; Scheithauer, B. W.; Sandler, H. M.; Marks, R. S.; O'Fallon, J. R. Phase Iii Trial of Carmustine and Cisplatin Compared with Carmustine Alone and Standard Radiation Therapy or Accelerated Radiation Therapy in Patients with Glioblastoma Multiforme: North Central Cancer Treatment Group 93-72-52 and Southwest Oncology Group 9503 Trials. *J. Clin. Oncol.* **2006,** *24* (24), 3871-3879. DOI: 10.1200/jco.2005.04.6979.
(122) Aroui, S.; Dardevet, L.; Ben Ajmia, W.; de Boisvilliers, M.; Perrin, F.; Laajimi, A.; Boumendjel, A.; Kenani, A.; Muller, J. M.; De Waard, M. A Novel Platinum-Maurocalcine Conjugate Induces Apoptosis of Human Glioblastoma Cells by Acting through the Ros-Erk/Akt-P53 Pathway. *Mol. Pharm.* **2015,** *12* (12), 4336-4348. DOI: 10.1021/acs.molpharmaceut.5b00531.
(123) Ferrari, B.; Urselli, F.; Gilodi, M.; Camuso, S.; Priori, E. C.; Rangone, B.; Ravera, M.; Veneroni, P.; Zanellato, I.; Roda, E.; Osella, D.; Bottone, M. G. New Platinum-Based Prodrug Pt(Iv)Ac-Poa: Antitumour Effects in Rat C6 Glioblastoma Cells. *Neurotox. Res.* **2020,** *37* (1), 183-197. DOI: 10.1007/s12640-019-00076-0.
(124) Macieja, A.; Kopa, P.; Galita, G.; Pastwa, E.; Majsterek, I.; Poplawski, T. Comparison of the Effect of Three Different Topoisomerase Ii Inhibitors Combined with Cisplatin in Human Glioblastoma Cells Sensitized with Double Strand Break Repair Inhibitors. *Mol. Biol. Rep.* **2019,** *46* (4), 3625-3636. DOI: 10.1007/s11033-019-04605-0.
(125) Carminati, P. O.; Donaires, F. S.; Marques, M. M.; Donadi, E. A.; Passos, G. A. S.; Sakamoto-Hojo, E. T. Cisplatin Associated with Ly294002 Increases Cytotoxicity and Induces Changes in Transcript Profiles of Glioblastoma Cells. *Mol. Biol. Rep.* **2014,** *41* (1), 165-177. DOI: 10.1007/s11033-013-2849-z.

(126) Gwak, H.-S.; Shingu, T.; Chumbalkar, V.; Hwang, Y.-H.; DeJournett, R.; Latha, K.; Koul, D.; Alfred Yung, W. K.; Powis, G.; Farrell, N. P.; Bögler, O. Combined Action of the Dinuclear Platinum Compound Bbr3610 with the Pi3-K Inhibitor Px-866 in Glioblastoma. *Int. J. Cancer* **2011,** *128* (4), 787-796. DOI: 10.1002/ijc.25394.
(127) Rosa, P.; Catacuzzeno, L.; Sforna, L.; Mangino, G.; Carlomagno, S.; Mincione, G.; Petrozza, V.; Ragona, G.; Franciolini, F.; Calogero, A. Bk Channels Blockage Inhibits Hypoxia-Induced Migration and Chemoresistance to Cisplatin in Human Glioblastoma Cells. *J. Cell. Physiol.* **2018,** *233* (9), 6866-6877. DOI: 10.1002/jcp.26448.
(128) Li, J.; Song, J.; Guo, F. Mir-186 Reverses Cisplatin Resistance and Inhibits The formation of the Glioblastoma-Initiating Cell phenotype by Degrading Yin Yang 1 in Glioblastoma. *Int. J. Mol. Med.* **2019,** *43* (1), 517-524. DOI: 10.3892/ijmm.2018.3940.
(129) Tallen, U. G.; Truss, M.; Kunitz, F.; Wellmann, S.; Unryn, B.; Sinn, B.; Lass, U.; Krabbe, S.; Holtkamp, N.; Hagemeier, C.; Wurm, R.; Henze, G.; Riabowol, K. T.; von Deimling, A. Down-Regulation of the Inhibitor of Growth 1 (Ing1) Tumor Suppressor Sensitizes P53-Deficient Glioblastoma Cells to Cisplatin-Induced Cell Death. *J. Neurooncol.* **2008,** *86* (1), 23-30. DOI: 10.1007/s11060-007-9436-x.
(130) Baldwin, R. M.; Garratt-Lalonde, M.; Parolin, D. A. E.; Krzyzanowski, P. M.; Andrade, M. A.; Lorimer, I. A. J. Protection of Glioblastoma Cells from Cisplatin Cytotoxicity Via Protein Kinase Cι-Mediated Attenuation of P38 Map Kinase Signaling. *Oncogene* **2006,** *25* (20), 2909-2919. DOI: 10.1038/sj.onc.1209312.
(131) Ding, L.; Yuan, C.; Wei, F.; Wang, G.; Zhang, J.; Bellail, A. C.; Zhang, Z.; Olson, J. J.; Hao, C. Cisplatin Restores Trail Apoptotic Pathway in Glioblastoma-Derived Stem Cells through up-Regulation of Dr5 and Down-Regulation of C-Flip. *Cancer Invest.* **2011,** *29* (8), 511-520. DOI: 10.3109/07357907.2011.605412.
(132) Wang, M.; Wu, Q.; Fang, M.; Huang, W.; Zhu, H. Mir-152-3p Sensitizes Glioblastoma Cells Towards Cisplatin Via Regulation of Sos1. *Onco Targets Ther.* **2019,** *12*, 9513-9525. DOI: 10.2147/ott.s210732.
(133) Shi, M.; Fortin, D.; Sanche, L.; Paquette, B. Convection-Enhancement Delivery of Platinum-Based Drugs and Lipoplatintm to Optimize the Concomitant Effect with Radiotherapy in F98 Glioma Rat Model. *Invest. New Drugs* **2015,** *33* (3), 555-563. DOI: 10.1007/s10637-015-0228-4.
(134) Rousseau, J.; Barth, R. F.; Fernandez, M.; Adam, J.-F.; Balosso, J.; Estève, F.; Elleaume, H. Efficacy of Intracerebral Delivery of Cisplatin in Combination with Photon Irradiation for Treatment of Brain Tumors. *J. Neurooncol.* **2010,** *98* (3), 287-295. DOI: 10.1007/s11060-009-0074-3.
(135) White, E.; Bienemann, A.; Pugh, J.; Castrique, E.; Wyatt, M.; Taylor, H.; Cox, A.; McLeod, C.; Gill, S. An Evaluation of the Safety and Feasibility of Convection-Enhanced Delivery of Carboplatin into the White Matter as a Potential Treatment for High-Grade Glioma. *J. Neurooncol.* **2012,** *108* (1), 77-88. DOI: 10.1007/s11060-012-0833-4.
(136) Balaña, C.; López-Pousa, A.; Berrocal, A.; Yaya-Tur, R.; Herrero, A.; García, J. L.; Martín-Broto, J.; Benavides, M.; Cerdá-Nicolás, M.; Ballester, R.; Balart, J.; Capellades, J. Phase Ii Study of Temozolomide and Cisplatin as Primary Treatment Prior to Radiotherapy in Newly Diagnosed Glioblastoma Multiforme Patients with Measurable Disease. A Study of the Spanish Medical Neuro-Oncology Group (Genom). *J. Neurooncol.* **2004,** *70* (3), 359-369. DOI: 10.1007/s11060-004-9175-1.
(137) Roci, E.; Cakani, B.; Brace, G.; Bushati, T.; Rroji, A.; Petrela, M.; Kaloshi, G. Platinum-Based Chemotherapy in Recurrent High-Grade Glioma Patients: Retrospective Study. *Medical archives (Sarajevo, Bosnia and Herzegovina)* **2014,** *68* (2), 140-143. DOI: 10.5455/medarh.2014.68.140-143.
(138) Jacobs, S.; McCully, C. L.; Murphy, R. F.; Bacher, J.; Balis, F. M.; Fox, E. Extracellular Fluid Concentrations of Cisplatin, Carboplatin, and Oxaliplatin in Brain, Muscle, and Blood Measured Using Microdialysis in Nonhuman Primates. *Cancer Chemother. Pharmacol.* **2010,** *65* (5), 817-824. DOI: 10.1007/s00280-009-1085-7.

(139) Prados, M. D.; Schold, S. C., Jr.; Fine, H. A.; Jaeckle, K.; Hochberg, F.; Mechtler, L.; Fetell, M. R.; Phuphanich, S.; Feun, L.; Janus, T. J.; Ford, K.; Graney, W. A Randomized, Double-Blind, Placebo-Controlled, Phase 2 Study of Rmp-7 in Combination with Carboplatin Administered Intravenously for the Treatment of Recurrent Malignant Glioma. *Neuro Oncol.* **2003,** *5* (2), 96-103. DOI: 10.1093/neuonc/5.2.96.
(140) Sheleg, S. V.; Korotkevich, E. A.; Zhavrid, E. A.; Muravskaya, G. V.; Smeyanovich, A. F.; Shanko, Y. G.; Yurkshtovich, T. L.; Bychkovsky, P. B.; Belyaev, S. A. Local Chemotherapy with Cisplatin-Depot for Glioblastoma Multiforme. *J. Neurooncol.* **2002,** *60* (1), 53-59. DOI: 10.1023/a:1020288015457.
(141) White, E.; Bienemann, A.; Taylor, H.; Hopkins, K.; Cameron, A.; Gill, S. A Phase I Trial of Carboplatin Administered by Convection-Enhanced Delivery to Patients with Recurrent/Progressive Glioblastoma Multiforme. *Contemp. Clin. Trials* **2012,** *33* (2), 320-331. DOI: 10.1016/j.cct.2011.10.010.
(142) Parsa, A. T.; Waldron, J. S.; Panner, A.; Crane, C. A.; Parney, I. F.; Barry, J. J.; Cachola, K. E.; Murray, J. C.; Tihan, T.; Jensen, M. C.; Mischel, P. S.; Stokoe, D.; Pieper, R. O. Loss of Tumor Suppressor Pten Function Increases B7-H1 Expression and Immunoresistance in Glioma. *Nat. Med.* **2007,** *13* (1), 84-88. DOI: 10.1038/nm1517.
(143) McWhinney, S. R.; Goldberg, R. M.; McLeod, H. L. Platinum Neurotoxicity Pharmacogenetics. *Mol. Cancer Ther.* **2009,** *8* (1), 10-16. DOI: 10.1158/1535-7163.mct-08-0840.
(144) Saida, Y.; Watanabe, S.; Tanaka, T.; Baba, J.; Sato, K.; Shoji, S.; Igarashi, N.; Kondo, R.; Okajima, M.; Koshio, J.; Ichikawa, K.; Nozaki, K.; Ishikawa, D.; Koya, T.; Miura, S.; Tanaka, J.; Kagamu, H.; Yoshizawa, H.; Nakata, K.; Narita, I. Critical Roles of Chemoresistant Effector and Regulatory T Cells in Antitumor Immunity after Lymphodepleting Chemotherapy. *J. Immunol.* **2015,** *195* (2), 726-735. DOI: 10.4049/jimmunol.1401468.
(145) Raghavan, S.; Baskin, D. S.; Sharpe, M. A. Mp-Pt(Iv): A Maob-Sensitive Mitochondrial-Specific Prodrug for Treating Glioblastoma. *Mol. Cancer Ther.* **2020,** *19* (12), 2445-2453. DOI: 10.1158/1535-7163.mct-20-0420.
(146) Sharpe, M.; Baskin, D. Cadd-18. Mp-Pt(Iv): A Maob Sensitive Mitochondrial Smart Bomb for Treating Glioma. *Neuro Oncol.* **2018,** *20* (suppl_6), vi279-vi279. DOI: 10.1093/neuonc/noy148.1163.
(147) Mihajlović, L. E.; Savić, A.; Poljarević, J.; Vučković, I.; Mojić, M.; Bulatović, M.; Maksimović-Ivanić, D.; Mijatović, S.; Kaluđerović, G. N.; Stošić-Grujičić, S.; Miljković, Đ.; Grgurić-Šipka, S.; Sabo, T. J. Novel Methylene Modified Cyclohexyl Ethylenediamine-N,N′-Diacetate Ligands and Their Platinum(Iv) Complexes. Influence on Biological Activity. *J. Inorg. Biochem.* **2012,** *109*, 40-48. DOI: 10.1016/j.jinorgbio.2012.01.012.
(148) Lazić, J. M.; Vučićević, L.; Grgurić-Šipka, S.; Janjetović, K.; Kaluđerović, G. N.; Misirkić, M.; Gruden-Pavlović, M.; Popadić, D.; Paschke, R.; Trajković, V.; Sabo, T. J. Synthesis and *in Vitro* Anticancer Activity of Octahedral Platinum(Iv) Complexes with Cyclohexyl-Functionalized Ethylenediamine-N,N′-Diacetate-Type Ligands. *ChemMedChem* **2010,** *5* (6), 881-889. DOI: https://doi.org/10.1002/cmdc.201000058.
(149) Mijatovic, S.; Maksimovic-Ivanic, D.; Radovic, J.; Miljkovic, D.; Kaludjerovic, G. N.; Sabo, T. J.; Trajkovic, V. Aloe Emodin Decreases the Erk-Dependent Anticancer Activity of Cisplatin. *Cellular and Molecular Life Sciences CMLS* **2005,** *62* (11), 1275-1282. DOI: 10.1007/s00018-005-5041-3.
(150) Perez, J. M.; Camazón, M.; Alvarez-Valdes, A.; Quiroga, A. G.; Kelland, L. R.; Alonso, C.; Navarro-Ranninger, M. C. Synthesis, Characterization and DNA Modification Induced by a Novel Pt(Iv)-Bis(Monoglutarate) Complex Which Induces Apoptosis in Glioma Cells. *Chem. Biol. Interact.* **1999,** *117* (2), 99-115. DOI: 10.1016/S0009-2797(98)00100-8.
(151) Arduino, I.; Depalo, N.; Re, F.; Dal Magro, R.; Panniello, A.; Margiotta, N.; Fanizza, E.; Lopalco, A.; Laquintana, V.; Cutrignelli, A.; Lopedota, A. A.; Franco, M.; Denora, N. Pegylated Solid Lipid Nanoparticles for Brain Delivery of Lipophilic Kiteplatin Pt(Iv) Prodrugs: An *in Vitro* Study. *Int. J. Pharm.* **2020,** *583*, 119351. DOI: 10.1016/j.ijpharm.2020.119351.

(152) Lajous, H.; Riva, R.; Lelievre, B.; Tetaud, C.; Avril, S.; Hindre, F.; Boury, F.; Jerome, C.; Lecomte, P.; Garcion, E. Hybrid Gd3+/Cisplatin Cross-Linked Polymer Nanoparticles Enhance Platinum Accumulation and Formation of DNA Adducts in Glioblastoma Cell Lines. *Biomaterials Science* **2018,** *6* (9), 2386-2409. DOI: 10.1039/c8bm00346g.
(153) Zhang, C.; Nance, E. A.; Mastorakos, P.; Chisholm, J.; Berry, S.; Eberhart, C.; Tyler, B.; Brem, H.; Suk, J. S.; Hanes, J. Convection Enhanced Delivery of Cisplatin-Loaded Brain Penetrating Nanoparticles Cures Malignant Glioma in Rats. *J. Control. Release* **2017,** *263*, 112-119. DOI: 10.1016/j.jconrel.2017.03.007.
(154) Karanam, V.; Marslin, G.; Krishnamoorthy, B.; Chellan, V.; Siram, K.; Natarajan, T.; Bhaskar, B.; Franklin, G. Poly (Ɛ-Caprolactone) Nanoparticles of Carboplatin: Preparation, Characterization and *in Vitro* Cytotoxicity Evaluation in U-87 Mg Cell Lines. *Colloids Surf. B. Biointerfaces* **2015,** *130*, 48-52. DOI: 10.1016/j.colsurfb.2015.04.005.
(155) Alex, A. T.; Joseph, A.; Shavi, G.; Rao, J. V.; Udupa, N. Development and Evaluation of Carboplatin-Loaded Pcl Nanoparticles for Intranasal Delivery. *Drug Deliv.* **2016,** *23* (7), 2144-2153. DOI: 10.3109/10717544.2014.948643.
(156) Arshad, A.; Yang, B.; Bienemann, A. S.; Barua, N. U.; Wyatt, M. J.; Woolley, M.; Johnson, D. E.; Edler, K. J.; Gill, S. S. Convection-Enhanced Delivery of Carboplatin Plga Nanoparticles for the Treatment of Glioblastoma. *PLoS One* **2015,** *10* (7), e0132266. DOI: 10.1371/journal.pone.0132266.
(157) Petri, B.; Bootz, A.; Khalansky, A.; Hekmatara, T.; Müller, R.; Uhl, R.; Kreuter, J.; Gelperina, S. Chemotherapy of Brain Tumour Using Doxorubicin Bound to Surfactant-Coated Poly(Butyl Cyanoacrylate) Nanoparticles: Revisiting the Role of Surfactants. *J. Control. Release* **2007,** *117* (1), 51-58. DOI: 10.1016/j.jconrel.2006.10.015.
(158) Ebrahimi Shahmabadi, H.; Movahedi, F.; Koohi Moftakhari Esfahani, M.; Alavi, S. E.; Eslamifar, A.; Mohammadi Anaraki, G.; Akbarzadeh, A. Efficacy of Cisplatin-Loaded Polybutyl Cyanoacrylate Nanoparticles on the Glioblastoma. *Tumour Biol.* **2014,** *35* (5), 4799-4806. DOI: 10.1007/s13277-014-1630-9.
(159) Dhami, N. K.; Pandey, R. S.; Jain, U. K.; Chandra, R.; Madan, J. Non-Aggregated Protamine-Coated Poly(Lactide-Co-Glycolide) Nanoparticles of Cisplatin Crossed Blood-Brain Barrier, Enhanced Drug Delivery and Improved Therapeutic Index in Glioblastoma Cells: *In Vitro* Studies. *J. Microencapsul.* **2014,** *31* (7), 685-693. DOI: 10.3109/02652048.2014.913725.
(160) Makharza, S. A.; Cirillo, G.; Vittorio, O.; Valli, E.; Voli, F.; Farfalla, A.; Curcio, M.; Iemma, F.; Nicoletta, F. P.; El-Gendy, A. A.; Goya, G. F.; Hampel, S. Magnetic Graphene Oxide Nanocarrier for Targeted Delivery of Cisplatin: A Perspective for Glioblastoma Treatment. *Pharmaceuticals (Basel)* **2019,** *12* (2). DOI: 10.3390/ph12020076.
(161) Kutwin, M.; Sawosz, E.; Jaworski, S.; Hinzmann, M.; Wierzbicki, M.; Hotowy, A.; Grodzik, M.; Winnicka, A.; Chwalibog, A. Investigation of Platinum Nanoparticle Properties against U87 Glioblastoma Multiforme. *Arch. Med. Sci.* **2017,** *13* (6), 1322-1334. DOI: 10.5114/aoms.2016.58925.
(162) Thanasupawat, T.; Bergen, H.; Hombach-Klonisch, S.; Krcek, J.; Ghavami, S.; Del Bigio, M. R.; Krawitz, S.; Stelmack, G.; Halayko, A.; McDougall, M.; Meier, M.; Stetefeld, J.; Klonisch, T. Platinum (Iv) Coiled Coil Nanotubes Selectively Kill Human Glioblastoma Cells. *Nanomedicine-Nanotechnology Biology and Medicine* **2015,** *11* (4), 913-925. DOI: 10.1016/j.nano.2015.01.014.
(163) Shein, S. A.; Kuznetsov, II; Abakumova, T. O.; Chelushkin, P. S.; Melnikov, P. A.; Korchagina, A. A.; Bychkov, D. A.; Seregina, I. F.; Bolshov, M. A.; Kabanov, A. V.; Chekhonin, V. P.; Nukolova, N. V. Vegf- and Vegfr2-Targeted Liposomes for Cisplatin Delivery to Glioma Cells. *Mol. Pharm.* **2016,** *13* (11), 3712-3723. DOI: 10.1021/acs.molpharmaceut.6b00519.
(164) Liang, S.; Zhou, Q.; Wang, M.; Zhu, Y.; Wu, Q.; Yang, X. Water-Soluble L-Cysteine-Coated Fept Nanoparticles as Dual Mri/Ct Imaging Contrast Agent for Glioma. *Int J Nanomedicine* **2015,** *10*, 2325-2333. DOI: 10.2147/IJN.S75174.

(165) Lopez Ruiz, A.; Bartomeu Garcia, C.; Navarro Gallon, S.; Webster, T. J. Novel Silver-Platinum Nanoparticles for Anticancer and Antimicrobial Applications. *Int J Nanomedicine* **2020,** *15*, 169-179. DOI: 10.2147/ijn.s176737.
(166) Setua, S.; Ouberai, M.; Piccirillo, S. G.; Watts, C.; Welland, M. Cisplatin-Tethered Gold Nanospheres for Multimodal Chemo-Radiotherapy of Glioblastoma. *Nanoscale* **2014,** *6* (18), 10865-10873. DOI: 10.1039/c4nr03693j.
(167) Coluccia, D.; Figueiredo, C. A.; Wu, M. Y.; Riemenschneider, A. N.; Diaz, R.; Luck, A.; Smith, C.; Das, S.; Ackerley, C.; O'Reilly, M.; Hynynen, K.; Rutka, J. T. Enhancing Glioblastoma Treatment Using Cisplatin-Gold-Nanoparticle Conjugates and Targeted Delivery with Magnetic Resonance-Guided Focused Ultrasound. *Nanomedicine* **2018,** *14* (4), 1137-1148. DOI: 10.1016/j.nano.2018.01.021.
(168) Aroui, S.; Dardevet, L.; Najlaoui, F.; Kammoun, M.; Laajimi, A.; Fetoui, H.; De Waard, M.; Kenani, A. Pten-Regulated Akt/Foxo3a/Bim Signaling Contributes to Human Cell Glioblastoma Apoptosis by Platinum-Maurocalcin Conjugate. *Int. J. Biochem. Cell Biol.* **2016,** *77*, 15-22. DOI: 10.1016/j.biocel.2016.05.013.
(169) Miura, Y.; Takenaka, T.; Toh, K.; Wu, S.; Nishihara, H.; Kano, M. R.; Ino, Y.; Nomoto, T.; Matsumoto, Y.; Koyama, H.; Cabral, H.; Nishiyama, N.; Kataoka, K. Cyclic Rgd-Linked Polymeric Micelles for Targeted Delivery of Platinum Anticancer Drugs to Glioblastoma through the Blood-Brain Tumor Barrier. *Acs Nano* **2013,** *7* (10), 8583-8592. DOI: 10.1021/nn402662d.
(170) Charest, G.; Sanche, L.; Fortin, D.; Mathieu, D.; Paquette, B. Glioblastoma Treatment: Bypassing the Toxicity of Platinum Compounds by Using Liposomal Formulation and Increasing Treatment Efficiency with Concomitant Radiotherapy. *International Journal of Radiation Oncology Biology Physics* **2012,** *84* (1), 244-249. DOI: 10.1016/j.ijrobp.2011.10.054.
(171) Charest, G.; Sanche, L.; Fortin, D.; Mathieu, D.; Paquette, B. Optimization of the Route of Platinum Drugs Administration to Optimize the Concomitant Treatment with Radiotherapy for Glioblastoma Implanted in the Fischer Rat Brain. *J. Neurooncol.* **2013,** *115* (3), 365-373. DOI: 10.1007/s11060-013-1238-8.
(172) Shi, M.; Fortin, D.; Paquette, B.; Sanche, L. Convection-Enhancement Delivery of Liposomal Formulation of Oxaliplatin Shows Less Toxicity Than Oxaliplatin yet Maintains a Similar Median Survival Time in F98 Glioma-Bearing Rat Model. *Invest. New Drugs* **2016,** *34* (3), 269-276. DOI: 10.1007/s10637-016-0340-0.
(173) Arvanitis, C. D.; Ferraro, G. B.; Jain, R. K. The Blood-Brain Barrier and Blood-Tumour Barrier in Brain Tumours and Metastases. *Nat. Rev. Cancer* **2020,** *20* (1), 26-41. DOI: 10.1038/s41568-019-0205-x.
(174) Chenthamara, D.; Subramaniam, S.; Ramakrishnan, S. G.; Krishnaswamy, S.; Essa, M. M.; Lin, F.-H.; Qoronfleh, M. W. Therapeutic Efficacy of Nanoparticles and Routes of Administration. *Biomaterials Research* **2019,** *23* (1), 20. DOI: 10.1186/s40824-019-0166-x.
(175) Yi, X.; Manickam, D. S.; Brynskikh, A.; Kabanov, A. V. Agile Delivery of Protein Therapeutics to Cns. *J. Control. Release* **2014,** *190*, 637-663. DOI: 10.1016/j.jconrel.2014.06.017.
(176) Bennewitz, M. F.; Saltzman, W. M. Nanotechnology for Delivery of Drugs to the Brain for Epilepsy. *Neurotherapeutics* **2009,** *6* (2), 323-336. DOI: 10.1016/j.nurt.2009.01.018.
(177) Lollo, G.; Vincent, M.; Ullio-Gamboa, G.; Lemaire, L.; Franconi, F.; Couez, D.; Benoit, J. P. Development of Multifunctional Lipid Nanocapsules for the Co-Delivery of Paclitaxel and Cpg-Odn in the Treatment of Glioblastoma. *Int. J. Pharm.* **2015,** *495* (2), 972-980. DOI: 10.1016/j.ijpharm.2015.09.062.
(178) Allard, E.; Jarnet, D.; Vessières, A.; Vinchon-Petit, S.; Jaouen, G.; Benoit, J. P.; Passirani, C. Local Delivery of Ferrociphenol Lipid Nanocapsules Followed by External Radiotherapy as a Synergistic Treatment against Intracranial 9l Glioma Xenograft. *Pharm. Res.* **2010,** *27* (1), 56-64. DOI: 10.1007/s11095-009-0006-0.
(179) Fourniols, T.; Randolph, L. D.; Staub, A.; Vanvarenberg, K.; Leprince, J. G.; Préat, V.; des Rieux, A.; Danhier, F. Temozolomide-Loaded Photopolymerizable Peg-Dma-Based Hydrogel for

the Treatment of Glioblastoma. *J. Control. Release* **2015,** *210*, 95-104. DOI: 10.1016/j.jconrel.2015.05.272.
(180) Huynh, N. T.; Passirani, C.; Allard-Vannier, E.; Lemaire, L.; Roux, J.; Garcion, E.; Vessieres, A.; Benoit, J.-P. Administration-Dependent Efficacy of Ferrociphenol Lipid Nanocapsules for the Treatment of Intracranial 9l Rat Gliosarcoma. *Int. J. Pharm.* **2012,** *423* (1), 55-62. DOI: 10.1016/j.ijpharm.2011.04.037.
(181) Laine, A.-L.; Huynh, N. T.; Clavreul, A.; Balzeau, J.; Béjaud, J.; Vessieres, A.; Benoit, J.-P.; Eyer, J.; Passirani, C. Brain Tumour Targeting Strategies Via Coated Ferrociphenol Lipid Nanocapsules. *Eur. J. Pharm. Biopharm.* **2012,** *81* (3), 690-693. DOI: 10.1016/j.ejpb.2012.04.012.
(182) Huynh, N. T.; Morille, M.; Bejaud, J.; Legras, P.; Vessieres, A.; Jaouen, G.; Benoit, J.-P.; Passirani, C. Treatment of 9l Gliosarcoma in Rats by Ferrociphenol-Loaded Lipid Nanocapsules Based on a Passive Targeting Strategy Via the Epr Effect. *Pharm. Res.* **2011,** *28* (12), 3189-3198. DOI: 10.1007/s11095-011-0501-y.
(183) Gregory, J. V.; Kadiyala, P.; Doherty, R.; Cadena, M.; Habeel, S.; Ruoslahti, E.; Lowenstein, P. R.; Castro, M. G.; Lahann, J. Systemic Brain Tumor Delivery of Synthetic Protein Nanoparticles for Glioblastoma Therapy. *Nat. Commun.* **2020,** *11* (1), 5687. DOI: 10.1038/s41467-020-19225-7.
(184) Meng, X.; Zhao, Y.; Han, B.; Zha, C.; Zhang, Y.; Li, Z.; Wu, P.; Qi, T.; Jiang, C.; Liu, Y.; Cai, J. Dual Functionalized Brain-Targeting Nanoinhibitors Restrain Temozolomide-Resistant Glioma Via Attenuating Egfr and Met Signaling Pathways. *Nat. Commun.* **2020,** *11* (1), 594. DOI: 10.1038/s41467-019-14036-x.
(185) Galstyan, A.; Markman, J. L.; Shatalova, E. S.; Chiechi, A.; Korman, A. J.; Patil, R.; Klymyshyn, D.; Tourtellotte, W. G.; Israel, L. L.; Braubach, O.; Ljubimov, V. A.; Mashouf, L. A.; Ramesh, A.; Grodzinski, Z. B.; Penichet, M. L.; Black, K. L.; Holler, E.; Sun, T.; Ding, H.; Ljubimov, A. V., et al. Blood–Brain Barrier Permeable Nano Immunoconjugates Induce Local Immune Responses for Glioma Therapy. *Nat. Commun.* **2019,** *10* (1), 3850. DOI: 10.1038/s41467-019-11719-3.
(186) Verreault, M.; Wehbe, M.; Strutt, D.; Masin, D.; Anantha, M.; Walker, D.; Chu, F.; Backstrom, I.; Kalra, J.; Waterhouse, D.; Yapp, D. T.; Bally, M. B. Determination of an Optimal Dosing Schedule for Combining Irinophore C™ and Temozolomide in an Orthotopic Model of Glioblastoma. *J. Control. Release* **2015,** *220* (Pt A), 348-357. DOI: 10.1016/j.jconrel.2015.10.053.
(187) Kumar, P.; Sharma, G.; Gupta, V.; Kaur, R.; Thakur, K.; Malik, R.; Kumar, A.; Kaushal, N.; Katare, O. P.; Raza, K. Oral Delivery of Methylthioadenosine to the Brain Employing Solid Lipid Nanoparticles: Pharmacokinetic, Behavioral, and Histopathological Evidences. *AAPS PharmSciTech* **2019,** *20* (2), 74. DOI: 10.1208/s12249-019-1296-0.
(188) Giese, A.; Bjerkvig, R.; Berens, M. E.; Westphal, M. Cost of Migration: Invasion of Malignant Gliomas and Implications for Treatment. *J. Clin. Oncol.* **2003,** *21* (8), 1624-1636. DOI: 10.1200/jco.2003.05.063.
(189) Sabir, F.; Ismail, R.; Csoka, I. Nose-to-Brain Delivery of Antiglioblastoma Drugs Embedded into Lipid Nanocarrier Systems: Status Quo and Outlook. *Drug Discov. Today* **2020,** *25* (1), 185-194. DOI: 10.1016/j.drudis.2019.10.005.
(190) Pires, P. C.; Santos, A. O. Nanosystems in Nose-to-Brain Drug Delivery: A Review of Non-Clinical Brain Targeting Studies. *J. Control. Release* **2018,** *270*, 89-100. DOI: 10.1016/j.jconrel.2017.11.047.
(191) Bruinsmann, F. A.; Richter Vaz, G.; de Cristo Soares Alves, A.; Aguirre, T.; Raffin Pohlmann, A.; Staniscuaski Guterres, S.; Sonvico, F. Nasal Drug Delivery of Anticancer Drugs for the Treatment of Glioblastoma: Preclinical and Clinical Trials. *Molecules (Basel, Switzerland)* **2019,** *24* (23). DOI: 10.3390/molecules24234312.

Chapter 2

Objectives

The main general objectives set for this Thesis are:

1. To design and synthesize through different approximations novel functional nanostructured polymers containing a cisplatin Pt(IV) prodrugs as building blocks: i) nanostructured coordination polymers (NCPs), and ii) polymeric nanoparticles (PNPs). The nanosystems obtained must demonstrate chemical and colloidal stability in physiological conditions.

2. To validate the potential use of the developed nanostructured systems as drug delivery systems and contrast agents for clinical imaging in the treatment of GB.

3. To study the *in vitro* and *in vivo* behavior of the set of nanoparticles and their therapeutic effect in comparison with cisplatin.

4. To validate preclinically the obtained nanoparticles as therapeutic agents for GB therapy using the intranasal administration as novel and alternative administration route.

To achieve the proposed main objectives, the following specific objectives were set:

- Synthesis of Pt(IV) prodrug starting from cisplatin molecule
- Synthesis of Pt(IV)-based polymeric nanoparticles establishing an specific protocol to ensure high yield synthesis and reproducibility
- Physicochemical characterization of the obtained nanoparticles
- Studied of the chemical and colloidal stability in physiological media
- Study of the *in vitro* cellular uptake and cytotoxic effect in glioblastoma cell lines.
- Study of the properties of the resulting nanoparticles as contrast agent for clinical imaging
- Evaluation of the *in vivo* therapeutic effect in GB mice models using intranasal administration as the administration route.

Chapter 3

Development of nanoscale coordination polymers for glioblastoma treatment based on Pt(IV) prodrug

In this chapter the state of the art related to the use of nanostructured coordination polymers (NCPs) in medicine is presented (section 3.1). Specifically, in section 3.2 different examples of Pt(IV)-based NCPs is presented in terms of synthetic methodology and therapeutic applications in cancer treatment. The rest of the chapter is devoted to detail the scope of this part and to show the results of the synthesis and characterization of an specific class of robust, reproducible and scalable Pt(IV)-based NCPs. Finally, the obtained Pt-Fe NCPs have been evaluated *in vitro* and *in vivo* to know the potentiality of the obtained nanoparticles in GB therapy. In our case, intranasal administration has been selected as the administration route in the *in vivo* experiments in order to evaluate its feasibility as an alternative methodology to administer the nanoformulation and reach the brain.

3.1 Nanoscale coordination polymers (NCPs) in medicine

Coordination polymers (CPs) are formed by the reaction of metal ions or clusters with organic bridging ligands via coordination bonds. The outstanding characteristic of CPs is their chemical versatility and flexibility permitting the rational design of novel multifunctional materials with interesting magnetic, electronic, optical, and catalytic properties. When the resulting polymers fall into the nanoscale range, they could merge the advantages of nanomaterials such as improvement of colloidal dispersion, increase of surface area and therefore improved catalytic/sensing/storage capabilities.[1]

According to the structural rigidity of the nanosized CPs, they can be divided into two categories: i) amorphous coordination polymer particles, referred as nanoscale coordination polymers (NCPs), also called infinite coordination polymers (ICPs) or coordination polymer particles (CPPs), and ii) nanoscale crystalline and porous coordination polymers, referred as nanoscale metal-organic frameworks (NMOFs).[2-5] The last family, NMOFs, allows control over the release of cargos by modification of tunable pores and the organic ligands to facilitate desired host-guest interactions. On the other hand, its amorphous counterpart, NCPs, allow more synthetic flexibility in the incorporation and release of cargos since they can be either physically entrapped or chemically attached as a composition of the building blocks of the nanostructures. NCPs have been investigated in many research fields, including gas storage and separation, catalysis, spin-crossover sensing, biomedical imaging, drug delivery or theragnostic platforms due to the virtually infinite combinations between metal ions and organic ligands.[3,6] Although both families of nanosized CPs have been utilized in the field of drug delivery, this work will focus on the first family of amorphous NCPs, especially their applications for cancer treatment.

Since the first report of NCPs for biomedical applications in 2005,[7-8] NCPs have attracted great attention in the field of nanomedicine due to their unique advantages. Typically, NCPs possess the following outstanding benefits over other existing nanomaterials (e.g., liposomes, inorganic NPs, among others) in biomedical applications: i) chemical diversities allowing tailoring in compositions, sizes, shapes, porous structures, and chemical properties; ii) possibility to incorporate active

pharmaceutical ingredients or bioactive molecules as building blocks permitting high loading efficiency or multifunctional integration; and iii) intrinsic biodegradability due to the relatively labile coordination bonds. Specifically, the application of NCPs covers main areas in nanomedicine such as bioimaging, chemotherapy, phototherapy, radiotherapy, immunotherapy, and the combination of bioimaging and therapy (theranostics).[9-10]

The presence of metal nodes in the NCPs allows taking advantage of the metal properties (optical, magnetic, and catalytic) for the design of nanoprobes showing multiple features with interesting applications in clinical diagnosis and/or therapy. For example, the integration of paramagnetic ions such Gd(III), Fe(III) and Mn(II) or the inclusion of radionuclei in the polymeric network afford NCPs active as contrast agents for MRI or radioimaging, respectively.[11-15] The incorporation of fluorescent or phosphorescent metal complexes has afforded nanoprobes able to be tracked by fluorescence imaging to work as contrast agents for optical imaing.[16]

Among the large number of NCPs reported for their use in nanomedicine, the vast majority of the research works focuses on their application for cancer therapy, either as therapeutic drug delivery systems, contras agents for diagnosis imaging or as theranostic systems. NCPs have demonstrated their function as nanocarriers to deliver various chemotherapeutic agents for cancer therapy.[17-18] Moreover, NCPs containing different photosensitizers as bridging ligands have been developed for phototherapy applications.[19] And many other examples also can be found for radiotherapy,[20-21] and immunotherapy[22].

Most of the materials developed by our group are based on the mixture of metal ions and organic ligands in the presence of a poor solvent that induces fast precipitation. This one-pot methodology usually leads to the formation of nanoparticles with spherical shape due to the tendency to minimize the interfacial free energy between the surface of the precipitated NCPs and the solvent. NCPs have demonstrated their ability for the encapsulation of therapeutic-active molecules through different approaches (Figure 3.1): i) using the drug or prodrug as building block in the NCPs, and ii) entrapping mechanically the therapeutic agent within the metal-organic matrix.[23] Moreover, the use of ligands with available functional groups for subsequent functionalization has allowed including extra functionalization after NCPs synthesis via condensation

reactions. In parallel, there were developed nanosystems including ligands sensitive to different external stimuli such as the presence of determinate enzymes,[24] or variation in pH,[25] what allow controlling the drug release properties.

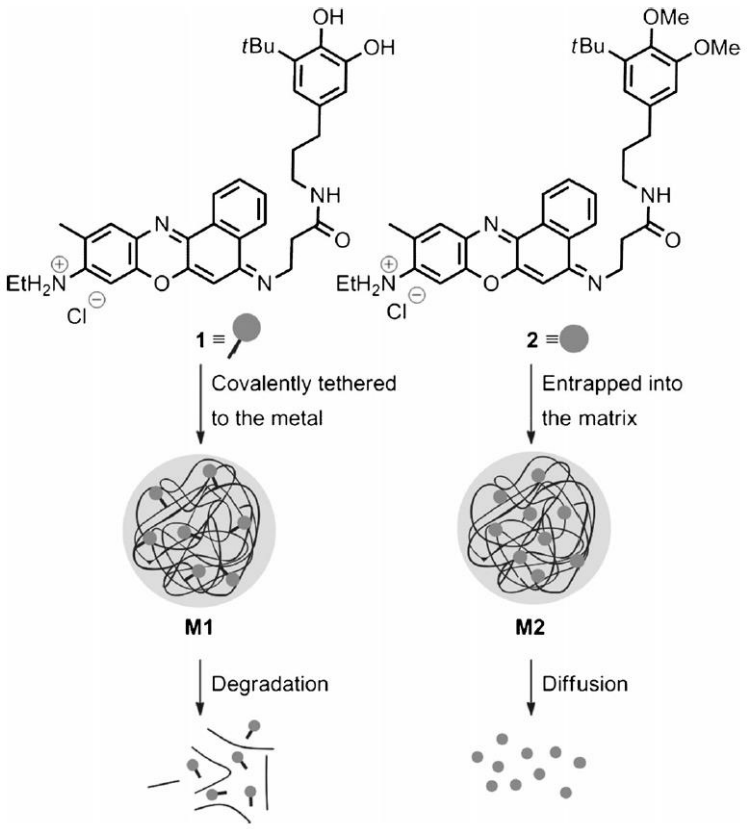

Figure 3.1 Chemical structures of fluorescent guest compounds 1 and 2 used to form the model NCPs M1 and M2, with which the degradation- and diffusion-controlled release mechanisms were studied.[23]

Our research group has previous experience in the synthesis of NCPs using cisplatin derivatives, specially Pt(IV) prodrugs, as anticancer drug delivery systems.[26] However, as most of the described in literature, there is not much information about the use of these nanosystems in *in vivo* studies. In this chapter, we have tried to go one step further and develop the design and synthesis of a Pt(IV)-based NCP with a specific application in GB treatment using preclinical GB *in vivo* models and using the intranasal delivery as the administration route.

3.2 NCPs based on Pt(IV) prodrugs for cancer treatment

Pt(IV) prodrugs and Pt(IV)-based nanomedicines have been increasingly studied due to their potential advantages over conventional Pt(II) complexes (e.g., increased stability, surface modification, and property tunability). Similarly, a host of Pt(IV)-based NCPs have also emerged and investigated for their potential medical applications. Herein, some interesting NCPs based on Pt(IV) prodrugs for cancer treatment have been summarized.

Lin W. has been a pioneer in the field of functional NCPs, who first summarized the modular synthesis of NCPs in 2009,[2] and published a series of papers about functional NCPs fabricated based on Pt(IV) prodrugs for cancer treatment. As Figure 3.2 shown, they synthesized NCPs with a Pt(IV) prodrug disuccinic cisplatin (DSCP) and Tb(III) as building blocks, and coated them with a silica shell to increase the stability, leading to controlled release with tunable release half-life ranging from 5.5 h to 9 h by tuning the coating shell thickness from 2 nm to 7 nm. Decorated with cyclic peptide c(RGDfK) targeting $\alpha v\beta 3$ integrin, the Pt(IV)-based NCPs displayed enhanced cytotoxicity compared to cisplatin due to the sufficient cellular uptake.[27] Later on, this same Pt(IV) prodrug was used to obtain NCPs by the coordination with Zr(IV) and La(III) ions, and stabilized by coating with a lipid layer to have a precise control on the drug release. In addition, the NCPs could specifically target sigma receptors by conjugating anisamide to the lipid, resulting in a significant increase in cytotoxicity and enhanced cellular uptake compared to non-targeted NCPs.[28]

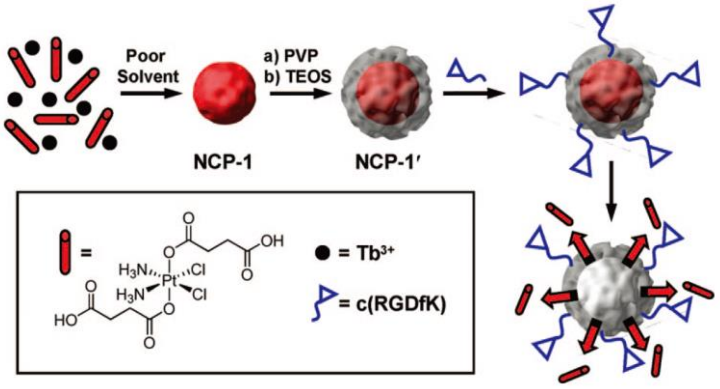

Figure 3.2 Scheme of cyclic peptide decorated Pt(IV) NCPs. Figure adapted from reference 27.

Lin W. reported other NCPs (Figure 3.3) based on bisphosphonate cisplatin or oxaliplatin Pt(IV) prodrug with Zn(II) and coated with cationic lipid layer. The resulting NCPs showed minimal RES uptake and excellent blood circulation half-lives of 16.4 ± 2.9 and 12.0 ± 3.9 h for cisplatin and oxaliplatin NCPs respectively, and exhibited significantly higher *in vivo* potency and efficacy compared with free drugs.[29] The oxaliplatin Pt(IV) prodrug NCP system was further studied to co-deliver another anticancer agent, gemcitabine monophosphate (GMP), resulting in strong synergistic therapeutic effect of oxaliplatin and GMP against pancreatic cancer cells. *In vivo* studies showed that the co-delivery NCPs can avoid RES uptake and gain prolonged circulation half-life, and potently inhibit growth of pancreatic tumor compared to NCPs carrying oxaliplatin or GMP alone.[30] Similarly, carboplatin Pt(IV) prodrug and GMP were incorporated into the NCP delivery system, leading to a strong synergistic effect against Pt-resistant ovarian cancer cells, and enhanced circulation half-life and improved tumor uptake, resulting in significant growth inhibition of resistant SKOV-3 and A2780/cis tumors *in vivo*.[31]

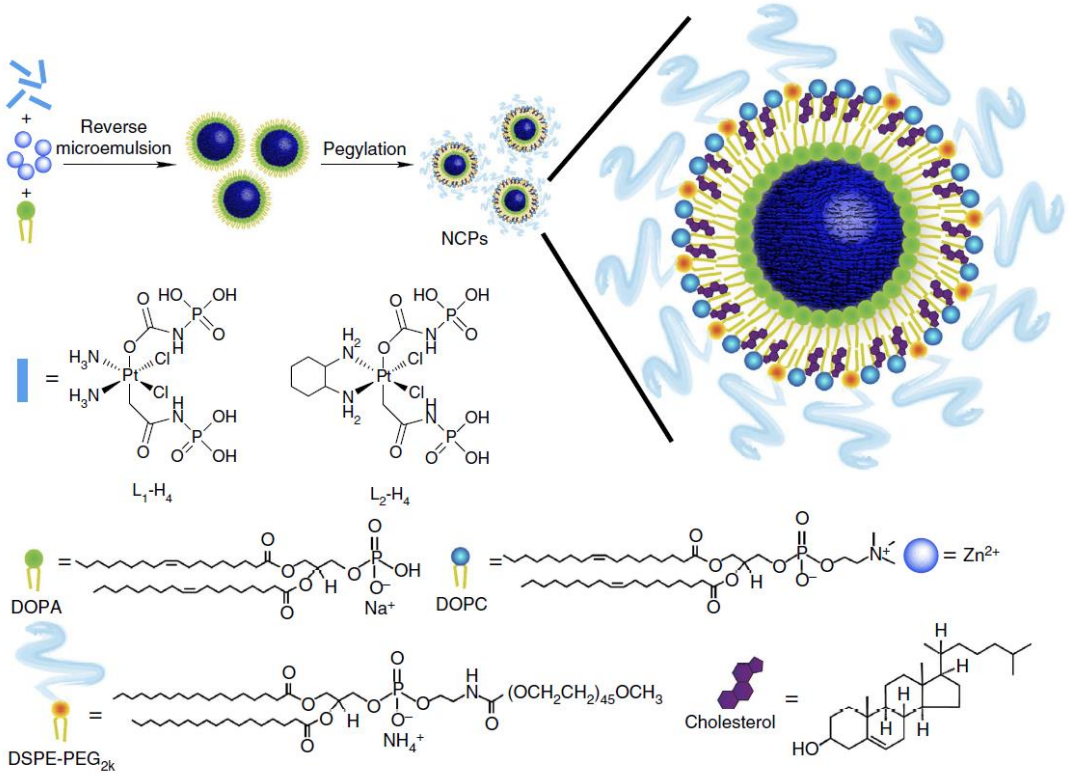

Figure 3.3 Schematic showing the composition of NCPs based on cisplatin/oxaliplatin prodrug. The figure was adapted from reference 29.

On the other hand, the cisplatin Pt(IV) prodrug NCP system was also investigated the combination with gene therapy by adsorption multidrug resistance (MDR) genes-targeting siRNA on the lipid shell. After surface modification, the NCPs promoted cellular uptake and enhanced the chemotherapeutic effects greatly by downregulating the expression of the MDR genes, and local administration effectively inhibited tumor growth of cisplatin-resistant SKOV-3 ovarian xenografts.[32-33] Recently, Lin et. al. fabricated a novel NCP platform containing nontoxic Pt(IV) prodrug to deliver miRNA, leading to inhibition on epithelial-to-mesenchymal transition by preventing β-catenin nuclear translocation and tumor cell invasion. The NCPs showed effective transfection to reduce liver colonization and tumor burden after systemic administrations in hepatic metastatic xenografts of HCT116 without observable toxicity.[34]

Despite the combination of chemotherapy and gene therapy, Lin and colleagues also explored the combined immunotherapy. Thus, the oxaliplatin Pt(IV) prodrug NCPs were coated with photosensitizer lipid shell, resulting in effectively synergistic effects of chemotherapy and photodynamic therapy. Combining with anti-PD-L1 therapy, the NCPs mediated regression of both light-irradiated primary tumors and non-irradiated distant tumors by inducing tumor-specific immune response.[22] More recently, they reported the Pt(IV) prodrug-based NCPs incorporating a ROS-inducing agent, which activated the co-delivered anti-PD-L1 antibody to synergize the immunotherapy and chemotherapy from oxaliplatin prodrug.[35] The NCPs can be dosed repeatedly to eradicate the murine colorectal tumors due to the favorable biodistribution and tumor uptake without peripheral neuropathy, and long-term antitumor immunity was elicited and prevented tumor relapse when cured mice were challenged with cancer cells.

Recently, the research group led by Liu Z. also published some papers regarding Pt(IV) prodrug-based NCPs for cancer treatment. For instance, they synthesized a pH-responsive charge-switchable PEGylated NCPs (Figure 3.4) using one-pot method with Pt(IV) prodrug and Ca(II). The NCPs were highly sensitive to pH changes, the acidic pH would switch the slightly negative NCPs to positive to enhance tumor retention and cellular internalization, and they could significantly inhibit the growth of 4T1 murine breast tumors in nude mice.[19] The same authors obtained a new NCP by integration of cisplatin prodrug DSCP and Fe(III) (Figure 3.4a) stabilized by PEG and coated with cRGD

(Figure 3.4b), which showed excellent targeting αvβ3 integrin-overexpressed tumor cells, and enabled chemotherapy and chemodynamic therapy with dramatically enhanced efficacy compared to relative monotherapies.[36]

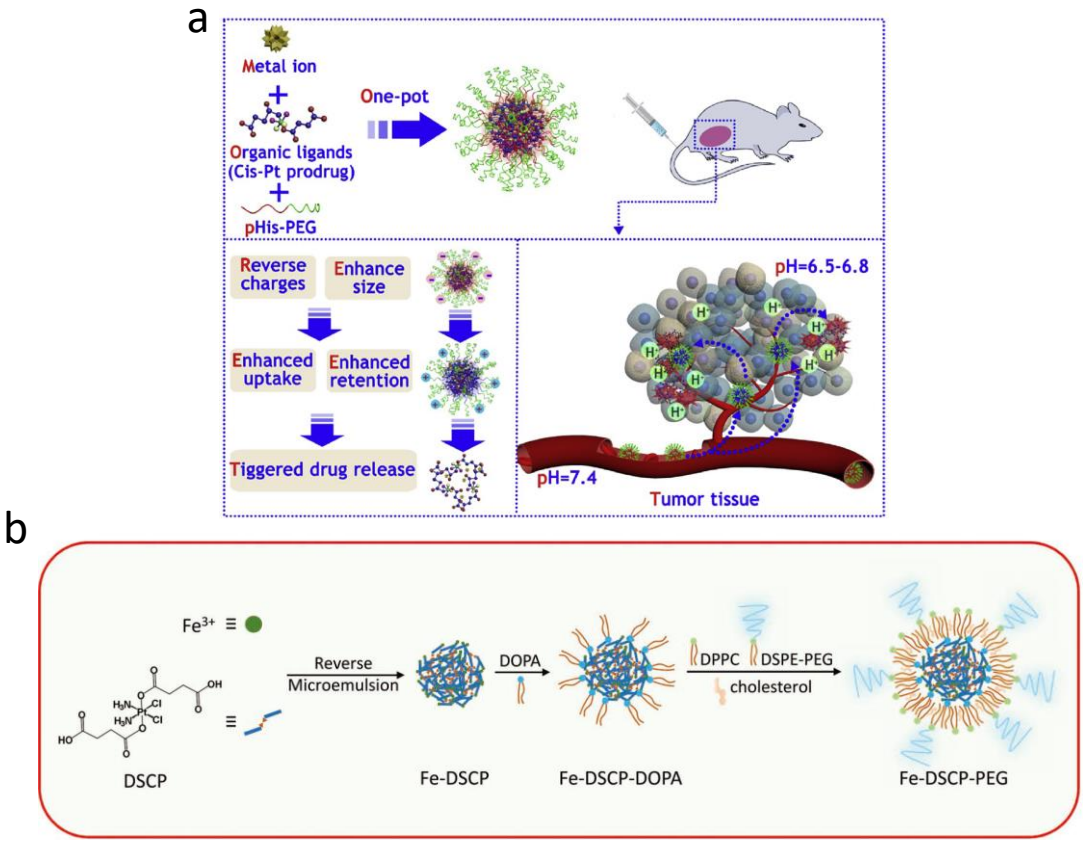

Figure 3.4 Schematic illustration of the NCPs developed by Liu et.al. a) One-pot synthesis of PEGylated NCPs and its application for TME-responsive anticancer therapy,[19] and b) scheme showing fabrication of Fe-DSCP NCPs, followed by PEG modification[36].

In 2018, our group reported Zn-Pt(IV)-NCPs consisting of a cisplatin Pt(IV) prodrug DSCP and Zn(II) with a linker ligand 1,4-Bis(imidazol-1-ylmethyl)benzene.[26] The resulting NCPs displayed a good stability in physiological environments, and a controlled Pt release *in vitro*. The NCPs showed enhanced cytotoxic effects against cervical cancer, neuroblastoma and human adenocarcinoma cells, in comparison to the free Pt(IV) prodrug. A higher amount of Pt was found bound to the DNA in the cells treated with the NCPs, although no difference was found in the cellular uptake of Pt, indicating that the nanostructure facilitated the activation of the prodrug and may induce a change in the mechanism of action resulting in an increased interaction with the DNA.

3.3 Scope of this chapter

Despite the progress of NCPs for anticancer diagnosis and treatment during the last decade, some challenges remain to be faced before the real application of these nanosystems in the clinics:

i. Facile and low-cost synthetic procedures for the synthesis of prodrugs and nanoparticles.

ii. Chemical stability in a biological environment being highly biocompatible, non-toxic and non-accumulative in the organism.

iii. Specific control of the drug delivery profile in the site of action.

iv. High efficiency in different tissues by suitable biodistribution

v. *In vitro* and *in vivo* proof-of-concept of their anticancer effect

vi. Design of nanoformulations to be administered by novel administration routes specifically to reach the brain (i.e., intranasal)

vii. Evaluation of multifunctional features (i.e., drug delivery systems and contrast agents for bioimaging)

As described previously, the standard of care for GB (temozolomide, TMZ) presents challenges related to poor drug delivery, degradation processes, limited BBB crossing and drug resistance. The integration of this chemotherapeutic compound in nanoparticles have showed interesting results at *in vitro* and *in vivo* level, but non-conclusive. Toxicity issues related to nanoparticles drive researchers to develop more efficient and safer alternatives with tunable options. Moreover, the interesting activity of TMZ for GB treatment has presumably diminished the number of developments of nanoparticles containing other potentially relevant therapeutic agents like platinum derivatives that have showed for long time a very remarkable anticancer activity. For this reason, providing novel systems aiming at efficient drug delivery into brain and GB could help to the increase of the effectiveness and decrease of side effects of therapies.

Based on this, in this work, it is proposed for the first time, the use of NCPs as potential candidates for GB therapy via IN delivery. In this Chapter, the synthetic protocol includes the synthesis of the Pt(IV) prodrug which is the building block of the nanostructured coordination polymers obtained by the reaction of the Pt(IV) complex with iron(III) ions (Figure 3.5). Through this rationale design, the NCPs named Pt-Fe NCPs have been proposed. The systems aim to accomplish: i) moderate chemical stability, ii) water-colloidal stability, iii) low toxicity and biocompatibility, iv) controlled drug delivery profile, vi) intrinsic properties to be used as contrast agents for clinical image, and v) potential anticancer activity *in vitro* against glioblastoma cell lines and *in vivo* against GB murine models using intranasal administration as the administration route. The nanoparticles will be characterized by different physicochemical techniques and its behavior in physiological environment both *in vitro* and *in vivo* will be tested. To evaluate the delivery into brain and GB tumor of the NCPs after intranasal administration, the *in vivo* studies will be the performed in orthotopic GL261 murine models. The syngeneic immunocompetent GL261 murine glioma model is one of the most widely used to study the glioblastoma, which is usually established by inoculation of GL261 murine cells into C57BL/6 substrain, resulting in invasive and infiltrative GB tumors, similar to those found in human patients.[37-41]

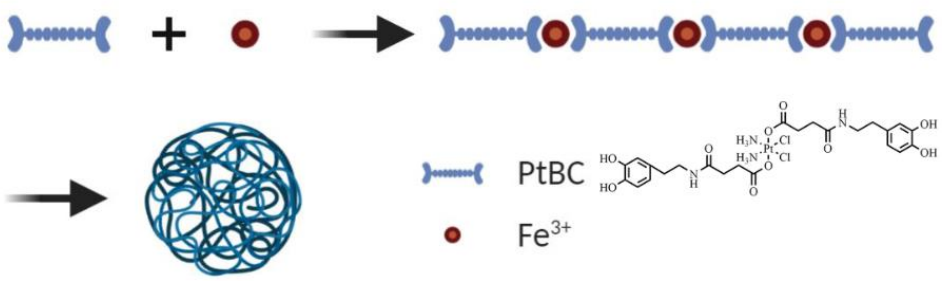

Figure 3.5 Scheme of the synthesis of the Fe-Pt NCPs developed in this chapter.

To sum up, the synthesis novel Pt-Fe NCPs for its potential use as therapeutic agents for GB is presented. Despite remarkable advances in basic and clinical research, the clinicians are yet unable to provide realistic therapy for this kind of tumors, and the use of Pt-based chemotherapies are not well developed. For this reason, providing to the

community with novel systems that enhance the effectiveness of therapies could help to find alternative and more suitable treatments.

The specific objectives for this Chapter are:

i. Synthesis of the nanoparticles Pt-Fe NCPs.

ii. Physicochemical characterization and chemical/colloidal stability studies of NCPs *in vitro.*

iii. Preclinical *in vivo* studies with a GB murine model

iv. Comparison of the therapeutic activity between Pt-Fe NCPs and cisplatin/prodrug

3.4 Results and discussion

3.4.1 Synthesis and characterization of Pt(IV) prodrug

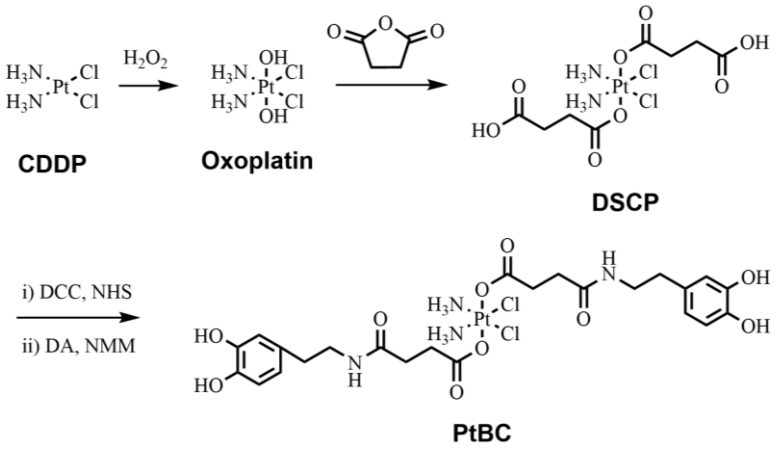

Figure 3.6 The synthetic route of Pt(IV) prodrug PtBC.

The synthesis of Pt(IV) prodrug was developed from the commercially available anticancer platinum agent, cisplatin. The synthetic route (Figure 3.6) comprised of several steps: 1) the oxidation of cisplatin to *c,c,t*-$Pt(NH_3)_2Cl_2(OH)_2$ (oxoplatin) by reacting with hydrogen peroxide; 2) oxoplatin was converted into of *c,c,t*-$Pt(NH_3)_2Cl_2(O_2CCH_2CH_2COOH)_2$ (DSCP) by the addition of succinic anhydride; and 3) dopamine was attached to DSCP via a typical DCC/NHS coupling using NMM as base. The synthesis of the intermediate DSCP was slightly modified according to previous report

from our group.[26] Specific reaction conditions and detailed synthetic method is described in section 3.6. PtBC was successfully synthesized with an overall yield of 24.7%.

All compounds obtained after reactions were characterized and compared by FT-IR (Figure 3.7). In the spectrum of oxoplatin, the peak at 559 cm^{-1} was characteristic from the vibration of Pt-O coordination bonding, and the intensely sharp peak at 3516 cm^{-1} belongs to O-H vibration.[42] In the spectrum of DSCP, the peak at 3516 cm^{-1} disappeared, and the new band around 1630-1734 cm^{-1} typically can be assigned to C-O stretching from the carboxyl groups, while new band at 1180-1347 cm^{-1} also implied the presence of succinic acid attached. Finally, in the spectrum of PtBC, the band from carboxyl groups shifted to lower wavenumber at 1527-1645 cm^{-1} indicating the formation of amide bond (Amide I at 1621 cm^{-1} and Amide II at 1559 cm^{-1}), and the characteristic peak of catechol showed up at 1198 cm^{-1} from C-O stretching on the aromatic ring. To further confirm the chemical syntheses results, DSCP, its NHS-activated ester and PtBC were checked by ^{1}H NMR spectra (Figures 3.8-3.10, respectively). In the ^{1}H NMR spectrum of DSCP (Figure 3.8), the ratio between all protons perfectly fit the theoretical value including the -OH group at ~12 ppm in deuterated DMSO. The ratios of protons also fit well for the activated intermediate DSCP-NHS (Figure 3.9) and final product PtBC (Figure 3.10a). Further ^{13}C NMR and 2D ^{1}H-^{1}H COSY NMR spectra (Figure 3.10b-c) of PtBC confirmed its expected chemical structure. High-resolution mass spectrum (Figure 3.11) also showed correct mass of PtBC (found 803.1284, calc. 803.1300). All these spectra substantiated that the compounds were all successfully synthesized with high purity level.

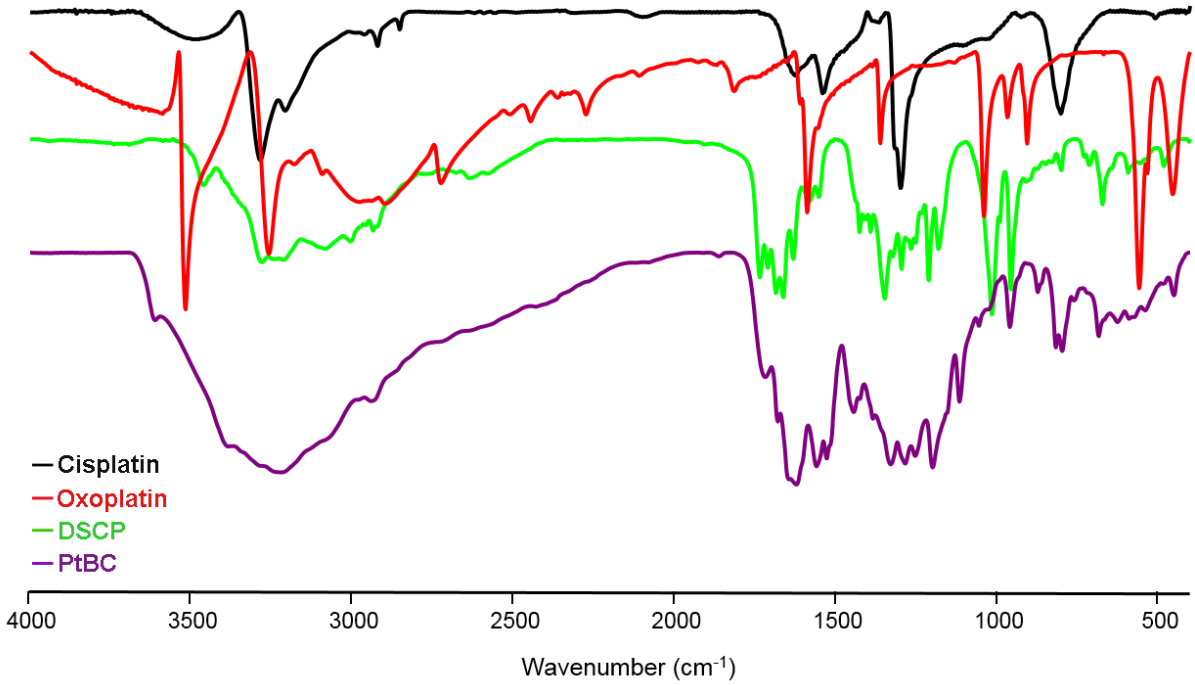

Figure 3.7 FT-IR spectra of cisplatin, oxoplatin, DSCP and PtBC.

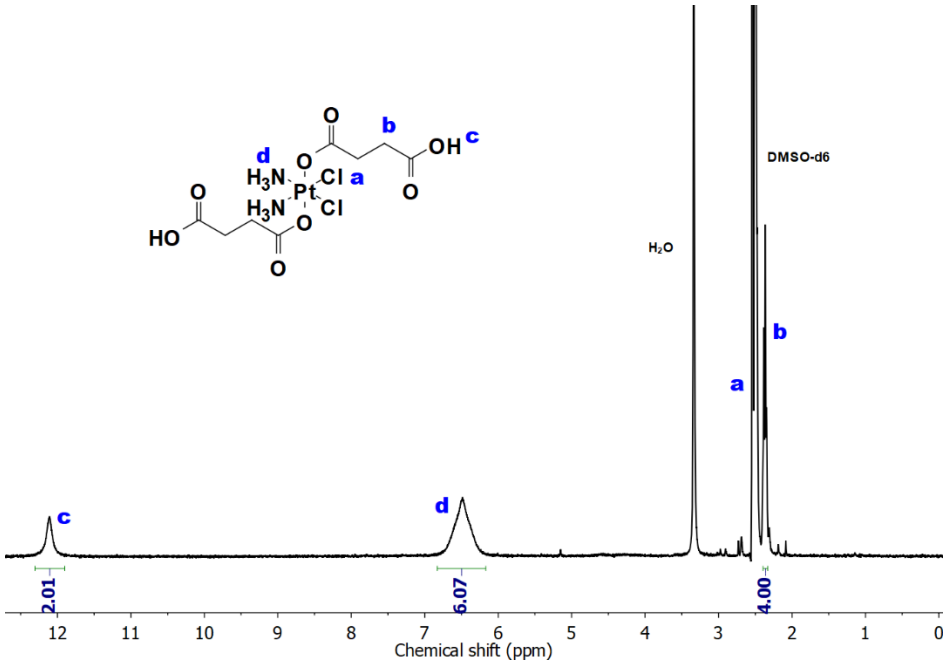

Figure 3.8 ^{1}H NMR spectrum of DSCP.

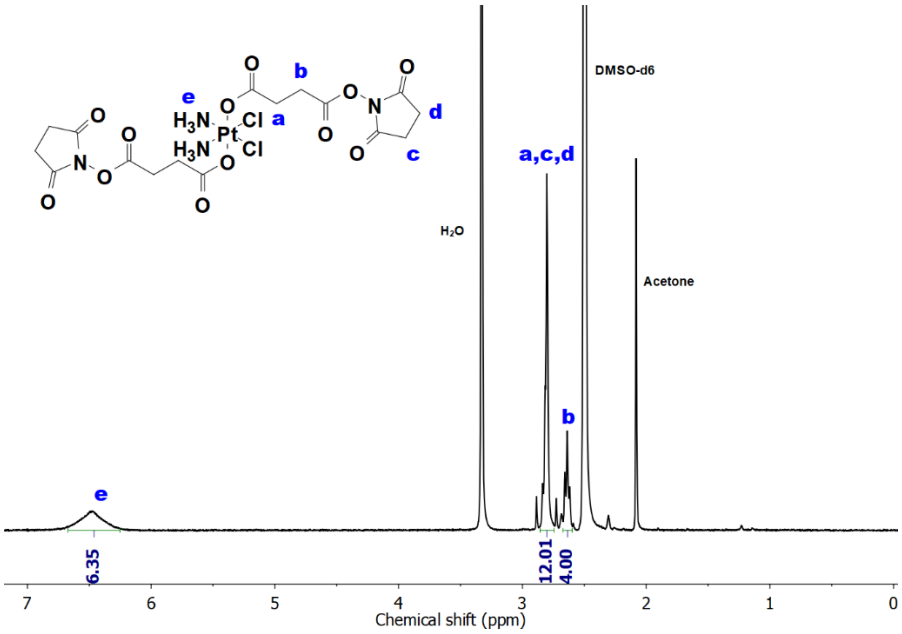

Figure 3.9 ^{1}H NMR spectrum of DSCP-NHS.

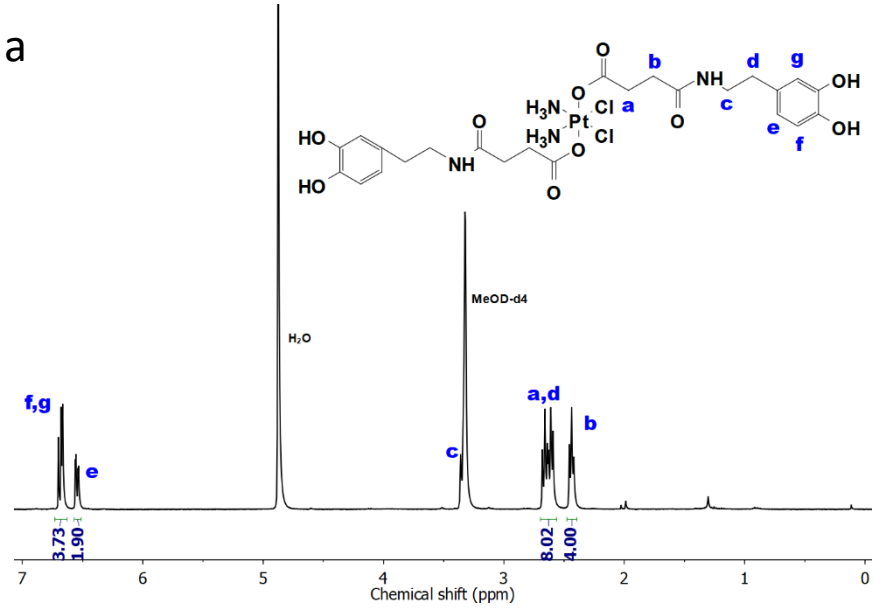

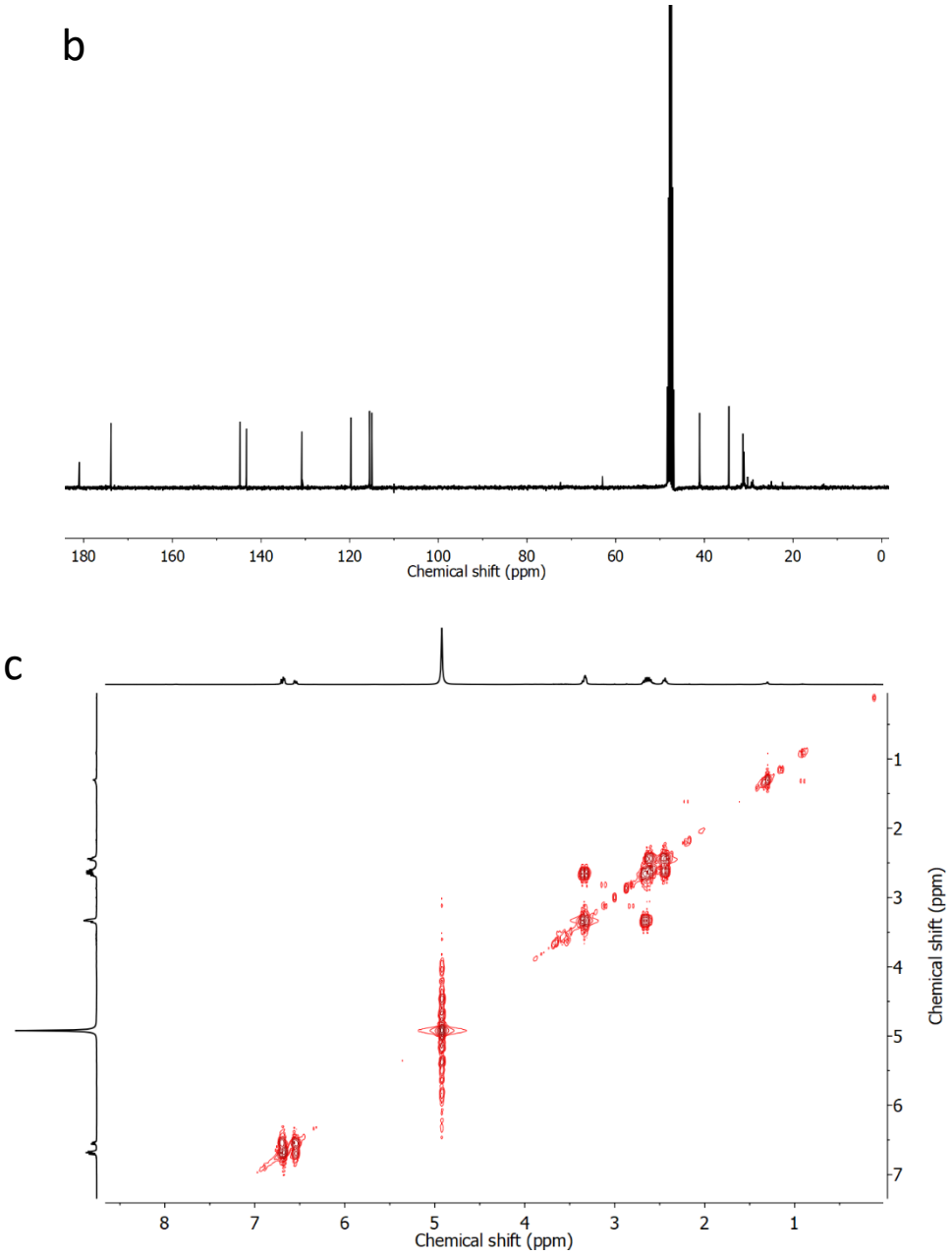

Figure 3.10 ^{1}H (a), ^{13}C (b), and 2D COSY (c) NMR spectra of PtBC.

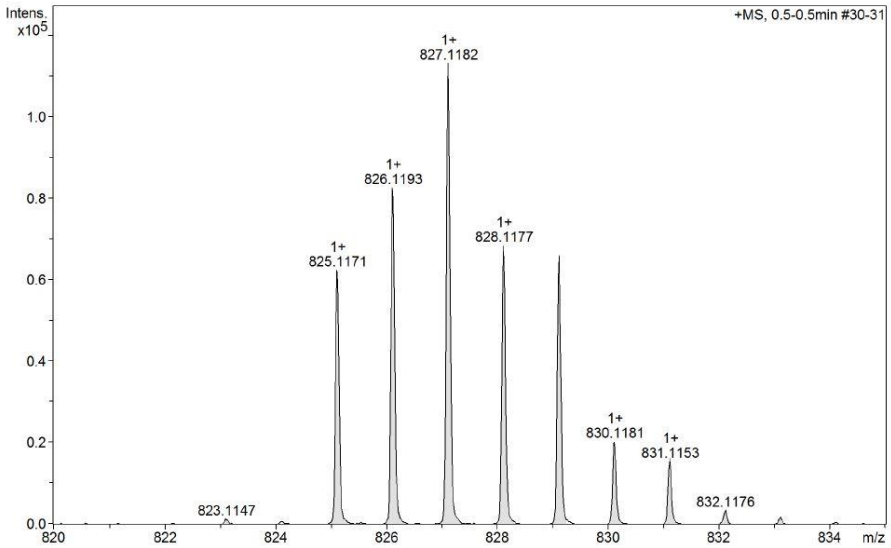

Figure 3.11 High-resolution mass spectrum of PtBC.

3.4.2 Synthesis and characterization of Pt-Fe NCPs

The Pt-Fe NCPs formed immediately after the addition of $Fe(OAc)_2$ into PtBC solution (1:1 in molar ratio). The reaction leads to the formation of a black precipitate, due to the coordination between the terminal catechol moieties and iron ions at rt, as shown in Figure 3.12. This reaction generated the Pt-Fe NCPs nanoparticles with a 49.3% yield and high reproducibility.

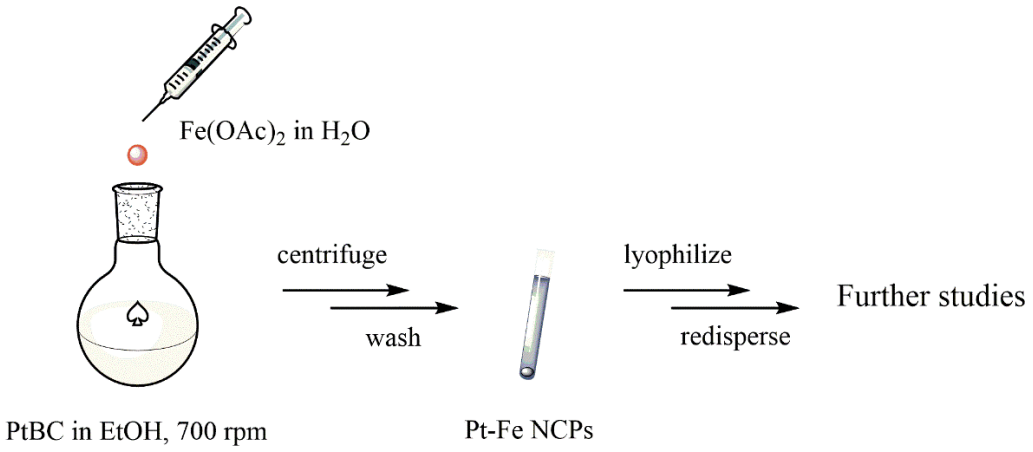

Figure 3.12 Schematic illustration of the synthesis of Pt-Fe NCPs.

The morphology and size of the NCPs was observed by SEM, STEM and TEM (Figure 3.13). Relatively monodispersed and uniform spherical NPs were observed under all electronic microscopy techniques, with a size around 70 nm. This size is in good accordance with the result of DLS after NCPs redispersion in phosphate buffer saline (PBS). In fact, both size and ζ-potential (Figure 3.14) of Pt-Fe NCPs were measured, showing an average size of 66.0 ± 2.3 nm, with a PDI of 0.258 ± 0.013, and a slightly negative ζ-potential of -8.53 ± 0.418 mV.

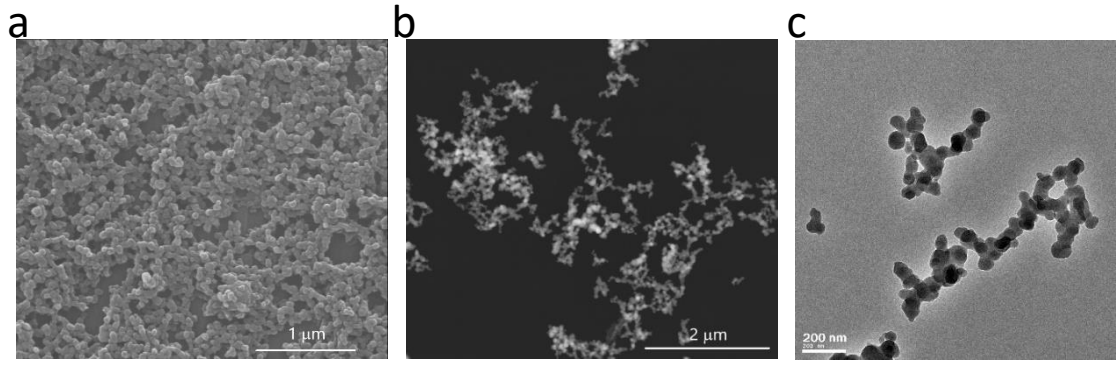

Figure 3.13 Representative morphologies of Pt-Fe NCPs under SEM (a), STEM (b, HAADF mode), and TEM (c).

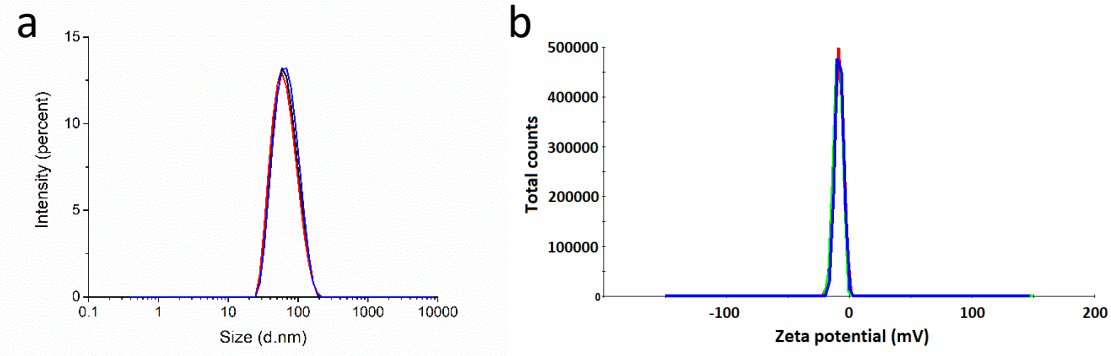

Figure 3.14 Representatively size distribution (a) and ζ-potential (b) of Pt-Fe NCPs by DLS.

The NCPs present good monodispersion values (PDI < 0.20) and colloidal properties. The sizes of the obtained NCPs are in an optimal range for their medical use. In fact, this parameter plays an important role in the pharmacology and metabolism of NPs. It is well know that nanoparticles < 30 nm are more likely to be cleared by the renal system, while particles > 300 nm tend to be phagocytosed by the reticuloendothelial system (RES) and accumulated in liver and spleen.[43-44] Particle sizes < 100 nm were reported to facilitate

NPs' transit across the BBB.[45-46] The relatively low PDI indicated the possibility of a more uniform behavior after administration and less pharmacokinetic irregularity and variability in therapeutic outcome.[47] The electrostatic adsorption with the mucosa occurs with positive ζ-potential substances which may facilitate transit retention but it can affect the stability and availability thereafter.[48] The almost neutral ζ-potential avoid excessive interaction before reaching the target sites and thus endow Pt-Fe NCPs better stability during transport.

X-ray powder diffraction data showed that these nanoparticles are amorphous (Figure 3.15a), and EDX spectrum (Figure 3.15b) obtained from TEM qualitatively confirmed the presence of Pt and Fe in the polymeric material, along with C, O and Cl (Cu comes from the grid). The comparison of FT-IR spectra (Figure 3.16) of the ligand and the NCPs showed noticeable changes, as described as follows. The intensity of the characteristic band of catechol around 1200-1400 cm^{-1} changed, peaks at 1527, 1328, and 1282 cm^{-1} disappeared, and the peak at 1198 cm^{-1} decreased in intensity and shifted to 1220 cm^{-1} in the NCPs. The appearance of two new intense peaks at 1484 cm^{-1} and 1261 cm^{-1} were reported to be evidence of the coordination of catechol rings and iron.[49] All these changes implied the occurrence of the coordination of PtBC with Fe.

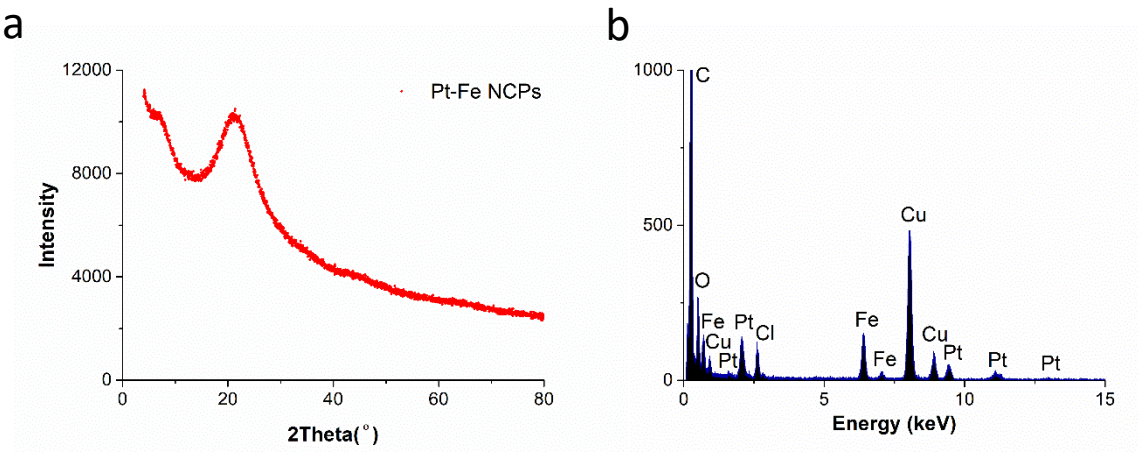

Figure 3.15 Powder XRD (a) and EDX (b) of PtBC-Fe NCPs.

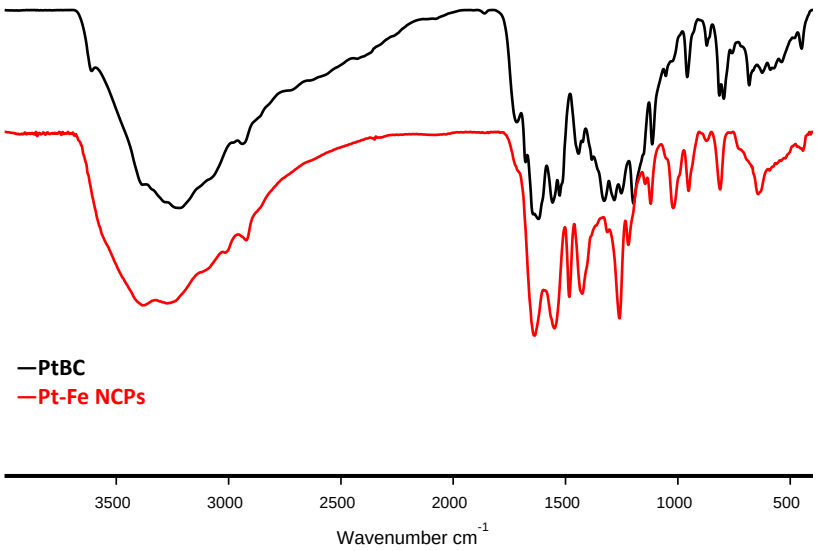

Figure 3.16 FT-IR spectra of the prodrug and Pt-Fe NCPs.

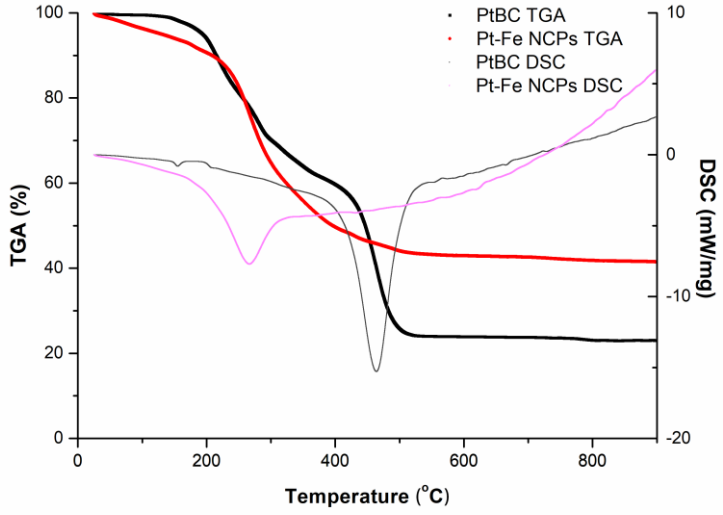

Figure 3.17 TGA and DSC of PtBC (black) and Pt-Fe NCPs (red).

Thermal gravimetric analysis (TGA) coupled with differential scanning calorimetry (DSC, Figure 3.17), elemental analysis (EA) and inductively coupled plasma mass spectrometry (ICP-MS) were employed to further determine the quantitative composition of Pt-Fe NCPs. From the TGA curves, the prodrug PtBC was stable till 200 ℃, and started to lose weight slowly to 50% at 400 ℃, then a fast loss occurred around 450 ℃ till reaching stable again at 540 ℃ with a total weight loss of 76%. In contrast,

the Pt-Fe NCPs started to lose weight slowly from the beginning with a 10% slow loss till 200 ℃, then lost weight quickly from 270 ℃ till 400 ℃, and slowly reached stable till 500 ℃ with a total weight loss around 43%. The decomposition of Pt-Fe NCPs went through a different pathway which was also indicated by the DSC curves with dissimilar valleys. The difference of the thermal stability between them could be attributed to the distinct structures of these two samples. The slow decomposition of Pt-Fe NCPs from the beginning may result from the labile coordination bonds between the metal nodes and the organic ligand. In Table 3.1, the results are shown obtained from analyses of C%, H%, N%, Pt% and Fe%, together with the calculated theoretical values. These correlations offer a proposed chemical formula $[(PtBC)_1Fe_3(OH^-)_5]_n$ for Pt-Fe NCPs.

	C	H	N	Pt	Fe
Exp. % wt	28.63	2.54	5.79	18.87	15.13
Cal. % wt	27.27	3.72	5.30	18.45	15.83
Error %	0.99	1.18	0.69	0.42	0.7

Table 3.1 Experimental composition obtained by elemental analysis and ICP-MS, and correlation with the theoretical values for the proposed chemical formula $[(PtBC)_1Fe_3(OH^-)_5]_n$.

Additionally, Mössbauer spectroscopy confirmed that Pt-Fe NCPs showed a high-spin Fe(III) oxidation state (Figure 3.18), thus corroborating the oxidation process from Fe(II) to Fe(III) during the synthesis of the Pt-Fe NCPs. This electronic modification results from a redox interplay during the synthesis reaction between the metal ion and the electroactive catechol ligands in the presence of oxygen, as previously reported.[50]

The hyperfine parameters of the fitting of Mössbauer at 300 K showed the isomer shift relative to the metallic iron ((δFe), quadrupolar splitting (ΔEq) and the full width at half maximum (Γ). The spectrum was fitted to a single doublet with a ΔEq= 0.81 ± 0.04 mm/s and Γ= 0.32 mm/s. The fitting was centered at an isomeric shift δ= 0.39±0.03 mm/s.

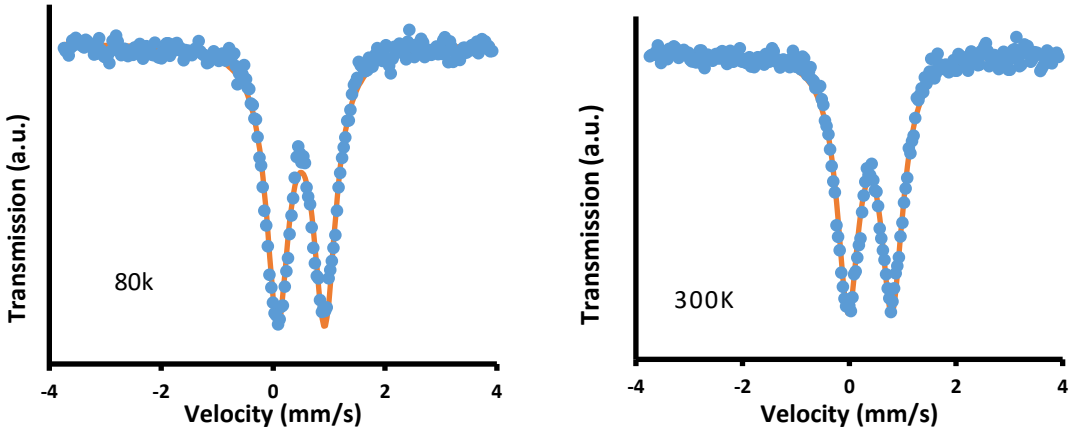

Figure 3.18 Representative Mössbauer spectra of Pt-Fe NCPs at 300 K and 80 K. Experimental data (blue dots), and computation fitted (orange line) spectra.

3.4.3 Colloidal stability of Pt-Fe NCPs

Since the naked NCPs tended to form small clusters ~ 300 nm even aggregates > 1 μm, it is necessary to improve the colloidal stability for further *in vitro* and *in vivo* studies. Different methods were adopted to improve the stability, such as 1) coating with polydopamine-like (PDA-like) polymer, or 2) using different stabilizers to increase the dispersity.

3.4.3.1 PDA-like coating for stabilizing Pt-Fe NCPs

Previous studies carried out in our group showed how NCPs could be coated with a PDA-like polymer to increase the stability of NCPs, overall achieving better biodistribution and favoring the delivery of cargos.[51] Therefore, the same idea was come up with to stabilize the Pt-Fe NCPs. The coating process commonly occurs in two main steps: 1) the primer formation of PDA via the oxidative polymerization of catechol which can adhere to a wide range of materials and surfaces, and 2) the deposition of the PDA onto the surface of the materials for coating. Following this approach, a catechol-based coating was obtained through the crosslinking of pyrocatechol (cat) and hexamethylenediamine (HMDA), as shown in Figure 3.19.

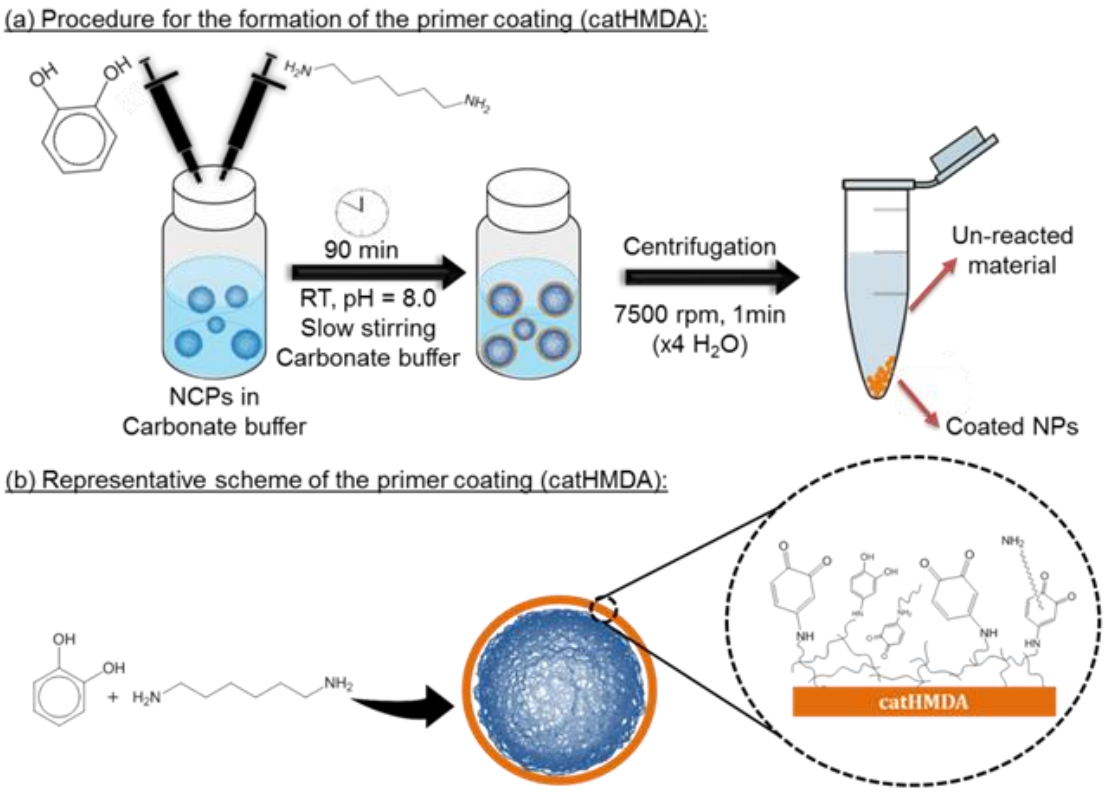

Figure 3.19 Two-step scheme of PDA-like coating for Pt-Fe NCPs.[52] (a) Procedure for the formation of primer coating in the NCPs system using pyrocatechol and HMDA; and (b) illustration of the primer coating nature deposited on the NCPs' surface of NCPs.

As observed in DLS measurements (Figure 3.20a), naked Pt-Fe NCPs dispersed in PBS (0.5 mg/mL) showed a gradual aggregation with time (PDI = 0.431). However, after coating (Figure 3.20b), a more uniform size distribution with a PDI of 0.182 obtained, suggesting an improved colloidal stability.

TEM images showed the morphological differences between coated and non-coated NPCs. Texture of NCPs changed after coating from relatively smooth to rough surface, as shown in Figure 3.21.

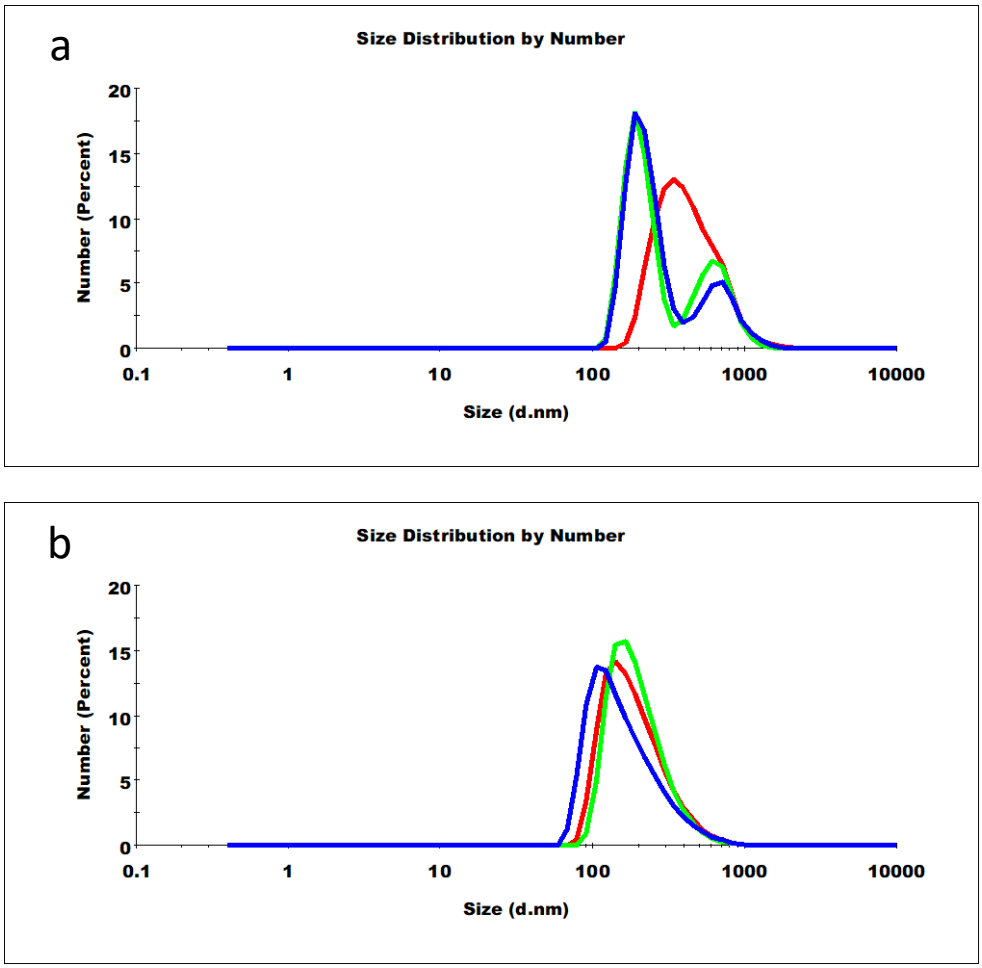

Figure 3.20 Representative size distribution of Pt-Fe NCPs before (a) and after (b) coating with time. In the graph, blue curve was measured at 0 h, green curve at 1 h, and red curve at 24 h after preparation, respectively.

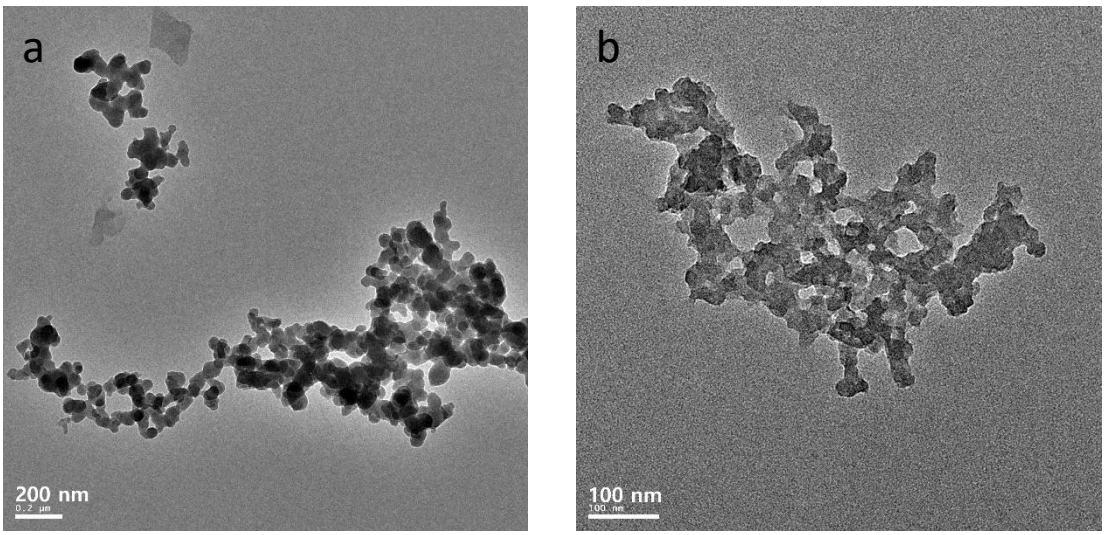

Figure 3.21 Representative TEM images of Pt-Fe NCPs before (left) and after (right) coating.

To confirm the presence of the coating layer, line profile EDX analysis was carried out using TEM, as shown in Figure 3.22. In this analysis the film covering the NCPs can be distinguished from the Pt-Fe NCPs as the PDA-like coating comparing carbon versus iron profile.

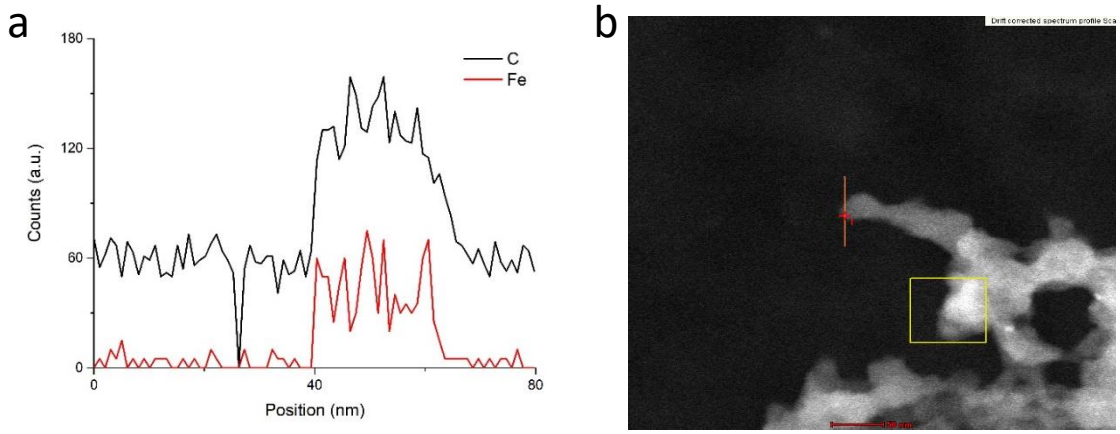

Figure 3.22 Line profiles (a) of carbon and iron across the surface of coated Pt-Fe NCPs (b)

To check the chemical composition of synthesized NCPs before and after coating, EDX (Figure 3.23) and ICP-MS were performed to compare the values of Pt and Fe. Although EDX indicate the persistence of Pt and Iron in the coated NCPs, ICP-MS corroborated a dramatic decrease of Iron and Platinum content. In fact, Pt decreased drastically by 85.746%, while Fe decreased by 50.485% (Table 3.2). With the organic coating, the contents of both metals should decrease, but the ratio between them should keep as a constant if the composition of the NCPs remains stable during the coating process. However, the ratio between Pt and Fe dropped drastically from 1.252 to 0.361, indicating a sharp reduction of Pt compared to Fe drop after coating. This probably is due to the competition between the catechol moieties from our ligand PtBC and those from pyrocatechol during the coating formation. In this dynamic competition of cleavage and re-coordination, the NCPs probably degraded somehow and lost Pt.

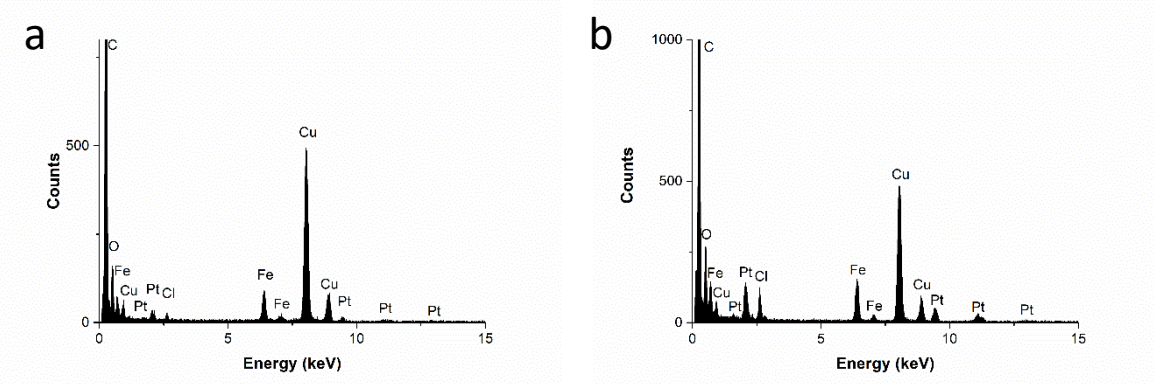

Figure 3.23 EDX spectra indicating a dramatic decrease in content of Pt after coating (b) compared to before coating (a).

	Before	After	Reduction/%
Fe (wt%)	15.130	7.492	50.485
Pt (wt%)	18.948	2.701	85.746
Pt/Fe	1.252	0.361	71.166

Table 3.2 Metal loss in Pt-Fe NCPs after coating.

3.4.3.2 Use of stabilizers for increasing dispersity of Pt-Fe NCPs

A wide range of compounds were utilized to improve the colloidal properties of Pt-Fe NCPs, including bovine serum albumin (BSA), polyethylene glycol derivatives (PEG, PEG-NH_2, PEG-$(COOH)_2$), Polyvinyl alcohol (PVA) and polyvinylpyrrolidone (PVP).

Corresponding size, PDI, and ζ-potential were recorded and compared by DLS (Table 3.3), while morphology was observed by STEM (Figure 3.24). For almost all the stabilizers notable aggregation was observed. Only in the case of PVP it seemed that the colloidal dispersion and stabilization was achieved. It was reported that NPs with absolute value of ζ-potential > 30 mV show relatively high stability.[53-54] As observed, the stabilizers had influence on the ζ-potential of the Pt-Fe NCPs, and none of these stabilizers can make the absolute ζ-potential to reach 30 mV, which may not be applicable to all NP systems.

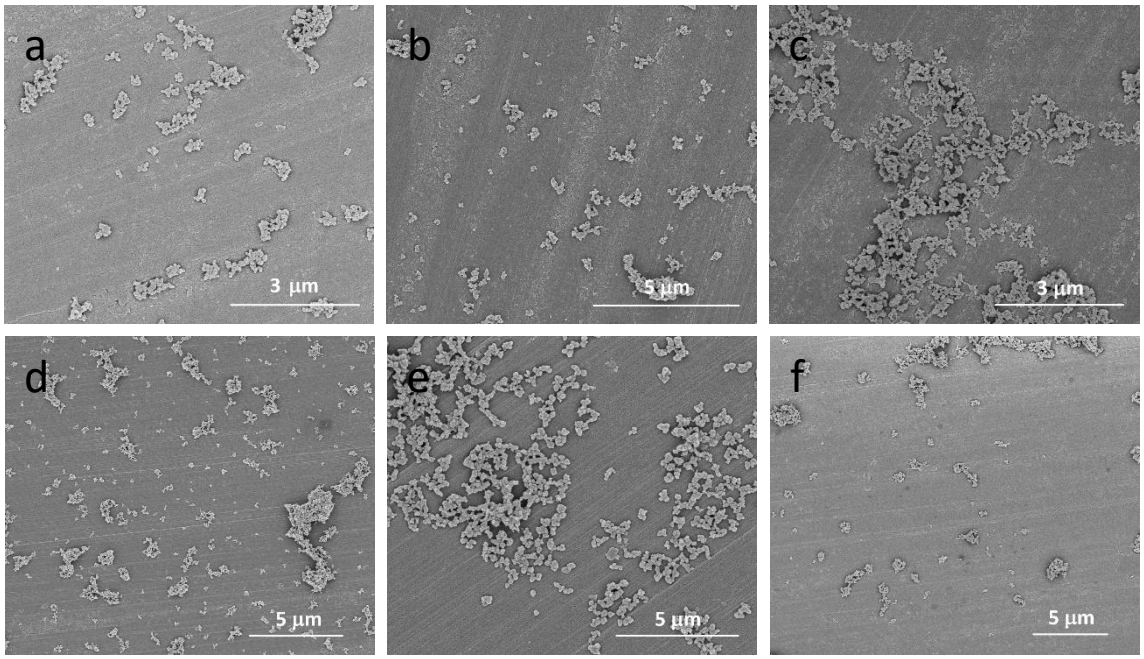

Figure 3.24 Pt-Fe NCPs stabilized by a) BSA, b) PEG, c) PEG-(COOH)2, d) PEG-(NH2)2, e) PVA, and f) PVP under STEM. BSA was added to a concentration of 10 mg/ml, other stabilizers at 1%, whereas, the NCPs at a concentration of 0.5 mg/mL.

	BSA	PVA	PEG	PEG-NH_2	PEG-$(COOH)_2$	PVP
Size / nm	548.5 ± 81.10	398.7 ± 125.9	681.4 ± 97.38	1181 ± 99.47	4491 ± 711.8	72.12 ± 0.86
PDI	0.585 ± 0.033	0.654 ± 0.206	0.66 ± 0.018	0.584 ± 0.02	0.516 ± 0.468	0.271 ± 0.006
ζ-pot. / mV	-10.3 ± 0.435	-7.47 ± 0.771	-13.2 ± 0.265	6.05 ± 0.754	-14.8 ± 0.44	-8.09 ± 0.100

Table 3.3 Colloidal stability of Pt-Fe NCPs using different stabilizers in terms of size, PDI, and ζ-potential.

Additionally, sucrose also was tested as a stabilizer. There has been some previous reports concerning the use of this sugar as stabilizer for NCPs.[24] Thus, different concentrations of sucrose (with final concentrations between 0.5% - 50% in PBS) were added into Pt-Fe NCPs suspension, and the dispersions were checked by DLS (Table 3.4). In basis of DLS measurements only the 50% concentrate solution was able to keep the NCPs suspension stable up to 3 days.

Sucrose/%	0	0.5	1	5	10	25	50
Size/nm	365.1	486.0	385.7	385.5	323.8	280.6	117.4
PDI	0.431	0.316	0.228	0.215	0.200	0.225	0.205

Table 3.4 Colloidal stability of NCPs in PBS with different concentrations of sucrose in terms of size and PDI.

However, such a high concentration (50%) of sucrose was not reasonable to add into a formulation for anticancer treatment. Taken previously tested substances into consideration, PVP was finally chosen as the stabilizer for the Pt-Fe NCPS for further studies.

3.4.4 Relaxivity properties of Pt-Fe NCPs: *in vitro* magnetic resonance imaging (MRI) studies

The presence of high-spin Fe(III) within the NCPs provided the possibility for this material to serve as a MRI contrast agent. MRI contrast agents are able to improve intrinsic contrast by modifying the relaxation times of water protons under a magnetic field in the tissues, thus enhancing the contrast to better visualize the interested anatomical region. Contrast agents can be classified into two categories: positive ones, which are usually based on paramagnetic metal ions, like Gd(III) and Mn(II), to shorten longitudinal relaxation time (T_1); and negative ones, which mainly involve superparamagnetic iron oxide compounds to shorten transversal relaxation time (T_2). To confirm the features of Pt-Fe NCPs, magnetic resonance relaxometry experiments were carried out at escalated concentrations under an external magnetic field in two phantom sequences.

Quantitative MRI phantoms were carried out which further substantiated the results from Mössbauer spectra. As shown in Figure 3.25, T_1-weighted (T_{1W}) and T_2-weighted (T_{2W}) imaging maps were obtained at a series of Fe concentrations of the NCPs dispersed in 1% agarose PBS measured by a Biospec MRI 7 T horizonal scanner. The longitudinal (r_1) and transversal (r_2) relaxivity parameters were determined by the obtained T_{1W} and T_{2W} map acquisitions, which indicates how the corresponding relaxation changes as a

function of the concentration. The agarose-based method has been widely used in reports to ensure the good dispersion of nanoparticles and to mimic the viscosity and consistency of biological tissues.[55]

Along with the increased Fe concentration, the intensity of T_{1w} image increased while the intensity of T_{2W} image decreased. According to the calculation of the slopes of the regression curves (Figure 3.25), the relaxivities r_1 and r_2 were 0.407 and 21.613 $mM^{-1}s^{-1}$ respectively. Interestingly, the NCPs exhibited a low r_1 compared to the commercial gadolinium contrast agents, for example Gd-DTPA with a r_1 of 3.3 $mM^{-1}s^{-1}$.[56] Similar low r_1 values were reported in Gd-based NCPs and attributed to a low water accessibility to the metal ions.[57] On the other hand, the Pt-Fe NCPs showed a high r_2 value, and the ratio of r_2/r_1 was as high as 53.15, which implies that Pt-Fe NCPs bear the potential to serve as a promising contrast agent for T_2 MRI.

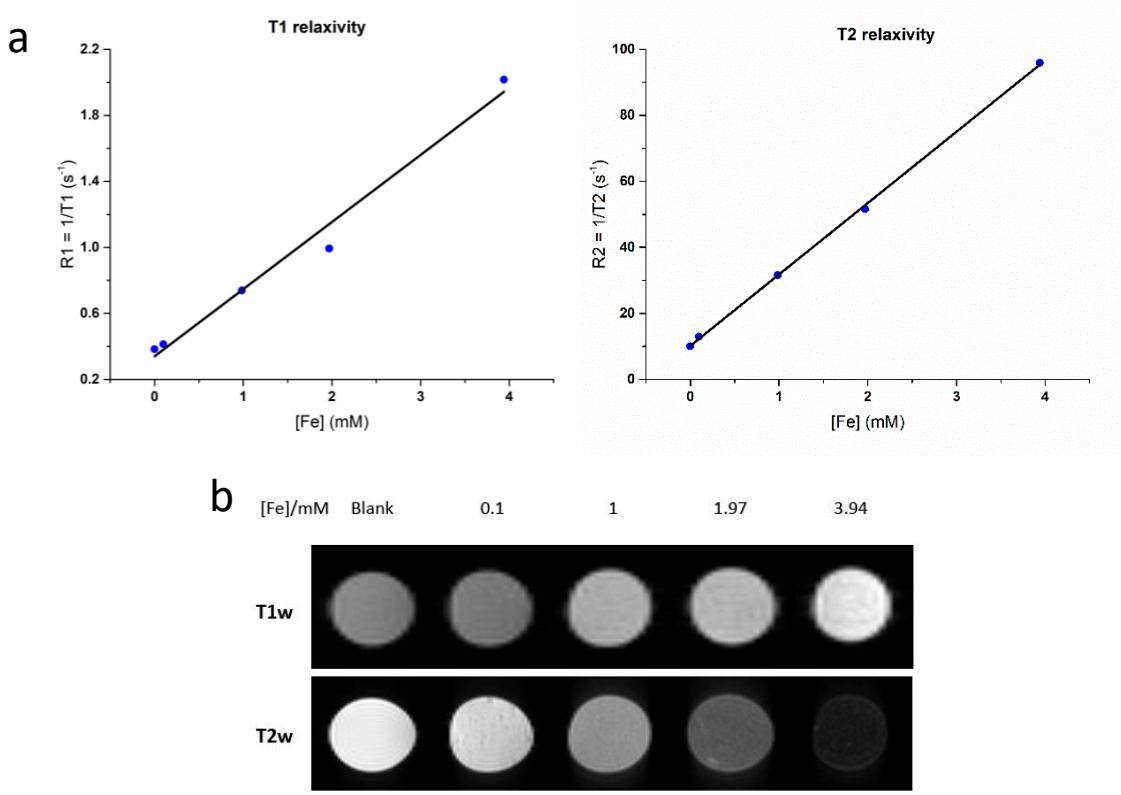

Figure 3.25 a) *In vitro* results obtained with relaxometry studies with Pt-Fe NCPs at different Fe concentrations. b) T_{1W} and T_{2W} MRI obtained with Pt-Fe NCPs which were suspended in PBS containing 1% agarose at pH 7.4 at different concentrations (0, 0.1, 1, 1.97 and 3.94 mM, referred to Fe concentration).

3.4.5 *In vitro* drug release of Pt-Fe NCPs

In our work, the Pt(IV) prodrug and resulting Pt-Fe NCPs were supposed to be pH-responsive due to the presence of ester bonds and amide bonds in the molecule which can remain stable in physiological conditions and be cleaved in the weekly acidic extracellular environment of tumors or in endo/lysosomal compartments.[24] Furthermore, the coordination bonds between catechol and iron are usually stable under slightly basic conditions but can cleave due to the demetallation process with decreased pH.[58-60]

Herein, the drug release from Pt-Fe NCPs was first studied in phosphate buffers at different pH using dialysis method. The release profiles were obtained at different pH (pH 7.4 and pH 5.5) to mimic the physiological and mildly acidic conditions for the drug release study *in vitro*. In a typical experiment, Pt-Fe NCPs were incubated in the dialysis bag at 37 ℃ over 48 h in presence of buffers and the released Pt outside the bag was determined by ICP-MS to obtain the release profiles in terms of concentration as a function of time. As observed in Figure 3.26, both release curves are typically bimodal, while Pt was released faster from the NCPs in the first 6-8 hours, a more sustained and slower release was observed after that time in both pH values. Pt was released faster at pH 5.5 than that at pH 7.4, indicating the nanoparticles' pH-responsive behavior. Specifically, 46.78 ± 0.33% of Pt was released at pH 7.4 in the first 4 h, and 67.92 ± 2.01% released after 48 h. At acidic pH, the release of Pt was slightly faster with around 60.45 ± 0.32% of Pt released after 4 h of incubation, and 72.43 ± 1.56% at 48 h. This corroborated the effect of pH on the release profile that was notable increased in acidic pH.

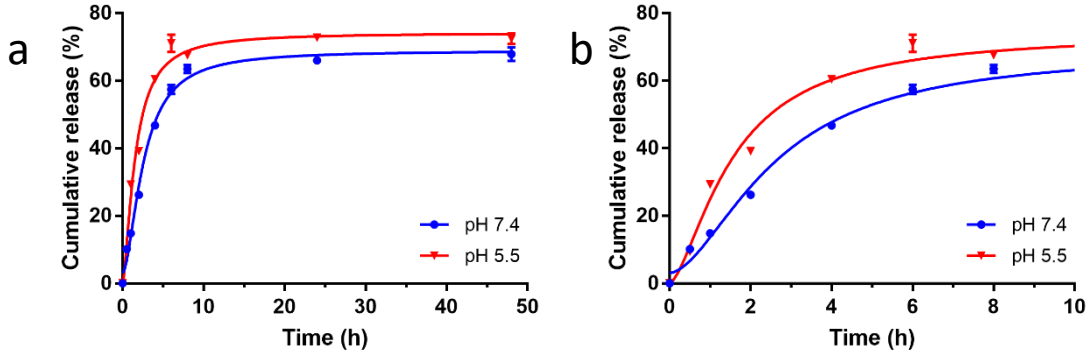

Figure 3.26 a) Release profiles of Pt from Pt-Fe NCPs at 37 ℃ at pH 7.4 and 5.5 in PBS using dialysis method; b) Inset of release in the first 8 h of the whole release profiles. Each value represents the mean ± SE of three independent experiments.

We also evaluated the effect of reducing agents on the release profile. The redox couple, glutathione (GSH) and glutathione disulfide (GSSG), plays a pivotal role in the anti-oxidative capacity of cells. The most important function of GSH is to serve as a reducing agent in intracellular ambient protecting cells from oxidative damage and the toxicity of xenobiotic electrophiles, and maintaining redox homeostasis.[61] Usually, the intracellular concentration of GSH is reported to be 1 - 10 mM in normal cells, while its concentration decreased to 2-3 orders of magnitude lower levels in extracellular fluids.[62] However, the intracellular level of GSH increases up to fourfold more in cancer cells than that in normal cells. The elevated levels of GSH protect tumor cells from the anticancer action of numerous therapeutics, including cisplatin, contributing to the multidrug resistance (MDR).[63] The different GSH levels in extra- and intra-cellular circumstances and in normal and tumor tissues have prompted the emergence of GSH-responsive nano-formulations to facilitate the preferential drug release in tumor tissues and cells.[64-66]

GSH has been reported to enable the reduction of Pt(IV) prodrugs into their active Pt(II) forms, which induced apoptosis of cancer cells by covalent binding to DNA.[67-69] Therefore, the release behavior of Pt-Fe NCPs was furthermore assayed in the presence of GSH at different pH values. The GSH levels in brain were reported to be around 1 - 2 mM in normal conditions.[70] Therefore, 2 mM and 10 mM were chosen as the concentrations of GSH to be tested at pH 7.4 and 5.5, using the same method described previously. As Figure 3.27 shown, indeed, the release of Pt was obviously promoted by GSH. Even at 2 mM, GSH accelerated the release of Pt dramatically; 62.89 ± 0.54% of Pt was released from the NCPs after 4 h of incubation at pH 7.4, which was close to the amount of released Pt after 48 h (67.92 ± 2.01%) in the absence of GSH. After 48 h, 83.54 ± 0.24% of Pt was released in total with 2 mM of GSH. Notably, the release was further sped up while the concentration of GSH increased to 10 mM; about 70.23 ± 0.28% of Pt was released from the NCPs after 4 h of incubation, and the release reached 93.49 ±

0.39% after 48 h. At pH 5.5, the release of Pt was accelerated in the same trend as at pH 7.4 in the presence of GSH.

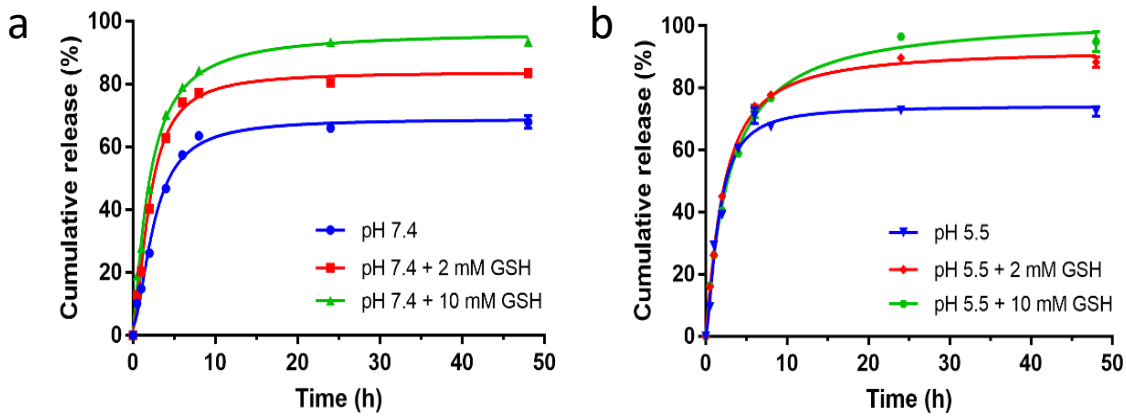

Figure 3.27 Cumulative release of Pt from Pt-Fe NCPs in the absence or in the presence of GSH at a) pH 7.4 and b) pH 5.5. Each value represents the mean ± SE of three independent experiments.

Therefore, the results demonstrated that Pt-Fe NCPs could be both pH- and GSH-responsive. These properties could provide a precise controlled release regulated by pH and the presence of a reducing ambient while keeping the nanoparticles stable in absence of these external stimuli. This behavior could increase the chemotherapy effectivity against cancer cells and avoiding side effects.

3.4.6 *In vitro* anticancer studies of Pt-Fe NCPs

3.4.6.1 Cytotoxicity assays

The cytotoxic effects of the prodrug PtBC and Pt-Fe NCPs were evaluated *in vitro* and compared to cisplatin (CDDP) using different cell lines, including Human cervical cancer cell HeLa, murine GB GL261 cells, ovarian cancer cells A2780 (including cisplatin resistant cell line A2780/cis) and non-malignant human fibroblast cell 1Br3G. We included a comparative study between non-resistant and resistant cancer cells because it has been reported that nanoformulations with proper modifications can bypass the efflux of resistant cells which the free drug is commonly subjected to, therefore modulating or overcoming the resistance of cancer cells.[71-72] The well-established PrestoBlue method was used to assess the cytotoxicity at 24 h and 72 h (Figure 3.28).

The half maximal inhibitory concentrations (IC_{50}s) referred to Pt concentration, calculated using Graphpad Prism 7, were summarized in Table 3.5 and 3.6. Interesting results were obtained for the three Pt-based species. As observed in Table 3.5, PtBC and Pt-Fe NCPs showed slightly lower cytotoxicity at 24 h for almost all cell lines in comparison with CDDP. Interestingly, both PtBC and Pt-Fe NCPs exerted higher cell killing capability than CDDP in 1Br3G cells, with IC_{50} of 27.78 ± 1.75 μM and 45.07 ± 4.60 μM respectively. Moreover, in the case of A2780 the Pt(IV) prodrug was highly effective against these cell lines, even more pronounced in the case of cisplatin-resistant A2780/cis cells. After 72 h (Table 3.6), the Pt(IV) prodrug and NCPs exhibited comparable or even slightly higher anticancer ability than CDDP. Whereas, in the case of A2780 and A2780/cis in which the prodrug and the nanoformulation exhibited less cytotoxic effectivity in comparison with cisplatin.

The difference between the results suggests different explanations. It could be attributed to the distinctive cellular internalization pathways of these three formulations. Due to their small size, CDDP and PtBC probably entered cells by passive diffusion common for small molecules, while the Pt-Fe NCPs internalized via endocytosis, which is typically slower than diffusion in a short term observed for other NCPs.[26] While at 24 h it is supposed that most of the NCPs entered the cells, the degradation of the nanoparticles and the subsequent reduction of Pt(IV) complexes to generate the active cisplatin retards the cytotoxic effect which is notably superior at 72 h reaching IC_{50} values comparable or even higher than cisplatin. Apart from the differences attributable to the delay concerning NCPs degradation and prodrug activation, different mechanisms of action should be taken into account as has been observed in previously published research in our group.[26] Concerning the molecular compounds (prodrug PtBC and cisplatin) that are supposed to internalize via passive diffusion, the observed effect depends notably of the studied cell line. In this case, different rates of cell internalization and/or mechanism of action could take part. We should have into account also that the uptake pathways and detoxification of NPs are greatly influenced by the cell type, as well as the intrinsic properties of NPs.[73] Moreover, recent reports pointed out that the presence of catechol moiety in structure contributed to the antibacterial or even anticancer potential in some compounds.[74-75] These

promising anticancer effects *in vitro* lay the foundation for the exploration of further biomedical evaluations.

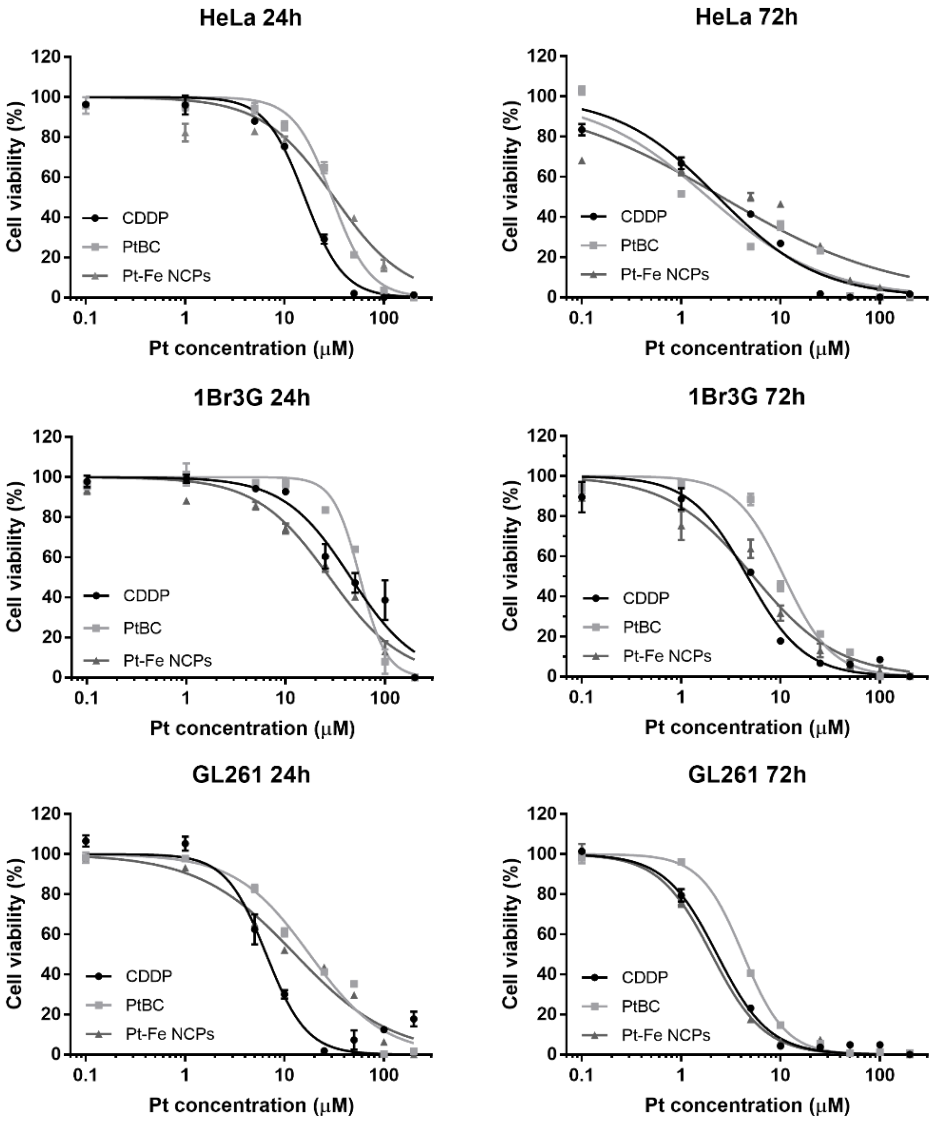

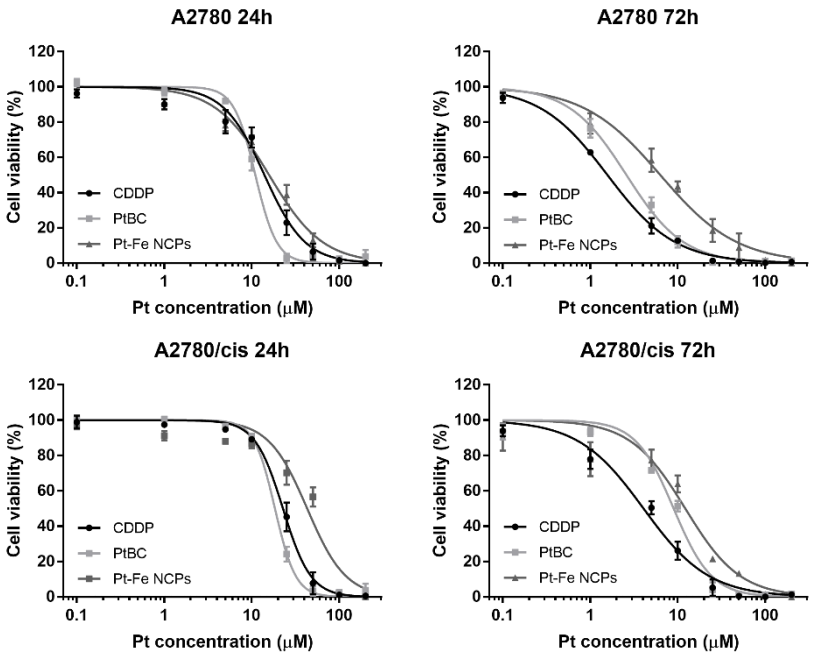

Figure 3.28 Cytotoxicity of CDDP, PtBC and Pt-Fe NCPs against a panel of cell lines for 24 h and 72 h. All data represented as mean ± SE of three independent experiments.

IC_{50} (μM)[a]					
	Cell line				
Compound	HeLa	1Br3G	GL261	A2780	A2780/cis
Pt-Fe NCPs	31.45 ± 1.10	27.78 ± 1.75	13.48 ± 0.90	15.76 ± 1.13	43.40 ± 3.75
PtBC	29.94 ± 1.04	56.09 ± 1.18	17.40 ± 1.08	10.98 ± 0.56	18.39 ± 1.85
CDDP	15.98 ± 1.04	45.07 ± 4.60	5.614 ± 0.28	13.95 ± 1.24	23.68 ± 1.74

[a] The IC_{50}s of the compounds against different cell lines were determined by PrestoBlue assay. Each value represented the mean ± SE of 3 independent experiments.

Table 3.5 Cytotoxicity after 24h.

IC_{50} (□M)[a]					
	Cell line				
Compound	HeLa	1Br3G	GL261	A2780	A2780/cis
Pt-Fe NCPs	2.56 ± 0.63	5.32 ± 1.10	2.00 ± 0.18	6.31 ± 1.56	11.04 ± 1.69
PtBC	1.85 ± 0.36	10.80 ± 0.60	4.17 ± 0.12	2.59 ± 0.33	9.12 ± 0.69
CDDP	2.34 ± 0.30	4.63 ± 0.42	2.16 ± 0.26	1.57 ± 0.08	5.22 ± 1.21

[a] The IC_{50}s of the compounds against different cell lines were determined by PrestoBlue assay. Each value represented the mean ± SE of three independent experiments.

Table 3.6 Cytotoxicity after 72h.

3.4.6.2 Generation of reactive oxygen species

The redox property of catechol moiety makes it an interesting functional group in biomedical field. On one hand, it can function as antioxidant with beneficial physiological effects. Many reports confirmed that compounds with catechol, generally polyphenols and flavonoids, exhibit hepatoprotective, anti-inflammatory, antioxidant, and even anticancer properties.[76] On the other hand, the high reactivity of catechol may trigger harmful effects including toxicity, damage, and inflammation in cells, which mainly arise from the excessive oxidative stress of reactive oxygen species (ROS) generated during the oxidation process of catechol.[77] Recently, researchers reported that singlet oxygen ($^1O_2$) was generated between catechol and transition metal ions.[78] Besides, ROS accumulation is considered a pivotal phenomenon related to apoptosis induced by DNA damage.[79]

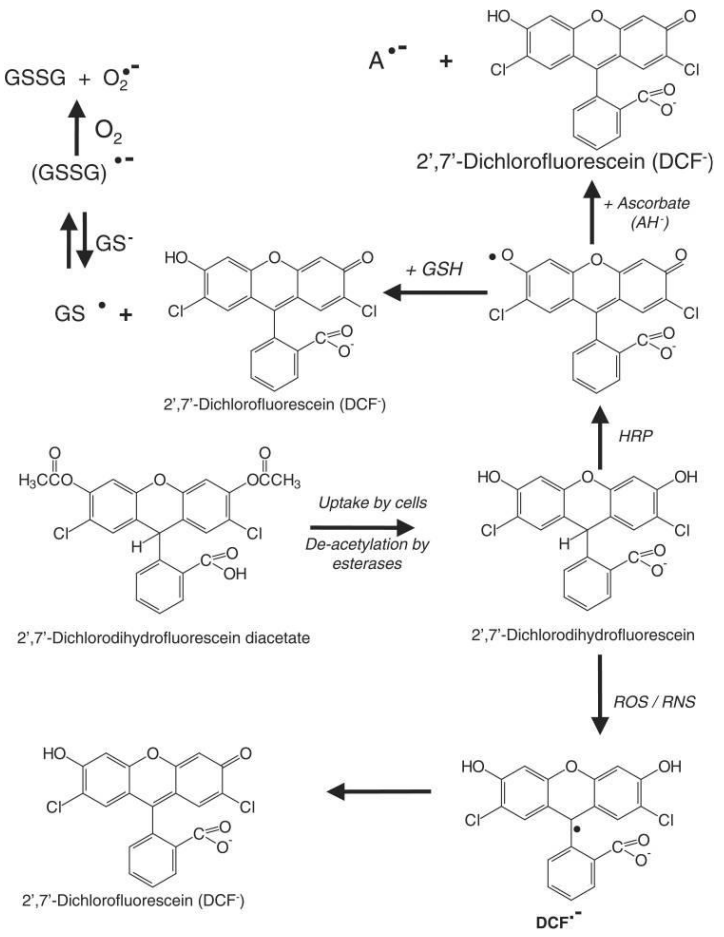

Figure 3.29 Conversion of DCFDA to a fluorescent product DCF.[80]

To assess if such oxidative stress also plays a role in the cytotoxicity of our prodrug and nanoparticles, the ROS generation was evaluated using a fluorescent probe 2',7'-

dichlorofluorescin diacetate (DCFCDA) in HeLa, 1Br3G and GL261 cells. DCFCDA is a non-fluorescent permeable compound which can be hydrolyzed by esterase and oxidized by intracellular ROS to generate fluorescent and non-permeable 2',7'-dichlorofluorescein (DCF) as detailed in Figure 3.29. DCF fluorescence intensity has been correlated well with the intracellular ROS levels.[80] The ROS production evaluation was carried out for cisplatin, Pt(IV) prodrug, Pt-Fe NCPs, H_2O_2 and $Fe(OAc)_2$. This latter specie was used to discard ROS production associated to the presence of Iron ions. As observed in Figure 3.30, after 24 h treatment, intensive DCF fluorescence was detected Pt-Fe NCPs in HeLa and 1Br3G cells, 4-fold and 2-fold respectively compared to the control group. Interestingly, no fluorescence was observed in GL261 cells for all agents. This implied that only Pt-Fe NCP triggered notable ROS formation in HeLa and 1Br3G cells, but not in the case of GL261 cells, indicating a cell-dependent effect. These results suggested that oxidative stress might contribute partially in the cytotoxic effect of Pt-Fe against HeLa and 1Br3G cells in addition to the chemotherapeutical effect of the generated cisplatin resulting from the reduction of Pt(IV) prodrug. However, it cannot rule out other possibilities since the sensitivity of cancer cells to oxidative stress is greatly dependent on the redox balance in the cells as well as on their antioxidative capacities.[81]

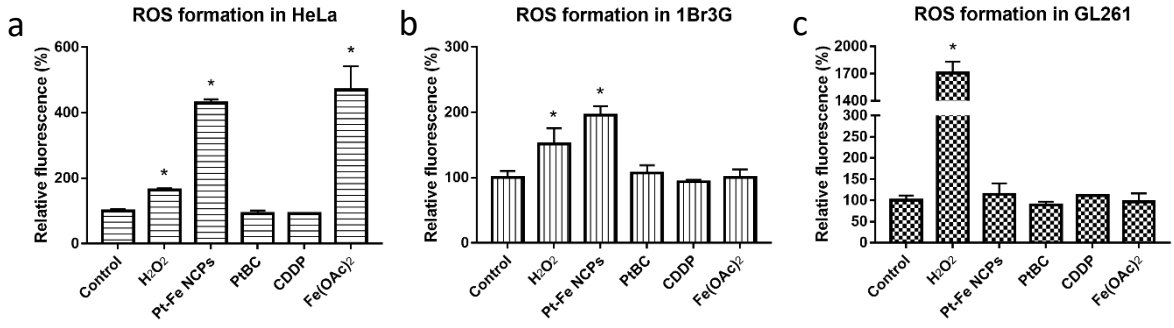

Figure 3.30 ROS generation triggered by different compounds and Pt-Fe NCPs in HeLa, 1Br3G and GL261 cells. The concentration of H_2O_2 and $Fe(OAc)_2$ were 0.1 mM, other agents at their corresponding IC_{50}. Data represented as Mean ± SE of three independent experiments. * stands for $p < 0.05$, ** for $p < 0.001$, *** for $p < 0.0001$.

It is well known that many transition metals may trigger the generation of ROS and cause cellular damage by interfering with cellular redox pathways via binding to biomolecules involved or affecting enzyme activities via lipid peroxidation.[82-83] Interestingly, $Fe(OAc)_2$ did trigger the formation of ROS in HeLa cells, but not in 1Br3G

or GL261 cells. These may be explained by the specific sensitivities to ROS and distinct antioxidative capabilities of these cell lines.

3.4.6.3 Cellular internalization and DNA-bound Pt

The cellular uptake of all formulations was quantitatively evaluated in HeLa, 1Br3G and GL261 cells at 6 h and 24 h using ICP-MS (Figure 3.31). Notably, at 6 h PtBC and Pt-Fe showed a significantly higher uptake than CDDP in all cell lines. In GL261, PtBC and Pt-Fe NCPs were internalized 4-fold and 11.6-fold of that from CDDP for 6 h. At 24 h, the enhancement trend remained in HeLa and 1Br3G cells. However, in GL261 cells, Pt-Fe NCPs accumulated significantly higher with a 4.1-fold increase compared to CDDP, while PtBC showed a less uptake than CDDP. Interestingly, the uptake of CDDP and PtBC did not increased significantly in a longer period while the uptake of Pt-Fe NCPs augmented dramatically at 24 h than 6 h. The cellular uptake of cisplatin and its analogues is commonly limited because of the tendency of thiol-containing biomolecules, like cytoplasmic GSH and metallothionein, to avidly bind with platinum therefore leading to the active efflux of platinum complexes from the cancer cells by corresponding export pumps.[84-86] Besides, the lipophilicity of the prodrug and nanocomposite increased compared to cisplatin which could endow the originally less lipid-soluble agents' ability to cross the cell membrane and thus enhance the cellular uptake.[87]

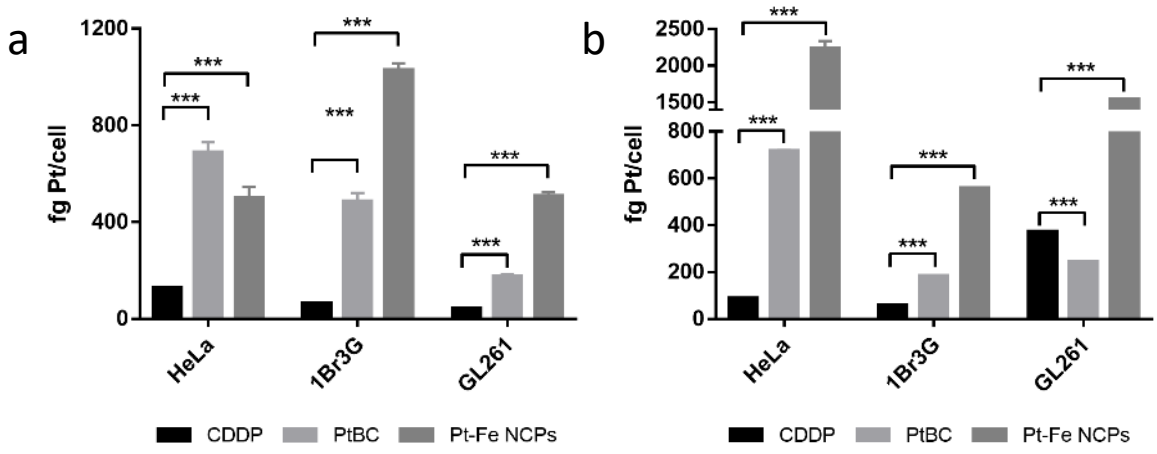

Figure 3.31 Cellular uptake of CDDP, PtBC and Pt-Fe NCPs in HeLa, 1Br3G and GL261 cells for 6 h (a) and 24 h (b). All agents were incubated at 0.1 mM Pt. Data represented as Mean ± SE of three independent experiments. * stands for $p < 0.05$, ** for $p < 0.001$, *** for $p < 0.0001$.

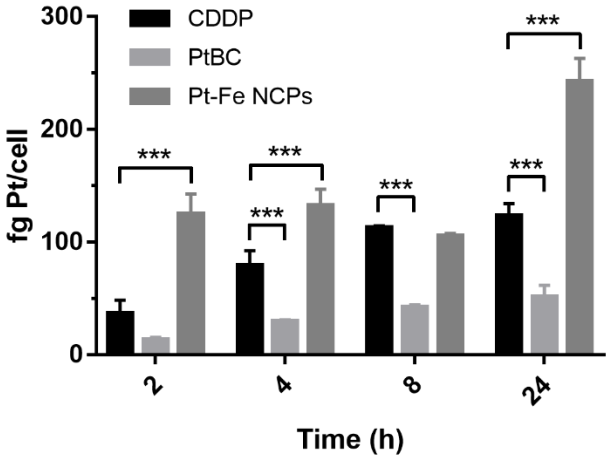

Figure 3.32 Cellular uptake of CDDP, PtBC and Pt-Fe NCPs at a concentration of 10 μM Pt along with time in GL261 cells. Data represented as Mean ± SE of three independent experiments. * stands for $p < 0.05$, ** for $p < 0.001$, *** for $p < 0.0001$.

Specifically, GL261 is the most intriguing cell line. To further investigate the internalization of these formulations, the concentration was decreased to 10 μM (referring to Pt concentration), in order to exclude the effect of saturated extracellular Pt agents on the cellular uptake. The results (Figure 3.33) showed that the cellular uptake of small molecules increased along with time, while the uptake of Pt-Fe NCPs kept at a high level and reached a maximum after 24 h. Except at 8 h, the uptake of NCPs was significantly higher than CDDP and PtBC at all time points. Compared to CDDP, the cellular uptake of PtBC was significantly lower. Apart from the different conformation of both species, the difference in cellular uptake could be explained in term of electrostatic interaction between the cellular membrane and charged molecules. CDDP is slightly positive in aqueous solution because of the hydrolysis which would justify the attraction by the negative cellular membrane, while the deprotonated PtBC is slightly negative which makes it more difficult to be internalized due to electrostatic repulsion. Additionally, it has been reported that the cancer cells generally have an increased demand for iron as an essential nutrient for various biochemical activities associated with cell growth and proliferation.[88] Some researchers have reported that pathobiological events, most notably mTORC1 hyperactivity, common to high-grade glioma can increase Fe(III) uptake into cancer cells by regulating the activity of the transferrin receptor (TfR) in preclinical models.[89] The presence of Fe(III) in the NCPs may

also contribute to the significantly higher cellular uptake of Pt-Fe NCPs compared to other agents.

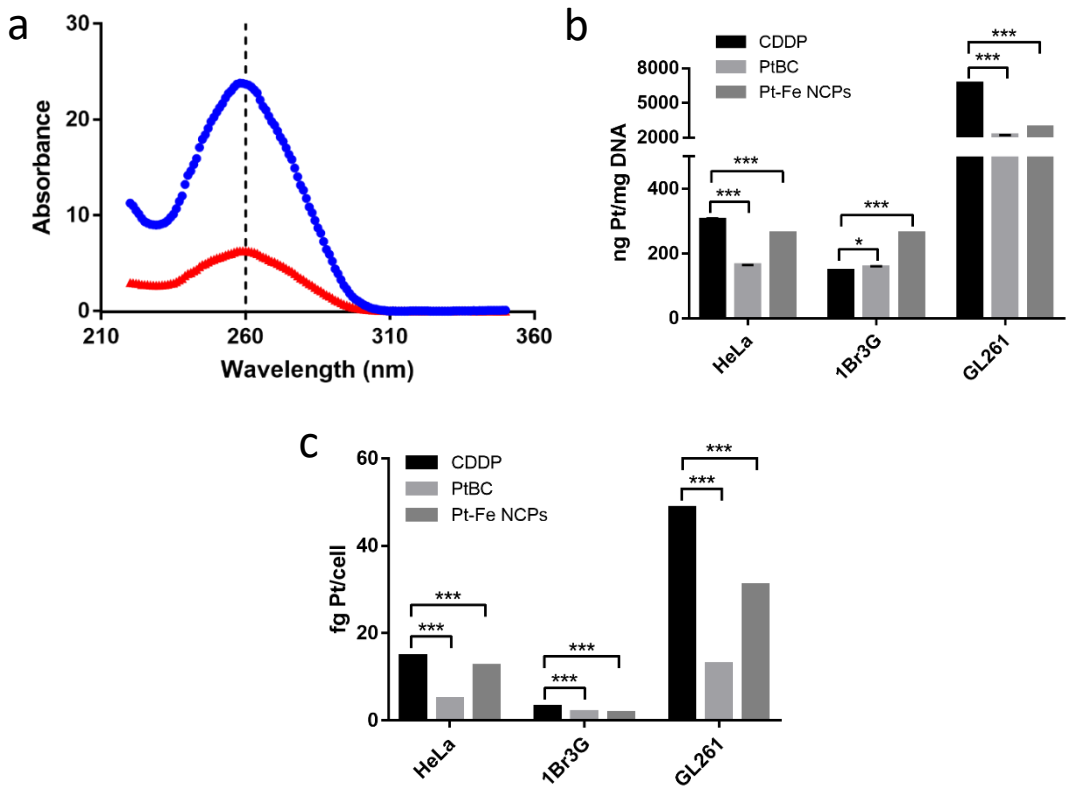

Figure 3.33 a) Representative UV absorbance curves for DNA concentration determined at 260 nm using NanoDrop™ spectrophotometer. b-c) DNA-bound Pt in HeLa, 1Br3G, and GL261 cells after exposure to CDDP, PtBC, and Pt-Fe NCPs for 24 h at a Pt concentration of 0.1 mM. Data represented as Mean ± SE of three independent experiments. * stands for $p < 0.05$, ** for $p < 0.001$, *** for $p < 0.0001$.

Notably, the cytotoxicity did not exhibit significant improvement, although the uptake increased significantly either the prodrug or the NCPs compared to CDDP. This imbalance urged us to figure out what fraction of the internalized agents can enter the nucleus and crosslink with the DNA to exert the cytotoxicity. DNA-bound Pt was quantified after internalization for 24 h for each formulation using ICP-MS (Figure 3.33). The normal fibroblast 1Br3G cells had least Pt bound to DNA in all cell lines. The nuclear pore complexes, the gatekeeper of nucleus, only allow the diffusion of ions and small metabolites, and molecules > 40 kDa cannot pass through except with active transport.[90] In another word, the permeability of nuclear pore complexes usually is limited to inert substances less than 10 nm.[91-93] Given that the disassociation of the NCPs may take time

to release the Pt(IV) prodrug and be reduced to Pt(II) active form to bind to DNA, it can partially explain that the increased cellular uptake of Pt-Fe NCPs did not result in augmented DNA-bound Pt or enhanced cytotoxicity in comparison to CDDP.

Combining the cellular uptake and DNA-bound Pt results, Pt-Fe NCPs were internalized by the cells quickly, but it might take a relatively long time for Pt-Fe NCPs to be reduced into the active form (cisplatin) and to bind to DNA to exhibit its anticancer activity. Thus, the intracellular release of active Pt was sustained from Pt-Fe NCPs which guarantee the effective concentration to exert anticancer efficacy. This was in good accordance with the higher cytotoxicity of 72 h than that of 24 h.

3.4.6.4 Cellular morphology alteration during cytotoxic studies

Cell morphology is a direct indicator of cytotoxicity of therapeutic agents. Therefore, the morphologies of GL261 cells incubated with CDDP, PtBC, and Pt-Fe NCPs were observed and recorded by optical microscopy.

As Figure 3.34 shown, the morphologies of GL261 cells changed a lot after incubation with those Pt agents for 24 h, which was more obvious with higher concentrations (Annex I). Specifically, exposure to PtBC at a concentration of 1 μM for 24 h, obvious decreased cell density, rounding-up, pseudopodes retraction, plasma membrane budding, and cell volume reduction were observed, but still the number of cells with normal morphology accounted for the majority. When the concentration increased to 10 μM, the proportion of tumoral cells with normal morphology decreased dramatically, and most of the cells got rounded and shrunken, with cellular debris observed. At the concentration of 25 μM, the shrunken cells disappeared, the cell fragments occupied the field, and little living cells could be found. The apoptotic morphologies were also observed in other two Pt agents to a more severe degree, which was in good accordance of cytotoxic effects of these agents indicated by their IC_{50}s.

After 72 h of exposure (Annex I) to these agents, morphology changes showed a similar trend to the high concentrations at 24 h, and the number of non-affected cells decreased drastically even at the lowest concentration of 1 μM. The intracellular vesicle swelling became extremely obvious in cells treated with 1 μM of Pt agents, which implied that probably the cells underwent necrosis as well as apoptosis.[94] When the

concentration went to 10 μM, almost only cell fragments were observed in the field, accompanied by a few rounding-up cells for all agents. With agents at 25 μM for 24 h, little living cells were observed but only floating dead cells or cell fragments.

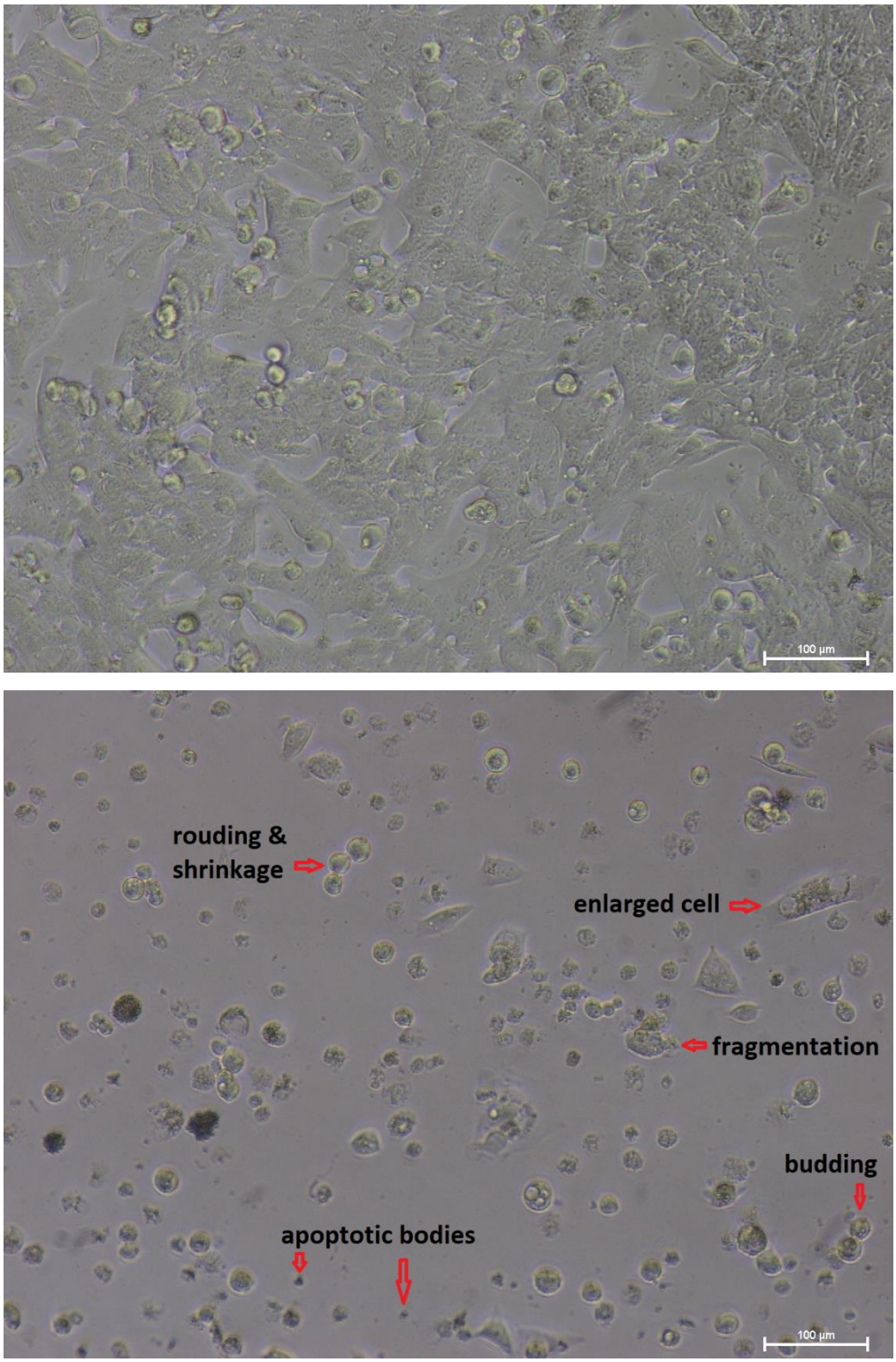

Figure 3.34 Representative morphologies of GL261 cells without/with exposure to Pt-Fe NCPs for 24 h.

3.4.7 *In vivo* anticancer studies of Pt-Fe NCPs

The *in vivo* studies of Pt-Fe NCPs were performed in collaboration with the *Biomedical Applications of Nuclear Magnetic Resonance* research group (GABRMN) led by Dr. Carles Arús at *Universitat Autònoma de Barcelona* (UAB, Cerdanyola del Vallès, Spain) under the supervision of Dr. Ana Paula Candiota with the contribution of Dr. Shuang Wu and Ms. Pilar Calero.

3.4.7.1 Preclinical models of GB

Repeated collection of brain tumor tissue from human subjects along treatment is not practical or advisable for obvious ethical reasons, whereas *in vitro* models generally lack TME, physiological reactions, and overall heterogeneity and are far too simplistic to predict organismal response to pharmaceuticals.[95] Therefore, preclinical models are essential surrogates to analyze the biology of GB, identify therapeutic targets, and evaluate the potential of novel therapeutic strategies.

Ideally, GB preclinical models should be reproducible and stable over time, reiterate key features of histopathology and evolution of human GB *in vivo*, be able to grow in immunocompetent way preferably in the same site of origin, be non-immunogenic, and allow accurate prediction of novel therapeutic strategies. However, the perfect preclinical model meeting all the conditions does not exist. Thus, it is very important to consider the relevancy, advantage, and disadvantage of different preclinical models to select the most suitable GB model based on the nature and purpose of the experiment.

The available GB models can be established on rodents or dogs. Spontaneous models in dogs are usually not chosen given their larger brains than rodents, since rodents are more feasible and easier to manipulate and to obtain homogeneous cohorts.[96] Among rodents, mice are commonly used to generate the preclinical models of GB. With mice, the preclinical models can be divided into three categories: (1) chemically induced models, (2) transplantation models, and (3) genetically engineered models.[95,97]

In chemically induced models, GB tumors were commonly induced in pregnant or adult rat by intravenous, local, oral or transplacental exposure to DNA alkylation agents like N-nitroso compounds. However, this approach is controversial, since resulting

tumors appear different from human GB and are questionable how valid they can reflect human GB.[95,98] Besides, other chemicals could be used to develop tumors in rats, however, no single chemical has been associated with causing GB in human brain. Therefore, use of these models should take careful consideration of histopathological features to avoid overestimation of therapeutic efficacy.

By transplanting GB cells in subjects, preclinical models can be generated, which are considered to be genetically closer to human GB than chemically induced models.[95] Depending on the source of the cells, these models can be divided into: (a) syngeneic and (b) xenograft models. Syngeneic models are transplantation models obtained by injecting a recipient with cell lines previously established through isolation of tumor cells from the subject of the same genetic background. Whereas, xenograft models are generated by transplanting human GB cells or graft materials into immunodeficient mice that do not reject human cells. Depending on the sites for implantation, the preclinical models can be classified into two categories: (a) ectopic/heterotopic and (b) orthotopic models. In ectopic preclinical models, the GB cells are transplanted in sites different from the sites of the original tumor. In contrast, in orthotopic models, tumor cells are implanted intracranially into immunocompetent subjects to match the original tumor histotype which can recapitulate host immunity and resemble human GB better.

In addition, genetically engineered mouse models are results from GB genesis via driver mutations. They make it possible to pinpoint genetic alterations involved in tumorigenesis and progression. They are particularly helpful for understanding the GB biology in genetic and molecular levels by identifying molecular events responsible for tumor initiation and progression, and mechanisms underlying the genetic alterations.[99] However, the tumor initiation time is uncontrollable which influences the reproducibility of this type of models. Besides, GEM tumors cannot completely reflect the intratumorally genomic and phenotypic heterogeneity of GB, as they are usually composed of cells with specific and homogeneous genetic changes.[99] Furthermore, generating GEM models usually are of high cost.

Both chemically induced models and genetically engineered mouse models are spontaneous, which make them more difficult to obtain homogeneous cohorts with consistent GB growth. Therefore, we have selected an immunocompetent syngeneic

murine model belonging to implanted orthotopic models by stereotactically injecting GB murine cell line GL261 in C57BL/6J mice, which has been widely used in GB research and represents the key features (e.g., invasiveness, angiogenesis) of human GB well.[96-97]

3.4.7.2 Safety and tolerability evaluation

Tolerability assay is a basic assessment for the safety of new formulations. Herein, intranasal (IN) administration was adopted in our animal studies. However, there are few papers reporting preclinical studies of Pt drugs by nose-to-brain delivery for GB treatment. Therefore, the safety or tolerability assay is necessary prior to proceed with *in vivo* studies. According to US FDA, in a phase I study, clinical therapeutics are often tested in either single-dose or limited-dose escalation pharmacokinetic studies, or in studies where the exposure is limited to a small number of doses or days, without regard to expected half-life of the drug.[100] In our case, the safety and tolerability of PtBC and Pt-Fe NCPs were assessed in a limited-dose escalation way, given that the volume of drug applied is usually confined via IN route to mouse.[101]

Herein, wt C57BL/6J mice were used for the short-term safety and tolerability assay. Three single escalated doses were administered consecutively in 2 weeks, from 0.9, 1.2 to 1.5 mg Pt/kg body weight. The body weights of mice were tracked three times every week to monitor any weight changes that could indicate toxicity. Besides, food consumption, and any adverse physical or behavioral effects concerning healthy conditions were closely observed by professional personnel in the animal facility daily. The whole study lasted for 4 weeks.

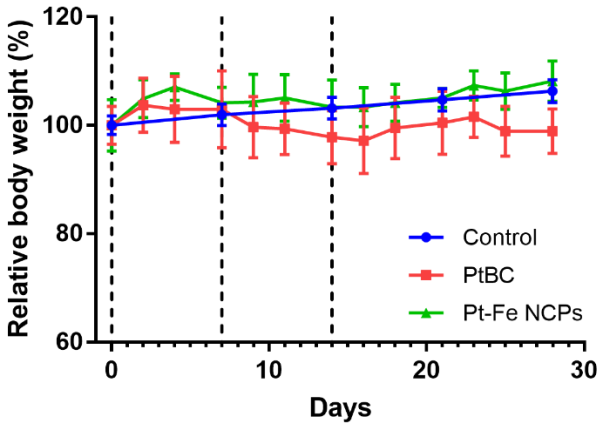

Figure 3.35 Tolerability assessment of mice for PtBC and Pt-Fe NCPs over 4 weeks. Both drugs were given in slightly increasing doses from 0.9, 1.2 to 1.5 mg Pt/kg body weight via I.N. once a week, n = 3. For control group, n = 360, data adapted from Jackson Laboratory (https://www.jax.org/jax-mice-and-services/strain-data-sheet-pages/body-weight-chart-000664). Data represented as mean ± SE. Vertical dash lines indicated days for administration.

As Figure 3.35 shown, the body weights of all treatment groups remained stable or slightly increasing in the same way as the control group till the end of the study, indicating no obvious systemic toxicity caused by PtBC or Pt-Fe NCPs, although the curve of PtBC seemed to be slightly worse than Pt-Fe NCPs, which was essentially similar to the control. The increasing trend with age were seen in both control and Pt-Fe NCPs groups, whereas, PtBC seemed to go worse, especially after the second dose. There were several points where the difference of PtBC was statistically significant from Pt-Fe NCPs (e.g., days 11, 14, 25 and 28). In this sense, it suggested that the nanostructured NCPs caused less systemic toxicity than the free prodrug, at least in wt mice. On the other hand, no treatment-related adverse effects on mortality, food consumption, or other clinical signs were observed for all mice during the study relative to control animals. Even with the highest dosage of 1.5 mg Pt/kg, all mice were still in good health status during the study. Since the side effects caused by cisplatin typically are acute nephrotoxicity and hepatotoxicity, the histopathological analyses (Annex II) were performed in 2 animals treated with PtBC and 2 mice treated with Pt-Fe NCPs from tolerability study. In all organs (heart, lungs, liver, spleen, and kidneys) under examination, the main findings were related to a black material in macrophages of lungs. The amount of the black material was not enough to produce animal death, but gave us hints that the therapeutic agents were captured by macrophages, and this might impair the overall outcome of therapy response (see more details in Annex II).

These results proved that Pt-Fe NCPs were well-tolerated by wt mice in given conditions, which guaranteed the safety of this nanocomposite and paved the way to further *in vivo* studies.

3.4.7.3 Biodistribution study via intranasal administration

Once the safety of the nanoparticles was validated, the fate of nanoparticles after their administration became the new focus of our study which plays an important role in the toxicity, biocompatibility, and therapeutic efficacy *in vivo*. Therefore, the

distribution of Pt-Fe NCPs in tumor and main organs was performed in GL261 GB-bearing mice.

The reticuloendothelial system (RES) or mononuclear phagocyte system (MPS) is responsible for the removal of colloidal stains in the blood circulation.[102] Generally, liver and spleen are the dominant organs to eliminate the NPs in bloodstream. However, they may clear a large fraction of NPs from the blood circulation, and the excessive NPs could accumulate in other macrophage-rich tissues such as lungs and adipose tissues.[103] The properties of the NPs affect considerably the biodistribution, while the size of NPs was considered as one of the most important factors that determine the biodistribution kinetics. [104] Figure 3.36 illustrated the size-dependent physiological barriers against NPs blood circulation.

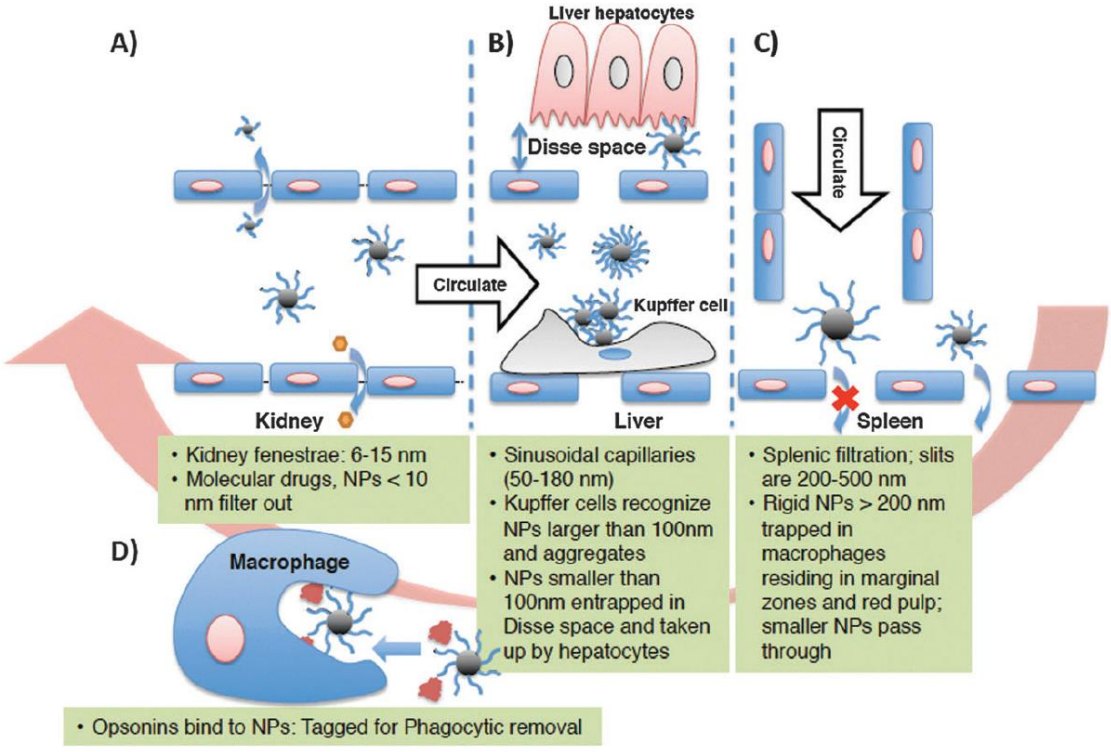

Figure 3.36 Scheme illustrating the size-dependent physiological barriers against NPs blood circulation.[104]

Unlike other administration routes, there are few reports about the biodistribution of Pt agents delivered by intranasal administration. It is intriguing and valuable to evaluate if Pt-Fe NCPs can gain access to the brain and GB tumor, the target sites, via intranasal

route. To reveal the distribution and the persistence of the Pt-Fe NCPs towards target and non-target tissues, the biodistribution study was performed after Pt-Fe NCPs were administered intranasally into mice bearing orthotopic GL261 GB. The murine GL261 GB model has been proved to be a valuable preclinical model closely mimicking human GB in significant ways, especially in its invasive and angiogenic properties.[105] Based on the tolerability assay, the highest but still safe dosage (1.5 mg Pt/kg body weight) was chosen to perform biodistribution. The major organs and tumors were excised 1 h after intranasal administration, and Pt retention in the tissues was determined using ICP-MS for comparison. As Figure 3.37 shows, in mice with small tumors (23.15 ± 2.68 mm^3), the majority of Pt accumulated in tumor and brain, following in the RES system, especially in kidney, lung, and spleen. However, in mice with bigger tumors (58.05 ± 3.35 mm^3), Pt tended to accumulate more in kidneys and lungs instead of in tumor or brain. Notably, the results (Table 3.7) showed that Pt content in small tumors was 10.34% initial dose (ID) per gram tissue, which was significantly higher than 2.44% ID/g in big tumors. Interestingly, no significant difference existed in the distribution of Pt in other organs. And in mice bearing small tumors, the retention of Pt in GB tumor was significantly higher than that in other organs; While in big tumor-bearing mice, no significance was found between the retention in tumor and other organs.

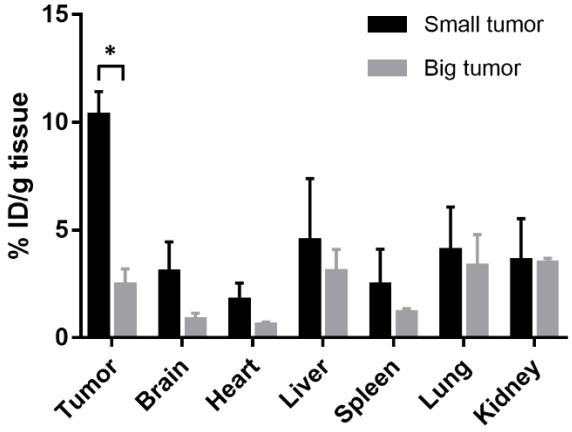

Figure 3.37 Biodistribution of Pt-Fe NCPs in mice 1 h after administration. Pt-Fe NCPs were given at a dosage of 1.5 mg/kg, n = 3 for both groups. Data represented as mean ± SE of three independent experiments. * stands for $p < 0.05$.

	Pt retention in mice with small tumors (% dose/g of tissue)	**Pt retention in mice with big tumors (% dose/g of tissue)**	**Significance**	**Average (% dose/g of tissue)**
Tumor	10.34 ± 1.09	2.44 ± 0.76	Yes	6.39 ± 0.95
Brain	3.06 ± 1.40	0.85 ± 0.30	No	1.95 ± 1.10
Heart	1.75 ± 0.78	0.60 ± 0.13	No	1.18 ± 0.58
Liver	4.50 ± 2.89	3.09 ± 1.02	No	3.80 ± 0.71
Spleen	2.44 ± 1.68	1.19 ± 0.17	No	1.82 ± 0.63
Lung	4.06 ± 2.0	3.35 ± 1.45	No	3.70 ± 0.36
Kidney	3.58 ± 2.0	3.48 ± 0.21	No	3.53 ± 0.05

Table 3.7 Biodistribution study of Pt-Fe NCPs in mice. Dose = 1.5 mg Pt/kg, biodistribution time = 1 h, n = 3. The statistical difference was examined between mice group with small tumors and that with big tumors.

The BBB was reported to be disrupted at early stages after implantation of GL261 cells, within 2 weeks post implantation.[105] The integrity of the BBB should be compromised in both cases with tumors 2-3 weeks post implantation, and the permeability of BBB/BBTB was supposed to be increased in mice with bigger tumors than that with smaller tumors. However, the distribution results demonstrated that the drug retention did not show positive correlation with tumor volume, which suggests the permeability of the BBB is not the determinant contributor to the drug retention in CNS herein. This might be explained partially by the angiogenic characteristics of GB, in which heterogeneous vasculature features substantially, resulting in hypoxia and high interstitial fluid pressure in the tumor core. These phenomena deteriorate considerably along with the growth of tumors, making the drug delivery into bigger tumors even more difficult.[106]

A recent paper reported blood-triggered Pt NPs with an average size of 86 nm and a surface charge of -9 mV, which were similar to our Pt-Fe NCPs. The biodistribution of this novel Pt NPs was also studied in C57BL/6 mice via IV injection which has been one of the main administration routes for *in vivo* studies. However, the Pt retention in brain was neglectable at both 4 h and 24 h post IV injection.[107] Another report showed that IN delivery resulted in significantly higher accumulation of Au NPs in cerebral cortex and cerebellum, as well as in olfactory lobe, compared to the retention of 10-fold higher

initial dose via intraperitoneal route 4 h post administration in C57BL/6 mice.[108] These results corroborated that intranasal administration could be an alternative route to bypass the BBB and to effectively deliver drugs to the CNS directly.

3.4.7.4 *In vivo* anticancer efficacy for GB treatment

The *in vivo* efficacy of Pt-Fe NCPs was evaluated in orthotopic GL261 GB-bearing C57BL/6J mice. GB is usually considered as an immunologically "cold" tumor, with limited clinical response to the therapy.[109] However, previous studies proved that it can be converted to immunologically "hot" tumor when immunogenic cell death was induced by TMZ treatment in "immune-enhancing metronomic schedule (IMS)".[110] This study, conducted by GABRMN researchers, found that therapeutic administration schedules respectful with the length described for mice immune cycle (6 days) produced improved results in comparison with previously described schedules.[111] The proposed hypothesis for the events triggered in IMS-TMZ administration is schematically shown in Figure 3.38.[41,112] Therefore, therapeutic approaches triggering immunogenic cell death/damage, when used in 6-day interval can trigger host immune response and be associated with long-term, tumor-specific antitumor immune memory to greatly increase the chemotherapy efficacy.[113] Given that Pt agents were reported to be able to trigger immunogenic effects,[114-115] the first round therapy of Pt-Fe NCPs was given in such IMS schedule starting on day 10 post implantation (p.i.) with a 6-day interval, and the tumor evolution was monitored by high-resolution T_{2w} MRI acquisition, as the treatment schedule shown in Figure 3.39.

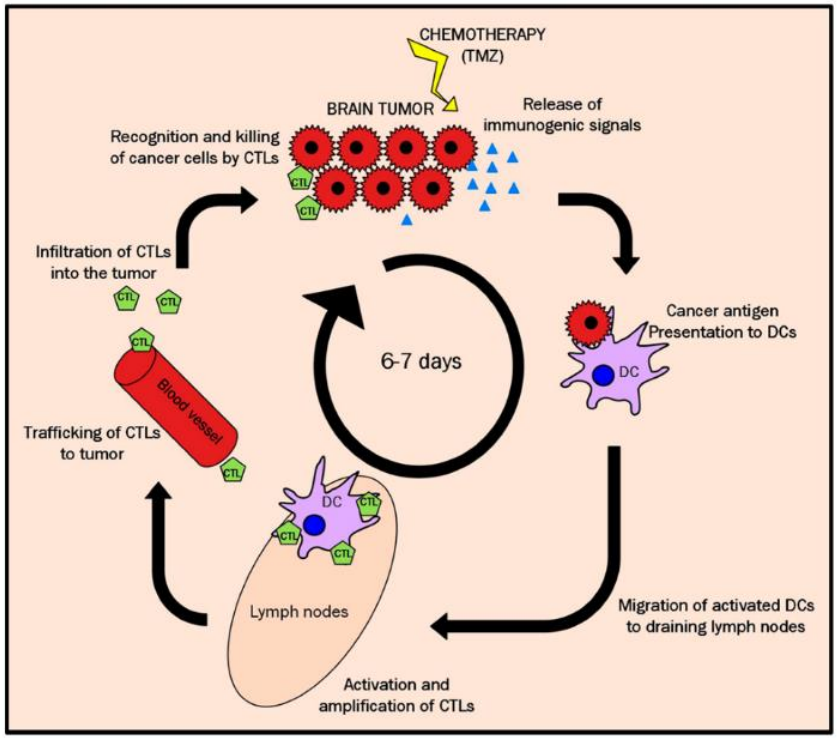

Figure 3.38 Hypothetic scheme of the cycle for immune response against a preclinical GL261 GB under IMS treatment.[112] The whole cycle in mouse brain is assumed to take 6-7 days. DCs - dendric cells, CTLs – cytotoxic T lymphocyte cells.

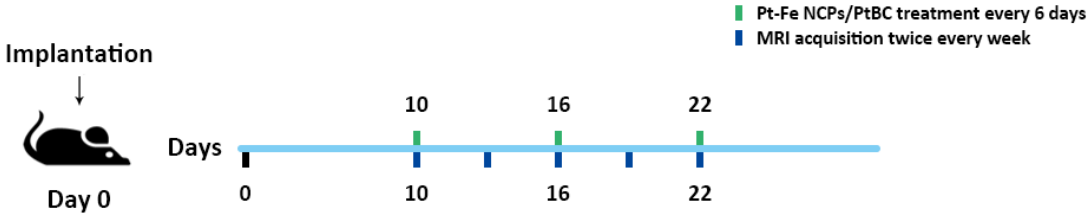

Figure 3.39 Immune-enhancing metronomic schedule (IMS) used for GL261 GB therapy in mice. PtBC or Pt-Fe NCPs was administered every 6 days, tumor volumes acquired by high-resolution MRI T_{2W} scanning twice per week.

In this *in vivo* study, in total 9 mice were randomly divided into three groups: control, PtBC, and Pt-Fe NCPs. The mice from control group were untreated, and the mice from Pt groups were administered intranasally at a dose of 1.5 mg Pt/kg body weight, which was the highest dose in the tolerability assessment and proved to be well-tolerated and safe for wt mice. The treatment initiated on day 10 p.i. when the GB volume was 6.07 ± 0.81 mm^3, and there were no significant differences in tumor volumes between three groups. As Figure 3.40 shown, both therapeutic drugs seemed to slightly slower down

the tumor growth in comparison with the control group. The average curve may be tricky to show a tumor growth arrest at day 21 p.i. but there was one case in both PtBC and Pt-Fe NCPs groups (as the arrows indicated in Figure 3.40) responded to the therapy and they showed transient growth shrinkage on day 23 p.i. but soon relapsed when scanned on day 26 p.i. (no deviation bars on day 23 and 26 p.i., n=1). The separated curves showed clearly that there was one case presenting more favorable evolution in both groups treated with PtBC and Pt-Fe NCPs.

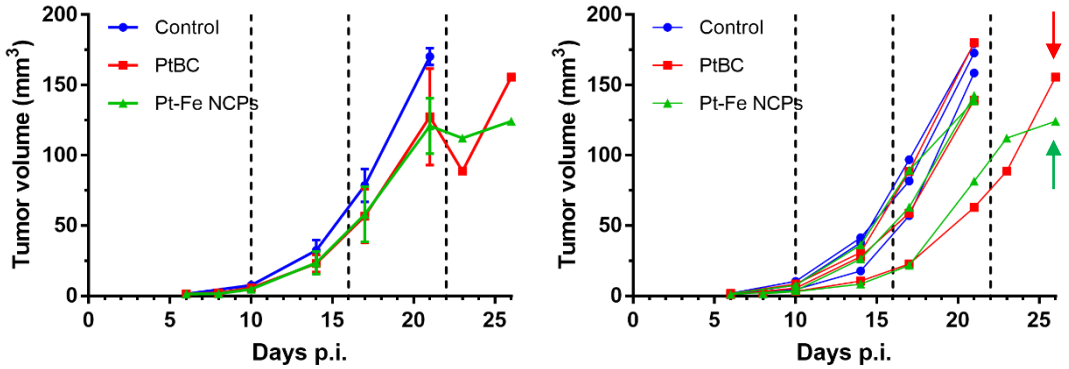

Figure 3.40 Tumor volume evolution of mice from control (untreated), treated with PtBC (1.5 mg Pt/kg), and Pt-Fe NCPs (1.5 mg Pt/kg), n = 3 for each group. Data represented as average ± SE. * stands for $p < 0.05$, all compared with control group. Vertical dash lines indicated the days for therapy administration.

Overall, the results suggested that both the prodrug and the NCPs can inhibit tumor growth provided the tumor volume was small enough, though no differences between themselves. This was confirmed by the increase rate in the tumor volume doubling time, which is defined as time needed for a given tumor to duplicate its volume. Doubling times were 2.1 ± 0.4 days, 2.5 ± 0.1 and 2.4 ± 0.3 days for control, PtBC and Pt-Fe NCPs, respectively, although no significant difference was found.

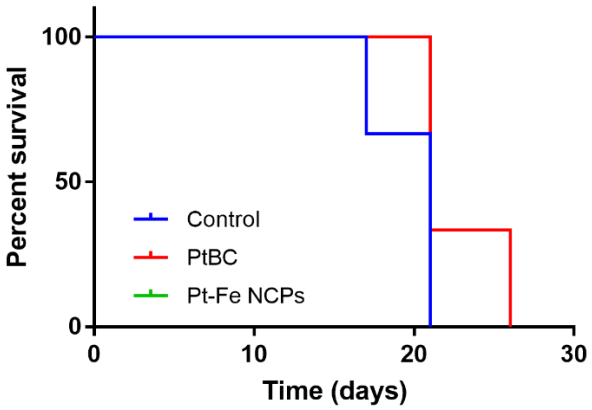

Figure 3.41 Kaplan-Meier survival curves of three groups (where the green curve from Pt-Fe NCPs was superimposed with the red line from PtBC due to the same survival time).

As Figure 3.41 shown, both Pt agents displayed same survival time whose survival curves were superimposed. The Log-rank test (typical for this type of data) did not show statistically significant differences between groups, although the average of the treated animals was slightly higher, driven by the single case surviving 26 days. The survival averages of control and Pt agents-treated groups were 19.7 ± 2.1 days and 22.7 ± 2.9 days, respectively.

The body weights of the mice during therapy were recorded twice a week (Figure 3.42). The body weights of control group dropped very fast under 80% of the initial weights on day 21 p.i., followed by other two groups. All animals had to be euthanized after their body weights reduction was more than 20% due to the welfare consideration.

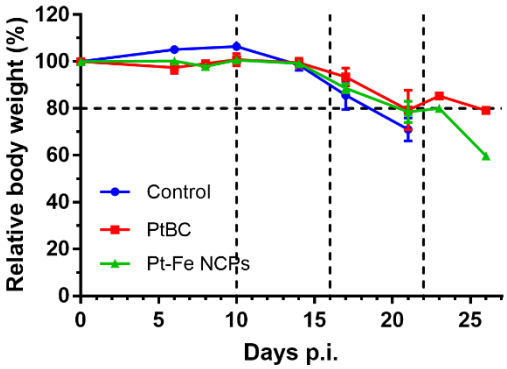

Figure 3.42 Evolution of body weights of mice in IMS schedule from control, PtBC (1.5 mg Pt/kg), and Pt-Fe NCPs (1.5 mg Pt/kg), n = 3 for each group. Data represented as average ± SE. Vertical dash lines indicated the days for administration. Horizontal dash line indicated the 20% weight reduction point, below which the mice had to be euthanized due to welfare consideration.

Since results with IMS schedule were not as impressive as it was expected, a more frequent schedule was attempted as described in other papers,[116-118] shortening the treatment interval from 6 days to 3 days while starting the treatment on the same day and keeping the same dose, as Figure 3.43 shown. In total 18 mice were used for the treatment, which were randomly divided into three groups. Treatment started on the same day (day 10 p.i.) like the previous round with an initial tumor size of 5.41 ± 0.67 mm^3 without statistically differences, and there were no differences in body weights of all groups at the beginning. In this case, any differences would be strictly attributed to the therapeutic agents. Tumor volume and body weight were still measured twice every week.

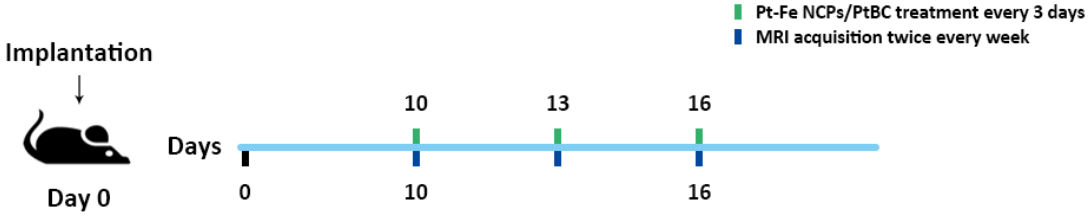

Figure 3.43 Adjusted intensive treatment schedule for GL261 GB therapy in mice. PtBC or Pt-Fe NCPs was administered intranasally every 3 days, tumor volumes acquired by high-resolution MRI T_{2W} scanning twice per week.

In this round, both PtBC and Pt-Fe NCPs significantly inhibited the tumor growth (Figure 3.44) on day 21 p.i. compared with the control group, although there was no significant difference between these two treated groups. This was reinforced when performing punctual Student's t-tests for the coincident time point as 16-17 days, showing no difference between Pt-treated groups, but significant differences ($p < 0.05$) between these groups and control group. This result suggested that PtBC and Pt-Fe NCPs slowed tumor growth rate, which was confirmed by an increase in the tumor volume doubling time, although it was non-significant. Doubling time was 2.1 ± 0.4 days for control tumors, while 2.3 ± 0.2 and 2.4 ± 0.3 for PtBC and Pt-Fe NCPs, respectively.

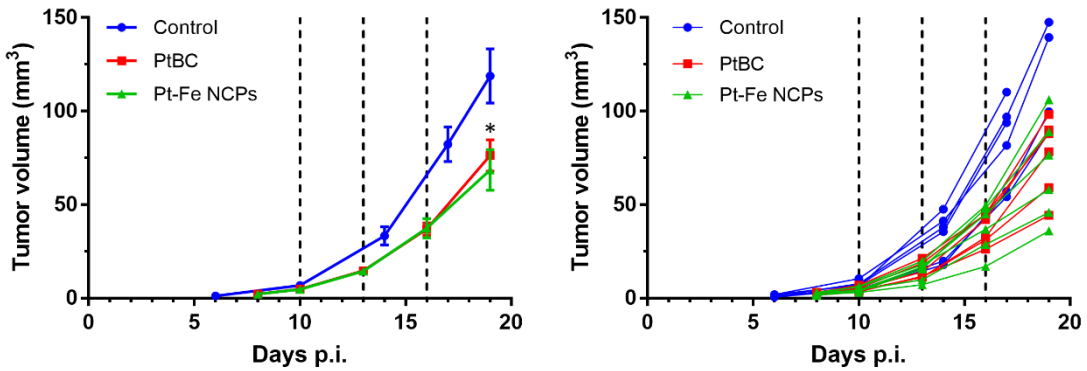

Figure 3.44 Tumor volume evolution of mice from control (untreated), PtBC (1.5 mg Pt/kg), and Pt-Fe NCPs (1.5 mg Pt/kg), n = 6 for each group. Data represented as average ± SE. * stands for $p < 0.05$, all compared with control group. Vertical dash lines indicated the days for administration.

However, the survival time (Figure 3.45) seemed not beneficial from this intensive schedule. The control cases had a survival of 19.7 ± 2.1 days, compared to 19 days' survivals for both groups treated with Pt agents (all of them presented equal or less than 20% body weight decrease as Figure 3.46 indicated, signal of animal suffering and euthanasia recommended). So, in this sense we can affirm that the tumor volumes were smaller and far from the sizes that can kill animals (that may reach 150 - 200 mm^3 easily at final stages as the control), but animals showed signals of suffering. Therefore, the intensive dosing significantly slowed down the growth rate of GB tumors, but failed to prolong survival time.

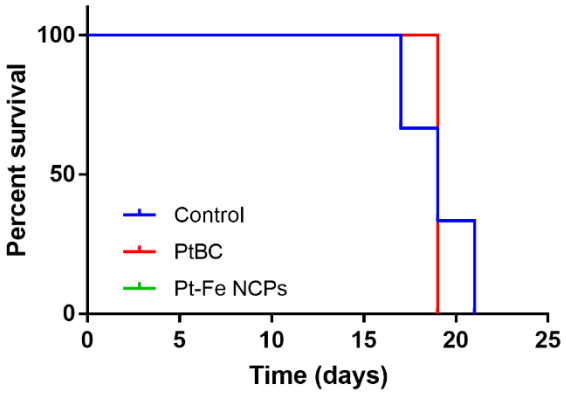

Figure 3.45 Kaplan-Meier survival curves of three groups (where the green curve from Pt-Fe NCPs was superimposed with the red line from PtBC due to the same survival time).

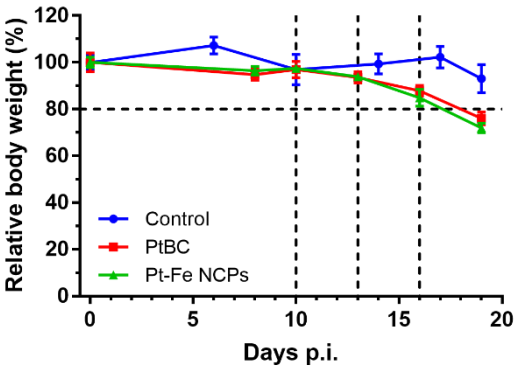

Figure 3.46 Body weight evolution of mice treated with vehicle, PtBC and Pt-Fe NCPs, n = 6 for each group. Data represented as average ± SE. Vertical dash lines indicated the days for administration. Horizontal dash line indicated the 20% weight reduction point, below which the mice had to be euthanized due to welfare consideration.

The survival results obtained with the dose-intense treatment schedule were not encouraging, and indicated possible toxicity arisen from the intensive dosing. Previous studies suggested that GB tumors with smaller volumes presented more favorable responses,[119] and it was in accordance to the results obtained in the first round of *in vivo* therapy where the case with smallest volume ended with largest survival and smallest tumor volume. So, the treatment schedule was adapted again, turning back to IMS schedule but starting the treatment earlier on day 6 p.i. as Figure 3.47 shown. The average tumor volume was 0.89 ± 0.26 mm^3 on day 6 p.i., without significant differences between groups, no difference of body weights as well.

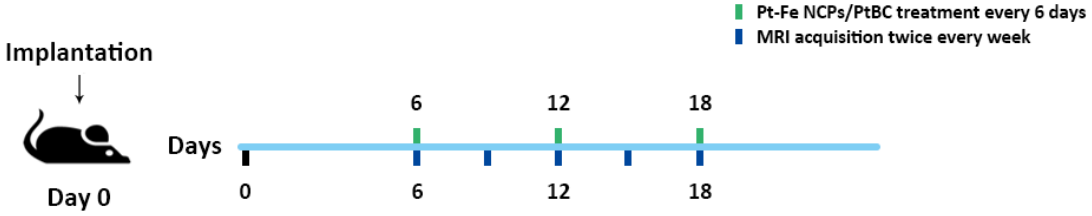

Figure 3.47 IMS treatment schedule used for GL261 GMB therapy in mice starting on day 6 p.i. PtBC or Pt-Fe NCPs was administered every 6 days starting at day 6 p.i., tumor volumes acquired by MRI high-resolution T_{2W} scanning twice per week.

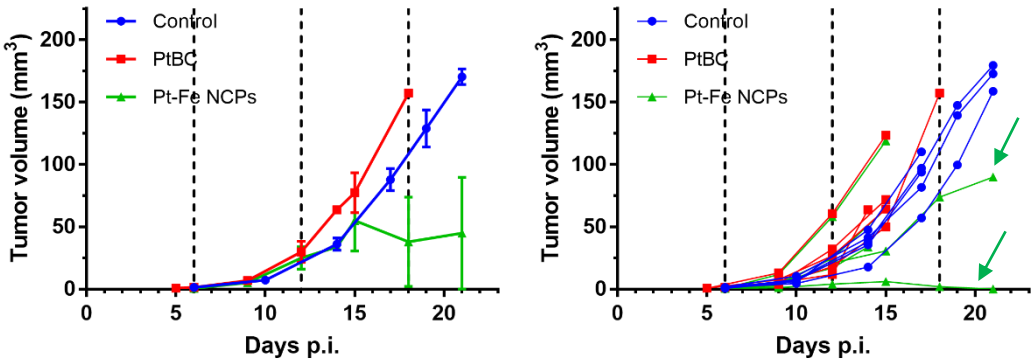

Figure 3.48 Tumor volume evolution of mice of mice from control (untreated), PtBC (1.5 mg Pt/kg), and Pt-Fe NCPs (1.5 mg Pt/kg), n = 5 for each group. Data represented as average ± SE. * stands for $p < 0.05$, all compared with control group. Vertical dash lines indicated the days for administration.

The evolution of tumor volume (Figure 3.48) displayed that treatment with PtBC did not slower down tumor growth rate, in which, in fact, the GB tumors grew even faster than the control, and all mice lost more than 20% of body weights on day 15 p.i. (Figure 3.49). Nevertheless, the inflection point in Pt-Fe NCPs indicated that the growth of tumor was successfully inhibited. Herein, the response to therapy of Pt-Fe NCPs was variable. The evolution was fast at initial stages, then the tumor growth got arrested after day 15 p.i. The separated figure showed clearly that one case in Pt-Fe NCPs group got cured which reached the largest volume of 6.03 mm^3 on day 15 p.i., then shrunk and disappeared without relapse afterwards until it died on day 61 p.i., achieving the criteria of cured mice. Commonly, when GL261 tumors shrunk until abnormal mass detection by MRI became no longer possible, or the volume remained stable (usually less than 2 mm^3), the treatment was halted. Then, MR monitoring kept twice a week. Whenever the tumor volume of the residual/abnormal mass kept stable or non-detectable for 1 month, mice were transiently declared "cured" as in reference.[41,120] To demonstrate clearly the tumor evolution, two cases in Pt-Fe NCPs (Figure 3.50) were chosen to show the follow-up MRI T_{2W} images (Figure 3.51).

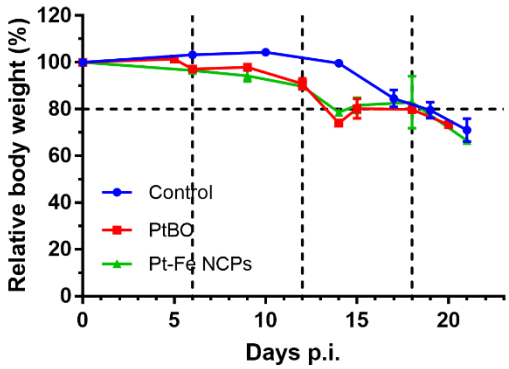

Figure 3.49 Body weight evolution of mice treated with vehicle, PtBC and Pt-Fe NCPs, n = 5 for each group. Data represented as average ± SE. Vertical dash lines indicated the days for administration. Horizontal dash lines indicated the 20% weight reduction point, below which the mice had to be euthanized due to welfare consideration.

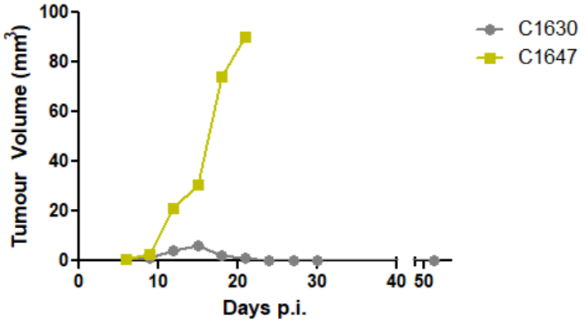

Figure 3.50 Tumor volume evolution of two representative cases in the group treated with Pt-Fe NCPs.

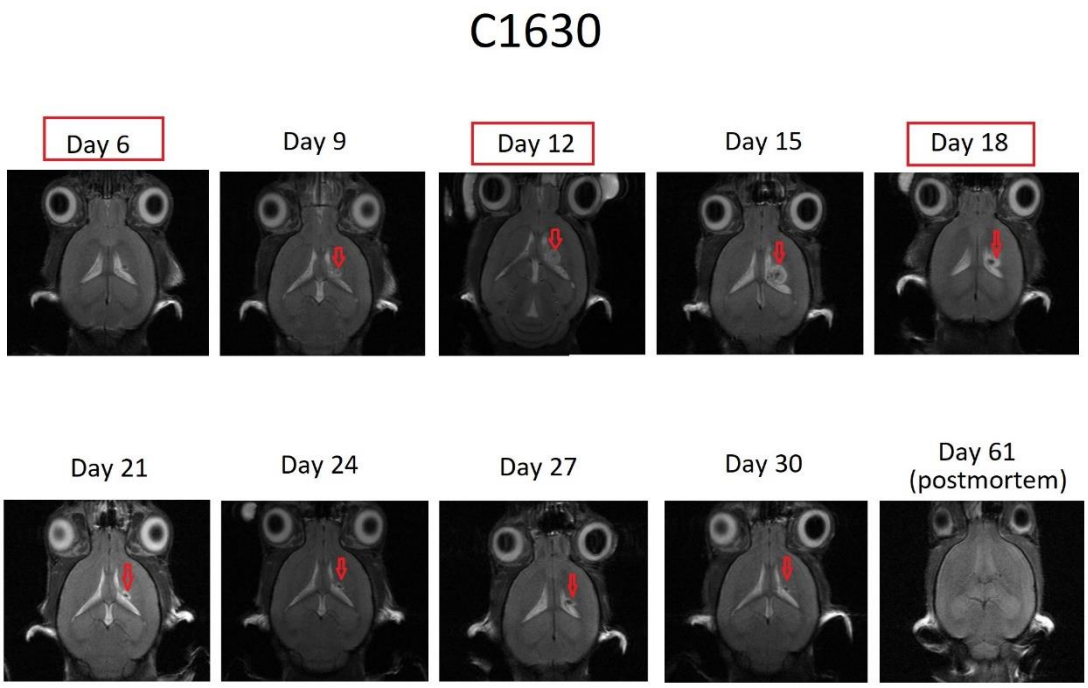

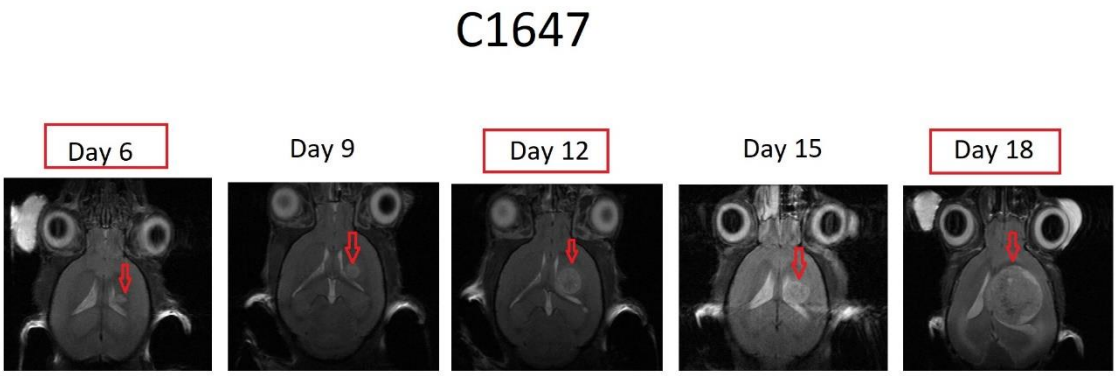

Figure 3.51 Axial T_{2w} high-resolution MRI acquired at 7 T for animals C1630 and C1647 at the different time points assessed. The tumor was highlighted with a red arrow. From day 21-24 p.i. mouse C1630 was declared cured and tumor reduced to a visible but stable scar with no evolution in further follow-up. This animal was found dead at day 61 p.i. and a post-mortem fast MRI exploration was performed in order to discard presence of visible tumor.

Thus, with this round of Pt-Fe NCPs treatment, 20% of the cases responded to the therapy with a curation rate of 20%, 20% of the cased presented growth arrest after the second therapy cycle, while the remaining cased had the same behavior as the PtBC group showing no therapeutic effects. Regarding the survival (Figure 3.52), Log-rank test gave significant difference for PtBC which presented lower survival than other groups in this case. Control cases had a survival of 19.7 ± 2.1 days, while PtBC had a survival of 14.8 ± 0.8 days and Pt-Fe NCPs in average 25 ± 19.8 days.

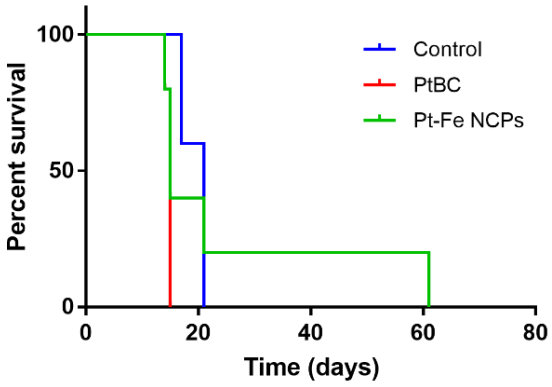

Figure 3.52 Kaplan-Meier survival curves of three groups for IMS treatment starting on day 6 p.i.

For GB treatment, current chemotherapies failed to provide substantial clinical benefits and long-term control. The development of new chemotherapeutic agents is at an early stage with uncertain output.[121] Parallel efforts should be undertaken in

optimizing/repurposing the delivery and efficacy of existing anticancer agents.[122] There were some clinical trials attempting to incorporate cisplatin into the GB treatment regimen, commonly combined with concurrent TMZ chemotherapy in recurrent GB patients. However, limited clinical benefits were obtained with an overall response rate about 20%.[123-125] Therefore, it is urgent and worthy to explore the potential efficacy of Pt agents against GB with alternative delivery routes and treatment patterns, especially in in-vivo preclinical models.

Our *in vivo* studies suggested that the therapy starting volume and treatment schedule matter a lot for the GB therapy. Herein, 6 days-interval IMS and intense every-3-days schedule were adopted during the *in vivo* studies. And the IMS schedule turned out to be more effective and can prolong the survival time, even cure the experimental animal when starting the therapy at earlier stage on day 6 p.i. On the other hand, the intense dosing schedule successfully inhibited the GB tumor growth, but shortened the survival time of treated animals due to the possible cumulative side toxicity. This was in good accordance with other chemotherapeutic agents administered in such a metronomic manner while receiving optimal therapeutic output.[41,113,120] In addition, the starting point for the therapy also played an important role for the efficacy of chemotherapy. When comparing the *in vivo* therapies started on day 10 p.i. and on day 6 p.i., both in IMS schedule, the therapeutic outcome of therapy starting with small tumors (0.89 ± 0.26 mm^3) prevailed much compared to that of therapy starting with big ones (6.07 ± 0.81 mm^3). The therapy starting on day 6 p.i. resulted in significant inhibition on tumor growth with 20% curation, 20% partial response, and prolonged survival time; while the therapy starting with bigger tumor volume led to non-significant difference in tumor growth, and close survival time as control. This was also in good agreement with other studies.[119,126-127]

The presence of low-permeable BBB/BBTB has long been an obstacle to the successful drug delivery for GB treatment, which compromises greatly the antitumor effects of most chemotherapeutic agents.[128-129] It is worth noting that the intranasal administration can work as a great alternative which is a noninvasive, direct and more effective route to deliver therapeutic drugs into CNS compared to other administration routes. Our *in vivo* therapy proved that Pt-Fe NCPs administered intranasally could

inhibit the GB tumor growth and prolong the survival time of GL261 tumor-bearing mice, given optimized treatment schedule. A previous study evaluated the *in vivo* anticancer efficacy of cisplatin-loaded polybutylcyanoacrylate (PBCA) NPs in C6 GB bearing-rats via intraperitoneal injection.[130] The treatment started as early as 2 days p.i. at a at a dose of 1 mg/kg (referred to cisplatin) and administered for 4 doses every 3 days. However, the mean survival time of mice treated with cisplatin-PBCA NPs was 17.5 days compared to 19.6 days of free cisplatin group, indicating the possible toxicity induced by the nanoformulation, which was confirmed by hematoxylin and eosin staining of liver tissues with acute tubular necrosis. In this case, the therapy with nanosized formulation of cisplatin did not work even starting with extremely small tumor volumes and intense-dosing schedule via intraperitoneal route.

Despite IN route, other delivery routes have been also investigated for GB treatment *in vivo*. Among others, local administration has been widely explored due to its potential effectiveness arisen from direct delivery into GB tumors. For instance, the anticancer activity of Pt(IV) prodrug-loaded coiled nanotubes in GB cells and in U87MG xenograft-bearing mice.[131] After a single intratumoral injection with the drugs, the reduced bioluminescence intensity indicated that Pt(IV) coiled nanotubes induced significant GB cell death in the xenograft in comparison to the PBS group, though no significant difference was found compared to the Pt(IV) prodrug. This result was confirmed by TUNEL assay and histological examination. However, no further quantitative *in vivo* studies were revealed in this report, which was insufficient to have insight into the *in vivo* antitumor efficacy of the reported Pt(IV) prodrug-based nanotubes.

Our *in vivo* results displayed that synchronized IMS administration of Pt-Fe NCPs with the cancer-immunity cycle brought certain chemotherapeutic effects in the preclinical GL261 orthotopic models. The cured case treated with Pt-Fe NCPs was not detected any signs of recurrence, which was an encouraging information. Together with other studies, this implied that host immunity may play a pivotal role during the chemotherapy and can be harnessed as an incredible comrade for the treatment of GB.[41,132] Interestingly, a recent report demonstrated that CED cisplatin induced cure in immunocompetent GL261 models, but failed to cure immunocompromised NSG mice with intracranial tumors, revealing that the therapeutic effects of CED cisplatin was immune-

dependent.[133] This provides an important hint that the administration schedule of chemotherapeutic agents should be in harmony with the immune cycle to recruit the host immune system into the battle against GB. Nevertheless, the role of host immunity in our *in vivo* studies should be elucidated by further experiments in the future to investigate the possible modulation of immunogenic effects.

3.4.7.5 *in vivo* imaging

The experimental results derived from *in vitro* relaxivity studies (see section 3.6) suggested that Pt-Fe NCPs could have potential as a promising T_2 contrast agent. However, it was necessary to evaluate the contrast effect *in vivo*. The complexity of *in vivo* environment can influence CA performances and *in vitro* results do not always translate in suitable *in vivo* performances.[134] Therefore, *in vivo* contrast enhancement studies were carried out using orthotopic GL261 GB-bearing mice. Briefly, the experimental mice were subjected to scanning with both T_1 and T_2 MRI and maps acquisition prior to and after administration. The obtained images were compared as the representative images shown in Figure 3.53.

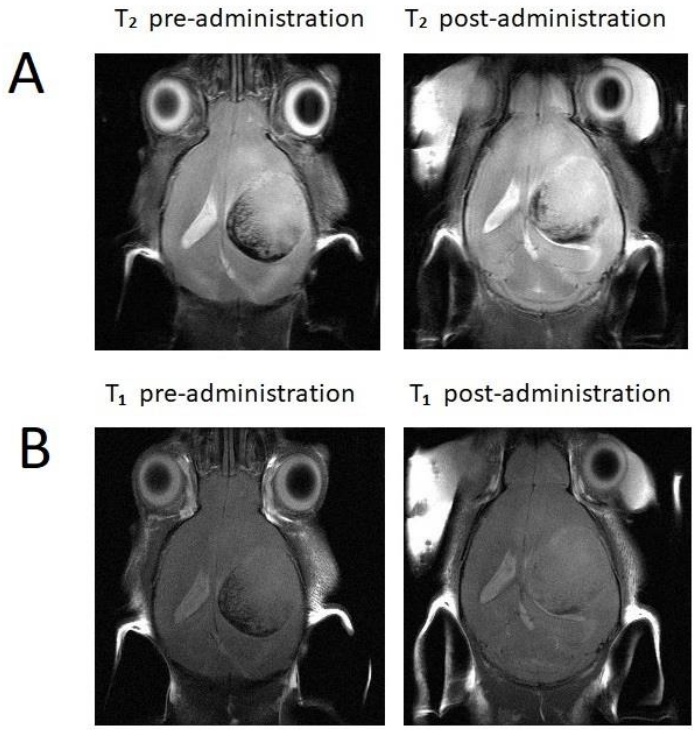

Figure 3.53 A) T2 and B) T1 weighted coronal MRI, acquired at 7 T horizontal preclinical scanner, of C1639 GL61 GB bearing mouse, 15 days after tumor implantation. Images were acquired pre (left) and post (right) after intranasal administration of Pt-Fe NCPs at a dose of 1.5 mg Pt/kg body weight. Note that since

mice should be moved out from MR scanner for intranasal CA administration, the acquisition geometry is not fully coincident in pre- and post-administration MRI acquisitions. T_1 and T_2 maps were also acquired (not shown) and no significant differences were found. For this mouse, values found in tumor regions were 55.8ms and 2470.4ms (T_2 and T_1 respectively) pre-administration and 57.4ms and 2646.9ms (T_2 and T_1 respectively) post-administration. See section 3.5 for more acquisition parameter details.

The corresponding T_1 and T_2 values were calculated pre- and post-administration (Table 3.8) for Pt-Fe NCPs. Variance homogeneity tests were non-significant; hence Student's t-tests were used for comparisons. The only significant one was T_1 ipsilateral (tumor) zone pre- and post-administration. However, it is also true that the decrease in T_1 was very limited, in average 4.7%, clearly not enough to produce a visible effect in images. In T_2, the values were non-significant pre- and post-administration, showing no enhancement for contrast. In a previous work from our group, another type of Fe-NCPs was synthesized and assessed its potential as a dual-mode CA.[135] Notably, the maximal contrast enhancement was observed at 9.4 ± 1.1 min for T_1 and 5.3 ± 1.1 min for T_2 after IV injection of Fe-NCPs at a dose of 0.4 mmol Fe/kg in the GL261 tumor-bearing mice. The iron amount injected from Fe-NCPs was 16-fold higher than that from Pt-Fe NCPs in our case. This might explain the situation that such low concentration of Pt-Fe NCPs may result in low intratumoral concentration of Fe, which may be not sufficient to enhance contrast at the given conditions. To work as a theranostic agent, optimization need to be further investigated in the future.

	T_1 pre-adm.	T_1 post-adm.	T_2 pre-adm.	T_2 post-adm.
Ipsilateral (tumor) zone	2686.92±84.4	2560.04±128.17	55.01±2.19	56.16±3.45
Contralateral zone	2229.75±69.34	2173.44±78.87	46.71±0.81	46.82±1.31

Observation: if there were some irregular zones suggestive of bleeding, these zones were avoided in calculation, since T_2 values would be artificially reduced.

Table 3.8 T_1 and T_2 values pre- and post-administration (all values shown in ms)

3.5 Conclusion

Novel Pt(IV) prodrug-based nanoscale coordination polymers with an average size of 66.0 ± 2.3 nm, a PDI of 0.258 ± 0.013, and a slightly negative ζ-potential of -8.53 ± 0.418 mV, were designed and successfully synthesized and evaluated as drug delivery systems for GB treatment. The obtained NCPs shows relevant advantages such as:

- Chemical and colloidal stability, controlled drug release, and MRI relaxivity properties compatible with its use as contrast agent for MRI.
- Pt-Fe NCPs exhibited comparable even superior cytotoxic effect compared to cisplatin against HeLa, 1Br3G, and GL261 cell lines, while ROS generation was notably dependent on the cell lines. Interestingly, Pt-Fe NCPs and PtBC did not induce ROS formation in the GL261 glioblastoma cell line, which corroborated that the cytotoxic effect was totally attributed to the chemotherapeutic effect of the released Pt compounds.
- One of the factors that determine the notable cytotoxic effect against cancer cells was the superior intracellular uptake of Pt-Fe NCPs in comparison to cisplatin or PtBC. However, the DNA-bound Pt from Pt-Fe NCPs was significantly lower than cisplatin after 24 h of exposure, indicating slower intracellular activation process.
- Pt-Fe NCPs were proved to be well-tolerated and biosafe at a dose up to 1.5mg Pt/kg body weight in wt mice, and displayed favorable accumulation of Pt in GB tumor and brain, implying the effective delivery of intranasal administration.
- Optimized therapy with Pt-Fe NCPs in immune-enhancing metronomic schedule starting at day 6 post implantation resulted in significant inhibition on tumor growth in GL261 orthotopic models, with 20% curation rate, 20% partial response, and prolonged survival time.
- These results indicated that Pt-Fe NCPs possess a potential anti-GB activity both *in vitro* and *in vivo*. Intranasal administration has been established as a noteworthy alternative to typical IV systemic administration what represents a notable advance for the design of novel therapeutic methodology that could be used in combination with other therapies.

3.6 Experimental

Characterization methods. 250 MHz ^{1}H NMR spectra were recorded on a Bruker DPX 250 MHz spectrometer; 360 MHz ^{1}H NMR, ^{1}H-^{1}H COSY, and 100 MHz ^{13}C NMR were recorder on a Bruker DPX 360 MHz spectrometer; 400 MHz ^{1}H NMR, ^{1}H-^{1}H COSY, and 100 MHz ^{13}C NMR were recorder on a Bruker DPX 400 MHz spectrometer. Chemical shifts (δ) are given in ppm, using the residual non-deuterated solvent as internal reference. Signal multiplicities are described using the following abbreviations: singlet (s), doublet (d), triplet (t), quartet (q), quintet (quint), doublet of doublets (dd), doublet of triplets (dt), doublet of doublet of doublets (ddd), multiplet (m) and *J* to indicate the coupling constant (Hz). High-resolution mass spectra were obtained by direct injection of the sample with electrospray techniques in a Bruker microTOF-Q instrument. FT-IR spectra were recorded using a Tensor 27 spectrophotometer (Bruker Optik GmbH, Germany) with KBr pellets. Powder X-ray diffraction (PXRD) patterns were recorded at room temperature on a PANalytical X'Pert PRO MRD diffractometer (Malvern PANalytical, Germany) equipped with a CuKα radiation source (λ = 1.54184 Å) and operating in reflection mode, where the solid samples were placed on an amorphous silicon oxide plate and measured directly. UV-vis was performed using a Cary 4000 UV-vis spectrometer (Agilent Technologies, USA) within a wavelength range of 400-4000 nm and a 1 cm path length quartz cuvette (QS 10mm).

DLS measurements. Size distribution and surface charge of the nanoparticles (0.5 mg/mL) were measured by DLS, using a ZetasizerNano 3600 instrument (Malvern Instrument, UK), with size range limit from 0.6 nm to 6 nm. (Note: the diameter measured by DLS is the hydrodynamic diameter. The samples were comprised of aqueous dispersions of the nanoparticles in distilled water or in buffer. All samples were diluted to obtain an adequate nanoparticle concentration.)

Electron Microscopies. SEM images were obtained using a scanning electron microscope (FEI Quanta 650 FEG) at acceleration voltages of 5-20 kV. SEM samples were prepared by drop-casting of corresponding dispersions of NPs on an aluminum tape followed by evaporation of the solvent under room conditions. Before analysis, the samples were metalized with a thin layer of platinum (thickness: 5 nm) using a sputter

coater (Emitech K550). STEM images were obtained using a scanning-transmission electron microscope (Magellan 400L, FEI), while TEM images were obtained using a transmission electron microscope (Tecnai G2 F20, FEI) at a voltage of 200 kV. Samples for STEM and TEM were prepared by drop-casting corresponding dispersions on TEM grids (ultrathin carbon type-A, 400 mesh Cu grid, Ted Pella Inc., Redding, USA) and drying overnight under room conditions prior to examination.

Mössbauer spectroscopy measurements. ^{57}Fe Mössbauer spectra were recorded in transmission geometry with a conventional Mössbauer spectrometer equipped with a ^{57}Co(Rh) radioactive source operating at room temperature 300 K and relatively low temperature 80 K. The samples were sealed in aluminum foil and mounted on a nitrogen bath cryostat (Oxford Instruments). The spectra were fitted to the sum of Lorentzians by a least-squares refinement using Recoil 1.05 Mössbauer Analysis Software. All isomer shifts refer to α-Fe at room temperature.

Quantitative magnetic resonance imaging phantoms (MRI-Phantoms). The longitudinal r1 and transverse r2 relaxation rates for Pt-Fe NCPs at different concentrations were measured in 1% agarose/PBS gelation under an external magnetic field of 7 T (300 MHz) Bruker Biospec 70/30 SUR spectrometer (Bruker BioSpin GmbH, Germany) with corresponding acquisition sequences. Specifically, the NCPs were dispersed in 1.5 mL of 1% agarose/PBS solutions at 65 ℃ in an ultrasound bath to ensure a good colloidal suspension, and solidified at room temperature, resulting in a series of gel with different metal concentrations (3.94, 1.97, 1, 0.1, and 0 mM of Fe). The obtained relaxation rate values were plotted versus the concentrations of iron.

Thermogravimetric analysis (TGA) and calorimetric measurements (DSC). Samples were run on a Netzsch TG 209 F1 thermal gravimetric analyzer, holding in aluminium crucibles at a heating rate of 10 K/min from 25 to 900 ℃ under air atmosphere. Differential scanning calorimetry (DSC) were measured using the same equipment with a cryostat under same conditions.

Inductively coupled plasma-Mass spectrometry (ICP-MS). Standard solutions were prepared prior to the measurements at a range from 0 – 200 parts per billion (ppb) using

atomic spectroscopic analytical ICP-MS standards (PerkinElmer Inc., Germany). The isotope ^{54}Fe and ^{57}Fe were selected as Fe tracers, while ^{194}Pt, ^{195}Pt and ^{196}Pt as Pt tracers.

Digestion procedures for ICP-MS measurement. All glassware was immersed in 20% HNO_3 for 48 h, and plasticware in 5% HNO_3 for 4 h prior to use for ICP-MS. All samples were digested using wet digestion method. Depending on the materials to digest, different procedures were adopted.

(1) Chemical samples: samples, 5.0 mg of NPs for instance, were weighed accurately with an analytical balance, and transferred into a vial, then concentrated ultrapure HNO_3 (69%, Ultratrace®, ppb-trace analysis grade, Scharlab, Spain) was added. The samples were placed in the fume hood for 48 h to be fully digested, then were diluted with 0.5% (v/v) ultrapure HNO_3 for further measurements.

(2) Cell pellets: the cell pellets were immersed in 100 μL of concentrated ultrapure HNO_3 (69%, Ultratrace®, ppb-trace analysis grade, Scharlab, Spain) and left to digest overnight. Samples were then heated to 90 ℃ till the suspensions turned clear. The samples were diluted with 0.5% (v/v) ultrapure HNO_3 to appropriate volumes for later measurements.

(3) Tissues: the tissues were added with T-PER™ buffer (Thermo Fisher Scientific, USA) in a ratio of 10 mL : 1 g, then cut into small pieces, and homogenized with ultrasonication microtip (Branson Digital Sonifier 450, Emerson, USA) in cycles of 10 seconds on and 15 seconds off with an amplitude of 30%. Afterwards, the tissue suspensions were added with aqua regia (all ppb-trace analysis grade) and heated up to 300 ℃, while 30% H_2O_2 was added in the later digestion process till the suspensions turned clear. The clear solutions were transferred and made up with 0.5% (v/v) ultrapure HNO_3 to appropriate volumes for the determination of metal contents using ICP-MS.

Synthesis of Pt (IV) prodrug PtBC

Synthesis of oxoplatin. The synthetic sequence started from the commercially available cis-diamminedichloroplatinum(II), or cisplatin (CDDP). Into a suspension of cisplatin (1 g, 3.33 mmol) in Milli-Q water (44 mL), hydrogen peroxide aqueous solution (30%, 5.72 mL, 66.6 mmol) was added. The mixture was heated to 76℃ in darkness

under reflux for 5 h, then cooled down to room temperature overnight. The flask was placed in the fridge for 3 h, and filtered to get yellow pellet. The pellet was washed with cold H_2O, EtOH, and ether, and dried under vacuum to furnish oxoplatin (1.095 g, 3.28 mmol, 98%).

Synthesis of disuccinic cisplatin (DSCP). Anhydrous DMSO (4 mL) was added into the mixture of oxoplatin (1.09 g, 3.28 mmol) and succinic anhydride (1.32 g, 13.2 mmol). The suspension was heated to 76 ℃ in darkness under reflux for 24 h. The resulting clear yellow solution was lyophilized to remove the solvent. The slurred residue was sonicated with ethyl acetate to give light yellow solid. After centrifugation and drying, DSCP was obtained as a light-yellow powder (1.706 g, 97%).

^{1}H NMR (360 MHz, DMSO-d6): δ = 12.05 (s, 2H, H-c), 6.80 - 6.20 (br s, 6H, H-d), 2.40 (t, 4H, J = 6.9 Hz, H-b) ppm. *Note: peak H-a is overlapped with the DMSO residual solvent signal. The letters corresponded to the labels in the structure shown in spectrum.*

Synthesis of Pt(IV) prodrug PtBC. DSCP (0.5 g, 0.93 mmol), DCC (0.58 g, 2.8 mmol), and NHS (0.43 g, 3.75 mmol) were dissolved in anhydrous DMF (4 mL) under Ar in darkness. The solution was stirred overnight. Then the slurry mixture was placed in the freezer for 4 h, and the white precipitate dicyclohexylurea (DCU) was removed by filtration. A large amount of EtOAc was poured into the filtrate and sonicated to get an off-white precipitate, which was washed by cold ether and dried to give the activated ester (0.424g, 62.2%). This intermediate (0.42 g, 0.58 mmol) and dopamine hydrochloride (0.263 g, 1.39 mmol) were dissolved in anhydrous DMF (3 mL), and N-methylmorpholine (NMM, 2.3 mL, 20.9 mmol) was added in three batches. As a result, the milky suspension changed to clear yellow solution. The reaction was tracked by thin layer chromatography (TLC). 24 h later, the reaction was stopped and lyophilized to give a brownish residue. The off-white Pt (IV) prodrug PtBC (0.195 g, 41.8%) was obtained by flash column chromatography, with a mobile phase consisting of EtOAC: MeOH (9:1 in volume).

^{1}H NMR (400 MHz, MeOD-d4): δ = 6.69 (m, 4H, H-f,g), 6.54 (d, 2H, H-e), 2.61-2.70 (m, 8H, H-a,d), 2.46 (t, 4H, H-b) ppm. *Note: peak H-c is overlapped with the MeOD residual solvent signal*. *The letters corresponded to the labels in the structure shown in spectrum.*

^{13}C NMR (100MHz, MeOD-d4): δ 180.99, 173.85, 144.74, 143.26, 130.79, 119.71, 115.52, 114.96, 41.08, 34.45, 31.30, 31.00.

HRMS (EI): calcd 803.1300, found 803.1284.

Pt content by ICP-MS: calcd (%) 24.25, found (%) 24.12.

Synthesis of Pt-Fe NCPs. To prepare a material suitable for biological experiments, synthesis of the nanoparticles was carried out inside a biosafety cabinet (Telstar BioVanguard B green), and all materials and solvents were sterilized by autoclaving prior to use. PtBC (50 mg, 0.06 mmol) was dissolved in 96% EtOH (15 mL), and $Fe(OAc)_2$ (10.8 mg, 0.06 mmol) in 1 mL of H_2O was added dropwise. A black precipitate formed immediately with the addition of iron ions. After 30 min's stirring at 700 rpm, the precipitate was collected by centrifugation and then washed by EtOH and H_2O several times. The solid was then lyophilized to get black powder which was stored in the freezer for later use. Elemental analysis: found (%) C 28.63, H 2.54, N 5.79.

Metal contents by ICP-MS: 18.87% Pt, 15.13% Fe.

Coating for Pt-Fe NCPs. The two-step coating was carried out according to our previously reported method in our group. Specifically, NCPs (10 mg/mL) were dispersed in carbonate buffer (pH 8.2) in vial covered with pierced parafilm. HMDA (10 mM) and CAT (10 mM) were added into the NCP suspension slowly. The mixture was kept stirring gently for 90 min to form the coating. During this process, the dark suspension turned brownish while the colorless media got reddish. Afterwards, the suspension was centrifuged and washed by Milli-Q® water four times. The coated NCP was checked by FTIR, SEM and ICP-MS.

After primer coating with HMDA and CAT, a second coating layer with PEG-diamine was performed in order to improve the colloidal stability of the NCPs. Specifically, the NCPs with primer coating were redispersed in isopropanol, followed by the addition of PEG-diamine in isopropanol. The vial was closed and kept stirring gently for 90 min. Finally, the coated NPs were collected by centrifugation at (7000 rpm × 3 min), and washed with Milli-Q® water several times, then dried under vacuum and lyophilized for long-term storage. The coated NCP was checked by FTIR, SEM and ICP-MS.

Colloidal stability improvement of Pt-Fe NCPs. In order to improve the colloidal stability of Pt-Fe NCPs suspension, a range of stabilizers were used and compared, including PVP, PVA, PEG, PEG-amine, PEG-COOH, and BSA. Generally, the stabilizers were dissolved in the solvent at a concentration of 1% (BSA at 10 mg/mL) before the synthesis of Pt-Fe NCPs started. Once the reaction of NCPs finished, the precipitate was collected and washed. Then the NCPs were redispersed in PBS at a concentration of 0.5 mg/mL. And the colloidal dispersion was checked by DLS and STEM.

Drug release assay. Drug release from Pt-Fe NCPs was determined using dialysis method. Concentrated Pt-Fe NCPs at 1 mg/mL were resuspended into 1 mL of PB buffer in dialysis bags (MWCO = 6000 – 8000). The dialysis tubes were immersed into sealed beakers with 40 mL of PB buffers at pH 7.4 and 5.5. The beakers were incubated at 37 ℃ with gentle stirring during the study. Aliquot of 500 μL was taken from the dialysate at predetermined time points (0.5, 1, 2, 4, 6, 8, 24, and 48 h), followed by supplementing with fresh buffer in same volume immediately. The amount of released Pt was determined by ICP-MS. To test the influence of GSH, PB buffers with 2 mM and 10 mM GSH were used for dialysis, remaining same other conditions.

Cells. The cell lines were obtained from the Tumor Bank Repository at the National Cancer Institute (Frederick/MD, USA), including human cervical cancer cell HeLa, non-malignant human fibroblast cell 1Br3G, murine glioblastoma cell GL261, and a pair of human ovarian cancer cell lines, A2780 and its cisplatin resistant counterpart A2780/cis. Before starting any protocol, all solutions were prewarmed to 37 °C. All materials and equipment that came in contact with cells were sterile. All cell-related performances were carried out in Class II biosafety hoods in cell culture labs with a biosafety level 2 (BSL-2 with code A/ES/19/I-08).

Cell culture. All cell lines were grown in 75 cm^2 cell-culture flask with corresponding culture media. HeLa was cultured in MEM medium, 1Br3G in DMEM, GL261 in RPMI 1640, A2780 in RPMI 1640, and A2780/cis in RPMI 1640 containing 1 μM of cisplatin. All culture media were supplemented with 10% fetal bovine serum (FBS, Gibco®, Invitrogen, UK), 0.285 g/L glutamine, 2.0 g/L sodium bicarbonate, and 1% penicillin-streptomycin. Cells were cultured as adherent monolayers and maintained in an incubator (HERAcell, 150i, Thermo Scientific) at 37 °C in 5% CO_2 and relative humidity of 95%, except 1Br3G

with 10% CO_2. All cell culture media, FBS, supplements, antibiotics, trypsin, and Trypan Blue were purchased from Fisher Scientific (Gibco®, Invitrogen, UK).

To subculture/harvest the cells at log phase around 75% confluence, 4 mL of sterile PBS was added into the flask to rinse the cells after discarding spent cell culture media by aspiration with a vacuum pump. After washing, 3 mL of 0.05 % trypsin-ethylenediaminetetraacetic acid (EDTA, 0.2 g/L) were added and the flask was returned to incubator for 2 minutes. Observing the cells under the microscope, if ≥ 90% of the cells have detached, 6 mL of fresh cell media was added into the flask and detached the cells from the bottom. The cell suspension was transferred into a 15 mL flask (Falcon, Corning, USA) to centrifuge (Thermo Scientific, USA) at 1400 rpm for 5 min to collect cells. The supernatant was discarded, and the pellet was resuspended in fresh media or PBS for cell counting, then an appropriate number of cells was seeded in a new flask.

Cell counting. The cells were counted using a Neubauer hemocytometer cell counter and Trypan Blue (Gibco®, Invitrogen, UK) exclusion to count the cells and determine the viability. Trypan Blue is a dye used to distinguish the living cells from the dead, since the dead cells cannot extrude Trypan Blue without required energy mechanisms. An aliquot of 10 μL of the cell suspension obtained in the subculture step was added into 10 μL of Trypan Blue. Then, 10 μL of the resulting mixture was added onto the Neubauer hemocytometer and the number of living cells was counted under an optical microscopy, or counted using the TC10^{TM} automatic cell counter (Biorad, Hercules, California).

***In vitro* cytotoxicity assays.** The cells (HeLa, 1Br3G, GL261, A2780 and A2780/cis) in exponential growth were seeded in 96-well plate (Corning, USA) with proper density. HeLa cell line was seeded at a density of 2000 cells/well, 1Br3G at 3000 cells/well, GL261 at 4000 cells/well, A2780 and A2780/cis at 3000 cells/well. Specifically, the cisplatin-containing cell culture media was replaced with fresh RPMI media without drug 4 hours before seeding. After 24 hours' incubation, fresh media containing compounds (Pt-Fe NCPs, PtBC, and CDDP) at different concentrations (0, 0.1, 1, 5, 10, 25, 50, 100, 200 μM referred to Pt concentration) were added, and the plates were incubated for 24 or 72 hours. Afterwards, 10 μl of PrestoBlue® (0.15 mg/ml, Thermo Scientific, USA) was added

into each well and the plates were incubated for another 4 hours before measuring the fluorescence at 572 nm with excitation at 531 nm by the microplate reader Victor 3 (Perkin Elmer, USA). For 1Br3G, the incubation time with PrestoBlue® was prolonged to 7 h in order to achieve enough difference of fluorescence intensity between concentrations. All experiments were carried out in triplicate, data were treated and calculated to obtain IC_{50}s by GraphPad Prism software (version 7.0).

Estimation of ROS formation. HeLa, 1Br3G and GL261 were seeded in black 96-well plates (Corning, USA) at a density of 20,000 cells per well to achieve full confluence. After 24 hours' incubation, the spent medium was discarded and cells were washed out from the medium serum, and added prewarmed PBS with the fluorescent probe 2',7'-dichlorofluorescin diacetate (DCFCDA, final working concentration 10 μM), then incubated for 30 minutes. DCFCDA is a non-fluorescent permeable compound which can be hydrolyzed by esterase and oxidized by intracellular ROS and turn to fluorescent and non-permeable 2',7'-dichlorofluorescein (DCF). After the probe was internalized, the buffer with probe was replaced by only medium or media with compounds (H_2O_2, $Fe(OAc)_2$, Pt-Fe NCPs, PtBC, and CDDP) at the concentration of IC_{50} for 24 hours. 0.1 mM of H_2O_2 was added as positive control, while 0.1 mM of $Fe(OAc)_2$ was added for comparison. After 24 hours, the fluorescence of each well was examined at 530 nm after excitation at 485 nm by a microplate reader Victor 3 (Perkin Elmer, USA). This experiment was repeated in triplicate independently. The results were normalized based on the negative control loaded with dye but without drug treatment.

Cellular internalization. HeLa, 1Br3G and GL261 cells were seeded in 6-well plates (Corning, USA) at a density of 300,000 cells per well with 1.5 ml of media. After 24 h of incubation, the media were replaced by 1 ml of fresh media w/wo CDDP, PtBC, and Pt-Fe NCPs at 100 μM referred to Pt concentration. The treated cells were allowed to internalize the compounds for 6 h in the incubator. Another cellular uptake assay was also performed with a decreased concentration of Pt agents to 10 μM, and increased time points of 2, 4, 8, and 24 h. The media were removed immediately and cells were rinsed twice by cold PBS in order to remove excessive compounds. Then 0.5 ml of trypsin was added to each well for 3 min and 2-fold volume of fresh media was added to neutralize the trypsin. After an aliquot was taken from each well for cell counting, the

rest cell suspensions were collected into 1.5 ml Eppendorf tubes (Corning, USA) and centrifuged at 12,000 rpm for 4 min. The supernatants were discarded while the cell pellets were stored at -80 ℃ for further quantification by ICP-MS.

DNA-bound Pt. In order to clarify the action mechanism of our Pt NPs, the DNAs were extracted and measured by ICP-MS to quantify the DNA-bound Pt after uptake for 24 h in HeLa, 1Br3G and GL261 cells. The cells in exponential growth were seeded onto cell culture dishes in optimal condition for each cell line to reach 50 - 60 % of confluence in 24 h before the treatment. Then the drugs (CDDP, PtBC, and Pt-Fe NCPs) were added at 100 μM referred to Pt concentration, and the cells were allowed to incubate for another 24 h. Afterwards, media with drugs were removed and the cells were rinsed, trypsinized and collected by centrifugation and rinsed with cold PBS twice to remove excessive drugs. The resulting cell pellets were resuspended in lysis buffer (pH 8.0, 150 mM Tris-HCl, 100 mM NaCl and 0.5 % (w/v) SDS). Pellets in buffer were incubated on ice for 15 min and centrifuged at 15000 rpm for 15 min. 0.1 volume of RNase A was added into each supernatant at 200 μg/mL and incubated for 1 h at 37 ℃. Afterwards, Proteinase K was added at 100 μg/mL and incubated for 3 h at 56 ℃. A volume of Phenol/Chloroform/Isoamyl alcohol (25:24:1 in volume, Thermo Scientific®) was added and mixed gently. And after a centrifugation of 3 min at 15000 rpm, aqueous phases containing DNA were transferred into sterile tubes. DNA was precipitated with 0.1 volume of 3 M sodium acetate and 1 volume of absolute ethanol at -20 ℃ overnight. Then, the DNA samples were centrifuged for 15 min at 15000 rpm, and finally DNA samples were dried and resuspended in 100 μL of elution buffer (pH 8.0, 10 mM Tris-HCl, 1 mM EDTA). The concentration of isolated DNA was quantified by measuring the absorbance at 260 nm using NanoDrop™ 1000 spectrophotometer (Thermo Fisher Scientific, USA). And remaining samples were frozen for further ICP-MS analyses.

Animals. Animal experiments and handling have been performed in collaboration with properly accredited personnel (Dr. Shuang Wu or Ms. Mª del Pilar Calero). Healthy female C57BL/6J mice (8 - 12 weeks, body weight 20 - 24 g) were used for all *in vivo* studies in this work, which were obtained from Charles River Laboratories (Charles River Laboratories Internacional, I'Abresle, France) and housed in the animal facility (Servei d'Estabulari, https://estabulari.uab.cat/) of the *Universitat Autònoma de Barcelona*. All

animal study protocols were approved by the local ethics committee (*Comissió d'Ètica en l'Experimentació Animal i Humana*, https://www.uab.cat/etica-recerca/) according to regional and state legislations (protocol CEEAH-3665). The animals were housed in cages with free access to standard food and water, under uniform housing and environmentally controlled conditions.

Figure 3.54 Illustration for unique identification of mice by ear-piercing.[136]

Herein, every studied mouse was given a unique alphanumerical identifier, CXXXX belonging to mice bearing GL261 tumors, while WTXXXX belonging to wild type (wt) mice without tumors. Besides, specific ear-piercing combinations were made with an ear-punching device for distinguishing animals in same cage. As shown in Figure 3.54, single or multiple ear notches were made in one or both ears.

Establishment of orthotopic intracranial glioblastoma model by stereotactic injection of GL261 cells. The orthotopic GB tumor models were generated by stereotactic injection of GL261 cells into C57BL/6J mice. Specifically, analgesia (Metacam, Boehringer Ingelheim) at 1 mg/kg was injected subcutaneously to each animal 15 minutes before anesthesia and also 24 and 48 h after implantation. Mice were anesthetized with a mixture of ketamine (Parke-Davis SL, Madrid, Spain) at 80 mg/kg and xylazine (Carlier, Barcelona, Spain) at 10 mg/kg via intraperitoneal administration. Once anesthetized, the mouse was immobilized on the stereotaxic holder (Kopf Instruments, Tujunga/CA, USA) in a prone position. Next, the head area was shaved, and the incision site was sterilized with iodophor disinfectant solution, a 1 cm incision was made exposing the skull and a 1 mm hole was drilled 0.1 mm posterior to the bregma and 2.32 mm to the right of the midline using a microdrill (Fine Science Tools, Heidelberg, Germany). A 26G Hamilton syringe (Reno/NV, USA), positioned on a digital

push-pull microinjector (Harvard Apparatus, Holliston/MA, USA) was then used for injection of 4 μL of RPMI cell culture medium containing 100,000 GL261 cells (obtained and counted as described in previous section) at a depth of 3.35 mm from the surface of skull at a rate of 2 μL/min.

Once the injection was completed, the Hamilton syringe was left untouched for 2 minutes more before its removal to prevent the cellular liquid leakage out of the skull. Finally, the Hamilton syringe was gently and slowly withdrawn and the scission site was closed with suture silk 6.0 (Braun, Barcelona, Spain). When the implantation was over, the animal was left in a warm environment to recover from anesthesia.

The C57BL/6J immunocompetent mice were exposed to enriched environment (EE) for 3 weeks before tumor implantation, since it was reported that it could significantly reduce glioma growth and improve mice survival by increasing immunological parameters in the brain of mice.[137] Moreover, since this is the current protocol used at GABRMN, the maintenance of basic parameters may help in further comparisons. Thus, all mice in this thesis were allowed to endure 3 weeks of guarantee housing in EE-like caging before tumor generation, and were maintained there from beginning to end (Figure 3.55).

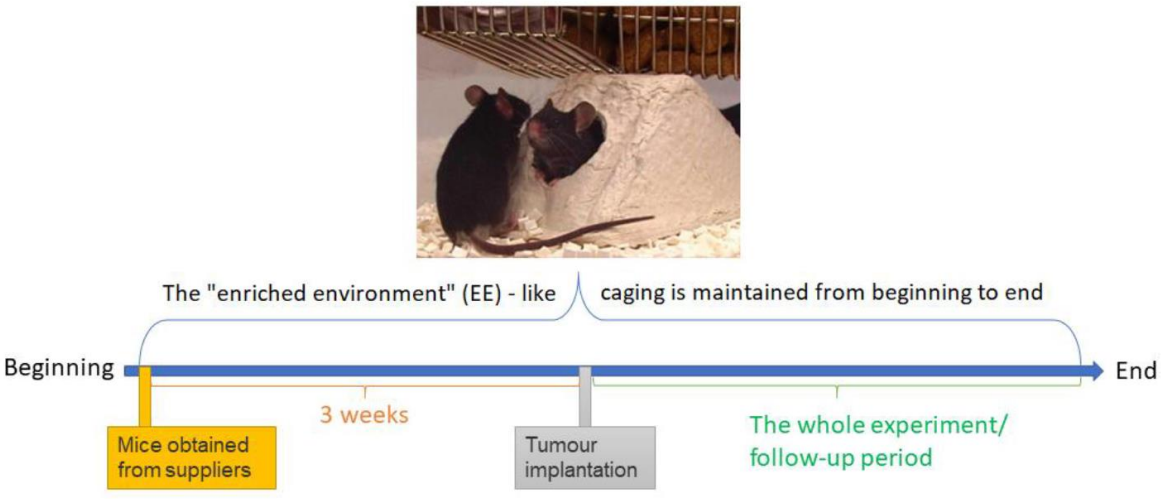

Figure 3.55 Illustration for "enriched environment"-like caging. Mice were allowed to endure 3 weeks of guarantee housing in EE-like caging before tumor generation, and EE was also maintained during the whole experiment and follow-up period. The 'Shepherd Shack' is cage insert composed of autoclavable paper, mice can shred it and use the paper for nesting.[136]

For intranasal administration, the animals were anesthetized by isoflurane for 1 min and kept in a horizontally supine position. The animals were administered with 2 μL of formulation for each nostril, with an interval about 2 minutes between each administration. Treated animals were followed-up to evaluate tumour volume evolution and the mice reaching endpoint criteria were euthanized for ethical considerations.

Tissue preservation procedures. When animals died or were euthanized by cervical dislocation to prevent suffering, the brains and main organs (heart, lungs, spleen, liver and kidneys) were excised and either frozen in liquid nitrogen or fixed in formalin, depending on the purpose. In case of freezing, tumors were dissected and collected from normal brain parenchyma, frozen in a liquid nitrogen container for further analysis. In case of fixation, tissue was preserved in 4% formalin for further autopsy or histopathological analysis. Tissues were resected after visual inspection of the whole brain and tumor, avoiding as much as possible the cross contamination with non-tumoral tissue.

***In vivo* MRI.** The animals were subjected to non-invasive brain MRI scan to measure the volumes, localization, and evolution of the GB. Each scan was performed at 7T BioSpec 70/30 USR spectrometer (Bruker BioSpin GmbH, Ettlingen, Germany) at *Servei de Ressonància Magnètica* from UAB (also part of Unit 25 of ICTS NANBIOSIS, NMR: Biomedical Applications I https://www.nanbiosis.es/portfolio/u25-nmr-biomedical-application-i/). Mice were positioned in a dedicated bed, which allowed the delivery of anaesthesia (isoflurane, 1.5-2 % in O_2 at 1 L/min), with an integrated heating circuit for body temperature regulation. Respiratory frequency was monitored with a pressure probe and kept between 60-80 breaths/min. GL261 tumor-bearing mice were scanned to acquire high-resolution T2w images using a rapid acquisition with relaxation enhancement (RARE) sequence to detect the brain tumors. The acquisition parameters were as following: repetition time (TR)/effective echo time (TEeff) = 4200/36 ms; echo train length (ETL) =8; field of view (FOV) = 19.2 × 19.2 mm; matrix size (MTX) = 256 ×256 (75 × 75 μm/pixel); number of slices (NS) = 10; slice thickness (ST) =0.5 mm; inter-ST = 0.1 mm; number of averages (NA) = 4; total acquisition time (TAT) = 6 min and 43 s. MRI data were acquired and processed on a Linux computer using ParaVision 5.1 software (Bruker BioSpin GmbH, Ettlingen, Germany).

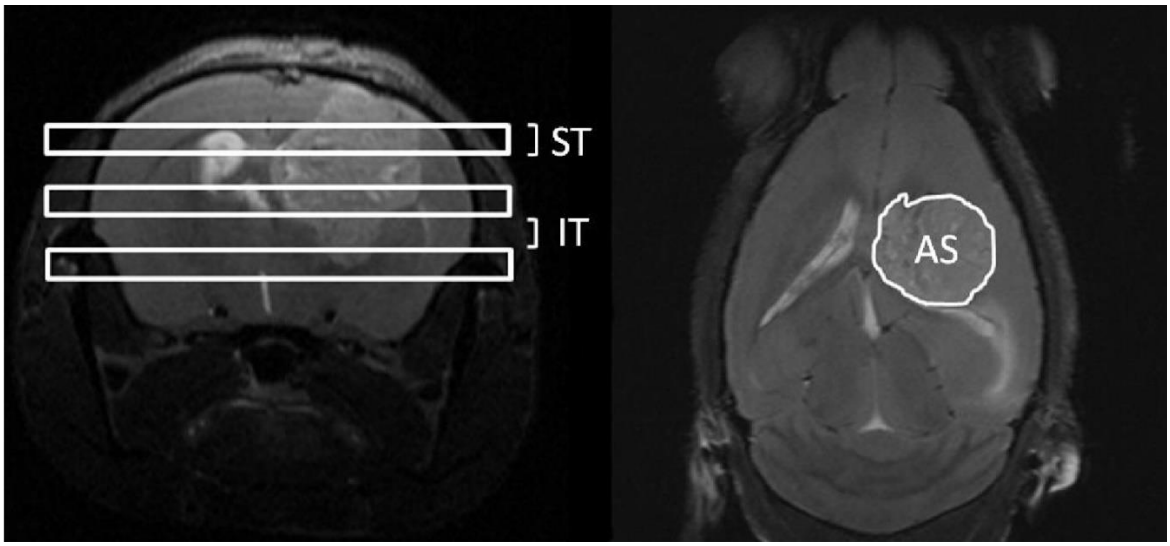

Figure 3.56 MRI measurement for tumor volume assessment. High resolution axial T_{2W} images (right) were acquired for this purpose. The surface area (AS) of the tumour (white line contour at right) was measured in each slice of the axial T_{2W} images. The slice thickness (ST) and the inter-slice thickness (IT) (represented by horizontal slices over a coronal image on the left) were considered for final volume calculation. Figure adapted from reference 138.

To calculate the tumor volume from MRI acquisitions, ParaVision software was used to generate regions of interest (ROIs) to measure the tumor area in each slice (Figure 3.56). And the tumor volume of the studied mice was calculated as following equation:

$$TV\ (mm^3) = [(AS_1 \times ST) + [(AS_2 + (\ldots) + AS_{10}) \times (ST + IT)]] \times 0.075^2$$

Where TV is the tumor volume; AS is the number of pixels contained in the ROI delimited by the tumor boundaries in each slice of the MRI sequence; ST is the slice thickness (0.5 mm), while IT is the inter-slice thickness (0.1 mm), and 0.075^2 is the individual pixel surface area in mm^2.

For *in vivo* contrast enhancement, GL261 tumor-bearing mice (n = 5, 16.5 ± 3.2 days after tumor implantation, tumor volume = 39.4 ± 23.3 mm^3) were placed in a mouse bed and anesthetized with isoflurane 0.5 - 1.5% in O_2. Breathing (60 - 80 breaths/min) and temperature (37 - 38 °C) were monitored continuously (SA Instruments, Inc., New York, USA). A first experiment was carried out prior to the administration of Pt-Fe NCPs. A second experiment was performed 1 h post administration with Pt-Fe NCPs. The amount of CA injected in tumor-bearing mice was 20 ± 4 µl (1.5mg Pt/kg). For T_1 maps acquisition, the parameters for the RARE-VTR sequence were set as the following: RARE

factor = 2; FOV = 1.92 × 19.2 mm; MTX = 256 × 128 (75 × 150 μm/pixel); NS = 3; ST = 1 mm; TEeff = 7.5 mg; TRs were set as following: 200, 400, 700, 1000, 1300, 1700, 2000, 2600, 3500 and 5000 ms; NA =1; TAT = 19 min 31 s. For T_2 maps acquisition, a multi-slice-multi-echo (MSME) sequence was used with parameters as: FOV = 1.92 × 19.2 mm, MTX = 256 × 128 (75 × 150 μm/pixel); NS = 3; ST = 1 mm; TR = 3000 ms; TEs were set as following: 10, 20, 30, 40, 50, 60, 70, 80, 90, 100, 110, 120, 130, 140, 150, 160, 170, 180, 190 and 200 ms; NA = 4; TAT = 6 min 24 s.

Tolerability assessment. Healthy female C57BL/6 mice (8-12 weeks, 20-24 g) were randomly divided into three groups, control, PtBC, and Pt-Fe, n = 3. After one min's anesthetized, the mice were administered with drugs intranasally using a micropipette (Gilson, Limburg, Germany) in horizontally supine position. The dosage increased from 0.9, 1.2, to 1.5 mg Pt/kg body weight every week, scaling dosages based in work described by reference[139]. The body weights of mice were recorded prior to the first dose of treatment and were monitored 3 times a week thereafter. The animals were inspected by veterinary and technicians from the animal facility, in particular for abnormal behaviour, food and water consumption, and possible suffering clinical signs.[140] The whole study lasted for 4 weeks. Mice were euthanized under terminal anesthesia, and bodies were preserved either in liquid nitrogen or in formalin for further histological study.

Biodistribution study. Mice bearing GL261 gliomas were used for the biodistribution study. According to the sizes of the GB, the mice were divided into two groups, one with bigger tumors and the other with smaller tumors, as indicated in Table 3.9. Pt-Fe NCPs were administrated intranasally at a dosage of 1.5 mg Pt/kg body weight. After 1 h, mice were euthanized. Brain, tumor, heart, lungs, spleen, liver, and kidneys were excised and weighed immediately. These tissues were then homogenized in T-PER buffer (10 mL/g tissue) using ultrasound probe (Branson Digital Sonifier 450, Emerson, USA) at an amplitude of 30%, with cycles of 10 seconds on and 15 seconds off. Afterwards, they were centrifuged at 10000 rpm for 10 min. An aliquot was taken from each supernatant for total protein quantification. The remaining part was digested as described in previous procedure and prepared for ICP-MS measurement to determine the metal concentration.

Tumor volumes & body weights of mice for biodistribution					
	Mice	**C1556**	**C1561**	**C1570**	**AV ± SE**
Big tumors	Volume (mm^3)	27.78	18.51	23.15	23.15 ± 2.68
	Weight (g)	19.9	18.8	21.6	20.1 ± 0.81
	Mice	**C1568**	**C1573**	**C1574**	**AV ± SE**
Small tumors	Volume (mm^3)	54.16	55.28	64.71	58.05 ± 3.35
	Weight (g)	18.5	19.4	19.9	19.27 ± 0.41

Table 3.9 Average ± standard error (AV ± SE) for tumor volume (mm^3) and body weights (g) of mice for biodistribution.

Assessment of antitumor efficacy *in vivo.* The antitumor efficacy was evaluated against orthotopic intracerebral tumor-bearing C57BL/6J mice. A GL261 syngeneic tumor-bearing model was established as described in previous part of section 3.6. All animals included in the study were confirmed to have localized intracerebral tumors with homogeneous volume using MRI T_2 scanning as described in previous part of section 3.6. They were randomly divided into 3 groups: Control (untreated), PtBC, and Pt-Fe NCPs. All formulations were given at a dose of 1.5 mg Pt/kg weight via intranasal administration. Therapeutic agents were administered with different schedules, as follows (table 3.10):

Therapeutic Agent	*Starting day (p.i.)*	*Frequency of administration (days)*
PtBC or Pt-Fe NCPs	10	Every 6 days (IMS)
PtBC or Pt-Fe NCPs	10	Every 3 days
PtBC or Pt-Fe NCPs	6	Every 6 days (IMS)

Table 3.10 Summary of the administration schedules used in therapeutic assessment used for GL261 GB in this thesis.

Histological examination. Necropsy of chosen tolerability Pt-administered mice was performed by Unitat de Patologia Murina i Comparada (UPMiC, https://sct.uab.cat/upmic/es) and main findings can be found in Annex II.

3.7 References

(1) Chen, L.-J.; Yang, H.-B. Construction of Stimuli-Responsive Functional Materials Via Hierarchical Self-Assembly Involving Coordination Interactions. *Acc. Chem. Res.* **2018,** *51* (11), 2699-2710. DOI: 10.1021/acs.accounts.8b00317.
(2) Lin, W.; Rieter, W. J.; Taylor, K. M. L. Modular Synthesis of Functional Nanoscale Coordination Polymers. *Angew. Chem. Int. Ed.* **2009,** *48* (4), 650-658. DOI: 10.1002/anie.200803387.
(3) Spokoyny, A. M.; Kim, D.; Sumrein, A.; Mirkin, C. A. Infinite Coordination Polymer Nano- and Microparticle Structures. *Chem. Soc. Rev.* **2009,** *38* (5), 1218-1227. DOI: 10.1039/B807085G.
(4) Lee, H. J.; Cho, Y. J.; Cho, W.; Oh, M. Controlled Isotropic or Anisotropic Nanoscale Growth of Coordination Polymers: Formation of Hybrid Coordination Polymer Particles. *ACS Nano* **2013,** *7* (1), 491-499. DOI: 10.1021/nn304597h.
(5) Dang, S.; Zhu, Q.-L.; Xu, Q. Nanomaterials Derived from Metal–Organic Frameworks. *Nature Reviews Materials* **2017,** *3* (1), 17075. DOI: 10.1038/natrevmats.2017.75.
(6) Morsali, A.; Hashemi, L., Chapter Two - Nanoscale Coordination Polymers: Preparation, Function and Application. In *Adv. Inorg. Chem.*, Ruiz-Molina, D.; van Eldik, R., Eds. Academic Press: 2020; Vol. 76, pp 33-72. ISBN: 0898-8838.
(7) Sun, X.; Dong, S.; Wang, E. Coordination-Induced Formation of Submicrometer-Scale, Monodisperse, Spherical Colloids of Organic−Inorganic Hybrid Materials at Room Temperature. *J. Am. Chem. Soc.* **2005,** *127* (38), 13102-13103. DOI: 10.1021/ja0534809.
(8) Oh, M.; Mirkin, C. A. Chemically Tailorable Colloidal Particles from Infinite Coordination Polymers. *Nature* **2005,** *438* (7068), 651-654. DOI: 10.1038/nature04191.
(9) Zhu, W.; Zhao, J.; Chen, Q.; Liu, Z. Nanoscale Metal-Organic Frameworks and Coordination Polymers as Theranostic Platforms for Cancer Treatment. *Coord. Chem. Rev.* **2019,** *398*, 113009. DOI: 10.1016/j.ccr.2019.07.006.
(10) Novio, F. Design of Targeted Nanostructured Coordination Polymers (Ncps) for Cancer Therapy. *Molecules (Basel, Switzerland)* **2020,** *25* (15), 3449. DOI: 10.3390/molecules25153449.
(11) Jin, Q.; Zhu, W.; Jiang, D.; Zhang, R.; Kutyreff, C. J.; Engle, J. W.; Huang, P.; Cai, W.; Liu, Z.; Cheng, L. Ultra-Small Iron-Gallic Acid Coordination Polymer Nanoparticles for Chelator-Free Labeling of 64cu and Multimodal Imaging-Guided Photothermal Therapy. *Nanoscale* **2017,** *9* (34), 12609-12617. DOI: 10.1039/C7NR03086J.
(12) Chao, Y.; Liang, C.; Yang, Y.; Wang, G.; Maiti, D.; Tian, L.; Wang, F.; Pan, W.; Wu, S.; Yang, K.; Liu, Z. Highly Effective Radioisotope Cancer Therapy with a Non-Therapeutic Isotope Delivered and Sensitized by Nanoscale Coordination Polymers. *ACS Nano* **2018,** *12* (8), 7519-7528. DOI: 10.1021/acsnano.8b02400.
(13) Zhao, J.; Yang, Y.; Han, X.; Liang, C.; Liu, J.; Song, X.; Ge, Z.; Liu, Z. Redox-Sensitive Nanoscale Coordination Polymers for Drug Delivery and Cancer Theranostics. *ACS Appl. Mater. Interfaces* **2017,** *9* (28), 23555-23563. DOI: 10.1021/acsami.7b07535.
(14) Liu, J.; Chen, Q.; Zhu, W.; Yi, X.; Yang, Y.; Dong, Z.; Liu, Z. Nanoscale-Coordination-Polymer-Shelled Manganese Dioxide Composite Nanoparticles: A Multistage Redox/Ph/H2o2-Responsive Cancer Theranostic Nanoplatform. *Adv. Funct. Mater.* **2017,** *27* (10), 1605926. DOI: https://doi.org/10.1002/adfm.201605926.
(15) Suárez-García, S.; Solórzano, R.; Novio, F.; Alibés, R.; Busqué, F.; Ruiz-Molina, D. Coordination Polymers Nanoparticles for Bioimaging. *Coord. Chem. Rev.* **2020**, 213716. DOI: 10.1016/j.ccr.2020.213716.
(16) Liu, D.; Huxford, R. C.; Lin, W. Phosphorescent Nanoscale Coordination Polymers as Contrast Agents for Optical Imaging. *Angew. Chem. Int. Ed.* **2011,** *50* (16), 3696-3700. DOI: 10.1002/anie.201008277.
(17) Sun, C.-Y.; Qin, C.; Wang, C.-G.; Su, Z.-M.; Wang, S.; Wang, X.-L.; Yang, G.-S.; Shao, K.-Z.; Lan, Y.-Q.; Wang, E.-B. Chiral Nanoporous Metal-Organic Frameworks with High Porosity as Materials

for Drug Delivery. *Adv. Mater.* **2011,** *23* (47), 5629-5632. DOI: https://doi.org/10.1002/adma.201102538.
(18) Xing, L.; Cao, Y.; Che, S. Synthesis of Core–Shell Coordination Polymer Nanoparticles (Cpns) for Ph-Responsive Controlled Drug Release. *Chem. Commun.* **2012,** *48* (48), 5995-5997. DOI: 10.1039/C2CC30877K.
(19) Yang, Y.; Xu, L.; Zhu, W.; Feng, L.; Liu, J.; Chen, Q.; Dong, Z.; Zhao, J.; Liu, Z.; Chen, M. One-Pot Synthesis of Ph-Responsive Charge-Switchable Pegylated Nanoscale Coordination Polymers for Improved Cancer Therapy. *Biomaterials* **2018,** *156*, 121-133. DOI: 10.1016/j.biomaterials.2017.11.038.
(20) Hoang, V. L. T.; Foote, M. C.; Prow, T. W., Chapter 17 - the Potential for Metal Nanoparticle-Enhanced Radiotherapy in Dermatology. In *Nanoscience in Dermatology*, Hamblin, M. R.; Avci, P.; Prow, T. W., Eds. Academic Press: Boston, 2016; pp 217-227. ISBN: 978-0-12-802926-8.
(21) Estève, F.; Adam, J. F.; Biston, M. C.; Joubert, A.; Corde, S.; Boudou, C.; Rousseau, J.; Gastaldo, J.; Bencokova, Z.; Rousseau, J.; Charvet, A. M.; Foray, N.; Le Bas, J. F.; Balosso, J.; Elleaume, H. Cmr 2005: 3.07: High-Z Compounds for Synchrotron Stereotactic Radiotherapy: Developments and Perspectives. *Contrast Media & Molecular Imaging* **2006,** *1* (2), 60-60. DOI: https://doi.org/10.1002/cmmi.20.
(22) He, C.; Duan, X.; Guo, N.; Chan, C.; Poon, C.; Weichselbaum, R. R.; Lin, W. Core-Shell Nanoscale Coordination Polymers Combine Chemotherapy and Photodynamic Therapy to Potentiate Checkpoint Blockade Cancer Immunotherapy. *Nat. Commun.* **2016,** *7* (1), 12499. DOI: 10.1038/ncomms12499.
(23) Amorín-Ferré, L.; Busqué, F.; Bourdelande, J. L.; Ruiz-Molina, D.; Hernando, J.; Novio, F. Encapsulation and Release Mechanisms in Coordination Polymer Nanoparticles. *Chemistry – A European Journal* **2013,** *19* (51), 17508-17516. DOI: https://doi.org/10.1002/chem.201302662.
(24) Solórzano, R.; Tort, O.; García-Pardo, J.; Escribà, T.; Lorenzo, J.; Arnedo, M.; Ruiz-Molina, D.; Alibés, R.; Busqué, F.; Novio, F. Versatile Iron–Catechol-Based Nanoscale Coordination Polymers with Antiretroviral Ligand Functionalization and Their Use as Efficient Carriers in Hiv/Aids Therapy. *Biomaterials Science* **2019,** *7* (1), 178-186. DOI: 10.1039/C8BM01221K.
(25) Nador, F.; Novio, F.; Ruiz-Molina, D. Coordination Polymer Particles with Ligand-Centred Ph-Responses and Spin Transition. *Chem. Commun.* **2014,** *50* (93), 14570-14572. DOI: 10.1039/C4CC05299D.
(26) Adarsh, N. N.; Frias, C.; Ponnoth Lohidakshan, T. M.; Lorenzo, J.; Novio, F.; Garcia-Pardo, J.; Ruiz-Molina, D. Pt(Iv)-Based Nanoscale Coordination Polymers: Antitumor Activity, Cellular Uptake and Interactions with Nuclear DNA. *Chem. Eng. J.* **2018,** *340*, 94-102. DOI: 10.1016/j.cej.2018.01.058.
(27) Rieter, W. J.; Pott, K. M.; Taylor, K. M. L.; Lin, W. Nanoscale Coordination Polymers for Platinum-Based Anticancer Drug Delivery. *J. Am. Chem. Soc.* **2008,** *130* (35), 11584-11585. DOI: 10.1021/ja803383k.
(28) Huxford-Phillips, R. C.; Russell, S. R.; Liu, D.; Lin, W. Lipid-Coated Nanoscale Coordination Polymers for Targeted Cisplatin Delivery. *RSC Advances* **2013,** *3* (34), 14438-14443. DOI: 10.1039/C3RA42033G.
(29) Liu, D.; Poon, C.; Lu, K.; He, C.; Lin, W. Self-Assembled Nanoscale Coordination Polymers with Trigger Release Properties for Effective Anticancer Therapy. *Nat. Commun.* **2014,** *5*, 4182-4182. DOI: 10.1038/ncomms5182.
(30) Poon, C.; He, C.; Liu, D.; Lu, K.; Lin, W. Self-Assembled Nanoscale Coordination Polymers Carrying Oxaliplatin and Gemcitabine for Synergistic Combination Therapy of Pancreatic Cancer. *Journal of controlled release : official journal of the Controlled Release Society* **2015,** *201*, 90-99. DOI: 10.1016/j.jconrel.2015.01.026.
(31) Poon, C.; Duan, X.; Chan, C.; Han, W.; Lin, W. Nanoscale Coordination Polymers Codeliver Carboplatin and Gemcitabine for Highly Effective Treatment of Platinum-Resistant Ovarian Cancer. *Mol. Pharm.* **2016,** *13* (11), 3665-3675. DOI: 10.1021/acs.molpharmaceut.6b00466.

(32) He, C.; Liu, D.; Lin, W. Self-Assembled Nanoscale Coordination Polymers Carrying Sirnas and Cisplatin for Effective Treatment of Resistant Ovarian Cancer. *Biomaterials* **2015,** *36*, 124-133. DOI: 10.1016/j.biomaterials.2014.09.017.
(33) He, C.; Poon, C.; Chan, C.; Yamada, S. D.; Lin, W. Nanoscale Coordination Polymers Codeliver Chemotherapeutics and Sirnas to Eradicate Tumors of Cisplatin-Resistant Ovarian Cancer. *J. Am. Chem. Soc.* **2016,** *138* (18), 6010-6019. DOI: 10.1021/jacs.6b02486.
(34) Chan, C.; Guo, N.; Duan, X.; Han, W.; Xue, L.; Bryan, D.; Wightman, S. C.; Khodarev, N. N.; Weichselbaum, R. R.; Lin, W. Systemic Mirna Delivery by Nontoxic Nanoscale Coordination Polymers Limits Epithelial-to-Mesenchymal Transition and Suppresses Liver Metastases of Colorectal Cancer. *Biomaterials* **2019,** *210*, 94-104. DOI: 10.1016/j.biomaterials.2019.04.028.
(35) Duan, X.; Chan, C.; Han, W.; Guo, N.; Weichselbaum, R. R.; Lin, W. Immunostimulatory Nanomedicines Synergize with Checkpoint Blockade Immunotherapy to Eradicate Colorectal Tumors. *Nat. Commun.* **2019,** *10* (1), 1899. DOI: 10.1038/s41467-019-09221-x.
(36) Liu, J.; Wu, M.; Pan, Y.; Duan, Y.; Dong, Z.; Chao, Y.; Liu, Z.; Liu, B. Biodegradable Nanoscale Coordination Polymers for Targeted Tumor Combination Therapy with Oxidative Stress Amplification. *Adv. Funct. Mater.* **2020,** *30* (13), 1908865. DOI: https://doi.org/10.1002/adfm.201908865.
(37) Newcomb, E. W.; Zagzag, D., The Murine Gl261 Glioma Experimental Model to Assess Novel Brain Tumor Treatments. In *Cns Cancer: Models, Markers, Prognostic Factors, Targets, and Therapeutic Approaches*, Meir, E. G., Ed. Humana Press: Totowa, NJ, 2009; pp 227-241. ISBN: 978-1-60327-553-8.
(38) Cha, S.; Johnson, G.; Wadghiri, Y. Z.; Jin, O.; Babb, J.; Zagzag, D.; Turnbull, D. H. Dynamic, Contrast-Enhanced Perfusion Mri in Mouse Gliomas: Correlation with Histopathology. *Magn. Reson. Med.* **2003,** *49* (5), 848-855. DOI: https://doi.org/10.1002/mrm.10446.
(39) Delgado-Goñi, T.; Ortega-Martorell, S.; Ciezka, M.; Olier, I.; Candiota, A. P.; Julià-Sapé, M.; Fernández, F.; Pumarola, M.; Lisboa, P. J.; Arús, C. Mrsi-Based Molecular Imaging of Therapy Response to Temozolomide in Preclinical Glioblastoma Using Source Analysis. *NMR Biomed.* **2016,** *29* (6), 732-743. DOI: 10.1002/nbm.3521.
(40) Simões, R. V.; García-Martín, M. L.; Cerdán, S.; Arús, C. Perturbation of Mouse Glioma Mrs Pattern by Induced Acute Hyperglycemia. *NMR Biomed.* **2008,** *21* (3), 251-264. DOI: 10.1002/nbm.1188.
(41) Wu, S.; Calero-Pérez, P.; Villamañan, L.; Arias-Ramos, N.; Pumarola, M.; Ortega-Martorell, S.; Julià-Sapé, M.; Arús, C.; Candiota, A. P. Anti-Tumour Immune Response in Gl261 Glioblastoma Generated by Temozolomide Immune-Enhancing Metronomic Schedule Monitored with Mrsi-Based Nosological Images. *NMR Biomed.* **2020,** *33* (4), e4229. DOI: 10.1002/nbm.4229.
(42) Johnstone, T. C.; Lippard, S. J. Reinterpretation of the Vibrational Spectroscopy of the Medicinal Bioinorganic Synthon C,C,T-[Pt(Nh3)2cl2(Oh)2]. *J. Biol. Inorg. Chem.* **2014,** *19* (4-5), 667-674. DOI: 10.1007/s00775-014-1109-6.
(43) He, C.; Hu, Y.; Yin, L.; Tang, C.; Yin, C. Effects of Particle Size and Surface Charge on Cellular Uptake and Biodistribution of Polymeric Nanoparticles. *Biomaterials* **2010,** *31* (13), 3657-3666. DOI: 10.1016/j.biomaterials.2010.01.065.
(44) Gaumet, M.; Vargas, A.; Gurny, R.; Delie, F. Nanoparticles for Drug Delivery: The Need for Precision in Reporting Particle Size Parameters. *Eur. J. Pharm. Biopharm.* **2008,** *69* (1), 1-9. DOI: 10.1016/j.ejpb.2007.08.001.
(45) Masserini, M. Nanoparticles for Brain Drug Delivery. *ISRN Biochemistry* **2013,** *2013*, 238428. DOI: 10.1155/2013/238428.
(46) Abdel-Bar, H. M.; Abdel-Reheem, A. Y.; Awad, G. A.; Mortada, N. D. Evaluation of Brain Targeting and Mucosal Integrity of Nasally Administrated Nanostructured Carriers of a Cns Active Drug, Clonazepam. *J. Pharm. Pharm. Sci.* **2013,** *16* (3), 456-469. DOI: 10.18433/j30s31.
(47) Patel, R. B.; Patel, M. R.; Bhatt, K. K.; Patel, B. G.; Gaikwad, R. V. Evaluation of Brain Targeting Efficiency of Intranasal Microemulsion Containing Olanzapine: Pharmacodynamic and

Pharmacokinetic Consideration. *Drug Deliv.* **2016,** *23* (1), 307-315. DOI: 10.3109/10717544.2014.912694.
(48) Nour, S. A.; Abdelmalak, N. S.; Naguib, M. J.; Rashed, H. M.; Ibrahim, A. B. Intranasal Brain-Targeted Clonazepam Polymeric Micelles for Immediate Control of Status Epilepticus: *In Vitro* Optimization, e*x Vivo* Determination of Cytotoxicity, *in Vivo* Biodistribution and Pharmacodynamics Studies. *Drug Deliv.* **2016,** *23* (9), 3681-3695. DOI: 10.1080/10717544.2016.1223216.
(49) Zhang, F.; Sababi, M.; Brinck, T.; Persson, D.; Pan, J.; Claesson, P. M. In Situ Investigations of Fe3+ Induced Complexation of Adsorbed Mefp-1 Protein Film on Iron Substrate. *J. Colloid Interface Sci.* **2013,** *404*, 62-71. DOI: 10.1016/j.jcis.2013.05.016.
(50) Jo, D.-H.; Chiou, Y.-M.; Que, L. Models for Extradiol Cleaving Catechol Dioxygenases: Syntheses, Structures, and Reactivities of Iron(Ii)−Monoanionic Catecholate Complexes. *Inorg. Chem.* **2001,** *40* (13), 3181-3190. DOI: 10.1021/ic001185d.
(51) Suarez-Garcia, S.; Sedo, J.; Saiz-Poseu, J.; Ruiz-Molina, D. Copolymerization of a Catechol and a Diamine as a Versatile Polydopamine-Like Platform for Surface Functionalization: The Case of a Hydrophobic Coating. *Biomimetics (Basel, Switzerland)* **2017,** *2* (4). DOI: 10.3390/biomimetics2040022.
(52) Suárez-García, S.; Sedó, J.; Saiz-Poseu, J.; Ruiz-Molina, D. Copolymerization of a Catechol and a Diamine as a Versatile Polydopamine-Like Platform for Surface Functionalization: The Case of a Hydrophobic Coating. *Biomimetics* **2017,** *2* (4). DOI: 10.3390/biomimetics2040022.
(53) Patel, R. B.; Patel, M. R.; Bhatt, K. K.; Patel, B. G.; Gaikwad, R. V. Microemulsion-Based Drug Delivery System for Transnasal Delivery of Carbamazepine: Preliminary Brain-Targeting Study. *Drug Deliv.* **2016,** *23* (1), 207-213. DOI: 10.3109/10717544.2014.908980.
(54) Kumar, M.; Misra, A.; Mishra, A. K.; Mishra, P.; Pathak, K. Mucoadhesive Nanoemulsion-Based Intranasal Drug Delivery System of Olanzapine for Brain Targeting. *J. Drug Target.* **2008,** *16* (10), 806-814. DOI: 10.1080/10611860802476504.
(55) Portakal, Z. G.; Shermer, S.; Jenkins, C.; Spezi, E.; Perrett, T.; Tuncel, N.; Phillips, J. Design and Characterization of Tissue-Mimicking Gel Phantoms for Diffusion Kurtosis Imaging. *Med. Phys.* **2018,** *45* (6), 2476-2485. DOI: 10.1002/mp.12907.
(56) Borges, M.; Yu, S.; Laromaine, A.; Roig, A.; Suárez-García, S.; Lorenzo, J.; Ruiz-Molina, D.; Novio, F. Dual T1/T2 Mri Contrast Agent Based on Hybrid Spion@Coordination Polymer Nanoparticles. *RSC Advances* **2015,** *5* (105), 86779-86783. DOI: 10.1039/C5RA17661A.
(57) He, Z.; Zhang, P.; Xiao, Y.; Li, J.; Yang, F.; Liu, Y.; Zhang, J.-R.; Zhu, J.-J. Acid-Degradable Gadolinium-Based Nanoscale Coordination Polymer: A Potential Platform for Targeted Drug Delivery and Potential Magnetic Resonance Imaging. *Nano Research* **2018,** *11* (2), 929-939. DOI: 10.1007/s12274-017-1705-1.
(58) Han, K.; Zhang, W. Y.; Zhang, J.; Ma, Z. Y.; Han, H. Y. Ph-Responsive Nanoscale Coordination Polymer for Efficient Drug Delivery and Real-Time Release Monitoring. *Adv Healthc Mater* **2017,** *6* (19). DOI: 10.1002/adhm.201700470.
(59) Besford, Q. A.; Ju, Y.; Wang, T. Y.; Yun, G.; Cherepanov, P.; Hagemeyer, C. E.; Cavalieri, F.; Caruso, F. Self-Assembled Metal-Phenolic Networks on Emulsions as Low-Fouling and Ph-Responsive Particles. *Small* **2018,** *14* (39), e1802342. DOI: 10.1002/smll.201802342.
(60) Feng, L.; Gao, M.; Tao, D.; Chen, Q.; Wang, H.; Dong, Z.; Chen, M.; Liu, Z. Cisplatin-Prodrug-Constructed Liposomes as a Versatile Theranostic Nanoplatform for Bimodal Imaging Guided Combination Cancer Therapy. *Adv. Funct. Mater.* **2016,** *26* (13), 2207-2217. DOI: 10.1002/adfm.201504899.
(61) Wu, G.; Fang, Y. Z.; Yang, S.; Lupton, J. R.; Turner, N. D. Glutathione Metabolism and Its Implications for Health. *J. Nutr.* **2004,** *134* (3), 489-492. DOI: 10.1093/jn/134.3.489.
(62) Jeong, E. M.; Yoon, J.-H.; Lim, J.; Shin, J.-W.; Cho, A. Y.; Heo, J.; Lee, K. B.; Lee, J.-H.; Lee, W. J.; Kim, H.-J.; Son, Y. H.; Lee, S.-J.; Cho, S.-Y.; Shin, D.-M.; Choi, K.; Kim, I.-G. Real-Time Monitoring of Glutathione in Living Cells Reveals That High Glutathione Levels Are Required to Maintain Stem Cell Function. *Stem Cell Reports* **2018,** *10* (2), 600-614. DOI: 10.1016/j.stemcr.2017.12.007.

(63) Traverso, N.; Ricciarelli, R.; Nitti, M.; Marengo, B.; Furfaro, A. L.; Pronzato, M. A.; Marinari, U. M.; Domenicotti, C. Role of Glutathione in Cancer Progression and Chemoresistance. *Oxid. Med. Cell. Longev.* **2013,** *2013*, 972913. DOI: 10.1155/2013/972913.
(64) Shen, J.; Wang, Q.; Fang, J.; Shen, W.; Wu, D.; Tang, G.; Yang, J. Therapeutic Polymeric Nanomedicine: Gsh-Responsive Release Promotes Drug Release for Cancer Synergistic Chemotherapy. *RSC Advances* **2019,** *9* (64), 37232-37240. DOI: 10.1039/C9RA07051F.
(65) Gao, C.; Tang, F.; Zhang, J.; Lee, S. M. Y.; Wang, R. Glutathione-Responsive Nanoparticles Based on a Sodium Alginate Derivative for Selective Release of Doxorubicin in Tumor Cells. *Journal of Materials Chemistry B* **2017,** *5* (12), 2337-2346. DOI: 10.1039/C6TB03032G.
(66) Curcio, M.; Blanco-Fernández, B.; Costoya, A.; Concheiro, A.; Puoci, F.; Alvarez-Lorenzo, C. Glucose Cryoprotectant Affects Glutathione-Responsive Antitumor Drug Release from Polysaccharide Nanoparticles. *Eur. J. Pharm. Biopharm.* **2015,** *93*, 281-292. DOI: 10.1016/j.ejpb.2015.04.010.
(67) Ling, X.; Tu, J.; Wang, J.; Shajii, A.; Kong, N.; Feng, C.; Zhang, Y.; Yu, M.; Xie, T.; Bharwani, Z.; Aljaeid, B. M.; Shi, B.; Tao, W.; Farokhzad, O. C. Glutathione-Responsive Prodrug Nanoparticles for Effective Drug Delivery and Cancer Therapy. *ACS Nano* **2019,** *13* (1), 357-370. DOI: 10.1021/acsnano.8b06400.
(68) Tan, S.; Wang, G. Lung Cancer Targeted Therapy: Folate and Transferrin Dual Targeted, Glutathione Responsive Nanocarriers for the Delivery of Cisplatin. *Biomed. Pharmacother.* **2018,** *102*, 55-63. DOI: 10.1016/j.biopha.2018.03.046.
(69) Huang, H.; Dong, Y.; Zhang, Y.; Ru, D.; Wu, Z.; Zhang, J.; Shen, M.; Duan, Y.; Sun, Y. Gsh-Sensitive Pt(Iv) Prodrug-Loaded Phase-Transitional Nanoparticles with a Hybrid Lipid-Polymer Shell for Precise Theranostics against Ovarian Cancer. *Theranostics* **2019,** *9* (4), 1047-1065. DOI: 10.7150/thno.29820.
(70) Shukla, D.; Mandal, P. K.; Tripathi, M.; Vishwakarma, G.; Mishra, R.; Sandal, K. Quantitation of *in Vivo* Brain Glutathione Conformers in Cingulate Cortex among Age-Matched Control, Mci, and Ad Patients Using Mega-Press. *Hum. Brain Mapp.* **2020,** *41* (1), 194-217. DOI: 10.1002/hbm.24799.
(71) Mao, X. M.; Si, J. X.; Huang, Q.; Sun, X. R.; Zhang, Q. Z.; Shen, Y. Q.; Tang, J. B.; Liu, X. R.; Sui, M. H. Self-Assembling Doxorubicin Prodrug Forming Nanoparticles and Effectively Reversing Drug Resistance *in Vitro* and *in Vivo*. *Adv. Healthc. Mater.* **2016,** *5* (19), 2517-2527. DOI: 10.1002/adhm.201600345.
(72) Liu, Z.; Wang, M.; Wang, H.; Fang, L.; Gou, S. Platinum-Based Modification of Styrylbenzylsulfones as Multifunctional Antitumor Agents: Targeting the Ras/Raf Pathway, Enhancing Antitumor Activity, and Overcoming Multidrug Resistance. *J. Med. Chem.* **2020,** *63* (1), 186-204. DOI: 10.1021/acs.jmedchem.9b01223.
(73) Mahmoudi, M.; Laurent, S.; Shokrgozar, M. A.; Hosseinkhani, M. Toxicity Evaluations of Superparamagnetic Iron Oxide Nanoparticles: Cell "Vision" Versus Physicochemical Properties of Nanoparticles. *Acs Nano* **2011,** *5* (9), 7263-7276. DOI: 10.1021/nn2021088.
(74) Nair, P. K. R.; Melnick, S. J.; Wnuk, S. F.; Rapp, M.; Escalon, E.; Ramachandran, C. Isolation and Characterization of an Anticancer Catechol Compound from Semecarpus Anacardium. *J. Ethnopharmacol.* **2009,** *122* (3), 450-456. DOI: 10.1016/j.jep.2009.02.001.
(75) Bao, X.-Z.; Dai, F.; Wang, Q.; Jin, X.-L.; Zhou, B. Developing Glutathione-Activated Catechol-Type Diphenylpolyenes as Small Molecule-Based and Mitochondria-Targeted Prooxidative Anticancer Theranostic Prodrugs. *Free Radic. Biol. Med.* **2019,** *134*, 406-418. DOI: 10.1016/j.freeradbiomed.2019.01.033.
(76) Kumar, N.; Goel, N. Phenolic Acids: Natural Versatile Molecules with Promising Therapeutic Applications. *Biotechnology Reports* **2019,** *24*, e00370. DOI: 10.1016/j.btre.2019.e00370.
(77) Forooshani, P. K.; Meng, H.; Lee, B. P., Catechol Redox Reaction: Reactive Oxygen Species Generation, Regulation, and Biomedical Applications. In *Advances in Bioinspired and Biomedical Materials Volume 1*, American Chemical Society: 2017; Vol. 1252, pp 179-196. ISBN: 9780841232204.

(78) Zhang, Z.; He, X.; Zhou, C.; Reaume, M.; Wu, M.; Liu, B.; Lee, B. P. Iron Magnetic Nanoparticle-Induced Ros Generation from Catechol-Containing Microgel for Environmental and Biomedical Applications. *ACS Appl. Mater. Interfaces* **2020,** *12* (19), 21210-21220. DOI: 10.1021/acsami.9b19726.
(79) Aroui, S.; Dardevet, L.; Ajmia, W. B.; de Boisvilliers, M.; Perrin, F.; Laajimi, A.; Boumendjel, A.; Kenani, A.; Muller, J. M.; De Waard, M. A Novel Platinum–Maurocalcine Conjugate Induces Apoptosis of Human Glioblastoma Cells by Acting through the Ros-Erk/Akt-P53 Pathway. *Mol. Pharm.* **2015,** *12* (12), 4336-4348. DOI: 10.1021/acs.molpharmaceut.5b00531.
(80) Eruslanov, E.; Kusmartsev, S. Identification of Ros Using Oxidized Dcfda and Flow-Cytometry. *Methods Mol. Biol.* **2010,** *594*, 57-72. DOI: 10.1007/978-1-60761-411-1_4.
(81) Montero, A. J.; Jassem, J. Cellular Redox Pathways as a Therapeutic Target in the Treatment of Cancer. *Drugs* **2011,** *71* (11), 1385-1396. DOI: 10.2165/11592590-000000000-00000.
(82) Sharma, S. S.; Dietz, K.-J. The Relationship between Metal Toxicity and Cellular Redox Imbalance. *Trends Plant Sci.* **2009,** *14* (1), 43-50. DOI: 10.1016/j.tplants.2008.10.007.
(83) Zhang, P.; Sadler, P. J. Redox-Active Metal Complexes for Anticancer Therapy. *Eur. J. Inorg. Chem.* **2017,** *2017* (12), 1541-1548. DOI: 10.1002/ejic.201600908.
(84) Calandrini, V.; Arnesano, F.; Galliani, A.; Nguyen, T. H.; Ippoliti, E.; Carloni, P.; Natile, G. Platination of the Copper Transporter Atp7a Involved in Anticancer Drug Resistance. *Dalton Transactions* **2014,** *43* (31), 12085-12094. DOI: 10.1039/C4DT01339E.
(85) Volckova, E.; Dudones, L. P.; Bose, R. N. Hplc Determination of Binding of Cisplatin to DNA in the Presence of Biological Thiols: Implications of Dominant Platinum-Thiol Binding to Its Anticancer Action. *Pharm. Res.* **2002,** *19* (2), 124-131. DOI: 10.1023/a:1014268729658.
(86) Knipp, M. Metallothioneins and Platinum(Ii) Anti-Tumor Compounds. *Curr. Med. Chem.* **2009,** *16* (5), 522-537. DOI: 10.2174/092986709787458452.
(87) Blanco, E.; Shen, H.; Ferrari, M. Principles of Nanoparticle Design for Overcoming Biological Barriers to Drug Delivery. *Nat. Biotechnol.* **2015,** *33* (9), 941-951. DOI: 10.1038/nbt.3330.
(88) Manz, D. H.; Blanchette, N. L.; Paul, B. T.; Torti, F. M.; Torti, S. V. Iron and Cancer: Recent Insights. *Ann. N. Y. Acad. Sci.* **2016,** *1368* (1), 149-161. DOI: 10.1111/nyas.13008.
(89) Voth, B.; Nagasawa, D. T.; Pelargos, P. E.; Chung, L. K.; Ung, N.; Gopen, Q.; Tenn, S.; Kamei, D. T.; Yang, I. Transferrin Receptors and Glioblastoma Multiforme: Current Findings and Potential for Treatment. *J. Clin. Neurosci.* **2015,** *22* (7), 1071-1076. DOI: 10.1016/j.jocn.2015.02.002.
(90) D'Angelo, M. A.; Hetzer, M. W. Structure, Dynamics and Function of Nuclear Pore Complexes. *Trends Cell Biol.* **2008,** *18* (10), 456-466. DOI: 10.1016/j.tcb.2008.07.009.
(91) Puskas, J. E.; Chen, Y.; Kulbaba, K.; Kaszas, G. Comparison of the Molecular Weight and Size Measurement of Polyisobutylenes by Size Exclusion Chromatography/Multi-Angle Laser Light Scattering and Viscometry. *J. Polym. Sci., Part A: Polym. Chem.* **2006,** *44* (5), 1777-1783. DOI: https://doi.org/10.1002/pola.21272.
(92) Paine, P. L.; Moore, L. C.; Horowitz, S. B. Nuclear Envelope Permeability. *Nature* **1975,** *254* (5496), 109-114. DOI: 10.1038/254109a0.
(93) Keminer, O.; Peters, R. Permeability of Single Nuclear Pores. *Biophys. J.* **1999,** *77* (1), 217-228. DOI: 10.1016/S0006-3495(99)76883-9.
(94) Kroemer, G.; El-Deiry, W. S.; Golstein, P.; Peter, M. E.; Vaux, D.; Vandenabeele, P.; Zhivotovsky, B.; Blagosklonny, M. V.; Malorni, W.; Knight, R. A.; Piacentini, M.; Nagata, S.; Melino, G. Classification of Cell Death: Recommendations of the Nomenclature Committee on Cell Death. *Cell Death Differ.* **2005,** *12* (2), 1463-1467. DOI: 10.1038/sj.cdd.4401724.
(95) Ganipineni, L. P.; Danhier, F.; Préat, V. Drug Delivery Challenges and Future of Chemotherapeutic Nanomedicine for Glioblastoma Treatment. *J. Control. Release* **2018,** *281*, 42-57. DOI: 10.1016/j.jconrel.2018.05.008.
(96) Candolfi, M.; Curtin, J. F.; Nichols, W. S.; Muhammad, A. G.; King, G. D.; Pluhar, G. E.; McNiel, E. A.; Ohlfest, J. R.; Freese, A. B.; Moore, P. F.; Lerner, J.; Lowenstein, P. R.; Castro, M. G. Intracranial Glioblastoma Models in Preclinical Neuro-Oncology: Neuropathological

Characterization and Tumor Progression. *J. Neurooncol.* **2007,** *85* (2), 133-148. DOI: 10.1007/s11060-007-9400-9.
(97) Robertson, F. L.; Marqués-Torrejón, M.-A.; Morrison, G. M.; Pollard, S. M. Experimental Models and Tools to Tackle Glioblastoma. *Disease Models & Mechanisms* **2019,** *12* (9), dmm040386. DOI: 10.1242/dmm.040386.
(98) Huszthy, P. C.; Daphu, I.; Niclou, S. P.; Stieber, D.; Nigro, J. M.; Sakariassen, P. Ø.; Miletic, H.; Thorsen, F.; Bjerkvig, R. *In Vivo* Models of Primary Brain Tumors: Pitfalls and Perspectives. *Neuro Oncol.* **2012,** *14* (8), 979-993. DOI: 10.1093/neuonc/nos135.
(99) Kijima, N.; Kanemura, Y., Mouse Models of Glioblastoma. In *Glioblastoma*, De Vleeschouwer, S., Ed. Codon Publications

Copyright: The Authors.: Brisbane (AU), 2017. ISBN.
(100) Shader, R. I. Safety Versus Tolerability. *Clin. Ther.* **2018,** *40* (5), 672-673. DOI: 10.1016/j.clinthera.2018.04.003.
(101) Fox, J.; Barthold, S.; Davisson, M.; Newcomer, C.; Quimby, F.; Smith, A., *The Mouse in Biomedical Research*. UK: Academic Press: 2007. ISBN: 9780123694546.
(102) Gustafson, H. H.; Holt-Casper, D.; Grainger, D. W.; Ghandehari, H. Nanoparticle Uptake: The Phagocyte Problem. *Nano Today* **2015,** *10* (4), 487-510. DOI: 10.1016/j.nantod.2015.06.006.
(103) Feng, Q.; Liu, Y.; Huang, J.; Chen, K.; Huang, J.; Xiao, K. Uptake, Distribution, Clearance, and Toxicity of Iron Oxide Nanoparticles with Different Sizes and Coatings. *Sci. Rep.* **2018,** *8* (1), 2082. DOI: 10.1038/s41598-018-19628-z.
(104) Arami, H.; Khandhar, A.; Liggitt, D.; Krishnan, K. M. *In Vivo* Delivery, Pharmacokinetics, Biodistribution and Toxicity of Iron Oxide Nanoparticles. *Chem. Soc. Rev.* **2015,** *44* (23), 8576-8607. DOI: 10.1039/C5CS00541H.
(105) Oh, T.; Fakurnejad, S.; Sayegh, E. T.; Clark, A. J.; Ivan, M. E.; Sun, M. Z.; Safaee, M.; Bloch, O.; James, C. D.; Parsa, A. T. Immunocompetent Murine Models for the Study of Glioblastoma Immunotherapy. *J. Transl. Med.* **2014,** *12* (1), 107. DOI: 10.1186/1479-5876-12-107.
(106) Guerin, M. V.; Finisguerra, V.; Van den Eynde, B. J.; Bercovici, N.; Trautmann, A. Preclinical Murine Tumor Models: A Structural and Functional Perspective. *eLife* **2020,** *9*. DOI: 10.7554/eLife.50740.
(107) Zeng, X.; Sun, J.; Li, S.; Shi, J.; Gao, H.; Sun Leong, W.; Wu, Y.; Li, M.; Liu, C.; Li, P.; Kong, J.; Wu, Y.-Z.; Nie, G.; Fu, Y.; Zhang, G. Blood-Triggered Generation of Platinum Nanoparticle Functions as an Anti-Cancer Agent. *Nat. Commun.* **2020,** *11* (1), 567. DOI: 10.1038/s41467-019-14131-z.
(108) Yin, P.; Li, H.; Ke, C.; Cao, G.; Xin, X.; Hu, J.; Cai, X.; Li, L.; Liu, X.; Du, B. Intranasal Delivery of Immunotherapeutic Nanoformulations for Treatment of Glioma through in Situ Activation of Immune Response. *Int J Nanomedicine* **2020,** *15*, 1499-1515. DOI: 10.2147/ijn.s240551.
(109) Jackson, C. M.; Choi, J.; Lim, M. Mechanisms of Immunotherapy Resistance: Lessons from Glioblastoma. *Nat. Immunol.* **2019,** *20* (9), 1100-1109. DOI: 10.1038/s41590-019-0433-y.
(110) Wu, S.; Calero-Pérez, P.; Villamañan, L.; Arias-Ramos, N.; Pumarola, M.; Ortega-Martorell, S.; Julià-Sapé, M.; Arús, C.; Candiota, A. P. Anti-Tumour Immune Response in Gl261 Glioblastoma Generated by Temozolomide Immune-Enhancing Metronomic Schedule Monitored with Mrsi-Based Nosological Images. *NMR Biomed.* **2020,** *33* (4), e4229. DOI: 10.1002/nbm.4229.
(111) Karman, J.; Ling, C.; Sandor, M.; Fabry, Z. Initiation of Immune Responses in Brain Is Promoted by Local Dendritic Cells. *J. Immunol.* **2004,** *173* (4), 2353-2361. DOI: 10.4049/jimmunol.173.4.2353.
(112) Arias-Ramos, N.; Ferrer-Font, L.; Lope-Piedrafita, S.; Mocioiu, V.; Julià-Sapé, M.; Pumarola, M.; Arús, C.; Candiota, A. P. Metabolomics of Therapy Response in Preclinical Glioblastoma: A Multi-Slice Mrsi-Based Volumetric Analysis for Noninvasive Assessment of Temozolomide Treatment. *Metabolites* **2017,** *7* (2). DOI: 10.3390/metabo7020020.

(113) Wu, J.; Waxman, D. J. Immunogenic Chemotherapy: Dose and Schedule Dependence and Combination with Immunotherapy. *Cancer Lett.* **2018,** *419*, 210-221. DOI: 10.1016/j.canlet.2018.01.050.
(114) Hato, S. V.; Khong, A.; de Vries, I. J.; Lesterhuis, W. J. Molecular Pathways: The Immunogenic Effects of Platinum-Based Chemotherapeutics. *Clin. Cancer Res.* **2014,** *20* (11), 2831-2837. DOI: 10.1158/1078-0432.ccr-13-3141.
(115) Roberts, N. B.; Wadajkar, A. S.; Winkles, J. A.; Davila, E.; Kim, A. J.; Woodworth, G. F. Repurposing Platinum-Based Chemotherapies for Multi-Modal Treatment of Glioblastoma. *Oncoimmunology* **2016,** *5* (9), e1208876. DOI: 10.1080/2162402x.2016.1208876.
(116) Wang, Y.; Fan, X.; Wu, X. Ganoderma Lucidum Polysaccharide (Glp) Enhances Antitumor Immune Response by Regulating Differentiation and Inhibition of Mdscs Via a Card9-Nf-Kb-Ido Pathway. *Biosci. Rep.* **2020,** *40* (6), BSR20201170. DOI: 10.1042/BSR20201170.
(117) Qi, X.; Xu, W.; Xie, J.; Wang, Y.; Han, S.; Wei, Z.; Ni, Y.; Dong, Y.; Han, W. Metformin Sensitizes the Response of Oral Squamous Cell Carcinoma to Cisplatin Treatment through Inhibition of Nf-Kb/Hif-1α Signal Axis. *Sci. Rep.* **2016,** *6*, 35788-35788. DOI: 10.1038/srep35788.
(118) Miura, Y.; Takenaka, T.; Toh, K.; Wu, S.; Nishihara, H.; Kano, M. R.; Ino, Y.; Nomoto, T.; Matsumoto, Y.; Koyama, H.; Cabral, H.; Nishiyama, N.; Kataoka, K. Cyclic Rgd-Linked Polymeric Micelles for Targeted Delivery of Platinum Anticancer Drugs to Glioblastoma through the Blood-Brain Tumor Barrier. *Acs Nano* **2013,** *7* (10), 8583-8592. DOI: 10.1021/nn402662d.
(119) Wu, S.; Calero-Pérez, P.; Arús, C.; Candiota, A. P. Anti-Pd-1 Immunotherapy in Preclinical Gl261 Glioblastoma: Influence of Therapeutic Parameters and Non-Invasive Response Biomarker Assessment with Mrsi-Based Approaches. *Int J Mol Sci* **2020,** *21* (22). DOI: 10.3390/ijms21228775.
(120) Wu, J.; Waxman, D. J. Metronomic Cyclophosphamide Eradicates Large Implanted Gl261 Gliomas by Activating Antitumor Cd8(+) T-Cell Responses and Immune Memory. *Oncoimmunology* **2015,** *4* (4), e1005521. DOI: 10.1080/2162402x.2015.1005521.
(121) Staedtke, V.; Bai, R.-Y.; Laterra, J. Investigational New Drugs for Brain Cancer. *Expert Opin Investig Drugs* **2016,** *25* (8), 937-956. DOI: 10.1080/13543784.2016.1182497.
(122) Yadavalli, S.; Yenugonda, V. M.; Kesari, S. Repurposed Drugs in Treating Glioblastoma Multiforme: Clinical Trials Update. *Cancer J.* **2019,** *25* (2), 139-146. DOI: 10.1097/ppo.0000000000000365.
(123) Wang, Y.; Kong, X.; Guo, Y.; Wang, R.; Ma, W. Continuous Dose-Intense Temozolomide and Cisplatin in Recurrent Glioblastoma Patients. *Medicine (Baltimore)* **2017,** *96* (10), e6261. DOI: 10.1097/md.0000000000006261.
(124) Silvani, A.; Eoli, M.; Salmaggi, A.; Lamperti, E.; Maccagnano, E.; Broggi, G.; Boiardi, A. Phase Ii Trial of Cisplatin Plus Temozolomide, in Recurrent and Progressive Malignant Glioma Patients. *J. Neurooncol.* **2004,** *66* (1-2), 203-208. DOI: 10.1023/b:neon.0000013479.64348.69.
(125) Brandes, A. A.; Basso, U.; Reni, M.; Vastola, F.; Tosoni, A.; Cavallo, G.; Scopece, L.; Ferreri, A. J.; Panucci, M. G.; Monfardini, S.; Ermani, M. First-Line Chemotherapy with Cisplatin Plus Fractionated Temozolomide in Recurrent Glioblastoma Multiforme: A Phase Ii Study of the Gruppo Italiano Cooperativo Di Neuro-Oncologia. *J. Clin. Oncol.* **2004,** *22* (9), 1598-1604. DOI: 10.1200/jco.2004.11.019.
(126) Koo, T. R.; Moon, S. H.; Lim, Y. J.; Kim, J. Y.; Kim, Y.; Kim, T. H.; Cho, K. H.; Han, J.-Y.; Lee, Y. J.; Yun, T.; Kim, H. T.; Lee, J. S. The Effect of Tumor Volume and Its Change on Survival in Stage Iii Non-Small Cell Lung Cancer Treated with Definitive Concurrent Chemoradiotherapy. *Radiation Oncology* **2014,** *9* (1), 283. DOI: 10.1186/s13014-014-0283-6.
(127) Ahlawat, P.; Rawat, S.; Kakria, A.; Pal, M.; Chauhan, D.; Tandon, S.; Jain, S. Tumour Volumes: Predictors of Early Treatment Response in Locally Advanced Head and Neck Cancers Treated with Definitive Chemoradiation. *Rep Pract Oncol Radiother* **2016,** *21* (5), 419-426. DOI: 10.1016/j.rpor.2016.04.002.
(128) van Tellingen, O.; Yetkin-Arik, B.; de Gooijer, M. C.; Wesseling, P.; Wurdinger, T.; de Vries, H. E. Overcoming the Blood-Brain Tumor Barrier for Effective Glioblastoma Treatment. *Drug*

resistance updates : reviews and commentaries in antimicrobial and anticancer chemotherapy **2015,** *19*, 1-12. DOI: 10.1016/j.drup.2015.02.002.
(129) Shergalis, A.; Bankhead, A.; Luesakul, U.; Muangsin, N.; Neamati, N. Current Challenges and Opportunities in Treating Glioblastoma. *Pharmacol. Rev.* **2018,** *70* (3), 412. DOI: 10.1124/pr.117.014944.
(130) Ebrahimi Shahmabadi, H.; Movahedi, F.; Koohi Moftakhari Esfahani, M.; Alavi, S. E.; Eslamifar, A.; Mohammadi Anaraki, G.; Akbarzadeh, A. Efficacy of Cisplatin-Loaded Polybutyl Cyanoacrylate Nanoparticles on the Glioblastoma. *Tumour Biol.* **2014,** *35* (5), 4799-4806. DOI: 10.1007/s13277-014-1630-9.
(131) Thanasupawat, T.; Bergen, H.; Hombach-Klonisch, S.; Krcek, J.; Ghavami, S.; Del Bigio, M. R.; Krawitz, S.; Stelmack, G.; Halayko, A.; McDougall, M.; Meier, M.; Stetefeld, J.; Klonisch, T. Platinum (Iv) Coiled Coil Nanotubes Selectively Kill Human Glioblastoma Cells. *Nanomedicine-Nanotechnology Biology and Medicine* **2015,** *11* (4), 913-925. DOI: 10.1016/j.nano.2015.01.014.
(132) Karachi, A.; Yang, C.; Dastmalchi, F.; Sayour, E. J.; Huang, J.; Azari, H.; Long, Y.; Flores, C.; Mitchell, D. A.; Rahman, M. Modulation of Temozolomide Dose Differentially Affects T-Cell Response to Immune Checkpoint Inhibition. *Neuro Oncol.* **2019,** *21* (6), 730-741. DOI: 10.1093/neuonc/noz015.
(133) Enríquez Pérez, J.; Fritzell, S.; Kopecky, J.; Visse, E.; Darabi, A.; Siesjö, P. The Effect of Locally Delivered Cisplatin Is Dependent on an Intact Immune Function in an Experimental Glioma Model. *Sci. Rep.* **2019,** *9* (1), 5632. DOI: 10.1038/s41598-019-42001-7.
(134) Candiota, A. P.; Acosta, M.; Simões, R. V.; Delgado-Goñi, T.; Lope-Piedrafita, S.; Irure, A.; Marradi, M.; Bomati-Miguel, O.; Miguel-Sancho, N.; Abasolo, I.; Schwartz, S., Jr.; Santamaria, J.; Penadés, S.; Arús, C. A New Ex Vivo Method to Evaluate the Performance of Candidate Mri Contrast Agents: A Proof-of-Concept Study. *Journal of nanobiotechnology* **2014,** *12*, 12. DOI: 10.1186/1477-3155-12-12.
(135) Suárez-García, S.; Arias-Ramos, N.; Frias, C.; Candiota, A. P.; Arús, C.; Lorenzo, J.; Ruiz-Molina, D.; Novio, F. Dual T(1)/ T(2) Nanoscale Coordination Polymers as Novel Contrast Agents for Mri: A Preclinical Study for Brain Tumor. *ACS Appl Mater Interfaces* **2018,** *10* (45), 38819-38832. DOI: 10.1021/acsami.8b15594.
(136) Shuang, W. When Oncology Meets Immunology: Improving Gl261 Glioblastoma Treatment through Cancer-Related Immunity and Mrsi-Based Non-Invasive Follow-up of Response. Universitat Autònoma de Barcelona, 2020. ISBN: N/A.
(137) Garofalo, S.; D'Alessandro, G.; Chece, G.; Brau, F.; Maggi, L.; Rosa, A.; Porzia, A.; Mainiero, F.; Esposito, V.; Lauro, C.; Benigni, G.; Bernardini, G.; Santoni, A.; Limatola, C. Enriched Environment Reduces Glioma Growth through Immune and Non-Immune Mechanisms in Mice. *Nat. Commun.* **2015,** *6* (1), 6623. DOI: 10.1038/ncomms7623.
(138) Ferrer-Font, L. Tuning Response to Therapy in Preclinical Gl261 Glioblastoma through Ck2 Targeting and Temozolomide Metronomic Approaches: Non-Invasive Assessment with Mri and Mrsi-Based Molecular Imaging Strategies. Universitat Autònoma de Barcelona, 2017. ISBN: 9788449069857.
(139) Saldaña-Ruíz, S.; Soler-Martín, C.; Llorens, J. Role of Cyp2e1-Mediated Metabolism in the Acute and Vestibular Toxicities of Nineteen Nitriles in the Mouse. *Toxicol. Lett.* **2012,** *208* (2), 125-132. DOI: 10.1016/j.toxlet.2011.10.016.
(140) Robinson, S.; Chapman, K.; Hudson, S.; Sparrow, S.; Spencer-Briggs, D.; Danks, A.; Hill, R.; Everett, D.; Mulier, B.; Old, S. Guidance on Dose Level Selection for Regulatory General Toxicology Studies for Pharmaceuticals. *London: NC3Rs/LASA* **2009**. DOI: N/A.

Chapter 4

Development of nanoscale polymeric particles for glioblastoma treatment based on Pt(IV) prodrug

In this chapter, the state of the art related to polymeric nanoparticles in biomedical application is presented first (section 4.1). Specifically, in section 4.2 examples of catechol-based polymeric NPs is demonstrated in terms of synthetic methodology and therapeutic evaluation for glioblastoma treatment. The rest of this chapter is devoted to develop a novel polymeric nanoparticle based on the Pt(IV) prodrug, and to evaluate the anticancer activity of resulting polymeric NPs *in vitro* and *in vivo*.

4.1 Polymeric nanoparticles as drug delivery systems

Polymeric nanoparticles are one of the most studied organic nanomaterials which are sub-micron (1-1000 nm) solid colloidal particles made from polymers of natural or synthetic origin, comprising active molecules encapsulated or adsorbed or conjugated.[1] Depending on the demand, the loaded therapeutic agents could be hydrophilic or lipophilic, small molecules or macromolecular drugs, even a combination of them. Generally, polymeric NPs have been classified into two forms according to the distribution of the payloads inside: nanospheres and nanocapsules. In nanospheres, the drug is evenly distributed in the polymeric matrix; whereas the drug is enriched in the core surrounded by a drug-poor outer polymeric layer in nanocapsules.[2] In a broader context, more nanocarriers can also be regarded as polymeric NPs (Figure 4.1), including polymeric micelles, dendrimers, drug-polymer conjugates, and even nanogels.[2-3]

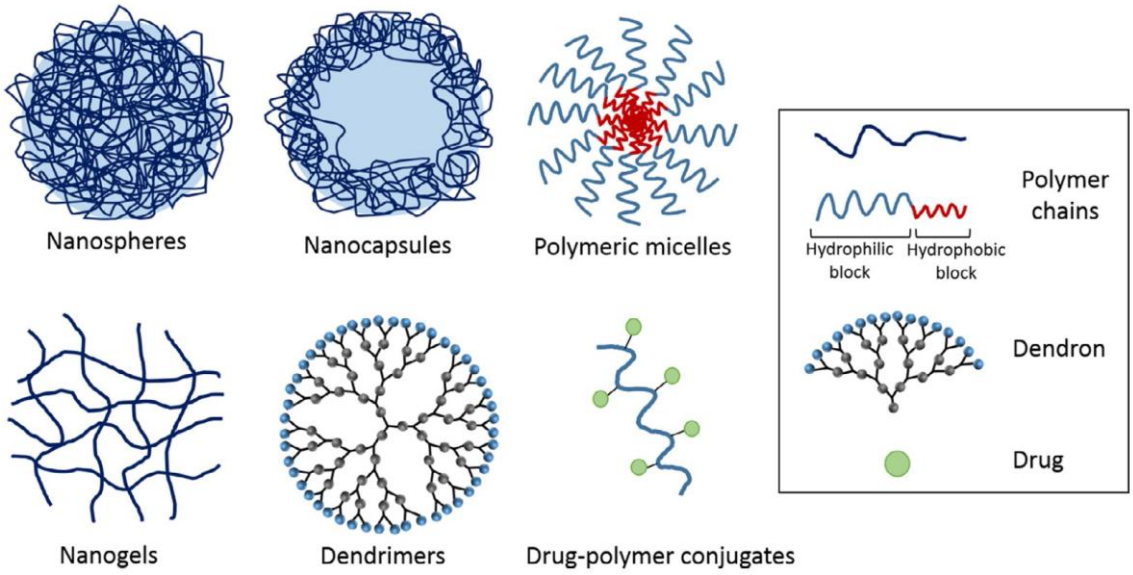

Figure 4.1 Polymeric nanocarriers for drug delivery, adapted from reference 2.

The main reasons or advantages of using polymeric NPs include the following: (1) protect the payloads from degradation, for instance, proteins, nucleic acids, among others; (2) realize controlled release of the cargos into desired sites; and (3) enable functionalization of the surfaces for targeting delivery with ligands or for stealth in blood stream.[4] Specifically, the majority of payloads is protected inside the polymeric NPs from possible degradation by enzymes or other substances influencing their stability, thus

increasing the effective drug concentration at the action site.[5] Due to the EPR effect, the polymeric NPs can passively target the tumor tissues thus enhance the accumulation of loaded drug in the tumors. Besides, the polymeric NPs are usually designed to provide either controlled release or triggered release of the cargos to increase the specificity and selectivity for targeting sites and reduce possible side effects.[6] The polymeric NPs commonly possess a relative longer residence in blood circulation by surface modification of stealthy polymers (e.g., PEG), which improve the circulation half-lives of the cargos in comparison to free molecules. To target the desired tissues, the surfaces of polymeric NPs can be decorated with targeting ligands (peptide, aptamer, antibody/antibody fragment, small molecules).[7]

A huge variety of polymers has been adopted for the fabrication of such polymeric nanocarriers, including both natural or synthetic polymers. However, the biosafety of these polymers is crucial for the drug delivery system, especially for drug delivery into the CNS. Therefore, the polymers used should be biodegradable and biocompatible, and the products from degradation must also be nontoxic and should be easily cleared from the body.[1,7] Currently, the frequently studied natural polymers include chitosan, alginate, gelatin, dextran, and albumin. In contrary, the widely used synthetic polymers include PEG, poly(lactide-co-glycolide) (PLGA), poly(lactide) (PLA), polyethyleneimine (PEI), poly(cyanoacrylates) (PCA), and polycaprolactone (PCL).[1,6-7] Although not all of these polymers have been approved by FDA, they have been found to be nontoxic in many studies.

Generally, there are two approaches to fabricate polymeric NPs: “top-down” and “bottom-up” methods. In the top-down approach, polymeric NPs are produced from preformed polymers, whereas in the bottom-up method the formation of polymeric NPs result from the polymerization of monomers.[8] The selection of preparation method depends on the nature of the polymers used, the purpose of application, the control of particle properties, and so on. On the methods, there are many excellent reviews already which will not be stated more here.[9-10]

4.2 Catechol-based polymeric nanoparticles for GB therapy

Catechols can be found in a vast host of natural compounds due to their physicochemical versatility. Catechol derivatives feature the presence of the basic catechol structure, o-dihydroxybenzene, comprising an aromatic moiety with two neighboring (ortho-) hydroxyl groups. Catechol derivatives, together with polyphenols, have become a hot research topic in recent decades, largely due to their antioxidant and anti-inflammatory activities. For instance, (−)-epigallocatechin-3-gallate (EGCG), quercetin, curcumin, resveratrol, chrysin, baicalein, luteolin, honokiol and silibinin are typical catechol derivatives (Figure 4.2) being actively investigated for their bioactive effects.

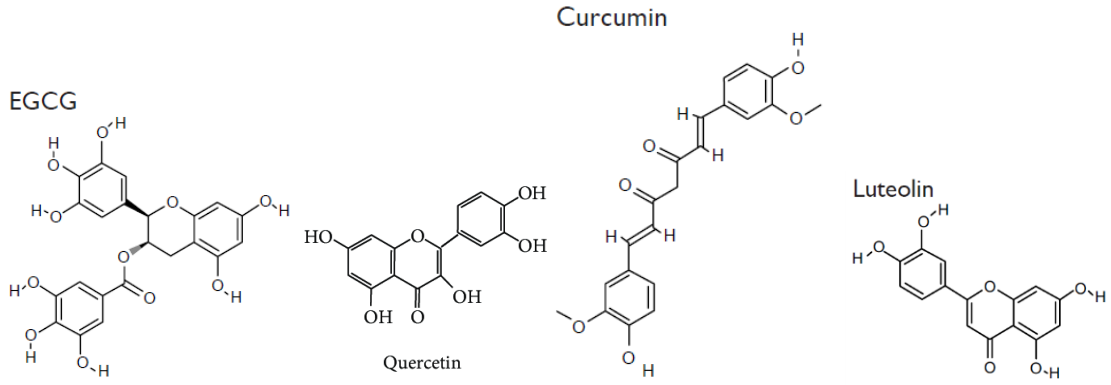

Figure 4.2 Chemical structures of typical catechol derivatives.

The potential therapeutic effects of catechol derivatives are constructed on their structural properties, for example the presence of catechol rings, and variable hydroxylation patterns, which endow them capability for metal-chelating, estrogen-like, fibril-disassembly, enzyme-binding, pro- and anti-oxidative properties.[11] Apart from the structural benefits, the unique functions of catechol family greatly arise from their redox chemical properties. Research implies that the cytotoxic and proapoptotic effects are attributed to their pro-oxidant activity, while their antioxidant activity is likely responsible for the protection effects. Thus, they can either provide protection for normal cells from oxidative stress as antioxidant agents or exert pro-apoptotic effects in cancer or malignant cells as cytotoxic pro-oxidants.[12] The anticancer potential of these catechol derivatives has greatly aroused scientists' interest recently. Combining with

nanotechnology, the potentiality of catechol-based systems has increasing the interest due to the combination of catechol properties with the nanostructuration advantages. In this section we review some interesting examples of catechol-based polymeric nanostructures with application in cancer therapy, and specifically in GB treatment.

One of the most used catechol in cancer therapy is quercetin. The bioavailability of this molecule was greatly restricted by the its poor solubility what limits the persistence in bloodstream and the BBB crossing. It is reported that Only 0.3% of quercetin reached the brain via intraperitoneal administration.[13] The encapsulation of quercetin into PLGA NPs (215 nm) improved its bioavailability and anticancer efficacy in C6 glioma cells compared to free drug. Moreover, this series of nanoparticles exhibited high cellular uptake and antioxidant activity while effectively inhibiting cell proliferation.[14] G. Wang published a series of papers concerning the anti-glioma effects of liposomal and micelle quercetin *in vitro* and *in vivo*.[15-19] In a recent work, quercetin-loaded nano-micelles (Figure 4.3) showed potent cytotoxicity in C6 glioma cells, accumulated in brain tissue effectively and exhibited significant antitumor efficacy *in vivo* with significantly longer survival.[20]

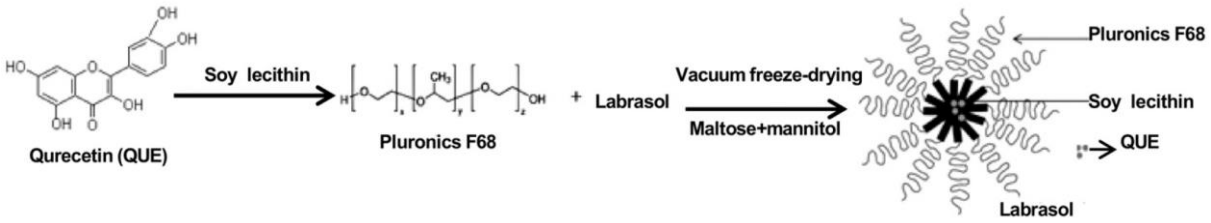

Figure 4.3 Preparation scheme for quercetin-loaded nanomicelles conjugated with Pluronic and Labrasol block copolymers, adapted from reference 20.

In another example (Figure 4.4), Pt-prodrug polyphenols and PEG-polyphenols were employed to form coordination NPs with ferric ions and loaded an anticancer agent Doxorubicin (DOX). DOX and Pt prodrug can both activate nicotinamide adenine dinucleotide phosphate oxidases and generate ROS, while polyphenols acted as a catalyzer to form highly toxic free radicals and to synergize the chemotherapy. This system prolonged blood circulation and enhanced tumor accumulation, thus effectively inhibited U87 glioma growth and mitigated side effects.[21] This nanoparticle was also able to encapsulate and deliver the phagocytic enzyme myeloperoxidase (MPO) in a

controlled manner. In this case the therapeutic efficacy was related to the release of Pt-drug and the *in-situ* production of HOCl. The results showed that the NPs induced a ROS cascade that enhanced Pt therapy. Moreover, this nanosystem exhibited prolonged circulation time in blood, high tumor accumulation, and effective inhibition of tumor growth *in vivo*.[22]

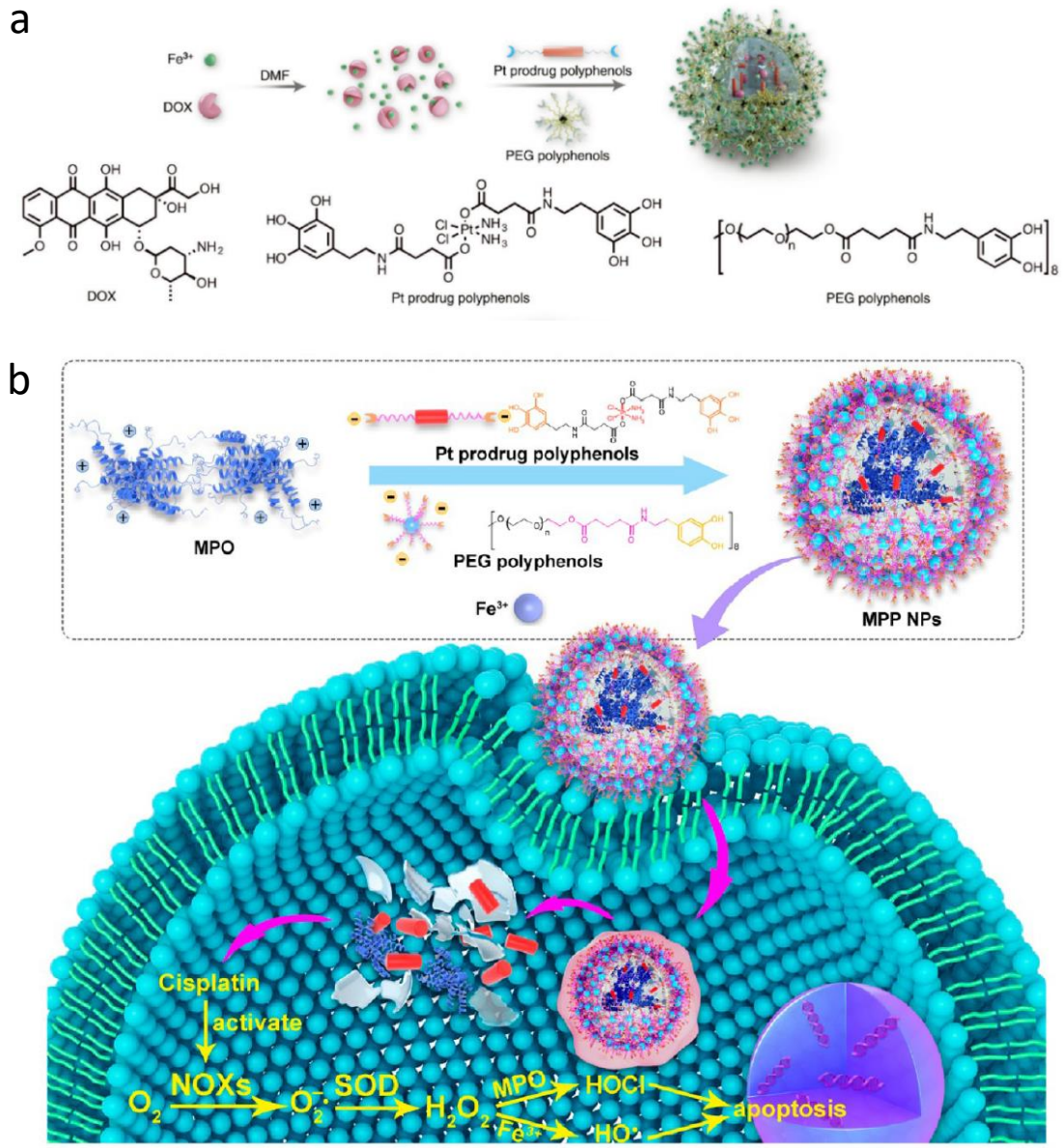

Figure 4.4 DOX-loaded (a) and MPO-loaded (b) NPs based on the coordination of Pt-prodrug and PEG polyphenols with Fe(III) ions, adapted from references 21-22.

Other catechol derivative like luteolin was loaded in PEG-PCL micelles and its anti-glioma effect was evaluated *in vitro* and *in vivo*. Luteolin-loaded micelles showed

stronger cytotoxicity in C6 and U87 GB cells than free luteolin. Within the U87 glioma-bearing zebrafish model, the micelles induced more apoptosis and inhibited neovascularization in tumor tissues, resulting significantly stronger inhibition on tumor growth.[23]

4.3 Scope of this chapter

Catechol-based polymeric NPs incorporating Pt(IV) prodrug PtBC will be synthesized, characterized and evaluated as drug delivery systems for GB chemotherapy. This chapter will focus on the following objectives:

(i) Synthesis of the polymeric pPtBC NPs (Figure 4.5).

(ii) Physicochemical characterization of the resulting polymeric NPs.

(iii) *In vitro* studies of the anticancer activity of pPtBC NPs against GB compared to CDDP and PtBC.

(iv) *In vivo* safety and biodistribution evaluation of pPtBC NPs in preclinical GB murine model

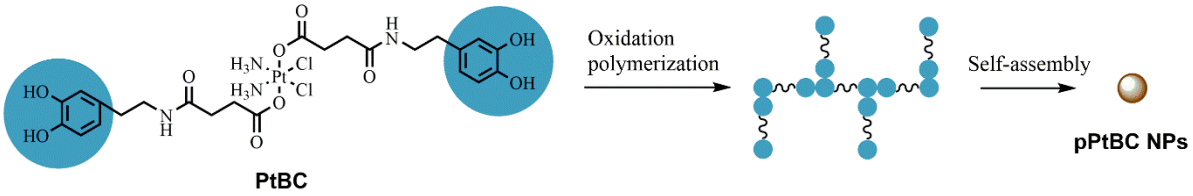

Figure 4.5 Synthesis of polymeric pPtBC NPs based on oxidation polymerization of the catechol-bearing Pt(IV) prodrug.

4.4 Results and discussion

The Pt(IV) prodrug (PtBC) was synthesized and characterized in the same way as described in previous section 3.1.

4.4.1 Synthesis and characterization of polymeric pPtBC NPs

The polymeric pPtBC NPs were synthesized based on the oxidation of terminal catechol moieties from Pt(IV) prodrug by sodium periodate. $NaIO_4$ in aqueous solution was added into the PtBC solution in EtOH/H_2O (1:1 in volume) slowly, and brown NPs formed after 4 h of reaction at rt. The pPtBC NPs were prepared as scheme shown in Figure 4.6.

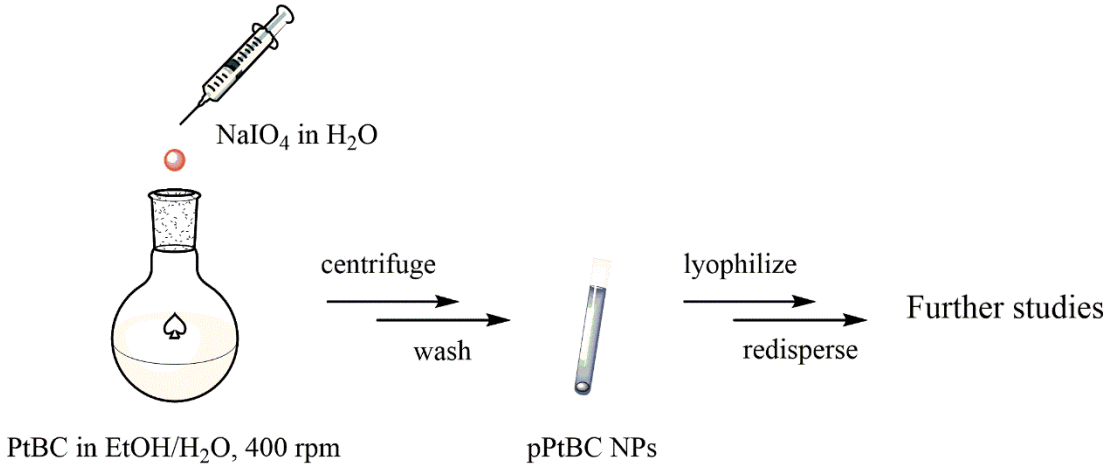

Figure 4.6 Schematic illustration of the synthesis of polymeric pPtBC NPs.

The properties of the nanocarriers play an important role for the performance of the drug delivery system, especially the particle size, surface charge, and morphology, among other factors. The physical properties will determine their circulation half-time, and biodistribution, as well as the cellular uptake pathways and body clearance.

The hydrodynamic size and ζ-potential (Figure 4.6) of pPtBC NPs were measured using DLS, showing an average size of 64.03 ± 6.58 nm, with a relatively low PDI of 0.143 ± 0.012, and a slightly negative ζ-potential of -6.18 ± 1.05 mV.

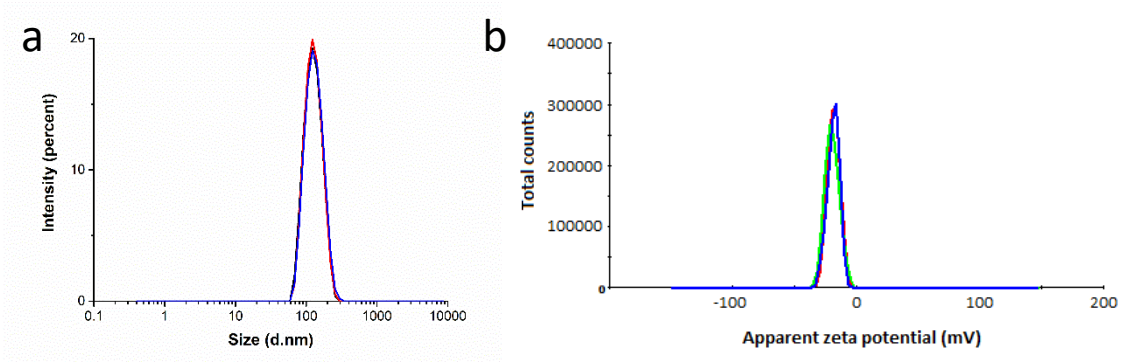

Figure 4.6 Representatively size distribution (a) and ζ-potential (b) of pPtBC NPs by DLS.

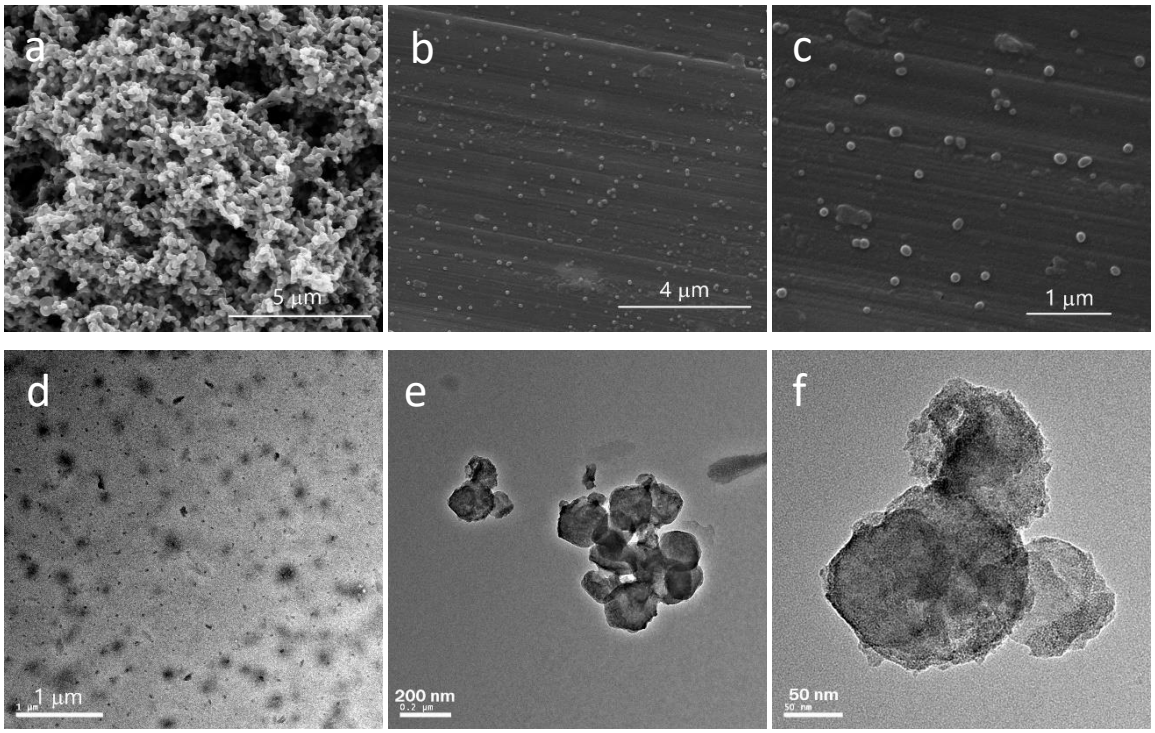

Figure 4.7 Representative morphologies of pPtBC NPs under SEM (a-c), and TEM (d-f).

The morphologies of the polymeric NPs were observed by SEM and TEM (Figure 4.7). Relatively monodispersed and uniform spherical NPs were observed under SEM, showing a size around 70 nm which was in good accordance with the result of DLS. Under TEM, the NPs cannot be observed well due to their polymeric nature, whose nanostructures probably collapsed because of the high voltage and presented as irregular particles with blurry edges. As discussed in section 3.3, the size can influence considerably the biodistribution of NPs *in vivo*. Nanoparticles with a size around 100 nm

are favorable as nanocarriers, which usually can offer longer circulation half-lives and lead to improved therapeutic effects. And sizes less than 100 nm were reported to facilitate the transport of nanoparticles across the BBB.[24-25] The low PDI indicated the uniform size distribution of the NPs and ensured the possibility of a more similar behavior after administration and less pharmacokinetic irregularity and variability in therapeutic outcome.[26] The surface charge of the NPs influences mostly the interaction of NPs and proteins in blood stream, thus affecting the pharmacokinetics and biodistribution. And cationic NPs have been observed to be rapidly removed from circulation due to their enhanced protein absorption, resulting in nonspecific uptake by macrophages. Although positively-charged particles are reported to feature an enhanced cellular uptake due to their interaction with the cell membrane, their rapid clearance makes this meaningless without reaching target sites.[27] In contrast, the almost neutral or slightly negative ζ-potential avoids excessive interaction between the NPs and proteins or non-target cell membranes before reaching the target sites, and thus prolongs the half-lives and provide polymeric pPtBC NPs better stability during transport.

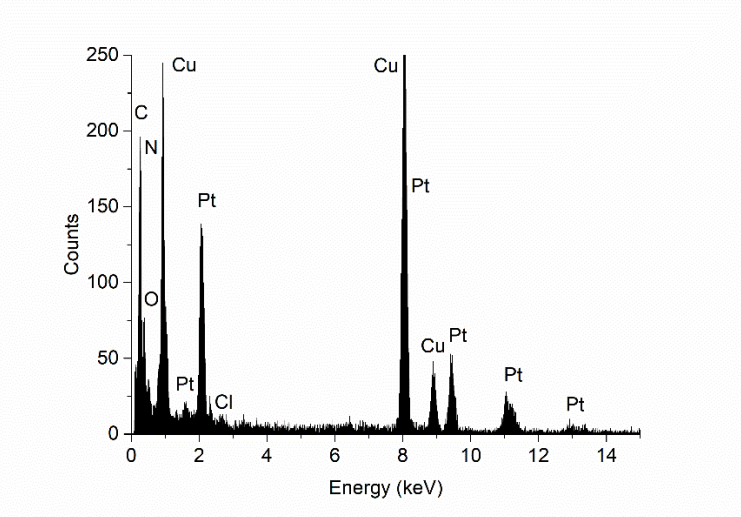

Figure 4.8 Representative EDX spectrum of polymeric pPtBC NPs by TEM.

To confirm the chemical composition, a combination of characterization techniques was used, including EDX and ICP-MS. All characterizations were performed with three independent batches of pPtBC NPs, displaying comparable results between batches and therefore proving the robustness and reproducibility of the synthetic procedure. EDX

was first used to check the elements qualitatively present in the polymeric pPtBC NPs (Figure 4.8). All major elements in the prodrug PtBC were found in the NPs such as C, N, O, Pt, and Cl, whereas Cu in the spectrum belonged to the copper grid for supporting the TEM sample. ICP-MS measurements allowed the determination of Pt content in the NPs, which also gave a reproducible percentage of Pt in the NPs in weight. Compared to the pure prodrug, the Pt content decreased slightly from 24 .04% to 16.16%.

4.4.2 *In vitro* drug release

Numerous strategies have been developed to enhance the selectivity and targeting capability of nanoscale drug delivery systems for tumor treatment. Among them, drug delivery systems with stimuli-responsiveness have been increasingly investigated due to their sensitivity to specific subtle changes in tumor or tumor microenvironment (TME) from normal tissues, including mildly acidic pH, high GSH level, overexpressed proteins or receptors, altered enzyme activity, etc.[28-29] The unique features have been harnessed to develop drug delivery systems which can actively target tumors or TME, thus increase drug accumulation in tumor, improve therapeutic effects and reduce side toxicity.[30]

In our work, the Pt(IV) prodrug and resulting pPtBC NPs were designed to be pH-responsive due to the presence of ester and amide bonds in the molecule which can remain stable in physiological conditions and be cleaved in the weekly acidic extracellular environment of tumors or in acidic endo/lysosomal compartments of tumor cells. Besides, the linkage bonds also can be enzymatically cleaved by the endogenous esterase and amidase/proteinase. Herein, drug release from polymeric pPtBC NPs was studied in phosphate buffers at different pH, and released Pt was determined using ICP-MS.

The release profiles (Figure 4.9) were obtained using dialysis method. pH 7.4 and pH 5.5 were chosen to mimic the physiological and mildly acidic conditions for the drug release study *in vitro*. pPtBC NPs were incubated in the dialysis bags at 37 °C over 48 h against phosphate buffers and released Pt was quantified by ICP-MS to yield the release profiles. Both release curves are typically biphasic, while the release was faster in the first few hours, and later in a more sustained and slower manner at both pH. However, the release of Pt from pPtBC NPs was drastically accelerated under the acidic condition.

As shown in Figure 4.9, 44.89 ± 4.64% of Pt was released in total after 48 h of incubation in PB buffer at pH 7.4, while the released Pt increased to 70.98 ± 1.99% with incubation for 48 h at pH 5.5. This substantiated that the pPtBC NPs are acid-sensitive, permitting the possibility that pPtBC NPs can maintain stable in physiological conditions and release the drug effectively in acidic tumoral tissues, thus realizing the controlled released of the payloads.

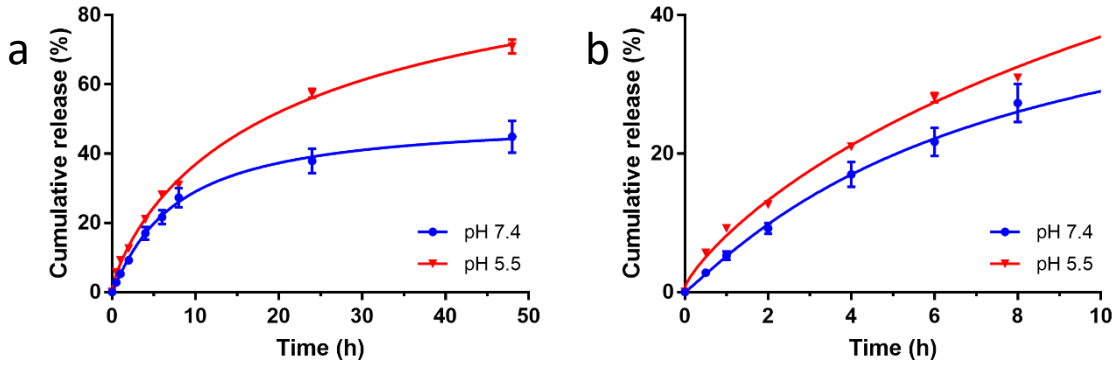

Figure 4.9 a) Cumulative Pt release from pPtBC NPs at pH 7.4 and pH 5.5. b) Inset of release profiles in first 8 h. All data represented as mean ± SE with three independent experiments.

As discussed in section 3.6, GSH and its oxidized form glutathione disulfide (GSSG) play a pivotal role in the redox hemostasis of cells. Generally, the intracellular concentration of GSH is reported to be 1 - 10 mM in normal cells, while its concentration decreased to 2 - 3 orders of magnitude lower levels in extracellular fluids. However, the intracellular level of GSH in cancer cells are reported to increase up to fourfold more than that in normal cells.[31] The elevated levels of GSH protect tumor cells from the anticancer action of numerous therapeutics, including Pt agents, contributing to the multidrug resistance (MDR) of therapeutic agents.[32] The different GSH levels in extra- and intra-cellular circumstances and in normal and tumor tissues have prompted the emergence of GSH-responsive nano-formulations to facilitate the preferential drug release in tumor tissues and cells. [33-34] Commonly, this type of nanocarriers bear sensitive bonds to GSH as structural features. The polymerization products from catechol moieties have been reported to disassociate in acidic conditions and show GSH-responsiveness.[35-37] In this work, the catechol moieties presented in the prodrug and

obtained pPtBC NPs may interplay with the redox of GSH and offer a GSH-responsive nanodrug delivery platform.

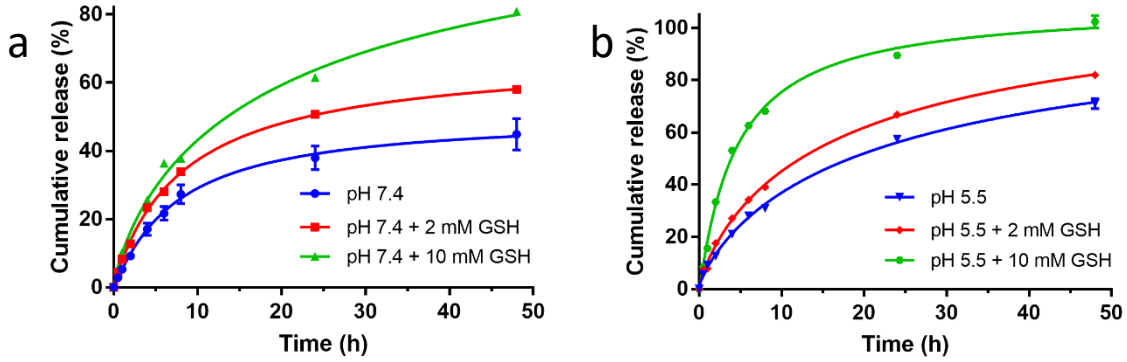

Figure 4.10 a) Cumulative Pt release from pPtBC NPs in the presence of GSH (2 and 10 mM) at pH 7.4 (a) and pH 5.5 (b). All data represented as mean ± SE with three independent experiments.

To check this possibility, the release behavior of pPtBC NPs was furthermore studied in the presence of GSH. The GSH level in brain was reported to be around 1 - 2 mM.[38] Therefore, 2 mM and 10 mM were chosen as the concentrations of GSH to be tested, using the same method described previously at pH 7.4 and 5.5. As Figure 4.10 shown, indeed, the release of Pt was obviously promoted by GSH. Even with a concentration of 2 mM, GSH accelerated the release of Pt dramatically; 50.71 ± 0.26% of Pt was released from the pPtBC NPs after 24 h of incubation at pH 7.4, which exceeded the amount of released Pt (44.89 ± 4.64%) after 48 h in the absence of GSH. After 48 h, 57.95 ± 1.18% of Pt was released in total in the presence of 2 mM GSH. Notably, the release was further sped up while the concentration of GSH increased to 10 mM; 61.5 ± 0.24% of Pt was released from the pPtBC NPs after 24 h of incubation, and the total release reached 80.89 ± 0.47% after 48 h. At pH 5.5, the release of Pt was accelerated in the same trend as at pH 7.4 in the presence of GSH, and all Pt was released after incubation with 10 mM GSH at pH 5.5 for 48 h.

In summary, the results demonstrated that pPtBC NPs are both pH- and GSH-responsive, favorably activating and releasing the therapeutic drug in tumor tissues and cells, providing selectivity of tumor tissues and cells over normal tissues and cells, ensuring the maximal anticancer effectiveness and minimal off-target side effects.

4.4.3 Anticancer efficacy of pPtBC NPs *in vitro*

Molecules with catechol moieties were reported to have antibacterial, antiviral, and other therapeutic effects mostly by modulating the redox balance.[39] To elucidate the origin of anticancer effect, a model compound nordihydroguaiaretic acid (NDGA), and the corresponding polymeric material (pNDGA NPs) prepared with same methodology as pPtBC NPs were included in the *in vitro* assays. As observed in Figure 4.11, NDGA shares structural similarity with the prodrug PtBC, but without cisplatin core in the structure.

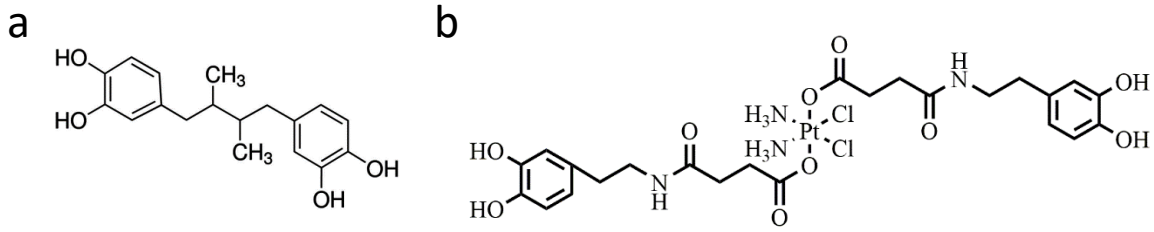

Figure 4.11 Chemical structures of NDGA (a) and the prodrug PtBC (b).

4.4.3.1 Cytotoxicity assays

Similarly, the cytotoxic effects of PtBC, pPtBC NPs, NDGA, and pNDGA NPs were evaluated *in vitro* and compared to cisplatin (CDDP) against a panel of cell lines, including cancer cells of different origins, cisplatin-resistant cells, and non-malignant cells. Human cervical cancer cell HeLa, murine glioma cell GL261, and non-malignant human fibroblast cell 1Br3G were chosen for the cell viability assays using the well-established PrestoBlue method for 24 h and 72 h (Figure 4.12). Except the three cell lines, the cytotoxicity of these formulations was also tested against a pair of human ovarian cancer cell lines, A2780 and its cisplatin resistant counterpart A2780/cis (Figure 4.12), hoping that the polymeric NPs may sensitize the resistant A2780/cis cells towards cisplatin. It has been reported that nanocarriers with proper modifications can bypass the efflux of resistant cells which the free drug is commonly subjected to, leading to modulating or overcoming the resistance of cancer cells.[40-41] The half maximal inhibitory concentrations (IC_{50}s) were calculated using Graphpad Prism 7 and summarized in Table 4.1 and 4.2.

After 24 h of exposure (Table 4.1), PtBC and pPtBC NPs showed slightly lower cytotoxicity against almost all cell lines compared to CDDP, while the cytotoxicity of pPtBC NPs was weaker in GL261 cells line. Specifically, the cytotoxic effect of pPtBC NPs was very similar to the prodrug in HeLa cells, with very close IC_{50}s of 22.09 μM and 29.94 μM respectively. But CDDP showed higher cytotoxicity with an IC_{50} of 15.98 μM in HeLa cells. In 1Br3G cells, they demonstrated the same trend, and the IC_{50}s of CDDP, PtBC, and pPtBC NPs were 45.07, 56.09, and 56.3 μM respectively.

After 72 h of exposure (Table 4.2), the cytotoxicity difference between the prodrug PtBC, pPtBC NPs and CDDP was decreased to comparable levels. And pPtBC NPs showed slightly higher cell killing ability than the prodrug in all cell lines. Specifically, in HeLa cells, pPtBC NPs demonstrated a lower IC_{50} of 0.65 μM than that of CDDP (2.34 μM), and PtBC also exhibited a slight stronger cytotoxicity than CDDP, with a IC_{50} of 1.85 μM. However, in the other two cell lines, the cytotoxicity of them was comparable, as CDDP > pPtBC NPs ≥ PtBC with very close IC_{50}s. For example, in GL261 cells, the IC_{50}s of CDDP, PtBC and pPtBC were 2.16, 4.17 and 4.64 μM respectively.

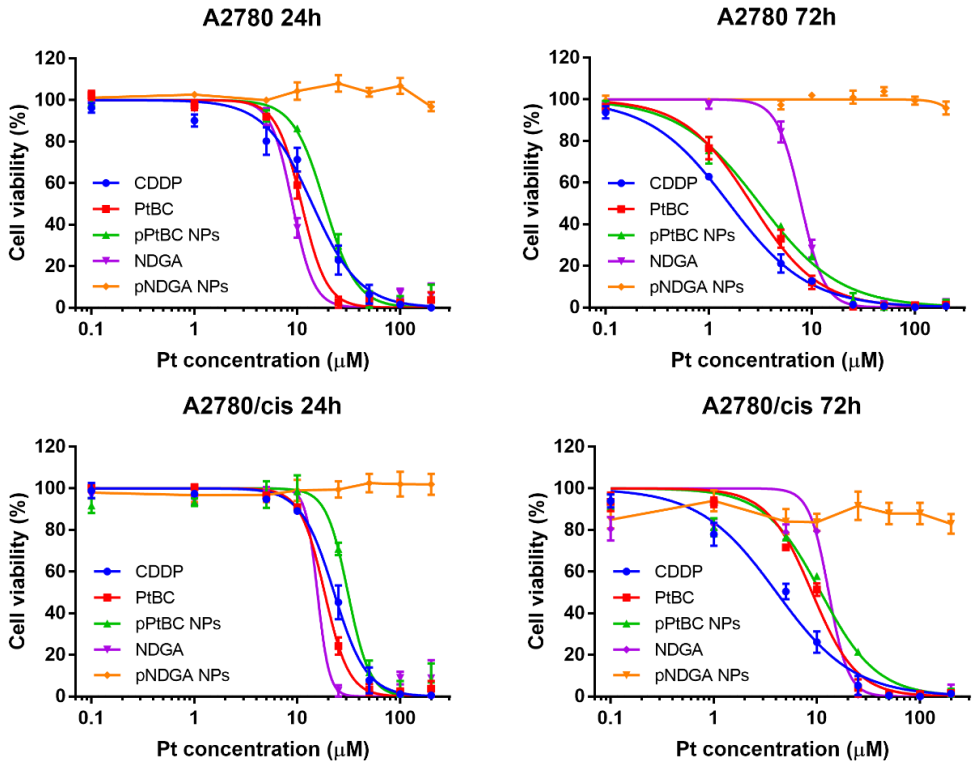

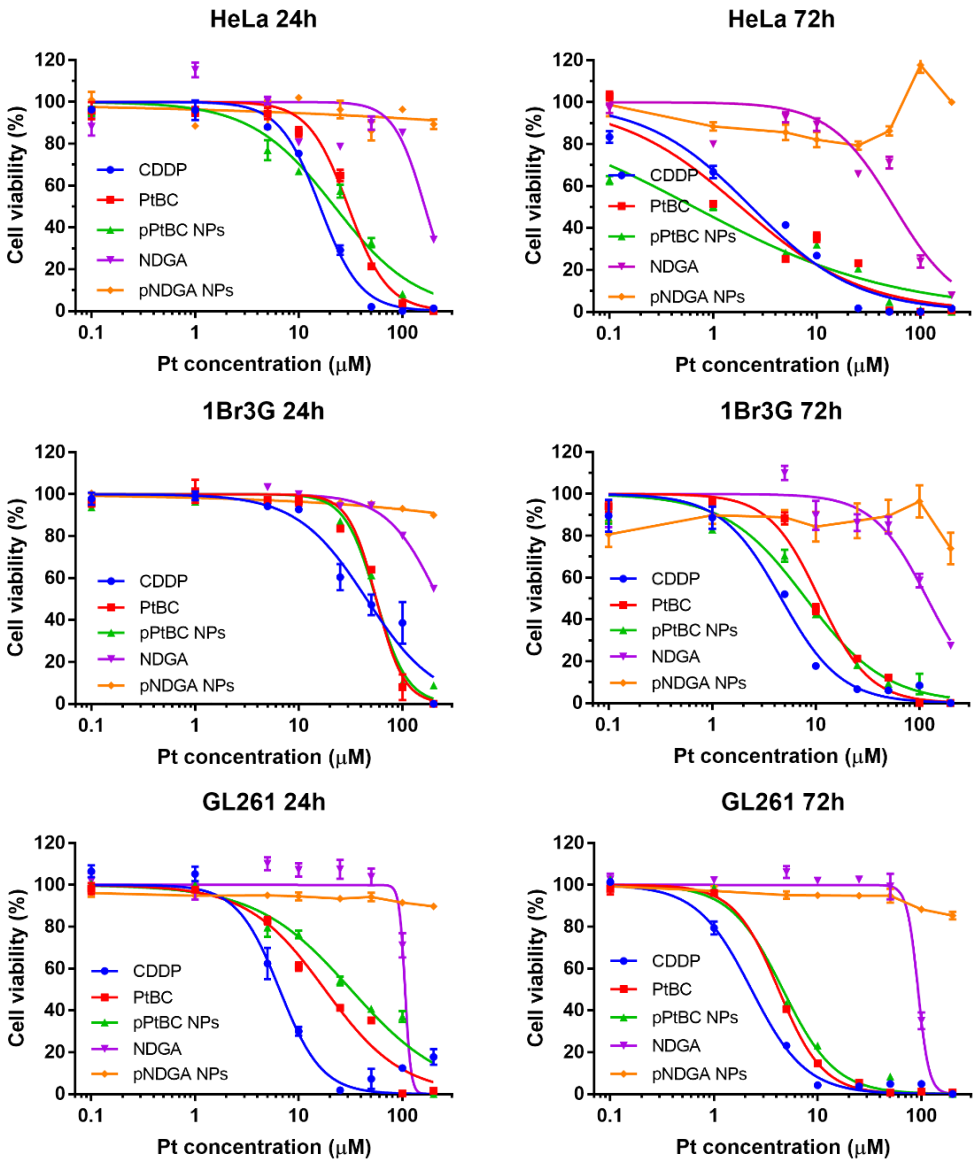

Figure 4.12 Cytotoxicity assays of CDDP, PtBC, pPtBC NPs, NDGA, and pNDGA NPs against a panel of cell lines for 24 h and 72 h. All data represented as mean ± SE of three independent experiments.

On the other hand, as the reference molecule, NDGA showed very low cytotoxicity in these cell lines except in A2780 or A2780/cis, and its polymeric counterpart pNDGA NPs was non-toxic in given concentration range with a cell viability close to 100% in all cell lines either for 24 h or for 72 h. This interesting comparison excluded the possibility that the catechol moieties may contribute to the cytotoxicity of PtBC and polymeric pPtBC in HeLa, 1Br3G, or GL261 cells. Unfortunately, in the ovarian cancer cell lines resistant to CDDP, neither the prodrug nor the NPs showed improvement in cytotoxicity compared to CDDP (Figure 4.12). Such cross resistance of A2780/cis cells to PtBC and pPtBC NPs

suggested common elements in their mechanism of action as CDDP. In contrast, the reference molecule NDGA exhibited slightly stronger cytotoxicity compared with CDDP in both cell lines after 24 h, while it showed comparable but slightly weaker cytotoxic effect as CDDP for 72 h. This indicated that NDGA could be a promising therapeutic agent against the ovarian cell lines which might bear poor antioxidative capacities and be hypersensitive to redox imbalance. However, we are well aware that the pathways for uptake and detoxification of NPs are greatly influenced by the cell type, as well as the intrinsic properties of NPs.[42] These promising anticancer effects *in vitro* open new avenues for the exploration of different biomedical applications.

IC_{50} (μM)[a]					
	Cell line				
Compound	HeLa	1Br3G	GL261	A2780	A2780/cis
pPtBC NPs	22.09 ± 1.09	56.30 ± 1.32	33.56 ± 1.36	18.44 ± 2.19	31.40 ± 2.28
pNDGA NPs	NT[b]	NT[b]	NT[b]	NT[b]	NT[b]
PtBC	29.94 ± 1.04	56.09 ± 1.18	17.40 ± 1.08	10.98 ± 0.56	18.39 ± 1.85
NDGA	164.15 ± 0.02	NT[b]	109.45 ± 1.95	8.94 ± 0.69	15.67 ± 2.14
CDDP	15.98 ± 1.04	45.07 ± 4.60	5.61 ± 0.28	13.95 ± 1.24	23.68 ± 1.74

[a] The IC_{50}s of the compounds against different cell lines were determined by PrestoBlue assay. Each value represented the mean ± SE of three independent experiments.

[b] NT represents non-toxic, which means the viability of cells is close to 100 % even at the maximum concentration.

Table 4.1 IC_{50}s of different formulations against a panel of cell lines for 24 h.

IC_{50} (μM)[a]					
	Cell line				
Compound	HeLa	1Br3G	GL261	A2780	A2780/cis
PPtBC NPs	0.65 ± 0.14	8.01 ± 0.72	4.64 ± 0.05	3.10 ± 0.32	10.50 ± 0.84
pNDGA NPs	NT[b]	NT[b]	NT[b]	NT[b]	NT[b]
PtBC	1.85 ± 0.36	10.80 ± 0.60	4.17 ± 0.12	2.59 ± 0.33	9.12 ± 0.69
NDGA	55.65 ± 6.21	119.00 ± 14.20	81.73 ± 2.40	7.82 ± 0.39	12.96 ± 1.48
CDDP	2.34 ± 0.30	4.63 ± 0.42	2.16 ± 0.26	1.57 ± 0.08	5.22 ± 1.21

[a] The IC_{50}s of the compounds against different cell lines were determined by PrestoBlue assay. Each value represented the mean ± SE of three independent experiments.

[b] NT represents non-toxic, which means the viability of cells is close to 100 % even at the maximum concentration.

Table 4.2 IC_{50}s of different formulations against a panel of cell lines for 72 h.

4.4.3.2 ROS generation

As discussed in previous chapter, the chemical property of catechol moiety makes it an interesting functional group in biomedical field. On one hand, its antioxidant and anti-inflammatory activities endow it with multiple beneficial physiological effects. Compounds with catechol moieties, generally polyphenols and flavonoids, were reported to exhibit hepatoprotective, anti-inflammatory, antioxidant, and even anticancer properties.[43] On the other hand, ROS can be generated during the oxidation process of the catechol moieties, which may induce excessive oxidative stress and cause harmful effects, such as toxicity, damage, and inflammation in cells.[4] Therefore, it's intriguing to check if the prodrug and the pPtBC NPs also generate ROS and possible influence in their therapeutic effects.

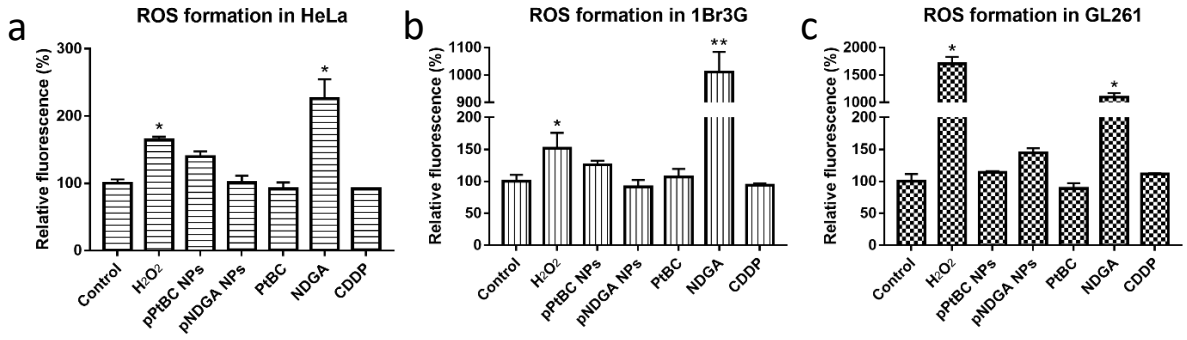

Figure 4.13 ROS generation triggered by different compounds and pPtBC NPs in HeLa (a), 1Br3G (b) and GL261 (c) cells. The concentration of H_2O_2 was 0.1 mM, pNDGA NPs at 0.2 mM, other agents at their corresponding IC_{50}s. Data represented as Mean ± SE of three independent experiments. * stands for $p < 0.05$, ** for $p < 0.001$, *** for $p < 0.0001$.

To assess if such oxidative stress also plays a role in the cytotoxicity of our prodrug and nanoparticles, the ROS generation of these compounds/formulations was evaluated using the fluorescent probe 2',7'-dichlorofluorescin diacetate (DCFCDA) in HeLa, 1Br3G and GL261 cells (Figure 4.13). DCFCDA has been proved that its fluorescence intensity is correlated well with the intracellular ROS levels.[44] After 24 h of exposure to the agents, strong DCF fluorescence was only observed from NDGA and H_2O_2, the positive control,

in all cell lines. Neither the prodrug PtBC nor the polymeric pPtBC/pNDGA NPs triggered the formation of ROS in all cell lines. This result proved that the cytotoxicity of these agents mainly arises from the Pt core which can be activated intracellularly to cisplatin. CDDP itself neither induced ROS generation. Thus, the possibility of oxidative stress caused by catechol moieties was excluded from the mechanisms of action of these agents, except NDGA where the oxidative stress might contribute partially to its therapeutic effects.

4.4.3.3 Cellular uptake and DNA-bound Pt

The therapeutic efficacy of an anticancer agent greatly depends on its accumulation in targeting cells, or its intracellular concentration, which in turn is directly related to its uptake pathways and kinetics, in addition to other factors such as its metabolism and/or cellular efflux. Increasing the Lipophilicity of NPs' surface was reported to obtain higher affinity to the cell membrane, even that of the BBB endothelial lining, compared to hydrophilic NPs.[45] The polymeric nature of the pPtBC NPs may facilitate their transport across the BBB, and enhance the cellular uptake in target tumor cells.

Both the reference molecule NDGA and its polymeric NPs were excluded from further studies since they did not show effective anticancer activity in previous cytotoxicity assays. To assess the cellular uptake, HeLa, 1Br3G, and GL261 cells were used for the study. All Pt-containing agents were co-incubated with the cells for 6 h and 24 h at a concentration of 0.1 mM (referred to Pt). Then the cells were digested, and the amount of intracellular Pt level was determined using ICP-MS.

As Figure 4.14a shown, with a relatively high extracellular concentration, the cellular uptake of these Pt agents exhibited a trend as PtBC > pPtBC > CDDP after exposure to the drugs for 6 h. And both the prodrug PtBC and the polymeric pPtBC NPs had a significantly higher cellular uptake compared with CDDP in all cell lines. And the uptake of the prodrug was generally higher than that of the polymeric NPs. CDDP and PtBC are all small molecules which usually enter cells by passive diffusion. However, the cellular entry pathway of CDDP is dominated by the carriers present on the cell membrane, especially copper transporters (CTRs) and organic cation transporters (OCTs).[46-47] The

carrier-mediated endocytosis requires energy consumption, but passive diffusion does not, which might be the reason why the cellular uptake of CDDP was less than that of PtBC. NPs commonly cannot easily enter the cell by passive diffusion but by endocytosis pathways, which is also energy-dependent. With a relatively high extracellular concentration, PtBC may enter cells easier than the NPs given the high concentration gradient.

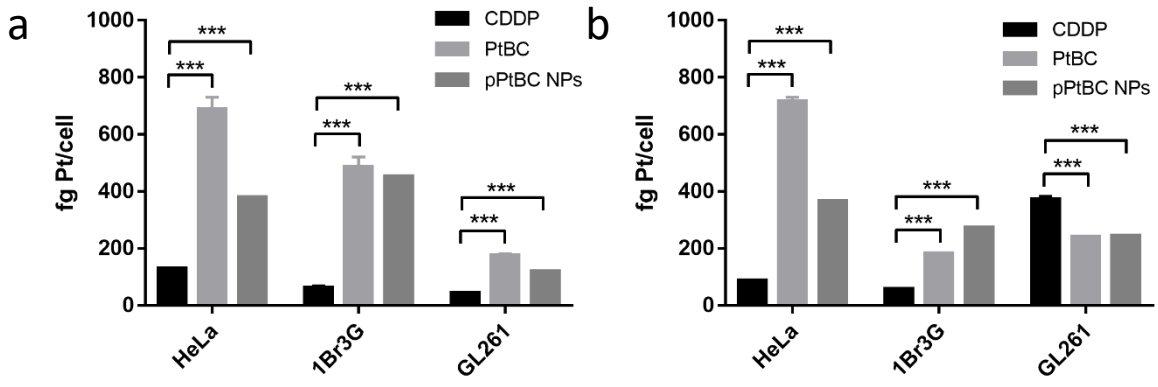

Figure 4.14 Cellular uptake of CDDP, PtBC and pPtBC NPs in HeLa, 1Br3G and GL261 cells for 6 h (a) and 24 h (b). All drugs were incubated at a concentration of 100 μM referred to Pt. Data represented as mean ± SE of three independent experiments. * stands for $p < 0.05$, ** for $p < 0.001$, *** for $p < 0.0001$.

After exposure for 24 h (Figure 4.14b), the cellular uptake of the agents remained similar levels in HeLa cells which implied that the internalization of these agents was fast and became dynamically stable after 6 h. However, the uptake in the other two cell lines did not reach the dynamic equilibrium after 6 h, and the levels changed after incubation for 24 h. In 1Br3G cells, the intracellular level of CDDP was comparable to that of 6 h, but the levels of PtBC and pPtBC NPs decreased dramatically, though they were still significantly higher than CDDP level. Interestingly, the trend in GL261 cells converted totally. The cellular uptake of CDDP augmented to 8.5 times in comparison to the intracellular concentration of 6 h, which turned significantly higher than that of PtBC or pPtBC NPs whose intracellular level also increased than 6 h.

The cellular uptake in GL261 (Figure 4.15) was further studied along time with a concentration decreased to 10 μM which was lower than the IC_{50}s of PtBC and pPtBC NPs, but slightly higher than that of CDDP, in order to exclude the impact from high concentration gradient of Pt agents which may be favorable for cell internalization. In

general, the cellular uptake of all Pt agents increased with time, and the trend remained similar to high initial concentration. At all time points (2, 4, 8 and 24 h), the intracellular concentrations of CDDP kept the highest compared to the prodrug or the NPs. The concentration difference at 2 h was not significant, whereas turned significantly higher than that of PtBC and pPtBC NPs afterwards.

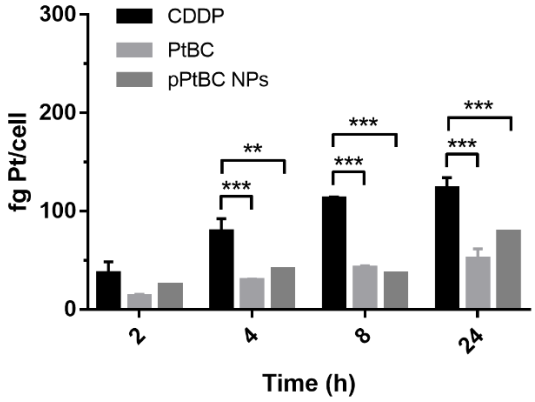

Figure 4.15 Cellular uptake of CDDP, PtBC and pPtBC NPs along with time at a concentration of 10 μM referred to Pt. Data represented as mean ± SE of three independent experiments. * stands for $p < 0.05$, ** for $p < 0.001$, *** for $p < 0.0001$.

Since the anticancer effects of Pt drugs was mainly attributed to its interaction with DNA, determination of DNA-bound Pt would be helpful to understand better the action mechanisms of these Pt agents. Similarly, HeLa, 1Br3G, and GL261 cells were incubated with CDDP, PtBC and pPtBC NPs at a Pt concentration of 100 μM for 24 h. Then the nuclear DNA of cells was further extracted and purified, and obtained DNA was quantified by the absorbance, meanwhile, the amount of Pt bound to the DNA was quantified using ICP-MS. As Figure 4.16 shown, the DNA-bound Pt concentration from intrinsically active CDDP was significantly higher than that of PtBC and pPtBC NPs in all cell lines. In HeLa and 1Br3G cells, the trends did not remain the same as cellular uptake, which meant that not all Pt agents entering cells can enter the nucleus and bind to DNA. In GL261, the trend was similar to that of cellular uptake, but the Pt concentration from polymeric NPs became the lowest. This could be expected that the process for pPtBC NPs was more difficult than CDDP or PtBC. After entering the cells, they had to dissociate first, release the prodrug and get reduced to the active Pt form, then enter nucleus and bind to DNA.

Although the DNA-bound Pt , they exhibited comparable anticancer activities for 24 h (see section 4.3.3.1). This suggested that the action mechanisms of PtBC and pPtBC NPs probably were not limited to Pt-DNA adducts in this case. Increasing reports demonstrated that Pt agents can also bind to other cellular macromolecules such as RNA and proteins, and even induce immunogenic effects. [48-50] Bose and colleagues even synthesized a novel Pt compound with high cytotoxicity similar to cisplatin, but not binding to DNA at all.[51]

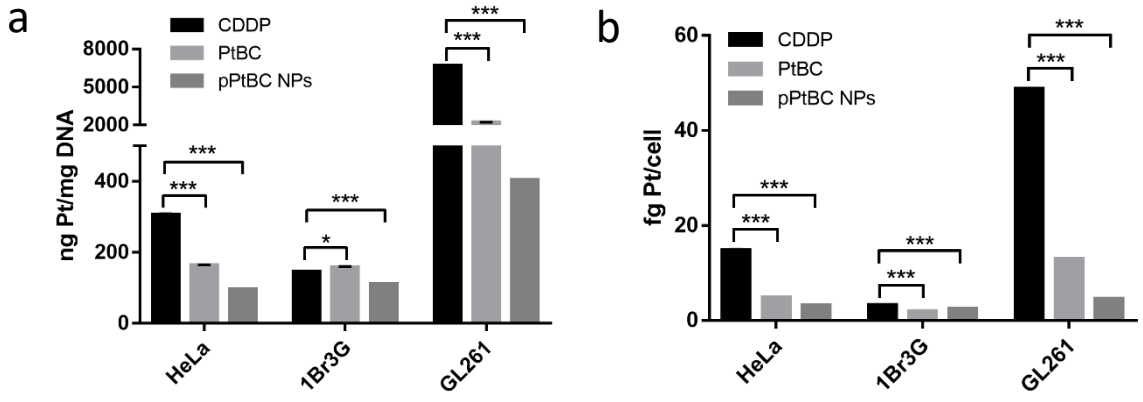

Figure 4.16 DNA-bound Pt after exposure to CDDP, PtBC, and pPtBC NPs for 24 h at a concentration of 100 μM referred to Pt. Each value represented as mean ± SE of three independent experiments. * stands for $p < 0.05$, ** for $p < 0.001$, *** for $p < 0.0001$.

4.4.3.4 Cell morphology observation

Cell morphology is a direct indicator of cytotoxicity of therapeutic agents. Therefore, the morphologies of GL261 cells incubated with CDDP, PtBC, and pPtBC NPs were observed and recorded by optical microscopy.

The morphologies of GL261 cells changed a lot after incubation with those Pt agents for 24 h (Annex I), which was more obvious with higher concentrations. Specifically, exposure to PtBC at a concentration of 1 μM for 24 h, obvious cell density decrease, rounding-up, pseudopodes retraction, plasma membrane blebbing/budding, and cell volume reduction were observed, but still the number of cells with normal morphology accounted for the majority. When the concentration increased to 10 μM, the proportion of healthy cells decreased dramatically, and most of the cells got rounded and shrunken, cellular fragments observed. At the concentration of 25 μM, the shrunken cells

disappeared, the fragments of cells occupied the vision, and little alive cell could be found. The apoptotic morphologies were also observed in other two Pt agents to a more severe degree, which was in good accordance of cytotoxic effects of these agents indicated by their IC_{50}s.

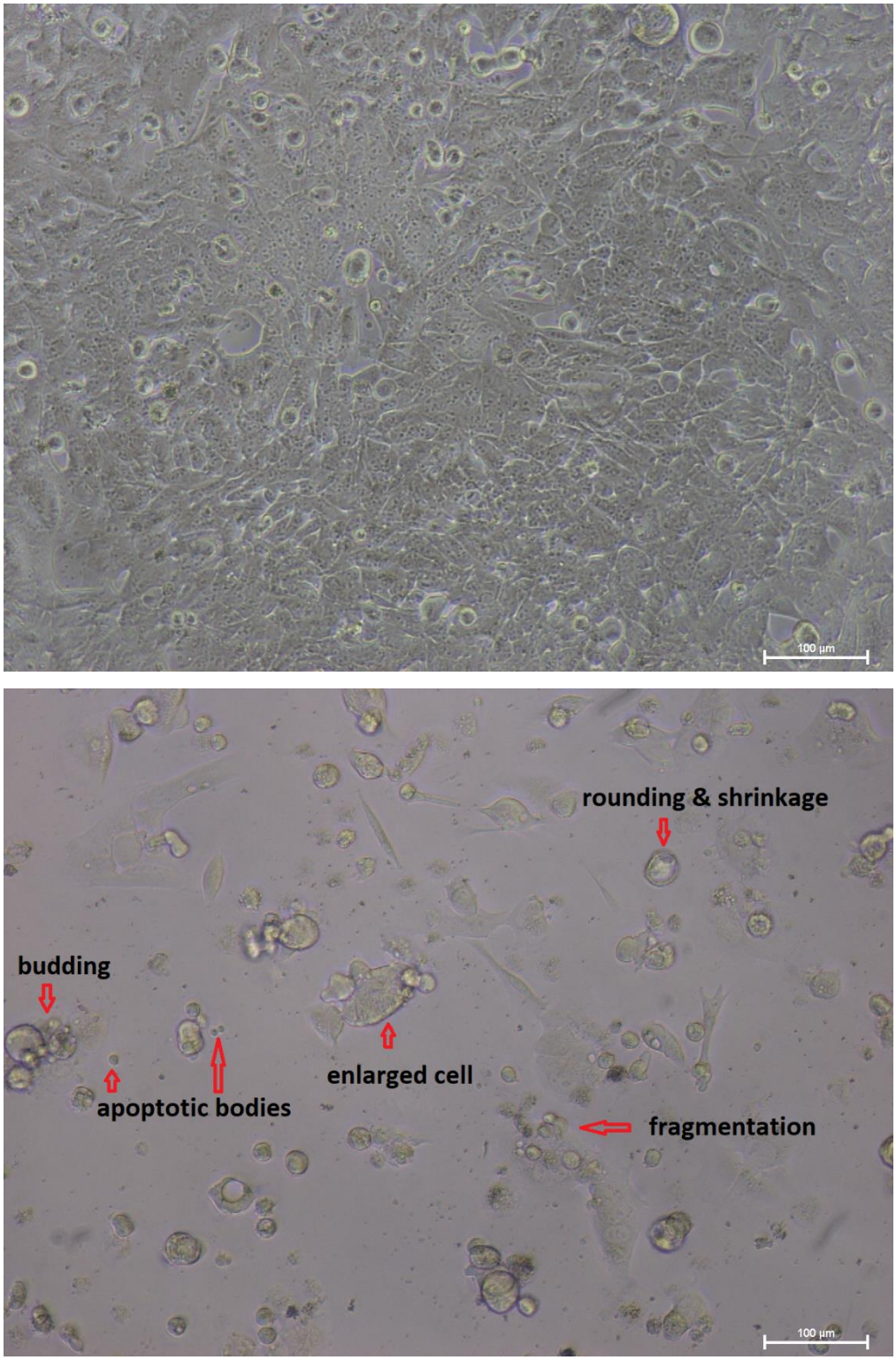

Figure 4.17 Representative morphologies of GL261 cells without/with exposure to pPtBC NPs for 72 h.

After 72 h of exposure (Figure 4.17 and Annex I) to these agents, the morphology changes showed a similar trend to that at 24 h, and the number of healthy cells decreased drastically even at the lowest concentration of 1 μM. the intracellular vesicle swelling became extremely obvious in cells treated with 1 μM CDDP, which implied that probably the cells also underwent necrosis except apoptosis.[52] When the concentration went to 10 μM, almost only fragments of cells were observed in the vision accompanied with a few rounding-up cells for all agents. With agents at 25 μM for 24 h, little alive cells were observed but only floating dead cells or cell fragments.

4.4.4 *In vivo* studies of tolerability and biodistribution

The *in vivo* studies of Pt-Fe NCPs were performed in collaboration with the *Biomedical Applications of Nuclear Magnetic Resonance* research group (GABRMN) led by Dr. Carles Arús at *Universitat Autònoma de Barcelona* (UAB, Cerdanyola del Vallès, Spain) under the supervision of Dr. Ana Paula Candiota with the contribution of Dr. Shuang Wu.

4.4.4.1 Safety and tolerability assessment

Tolerability assay is a fundamental assessment for the safety of new formulations. Herein, intranasal administration was adopted in our animal studies to bypass the impermeable BBB. However, there are few papers reporting about preclinical studies of Pt drugs by nose-to-brain delivery for GB treatment. Therefore, the safety or tolerability assay is extremely necessary prior to other *in vivo* studies. As discussed in previous chapter, in a typical phase I study complying with US FDA regulations, clinical therapeutics are often tested in either single-dose or limited-dose escalation pharmacokinetic studies, or in studies where the exposure is limited to a small number of doses or days, without regard to expected half-life of the drug.[53] In this work, a limited-dose escalation manner was chosen to assess the safety and tolerability of PtBC and pPtBC NPs via intranasal route. To date, there has not been authorized justification for the volume applied to IN administration, but commonly intranasal instillation in volumes more than 20 mL is considered deleterious which can result in suffocation and death of research mice.[54] Although some researcher found that a larger volume of 50 mL or more could be safe for the experimental mice in specific conditions, herein smaller and safer volumes no more than 20 mL were adopted for the *in vivo* study.[55]

Healthy C57BL/6J mice were used for the short-term safety and tolerability assay. Three single slightly escalated doses were administered consecutively every week, from 0.9, 1.2 to 1.5 mg Pt/kg body weight. The body weights of mice were tracked three times every week to monitor any weight changes which function as an important parameter indicating systemic toxicity. Besides, food consumption, and any adverse physical or behavioral effects concerning healthy conditions were closely observed by professional personnel in the animal facility daily. The whole study lasted for 4 weeks.

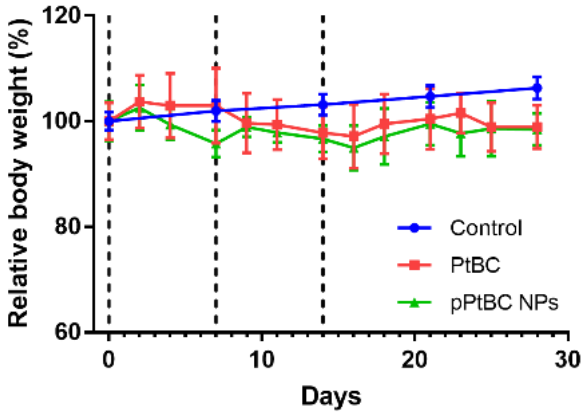

Figure 4.18 Tolerability assessment of mice for PtBC and pPtBC NPs over 4 weeks. Both drugs were given in slightly increasing doses from 0.9, 1.2 to 1.5 mg Pt/kg body weight via I.N. every week, n = 3. For control group, n = 360, data adapted from Jackson Laboratory (https://www.jax.org/jax-mice-and-services/strain-data-sheet-pages/body-weight-chart-000664). Data represented as mean ± SE. Dash lines indicated days for administration.

As Figure 4.18 shown, the body weights of all treatment groups remained stable as the control group till the end of the study, indicating no obvious systemic toxicity caused by PtBC or pPtBC NPs. No treatment-related adverse effects such as mortality, body weight, food consumption, or other clinical signs were observed for all mice during the study relative to control animals. Even with the highest dosage of 1.5 mg Pt/kg body weight, all mice were still in good status during the study. Since the side effects caused by cisplatin typically are acute nephrotoxicity and hepatotoxicity, the major organs of mice from tolerability study were harvested, fixed, and examined by histopathology to assess the biocompatibility and impact on cellular structures.

These results corroborated that PtBC and pPtBC NPs were well-tolerated by mice in given conditions, which proved the safety of this nano-formulation and paved the way to further *in vivo* studies.

4.4.4.2 Biodistribution in mice

As discussed in previous chapter, the biodistribution of NPs *in vivo* considerably contributes to the fate of the administered NPs, and directly influences the bioavailability of the formulations and therefore substantially affects the therapeutic effects. Many factors have been considered key to the final distribution of NPs *in vivo*, especially the size and surface properties of NPs, and interactions with biological barriers.[3,56] Currently, no report for the biodistribution of Pt nanosized agents via intranasal delivery was available. Therefore, it is worthy to study the *in vivo* distribution of polymeric pPtBC NPs via IN route, which could be valuable for related research in future. Same syngeneic implanted orthotopic models were established and used in this chapter as the previous by stereotactic injection of murine GB GL261 cells into C57BL/6J mice.

In the case of Pt-Fe NCPs, the Pt tended to accumulate favorably in the GB tumor and brain, especially in tumors with small volume (23.15 ± 2.68 mm^3) reaching a high retention of 10.34% ID/g tissue, which was significantly higher than that in other organs, and significantly higher than the retention in bigger tumors (58.05 ± 3.35 mm^3). Therefore, three mice bearing small orthotopic GB tumors were used for the biodistribution study of pPtBC NPs, with an average tumor volume of 24.96 ± 2.7 mm^3 and an average body weight of 22.7 ± 0.2 g. The tolerability study proved that the pPtBC NPs were relatively safe and well-tolerated by the mice, so the biodistribution of the polymeric NPs was studied with the highest dose, 1.5 mg Pt/kg, in tolerability assessment.

As Figure 4.19 and table 4.3 shown, 1 h post IN administration, the Pt mainly accumulated in GB tumor, followed by kidneys, lungs, and brain. Few accumulated in liver, spleen, and heart. The Pt retention in tumor was highest with 3.51 ± 0.36% ID/g, and 2.53 ± 0.98%, 2.6 ± 0.69, 3.0 ± 0.43% ID/g in brain, lungs, and kidneys, respectively. No significance was found in the Pt retention in tumor and in the aforementioned

organs, while the tumor accumulation of Pt was significantly higher than that in heart, liver and spleen. Taken tumor and brain together, the Pt accumulation in CNS was significantly higher than that in other organs.

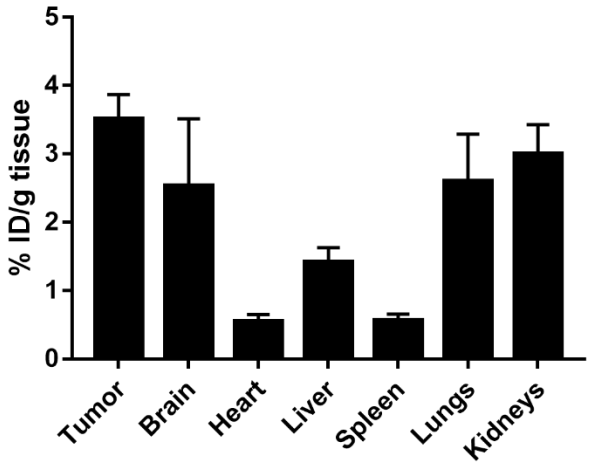

Figure 4.19 Biodistribution of pPtBC NPs in mice bearing GL261 tumors 1 h after administration. Mice were intranasally administered with pPtBC NPs at a dose of 1.5 mg Pt/kg, and sacrificed 1 h post administration. Each value represented as mean ± SE, n = 3.

	Tumor	Brain	Heart	Liver	Spleen	Lungs	Kidneys
Pt retention (% ID/g of tissue)	3.51 ± 0.36	2.53 ± 0.98	0.54 ± 0.11	1.41 ± 0.22	0.56 ± 0.10	2.60 ± 0.69	3.0 ± 0.43
Significance vs. tumor	N/A	No	Yes	Yes	Yes	No	No

Table 4.3 Pt biodistribution of pPtBC NPs in GL261 GB-bearing mice. Dose = 1.5 mg Pt/kg, biodistribution time = 1 h, n = 3. Comparison was made with Pt retention in tumor, with $p < 0.05$ considered significant by student's t-test.

The BBB has long been a hindrance to the successful delivery into brain and brain tumors, although the integrity of BBB could be disrupted and the permeability might increase due to the compromised BBB.[57] Still, the intra- and inter-tumoral heterogeneity of GB make the drug delivery into CNS a big challenge for conventional therapeutic agents. The nose-to-brain drug delivery by IN delivery was more effectively, compared to other systemic administration routes, like IV injection and intraperitoneal injection, which typically resulted in neglectable retention in brain.[58-59] Conventional polymeric NPs have been reported to favorably accumulate in RES/MPS organs via systemic administration, commonly in liver and spleen.[60-61] Notably, Pt accumulated more in

lungs and kidneys, instead of the typical RES organs (liver and spleen). The biodistribution of pPtBC NPs indicated distinctive pharmacokinetic pathways of IN delivery different from other systemic routes.

Interestingly, the accumulation of Pt from pPtBC NPs in GB tumor was significantly lower than the Pt retention from Pt-Fe NCPs in GB tumor, while there was no significance in the tumor volumes. This difference could be due to the different compositional/structural nature of these two nanoparticles. Although the fabrication of these NPs was both based on PtBC, the same Pt(IV) prodrug, pPtBC NPs were polymeric NPs formed from direct oxidation of catechol moieties, while Pt-Fe NCPs formed by more labile coordination between the ligand and iron ions. The presence of Fe(III) in Pt-Fe NCPs may make a contribution to the transport across the BBB and the internalization into GB tumor cells due to the receptor-mediated endocytosis, for example, transferrin receptors overexpressed in GB and closely related to Fe uptake.[62-63] Generally, the cancer cells have elevated demand of Fe(III) as a nutrient required for cell growth and proliferation.[64] And this is also common to high-grade glioma, resulting in enhanced uptake of Fe(III) by upregulating activity of transferrin receptor.[65] However, this advantage did not exist in pPtBC NPs, probably leading to significantly lower Pt accumulation than that of Pt-Fe NCPs.

4.5 Conclusions

Novel Pt(IV) prodrug-based polymeric nanoparticles with an average size of 64.03 ± 6.58 nm, a PDI of 0.143 ± 0.012, and a slightly negative ζ-potential of -6.18 ± 1.05 mV, were designed, synthesized successfully, and evaluated as drug delivery systems for GB treatment. The obtained polymeric pPtBC NPs showed relevant advantages such as:

- Chemical and colloidal stability, pH/GSH dual responsiveness and therefore controlled drug release.
- The cellular uptake and DNA-bound Pt from pPtBC NPs were significantly lower than that of cisplatin after 24 h of drug exposure, revealing a slower intracellular activation process for the polymeric NPs. However, pPtBC NPs exhibited comparable even superior cytotoxic effect in comparison to cisplatin

against HeLa, 1Br3G, and GL261 cell lines for 72 h, while no ROS generation was triggered in any of these cell lines by pPtBC NPs. This corroborated that the cytotoxic effect was totally attributed to the chemotherapeutic effect of the released Pt compounds.

- pPtBC NPs were proved to be biosafe and well-tolerated at a dose of 1.5 mg Pt/kg body weight in wt mice, and displayed favorable accumulation of Pt in GB tumor and brain, implying the effective delivery into CNS of intranasal administration.

- These results indicated that pPtBC NPs possess potential anti-GB activity *in vitro*, while the *in vivo* efficacy should be further evaluated in the near future. And intranasal administration could serve as an alternative to typical systemic administration routes for CNS delivery.

4.6 Experimental

Characterization methods. 250 MHz ^{1}H NMR spectra were recorded on a Bruker DPX 250 MHz spectrometer; 360 MHz ^{1}H NMR, ^{1}H-^{1}H COSY, and 100 MHz ^{13}C NMR were recorder on a Bruker DPX 360 MHz spectrometer; 400 MHz ^{1}H NMR, ^{1}H-^{1}H COSY, and 100 MHz ^{13}C NMR were recorder on a Bruker DPX 400 MHz spectrometer. Chemical shifts (δ) are given in ppm, using the residual non-deuterated solvent as internal reference. Signal multiplicities are described using the following abbreviations: singlet (s), doublet (d), triplet (t), quartet (q), quintet (quint), doublet of doublets (dd), doublet of triplets (dt), doublet of doublet of doublets (ddd), multiplet (m) and *J* to indicate the coupling constant (Hz). High-resolution mass spectra were obtained by direct injection of the sample with electrospray techniques in a Bruker microTOF-Q instrument. FT-IR spectra were recorded using a Tensor 27 spectrophotometer (Bruker Optik GmbH, Germany) with KBr pellets. Powder X-ray diffraction (PXRD) patterns were recorded at room temperature on a PANalytical X'Pert PRO MRD diffractometer (Malvern PANalytical, Germany) equipped with a CuKα radiation source (λ = 1.54184 Å) and operating in reflection mode, where the solid samples were placed on an amorphous

silicon oxide plate and measured directly. UV-vis was performed using a Cary 4000 UV-vis spectrometer (Agilent Technologies, USA) within a wavelength range of 400-4000 nm and a 1 cm path length quartz cuvette (QS 10mm).

DLS measurements. Size distribution and surface charge of the nanoparticles were measured by DLS, using a ZetasizerNano 3600 instrument (Malvern Instrument, UK), whose size range limit is from 0.6 nm to 6 nm. (Note: the diameter measured by DLS is the hydrodynamic diameter. The samples were comprised of aqueous dispersions of the nanoparticles in distilled water or in buffer. All samples were diluted to obtain an adequate nanoparticle concentration around 0.5 mg/mL.)

Electron Microscopies. SEM images were obtained using a scanning electron microscope (FEI Quanta 650 FEG) at acceleration voltages of 5-20 kV. SEM samples were prepared by drop-casting of corresponding dispersions of NPs on an aluminum tape followed by evaporation of the solvent under room conditions. Before analysis, the samples were metalized with a thin layer of platinum (thickness: 5 nm) using a sputter coater (Emitech K550). STEM images were obtained using a scanning-transmission electron microscope (Magellan 400L, FEI), while TEM images were obtained using a transmission electron microscope (Tecnai G2 F20, FEI) at a voltage of 200 kV. Samples for STEM and TEM were prepared by drop-casting corresponding dispersions on TEM grids (ultrathin carbon type-A, 400 mesh Cu grid, Ted Pella Inc., Redding, USA) and drying overnight under room conditions prior to examination.

Inductively coupled plasma-Mass spectrometry (ICP-MS). Standard solutions were prepared prior to the measurements at a range from 0 - 200 parts per billion (ppb) using atomic spectroscopic analytical ICP-MS standards (PerkinElmer Inc., Germany). The isotope ^{54}Fe and ^{57}Fe were selected as Fe tracers, while ^{194}Pt, ^{195}Pt and ^{196}Pt as Pt tracers.

Digestion procedures for ICP-MS measurement. All glassware was immersed in 20% HNO_3 for 48 h, and plasticware in 5% HNO_3 for 4 h prior to use for ICP-MS. All samples were digested using wet digestion method. Depending on the materials to digest, different procedures were adopted.

(1) Chemical samples: the appropriate amount of samples, NPs for instance, was weighed accurately with an analytical balance, and transferred into a vial, then

concentrated ultrapure HNO_3 (69%, Ultratrace®, ppb-trace analysis grade, Scharlab, Spain) was added. The samples were placed in the fume hood for 48 h to be fully digested, then were diluted with 0.5% (v/v) ultrapure HNO_3 for further measurements.

(2) Cell pellets: the cell pellets were resuspended in around 100 mL of concentrated ultrapure HNO_3 (69%, Ultratrace®, ppb-trace analysis grade, Scharlab, Spain) and left to digest overnight. Samples were then heated to 90 ℃ till the suspensions turned clear. The samples were diluted with 0.5% (v/v) ultrapure HNO_3 to appropriate volumes for later measurements.

(3) Tissues: the tissues were added with T-PER™ buffer (Thermo Fisher Scientific, USA) in a ratio of 10 mL per gram, then cut into small pieces, and sonicated with ultrasonication microtip (Branson Digital Sonifier 450, Emerson, USA) in cycles of 10 seconds on then 15 seconds off with an amplitude of 40%. Afterwards, the tissue suspensions were added with aqua regia (all ppb-trace analysis grade) and heated up to 300 ℃, while 30% H_2O_2 was added in the later digestion process till the suspensions turned clear. The clear solutions were transferred and made up with 0.5% (v/v) ultrapure HNO_3 to appropriate volumes for the determination of metal contents using ICP-MS.

Preparation of polymeric pPtBC/pNDGA NPs. PtBC (50 mg, 0.062 mmol) / NDGA (20 mg, 0.066 mmol) was dissolved in 30 mL of mixture solvent of EtOH: H2O (1:1). $NaIO_4$ in 1 mL of water was added slowly at room temperature and the reaction was allowed to continue for 4 h. Afterwards, the turbid solution was centrifuged and washed to furnish yellow or brownish precipitate.

Drug release assay. Drug release from pPtBC NPs was determined using dialysis method. Concentrated pPtBC NPs at 1 mg/mL were resuspended into 1 mL of Milli-Q water in dialysis bags (MWCO = 6000 - 8000). The dialysis tubes were immersed into sealed beakers with 40 mL of PB buffers at pH 7.4 and 5.5. The beakers were incubated at 37 ℃ with gentle stirring during the study. 500 mL of aliquot was taken from the dialysate at predetermined time point, followed by supplementing with fresh buffer in same volume immediately. The amount of released Pt was determined by ICP-MS.

Cells. The cell lines were obtained from the Tumor Bank Repository at the National Cancer Institute (Frederick/MD, USA), including human cervical cancer cell HeLa, non-

malignant human fibroblast cell 1Br3G, murine glioblastoma cell GL261, and a pair of human ovarian cancer cell lines, A2780 and its cisplatin resistant counterpart A2780/cis. Before starting any protocol, all solutions were prewarmed to 37 °C. All materials and equipment that came in contact with cells were sterile. All cell-related performance was carried out in Class II biosafety hoods in cell culture labs with a biosafety level 2 (BSL-2).

Cell culture. All cell lines were grown in 75 cm^2 cell-culture flask with corresponding culture media. HeLa was cultured in MEM medium, 1Br3G in DMEM, GL261 in RPMI 1640, A2780 in RPMI 1640, and A2780/cis in RPMI 1640 containing 1 μM of cisplatin. All culture media were supplemented with 10% fetal bovine serum (FBS, Gibco®, Invitrogen, UK), 0.285 g/L glutamine, 2.0 g/L sodium bicarbonate, and 1% penicillin-streptomycin. Cells were cultured as adherent monolayers and maintained in an incubator (HERAcell, 150i, Thermo Scientific) at 37 °C in 5% CO_2 and relative humidity of 95%, except 1Br3G with 10% CO_2. All cell culture media, FBS, supplements, antibiotics, trypsin, and Trypan Blue are purchased from Fisher Scientific (Gibco®, Invitrogen, UK).

To subculture/harvest the cells at log phase around 75% confluence, 4 mL of sterile PBS is added into the flask to rinse the cells after discarding spent cell culture media by aspiration with a vacuum pump. After washing, 3 mL of 0.05 % trypsin-ethylenediaminetetraacetic acid (EDTA, 0.2 g/L) was added and the flask was returned to incubator for 2 minutes. Observing the cells under the microscope, if ≥ 90% of the cells have detached, 6 mL of fresh cell media was added into the flask and dissociate the cells from the surface. The cell suspension was transferred into a 15 mL conical (Falcon, Corning, USA) to centrifuge (Thermo Scientific, USA) at 1400 rpm for 5 min to collect all the cells. The supernatant was discarded, and the pellet was resuspended in fresh media or PBS for cell counting, then an appropriate number of cells was seeded in a new flask.

Cell counting. The cells were counted using a Neubauer hemocytometer cell counter and Trypan Blue (Gibco®, Invitrogen, UK) exclusion to count the cells and determine the viability. Trypan Blue is a dye used to distinguish the living cells from the dead, since the dead cells cannot extrude Trypan Blue without required energy mechanisms. An aliquot of 10 mL of the cell suspension obtained in the subculture step was added into 10 mL of Trypan Blue. Then, 10 mL of the resulting mixture was added onto the Neubauer

hemocytometer and the number of living cells was counted under an optical microscopy.

***In vitro* cytotoxicity assays.** The cells (HeLa, 1Br3G, GL261, A2780 and A2780/cis) in exponential growth were seeded in 96-well plate (Corning, USA) in optimal condition. HeLa was seeded at a density of 2000 cells/well, 1Br3G at 3000 cells/well, GL261 at 4000 cells/well, A2780 and A2780/cis at 3000 cells/well. Specifically, the cisplatin-containing cell culture media was replaced with fresh RPMI media without drug 4 hours before seeding. After 24 hours' incubation, fresh media containing compounds (pPtBC NPs, PtBC, and CDDP) at different concentrations (0, 0.1, 1, 5, 10, 25, 50, 100, 200 μM referred to Pt concentration) were added, and the plates were incubated for 24 or 72 hours. Afterwards, 10 μl of PrestoBlue® (0.15 mg/ml, Thermo Scientific, USA) was added into each well and the plates were incubated for another 4 hours before measuring the fluorescence at 572 nm with excitation at 531 nm by the microplate reader Victor 3 (Perkin Elmer, USA). For 1Br3G, the incubation time with PrestoBlue® was prolonged to 7 hours in order to achieve enough difference of fluorescence intensity between concentrations. All experiments were carried out in triplicate, and data were treated by and Graphpad Prism (version 7.0). The calculated IC_{50}s were obtained by Graphpad Prism.

Estimation of ROS formation. HeLa, 1Br3G and GL261 were seeded in black 96-well plates (Corning, USA) at a density of 20,000 cells per well to achieve full confluence. After 24 hours' incubation, the spent medium was discarded and cells were washed out from the medium serum, and added prewarmed PBS with the fluorescent probe 2',7'-dichlorofluorescin diacetate (DCFCDA, final working concentration 10 mM), then incubated for 30 minutes. DCFCDA is a non-fluorescent permeable compound which can be hydrolyzed by esterase and oxidized by intracellular ROS and turn to fluorescent and non-permeable 2',7'-dichlorofluorescein (DCF). After the probe was internalized, the buffer with probe was replaced by only medium or media with compounds (H_2O_2, pPtBC NPs, pNDGA NPs, PtBC, NDGA, and CDDP) at the concentration of IC_{50} for 24 hours. 0.1 mM of H_2O_2 was added as positive control. After 24 hours, the fluorescence of each well was examined at 530 nm after excitation at 485 nm by a microplate reader Victor 3 (Perkin Elmer, USA). This experiment was repeated in triplicate independently. The

results were normalized based on the negative control loaded with dye but without drug treatment.

Cellular internalization. HeLa, 1Br3G and GL261 cells were seeded in 6-well plates (Corning, USA) at a density of 300,000 cells per well with 1.5 ml of media. After 24 hours' incubation, the media were replaced by 1 ml of fresh media w/wo CDDP, PtBC, and pPtBC NPs at 0.1 mM referred to Pt concentration. The treated cells were allowed to internalize the compounds for 6 h and 24 in the incubator. Another cellular uptake assay was also performed with a decreased concentration of Pt agents to 10 μM, and increased time points of 2, 4, 8, and 24 h. The media were removed immediately and cells were rinsed twice by cold PBS in order to remove excessive compounds. Then 0.5 ml of trypsin was added to each well for 3 min and 2-fold volume of fresh media was added to neutralize the trypsin. After an aliquot was taken from each well for cell counting, the rest cell suspensions were collected into 1.5 ml Eppendorf tubes (Corning, USA) and centrifuged at 12,000 rpm for 4 min. The supernatants were discarded while the cell pellets were stored at -80 ℃ for further quantification by ICP-MS.

DNA-bound Pt. In order to clarify the action mechanism of our Pt NPs, the DNAs were extracted and measured by ICP-MS to quantify the DNA-bound Pt after uptake for 24 h in HeLa, 1Br3G and GL261 cells. The cells in exponential growth were seeded onto cell culture dish in optimal condition for each cell line to reach 50-60 % of confluence in 24 h before the treatment. Then the drugs (CDDP, PtBC, and pPtBC NPs) were added at 0.1 mM referred to Pt concentration, and the cells were allowed to incubate for another 24 h. Afterwards, media with drugs were removed and the cells were rinsed, trypsinized and collected by centrifugation and rinsed with cold PBS twice to remove excessive drugs. The resulting cell pellets were resuspended in lysis buffer (pH 8.0, 150 mM Tris-HCl, 100 mM NaCl and 0.5 % (w/v) SDS). Pellets in buffer were incubated on ice for 15 min and centrifuged at 15000 rpm for 15 min. 0.1 volume of RNase A was added into each supernatant at 0.2 mg/mL and incubated for 1 h at 37 ℃. Afterwards, Proteinase K was added at 0.1 mg/mL and incubated for 3 h at 56 ℃. A volume of Phenol/Chloroform/Isoamyl alcohol (25:24:1 in volume, Thermo Scientific®) was added and mixed gently. And after a centrifugation of 3 min at 15000 rpm, aqueous phases containing DNA were transferred into sterile tubes. DNA was precipitated with 0.1

volume of 3 M sodium acetate and 1 volume of absolute ethanol at -20 ℃ overnight. Then, the DNA samples were centrifuged for 15 min at 15000 rpm, and finally DNA samples were dried and resuspended in 0.1 mL of elution buffer (pH 8.0, 10 mM Tris-HCl, 1 mM EDTA). The concentration of isolated DNA was quantified by measuring the absorbance at 260 nm using NanoDrop™ 1000 spectrophotometer (Thermo Fisher Scientific, USA). And remaining samples were frozen for further ICP-MS analyses.

Animals. Healthy female C57BL/6 mice (8 - 12 weeks, body weight 20 - 24 g) were used for all *in vivo* studies in this work, which were obtained from Charles River Laboratories (Charles River Laboratories Internacional, I'Abresle, France) and housed in the animal facility (Servei d'Estabulari, https://estabulari.uab.cat/) of the *Universitat Autònoma de Barcelona*. All animal study protocols were approved by the local ethics committee (*Comissió d'Ètica en l'Experimentació Animal i Humana*, https://www.uab.cat/etica-recerca/) according to regional and state legislations (protocol CEEAH-3665). The animals were housed in cages with free access to standard food and water, under uniform housing and environmentally controlled conditions.

Figure 4.20 Illustration for unique identification of mice by ear-piercing.

Herein, every studied mouse was given a unique alphanumerical identifier, CXXXX belonging to mice bearing GL261 tumors, while WTXXXX belonging to wild type (wt) mice without tumors. Besides, specific ear-piercing combinations were made with an ear-punching device for distinguishing animals in same cage. As shown in Figure 4.20, single or multiple ear notches were made in one or both ears.

Establishment of orthotopic intracranial glioblastoma model by stereotactic injection of GL261 cells. The orthotopic glioblastoma tumor models were generated by

stereotactic injection of GL261 cells into C57BL/6 mice. Specifically, analgesia (Metacam, Boehringer Ingelheim) at 1 mg/kg was injected subcutaneously to each animal 15 minutes before anesthesia and also 24 and 48 h after implantation. Mice were anesthetized with a mixture of ketamine (Parke-Davis SL, Madrid, Spain) at 80 mg/kg and xylazine (Carlier, Barcelona, Spain) at 10 mg/kg via intraperitoneal administration. Once anesthetized, the mouse was immobilized on the stereotaxic holder (Kopf Instruments, Tujunga/CA, USA) in a prone position. Next, the head area was shaved, and the incision site was sterilized with iodophor disinfectant solution, a 1 cm incision was made exposing the skull and a 1 mm hole was drilled 0.1 mm posterior to the bregma and 2.32 mm to the right of the midline using a microdrill (Fine Science Tools, Heidelberg, Germany). A 26G Hamilton syringe (Reno/NV, USA), positioned on a digital push-pull microinjector (Harvard Apparatus, Holliston/MA, USA) was then used for injection of 4 mL of RPMI cell culture medium containing 100,000 GL261 cells (obtained and counted as described in previous section) at a depth of 3.35 mm from the surface of skull at a rate of 2 mL/min.

Once the injection was completed, the Hamilton syringe was left untouched for 2 minutes more before its removal to prevent the cellular liquid leakage out of the skull. Finally, the Hamilton syringe was gently and slowly withdrawn and the scission site was closed with suture silk 6.0 (Braun, Barcelona, Spain). When the implantation was over, the animal was left in a warm environment to recover from anesthesia.

Once the injection was completed, the Hamilton syringe was left untouched for 2 min more before its removal to prevent the cellular liquid leakage out of the skull. Finally, the Hamilton syringe was gently and slowly withdrawn and the scission site was closed with suture silk 6.0 (Braun, Barcelona, Spain). When the implantation was over, the animal was left in a warm environment to recover from anesthesia.

The C57BL/6J immunocompetent mice were exposed to enriched environment (EE) for 3 weeks before tumor implantation, since it was reported that it could significantly reduce glioma growth and improve mice survival by increasing immunological parameters in the brain of mice.[66] Moreover, since this is the current protocol used at GABRMN, the maintenance of basic parameters may help in further comparisons. Thus, all mice in this thesis were allowed to endure 3 weeks of guarantee housing in EE-like

caging before tumor generation, and were maintained there from beginning to end (Figure 4.21).

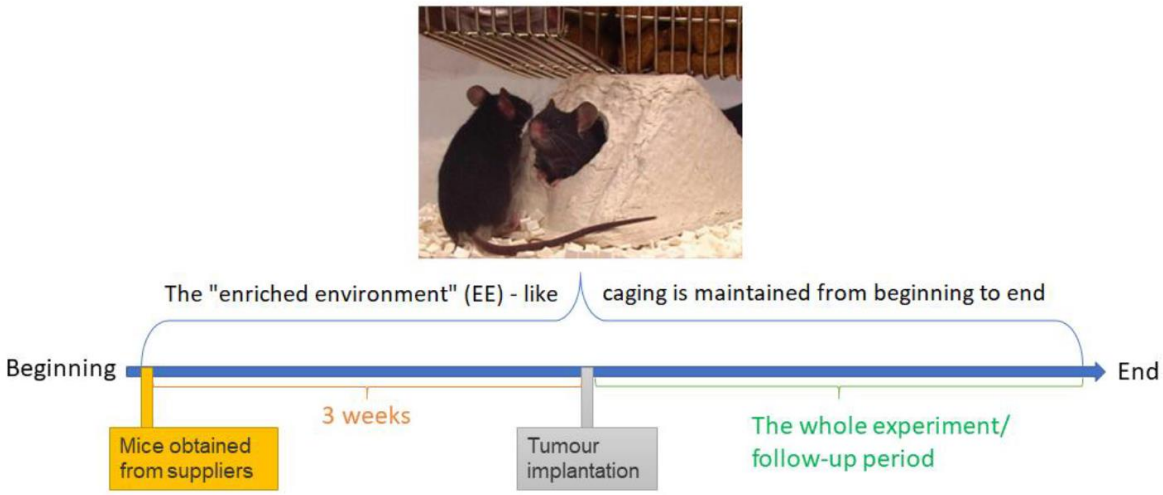

Figure 4.21 Illustration for "enriched environment"-like caging. Mice were allowed to endure 3 weeks of guarantee housing in EE-like caging before tumor generation, and EE was also maintained during the whole experiment and follow-up period. The 'Shepherd Shack' is cage insert composed of autoclavable paper, mice can shred it and use the paper for nesting.[67]

For intranasal administration, the animals were anesthetized by isoflurane for 1 min and kept in a horizontally supine position. The animals were administered with 2 μL of formulation for each nostril, with an interval of 1 - 2 min between each administration. Treated animals were observed for mortality and the moribund animals were sacrificed for ethical considerations.

Tissue preservation procedures. When animals died or were euthanized by cervical dislocation to prevent suffering, the brains and main organs were excised and either frozen in liquid nitrogen or fixed in formalin, depending on the purpose. In case of freezing, tumors were dissected and collected from normal brain parenchyma, frozen in a liquid nitrogen container for further analysis. In case of fixation, tissue was preserved in 4% formalin for further autopsy or histopathological analysis. Tissues were resected after visual inspection of the whole brain and tumor, avoiding as much as possible the cross contamination with non-tumoral tissue.

***In vivo* MRI.** The animals were subjected to non-invasive brain MRI scan to measure the volumes, localization, and evolution of the GB. Each scan was performed at 7 T

BioSpec 70/30 USR spectrometer (Bruker BioSpin GmbH, Ettlingen, Germany) at *Servei de Ressonància Magnètica* from UAB (also part of Unit 25 of ICTS NANBIOSIS, NMR: Biomedical Applications I https://www.nanbiosis.es/portfolio/u25-nmr-biomedical-application-i/). Mice were positioned in a dedicated bed, which allowed the delivery of anaesthesia (isoflurane, 1.5 - 2 % in O_2 at 1 L/min), with an integrated heating circuit for body temperature regulation. Respiratory frequency was monitored with a pressure probe and kept between 60-80 breaths/min. GL261 tumor-bearing mice were scanned to acquire high-resolution T_{2w} images using a rapid acquisition with relaxation enhancement (RARE) sequence to detect the brain tumors. The acquisition parameters were as following: repetition time (TR)/effective echo time (TEeff) = 4200/36 ms; echo train length (ETL) = 8; field of view (FOV) = 19.2 × 19.2 mm; matrix size (MTX) = 256 ×256 (75 × 75 µm/pixel); number of slices (NS) = 10; slice thickness (ST) =0.5 mm; inter-ST = 0.1 mm; number of averages (NA) = 4; total acquisition time (TAT) = 6 min and 43 s. MRI data were acquired and processed on a Linux computer using ParaVision 5.1 software (Bruker BioSpin GmbH, Ettlingen, Germany).

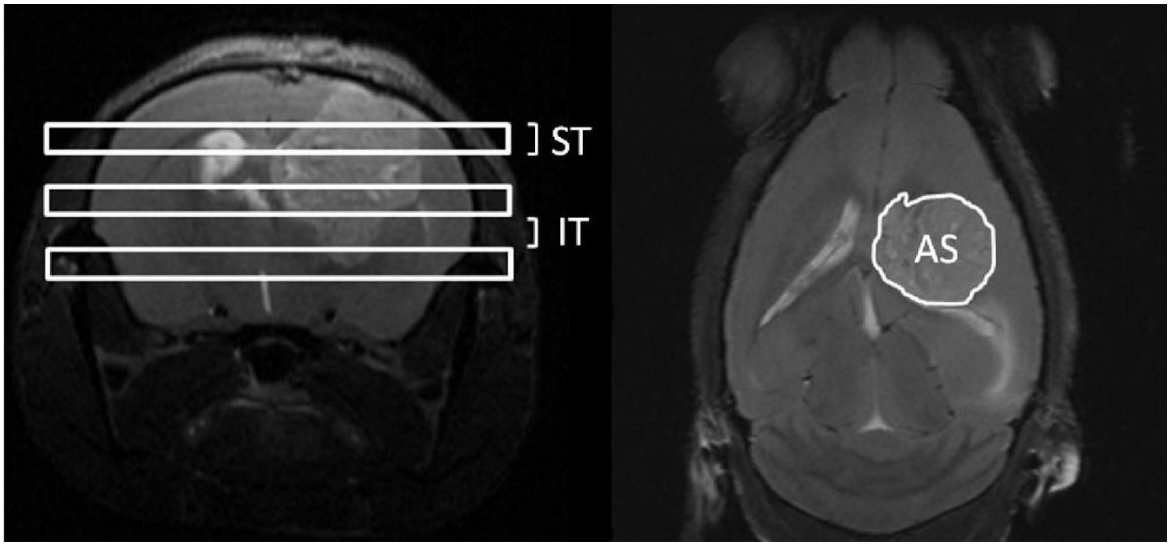

Figure 4.22 MRI measurement for tumor volume assessment. High resolution axial T_{2W} images (right) were acquired for this purpose. The surface area (AS) of the tumor (white line contour at right) was measured in each slice of the axial T_{2W} images. The slice thickness (ST) and the inter-slice thickness (IT) (represented by horizontal slices over a coronal image on the left) were considered for final volume calculation.[68]

To calculate the tumor volume from MRI acquisitions, ParaVision software was used to generate regions of interest (ROIs) to measure the tumor area in each slice (Figure 4.22). And the tumor volume of the studied mice was calculated as following equation:

$$TV\ (mm^3) = [(AS_1 \times ST) + [(AS_2 + (\ldots) + AS_{10}) \times (ST + IT)]] \times 0.075^2$$

Where TV is the tumor volume; AS is the number of pixels contained in the ROI delimited by the tumor boundaries in each slice of the MRI sequence; ST is the slice thickness (0.5 mm), while IT is the inter-slice thickness (0.1 mm), and 0.075^2 is the individual pixel surface area in mm^2.

Tolerability assessment. Healthy female C57BL/6 mice (8 - 12 weeks, 20-24 g) were randomly divided into three groups, control, PtBC, and pPtBC NPs, n = 3. After lightly anesthetized, the mice were administered with drugs intranasally using a micropipette (Gilson, Limburg, Germany) in horizontally supine position. The dosage increased from 0.9, 1.2, to 1.5 mg Pt/kg body weight every week, 3 slightly-escalated dosages in total. The body weights of mice were recorded prior to the first dose of treatment and were monitored 3 times a week thereafter. The animals were closely observed by professional personnel in the animal facility, in particular mortality, food and water consumption, and possible clinical signs. The whole study lasted for 4 weeks. Mice were humanely sacrificed under terminal anesthesia, and the opened mice bodies were preserved either in liquid nitrogen or in formalin for further histological study.

To evaluate tolerability of the vaccine in infected mice, comparisons between three or more groups were made by one-way analysis of variance followed by Bonferroni's multiple comparison's test with comparison between PBS and vaccine treated groups. Comparisons between two groups were made by an unpaired t-test assuming Gaussian distribution (GraphPad Prism 6). P value < 0.05 was considered statistically significant.

Biodistribution study. Mice bearing GL261 gliomas were used for the biodistribution study. According to the sizes of the GB, the mice were divided into two groups, one with bigger tumors and the other with smaller tumors, as indicated in Table 4.4. Pt-Fe NCPs were administrated intranasally at a dosage of 1.5 mg Pt/kg body weight. After 1 h, mice were euthanized. Brain, tumor, heart, lungs, spleen, liver, and kidneys were excised and weighed immediately. These tissues were then homogenized in T-PER buffer (10 mL/g

tissue) using ultrasound probe (Branson Digital Sonifier 450, Emerson, USA) at an amplitude of 30%, with cycles of 10 seconds on and 15 seconds off. Afterwards, they were centrifuged at 10000 rpm for 10 min. The remaining part was digested as described in previous procedure and prepared for ICP-MS measurement to determine the metal concentration.

Tumor volumes & body weights of mice for biodistribution				
Mice	**C1652**	**C1653**	**C1655**	**AV ± SE**
Volume (mm^3)	25.33	20.11	29.44	24.96 ± 2.7
Weight (g)	23.1	22.5	22.5	22.7 ± 0.2

Table 4.4 Average ± standard error of mean (AV ± SE) for tumor volume (mm^3) and body weights (g) of mice for biodistribution.

4.7 References

(1) Karim, R.; Palazzo, C.; Evrard, B.; Piel, G. Nanocarriers for the Treatment of Glioblastoma Multiforme: Current State-of-the-Art. *J. Control. Release* **2016,** *227*, 23-37. DOI: 10.1016/j.jconrel.2016.02.026.
(2) Bertoni, S.; Passerini, N.; Albertini, B., Chapter 3 - Nanomaterials for Oral Drug Administration. In *Nanotechnology for Oral Drug Delivery*, Martins, J. P.; Santos, H. A., Eds. Academic Press: 2020; pp 27-76. ISBN: 978-0-12-818038-9.
(3) Alexis, F.; Pridgen, E.; Molnar, L. K.; Farokhzad, O. C. Factors Affecting the Clearance and Biodistribution of Polymeric Nanoparticles. *Mol. Pharm.* **2008,** *5* (4), 505-515. DOI: 10.1021/mp800051m.
(4) Forooshani, P. K.; Meng, H.; Lee, B. P., Catechol Redox Reaction: Reactive Oxygen Species Generation, Regulation, and Biomedical Applications. In *Advances in Bioinspired and Biomedical Materials Volume 1*, American Chemical Society: 2017; Vol. 1252, pp 179-196. ISBN: 9780841232204.
(5) Tosi, G.; Costantino, L.; Ruozi, B.; Forni, F.; Vandelli, M. A. Polymeric Nanoparticles for the Drug Delivery to the Central Nervous System. *Expert opinion on drug delivery* **2008,** *5* (2), 155-174. DOI: 10.1517/17425247.5.2.155.
(6) Begines, B.; Ortiz, T.; Pérez-Aranda, M.; Martínez, G.; Merinero, M.; Argüelles-Arias, F.; Alcudia, A. Polymeric Nanoparticles for Drug Delivery: Recent Developments and Future Prospects. *Nanomaterials (Basel)* **2020,** *10* (7), 1403. DOI: 10.3390/nano10071403.
(7) Banik, B. L.; Fattahi, P.; Brown, J. L. Polymeric Nanoparticles: The Future of Nanomedicine. *WIREs Nanomedicine and Nanobiotechnology* **2016,** *8* (2), 271-299. DOI: 10.1002/wnan.1364.
(8) Krishnaswamy, K.; Orsat, V., Chapter 2 - Sustainable Delivery Systems through Green Nanotechnology. In *Nano- and Microscale Drug Delivery Systems*, Grumezescu, A. M., Ed. Elsevier: 2017; pp 17-32. ISBN: 978-0-323-52727-9.

(9) Crucho, C. I. C.; Barros, M. T. Polymeric Nanoparticles: A Study on the Preparation Variables and Characterization Methods. *Materials Science and Engineering: C* **2017,** *80*, 771-784. DOI: 10.1016/j.msec.2017.06.004.
(10) Rao, J. P.; Geckeler, K. E. Polymer Nanoparticles: Preparation Techniques and Size-Control Parameters. *Prog. Polym. Sci.* **2011,** *36* (7), 887-913. DOI: 10.1016/j.progpolymsci.2011.01.001.
(11) Renaud, J.; Martinoli, M.-G. Considerations for the Use of Polyphenols as Therapies in Neurodegenerative Diseases. *Int J Mol Sci* **2019,** *20* (8), 1883. DOI: 10.3390/ijms20081883.
(12) Gorlach, S.; Fichna, J.; Lewandowska, U. Polyphenols as Mitochondria-Targeted Anticancer Drugs. *Cancer Lett.* **2015,** *366* (2), 141-149. DOI: 10.1016/j.canlet.2015.07.004.
(13) Zamin, L. L.; Filippi-Chiela, E. C.; Vargas, J.; Demartini, D. R.; Meurer, L.; Souza, A. P.; Bonorino, C.; Salbego, C.; Lenz, G. Quercetin Promotes Glioma Growth in a Rat Model. *Food Chem. Toxicol.* **2014,** *63*, 205-211. DOI: 10.1016/j.fct.2013.11.002.
(14) Ersoz, M.; Erdemir, A.; Derman, S.; Arasoglu, T.; Mansuroglu, B. Quercetin-Loaded Nanoparticles Enhance Cytotoxicity and Antioxidant Activity on C6 Glioma Cells. *Pharm. Dev. Technol.* **2020,** *25* (6), 757-766. DOI: 10.1080/10837450.2020.1740933.
(15) Wang, G.; Jie, W. J.; Ping, Z. L.; Ming du, S.; Ying, L. J.; Lei, W.; Fang, Y. Liposomal Quercetin: Evaluating Drug Delivery *in Vitro* and Biodistribution *in Vivo*. *Expert opinion on drug delivery* **2012,** *9* (6), 599-613. DOI: 10.1517/17425247.2012.679926.
(16) Wang, G.; Wang, J. J.; Yang, G. Y.; Du, S. M.; Zeng, N.; Li, D. S.; Li, R. M.; Chen, J. Y.; Feng, J. B.; Yuan, S. H.; Ye, F. Effects of Quercetin Nanoliposomes on C6 Glioma Cells through Induction of Type Iii Programmed Cell Death. *Int J Nanomedicine* **2012,** *7*, 271-280. DOI: 10.2147/ijn.s26935.
(17) Wang, G.; Wang, J. J.; Chen, X. L.; Du, S. M.; Li, D. S.; Pei, Z. J.; Lan, H.; Wu, L. B. The Jak2/Stat3 and Mitochondrial Pathways Are Essential for Quercetin Nanoliposome-Induced C6 Glioma Cell Death. *Cell Death Dis.* **2013,** *4* (8), e746. DOI: 10.1038/cddis.2013.242.
(18) Wang, G.; Wang, J.; Luo, J.; Wang, L.; Chen, X.; Zhang, L.; Jiang, S. Peg2000-Dpse-Coated Quercetin Nanoparticles Remarkably Enhanced Anticancer Effects through Induced Programed Cell Death on C6 Glioma Cells. *J. Biomed. Mater. Res. A* **2013,** *101* (11), 3076-3085. DOI: 10.1002/jbm.a.34607.
(19) Wang, G.; Wang, J. J.; To, T. S. S.; Zhao, H. F.; Wang, J. Role of Sirt1-Mediated Mitochondrial and Akt Pathways in Glioblastoma Cell Death Induced by Cotinus Coggygria Flavonoid Nanoliposomes. *Int J Nanomedicine* **2015,** *10*, 5005-5023. DOI: 10.2147/IJN.S82282.
(20) Wang, G.; Wang, J. J.; Chen, X. L.; Du, L.; Li, F. Quercetin-Loaded Freeze-Dried Nanomicelles: Improving Absorption and Anti-Glioma Efficiency *in Vitro* and *in Vivo*. *J. Control. Release* **2016,** *235*, 276-290. DOI: 10.1016/j.jconrel.2016.05.045.
(21) Dai, Y.; Yang, Z.; Cheng, S.; Wang, Z.; Zhang, R.; Zhu, G.; Wang, Z.; Yung, B. C.; Tian, R.; Jacobson, O.; Xu, C.; Ni, Q.; Song, J.; Sun, X.; Niu, G.; Chen, X. Toxic Reactive Oxygen Species Enhanced Synergistic Combination Therapy by Self-Assembled Metal-Phenolic Network Nanoparticles. *Adv. Mater.* **2018,** *30* (8). DOI: 10.1002/adma.201704877.
(22) Dai, Y.; Cheng, S.; Wang, Z.; Zhang, R.; Yang, Z.; Wang, J.; Yung, B. C.; Wang, Z.; Jacobson, O.; Xu, C.; Ni, Q.; Yu, G.; Zhou, Z.; Chen, X. Hypochlorous Acid Promoted Platinum Drug Chemotherapy by Myeloperoxidase-Encapsulated Therapeutic Metal Phenolic Nanoparticles. *ACS Nano* **2018,** *12* (1), 455-463. DOI: 10.1021/acsnano.7b06852.
(23) Zheng, S.; Cheng, Y.; Teng, Y.; Liu, X.; Yu, T.; Wang, Y.; Liu, J.; Hu, Y.; Wu, C.; Wang, X.; Liu, Y.; You, C.; Gao, X.; Wei, Y. Application of Luteolin Nanomicelles Anti-Glioma Effect with Improvement *in Vitro* and *in Vivo*. *Oncotarget* **2017,** *8* (37), 61146-61162. DOI: 10.18632/oncotarget.18019.
(24) Masserini, M. Nanoparticles for Brain Drug Delivery. *ISRN Biochemistry* **2013,** *2013*, 238428. DOI: 10.1155/2013/238428.
(25) Abdel-Bar, H. M.; Abdel-Reheem, A. Y.; Awad, G. A.; Mortada, N. D. Evaluation of Brain Targeting and Mucosal Integrity of Nasally Administrated Nanostructured Carriers of a Cns Active Drug, Clonazepam. *J. Pharm. Pharm. Sci.* **2013,** *16* (3), 456-469. DOI: 10.18433/j30s31.

(26) Patel, R. B.; Patel, M. R.; Bhatt, K. K.; Patel, B. G.; Gaikwad, R. V. Evaluation of Brain Targeting Efficiency of Intranasal Microemulsion Containing Olanzapine: Pharmacodynamic and Pharmacokinetic Consideration. *Drug Deliv.* **2016,** *23* (1), 307-315. DOI: 10.3109/10717544.2014.912694.
(27) Arvizo, R. R.; Miranda, O. R.; Thompson, M. A.; Pabelick, C. M.; Bhattacharya, R.; Robertson, J. D.; Rotello, V. M.; Prakash, Y. S.; Mukherjee, P. Effect of Nanoparticle Surface Charge at the Plasma Membrane and Beyond. *Nano Lett.* **2010,** *10* (7), 2543-2548. DOI: 10.1021/nl101140t.
(28) Quail, D. F.; Joyce, J. A. The Microenvironmental Landscape of Brain Tumors. *Cancer Cell* **2017,** *31* (3), 326-341. DOI: 10.1016/j.ccell.2017.02.009.
(29) Klemm, F.; Maas, R. R.; Bowman, R. L.; Kornete, M.; Soukup, K.; Nassiri, S.; Brouland, J.-P.; Iacobuzio-Donahue, C. A.; Brennan, C.; Tabar, V.; Gutin, P. H.; Daniel, R. T.; Hegi, M. E.; Joyce, J. A. Interrogation of the Microenvironmental Landscape in Brain Tumors Reveals Disease-Specific Alterations of Immune Cells. *Cell* **2020**. DOI: 10.1016/j.cell.2020.05.007.
(30) Jin, M.-Z.; Jin, W.-L. The Updated Landscape of Tumor Microenvironment and Drug Repurposing. *Signal Transduction and Targeted Therapy* **2020,** *5* (1), 166. DOI: 10.1038/s41392-020-00280-x.
(31) Jeong, E. M.; Yoon, J.-H.; Lim, J.; Shin, J.-W.; Cho, A. Y.; Heo, J.; Lee, K. B.; Lee, J.-H.; Lee, W. J.; Kim, H.-J.; Son, Y. H.; Lee, S.-J.; Cho, S.-Y.; Shin, D.-M.; Choi, K.; Kim, I.-G. Real-Time Monitoring of Glutathione in Living Cells Reveals That High Glutathione Levels Are Required to Maintain Stem Cell Function. *Stem Cell Reports* **2018,** *10* (2), 600-614. DOI: 10.1016/j.stemcr.2017.12.007.
(32) Traverso, N.; Ricciarelli, R.; Nitti, M.; Marengo, B.; Furfaro, A. L.; Pronzato, M. A.; Marinari, U. M.; Domenicotti, C. Role of Glutathione in Cancer Progression and Chemoresistance. *Oxid. Med. Cell. Longev.* **2013,** *2013*, 972913. DOI: 10.1155/2013/972913.
(33) Cai, X.; Dong, C.; Dong, H.; Wang, G.; Pauletti, G. M.; Pan, X.; Wen, H.; Mehl, I.; Li, Y.; Shi, D. Effective Gene Delivery Using Stimulus-Responsive Catiomer Designed with Redox-Sensitive Disulfide and Acid-Labile Imine Linkers. *Biomacromolecules* **2012,** *13* (4), 1024-1034. DOI: 10.1021/bm2017355.
(34) Zhang, J.; Ren, X.; Tian, X.; Zhang, P.; Chen, Z.; Hu, X.; Mei, X. Gsh and Enzyme Responsive Nanospheres Based on Self-Assembly of Green Tea Polyphenols and Bsa Used for Target Cancer Chemotherapy. *Colloids Surf. B. Biointerfaces* **2019,** *173*, 654-661. DOI: 10.1016/j.colsurfb.2018.10.037.
(35) Zhang, Y.; Wu, X.; Hou, C.; Shang, K.; Yang, K.; Tian, Z.; Pei, Z.; Qu, Y.; Pei, Y. Dual-Responsive Dithio-Polydopamine Coated Porous Ceo(2) Nanorods for Targeted and Synergistic Drug Delivery. *Int J Nanomedicine* **2018,** *13*, 2161-2173. DOI: 10.2147/IJN.S152002.
(36) Lyu, Q.; Zhang, J.; Neoh, K. G.; Li Lin Chai, C. A One Step Method for the Functional and Property Modification of Dopa Based Nanocoatings. *Nanoscale* **2017,** *9* (34), 12409-12415. DOI: 10.1039/C7NR05293F.
(37) Hao, Y.-N.; Zheng, A.-Q.; Guo, T.-T.; Shu, Y.; Wang, J.-H.; Johnson, O.; Chen, W. Glutathione Triggered Degradation of Polydopamine to Facilitate Controlled Drug Release for Synergic Combinational Cancer Treatment. *Journal of Materials Chemistry B* **2019,** *7* (43), 6742-6750. DOI: 10.1039/C9TB01400D.
(38) Shukla, D.; Mandal, P. K.; Tripathi, M.; Vishwakarma, G.; Mishra, R.; Sandal, K. Quantitation of *in Vivo* Brain Glutathione Conformers in Cingulate Cortex among Age-Matched Control, Mci, and Ad Patients Using Mega-Press. *Hum. Brain Mapp.* **2020,** *41* (1), 194-217. DOI: 10.1002/hbm.24799.
(39) Rady, I.; Mohamed, H.; Rady, M.; Siddiqui, I. A.; Mukhtar, H. Cancer Preventive and Therapeutic Effects of Egcg, the Major Polyphenol in Green Tea. *Egyptian Journal of Basic and Applied Sciences* **2018,** *5* (1), 1-23. DOI: 10.1016/j.ejbas.2017.12.001.
(40) Mao, X. M.; Si, J. X.; Huang, Q.; Sun, X. R.; Zhang, Q. Z.; Shen, Y. Q.; Tang, J. B.; Liu, X. R.; Sui, M. H. Self-Assembling Doxorubicin Prodrug Forming Nanoparticles and Effectively Reversing Drug Resistance *in Vitro* and *in Vivo*. *Adv. Healthc. Mater.* **2016,** *5* (19), 2517-2527. DOI: 10.1002/adhm.201600345.

(41) Liu, Z.; Wang, M.; Wang, H.; Fang, L.; Gou, S. Platinum-Based Modification of Styrylbenzylsulfones as Multifunctional Antitumor Agents: Targeting the Ras/Raf Pathway, Enhancing Antitumor Activity, and Overcoming Multidrug Resistance. *J. Med. Chem.* **2020,** *63* (1), 186-204. DOI: 10.1021/acs.jmedchem.9b01223.
(42) Mahmoudi, M.; Laurent, S.; Shokrgozar, M. A.; Hosseinkhani, M. Toxicity Evaluations of Superparamagnetic Iron Oxide Nanoparticles: Cell "Vision" Versus Physicochemical Properties of Nanoparticles. *Acs Nano* **2011,** *5* (9), 7263-7276. DOI: 10.1021/nn2021088.
(43) Kumar, N.; Goel, N. Phenolic Acids: Natural Versatile Molecules with Promising Therapeutic Applications. *Biotechnology Reports* **2019,** *24*, e00370. DOI: 10.1016/j.btre.2019.e00370.
(44) Eruslanov, E.; Kusmartsev, S. Identification of Ros Using Oxidized Dcfda and Flow-Cytometry. *Methods Mol. Biol.* **2010,** *594*, 57-72. DOI: 10.1007/978-1-60761-411-1_4.
(45) Kreuter, J. Drug Delivery to the Central Nervous System by Polymeric Nanoparticles: What Do We Know? *Adv. Drug Del. Rev.* **2014,** *71*, 2-14. DOI: 10.1016/j.addr.2013.08.008.
(46) Howell, S. B.; Safaei, R.; Larson, C. A.; Sailor, M. J. Copper Transporters and the Cellular Pharmacology of the Platinum-Containing Cancer Drugs. *Mol. Pharmacol.* **2010,** *77* (6), 887-894. DOI: 10.1124/mol.109.063172.
(47) Yonezawa, A.; Masuda, S.; Yokoo, S.; Katsura, T.; Inui, K. Cisplatin and Oxaliplatin, but Not Carboplatin and Nedaplatin, Are Substrates for Human Organic Cation Transporters (Slc22a1-3 and Multidrug and Toxin Extrusion Family). *J. Pharmacol. Exp. Ther.* **2006,** *319* (2), 879-886. DOI: 10.1124/jpet.106.110346.
(48) Chapman, E. G.; DeRose, V. J. Enzymatic Processing of Platinated Rnas. *J. Am. Chem. Soc.* **2010,** *132* (6), 1946-1952. DOI: 10.1021/ja908419j.
(49) Akaboshi, M.; Kawai, K.; Maki, H.; Akuta, K.; Ujeno, Y.; Miyahara, T. The Number of Platinum Atoms Binding to DNA, Rna and Protein Molecules of Hela Cells Treated with Cisplatin at Its Mean Lethal Concentration. *Jpn. J. Cancer Res.* **1992,** *83* (5), 522-526. DOI: 10.1111/j.1349-7006.1992.tb01959.x.
(50) Tesniere, A.; Schlemmer, F.; Boige, V.; Kepp, O.; Martins, I.; Ghiringhelli, F.; Aymeric, L.; Michaud, M.; Apetoh, L.; Barault, L.; Mendiboure, J.; Pignon, J. P.; Jooste, V.; van Endert, P.; Ducreux, M.; Zitvogel, L.; Piard, F.; Kroemer, G. Immunogenic Death of Colon Cancer Cells Treated with Oxaliplatin. *Oncogene* **2010,** *29* (4), 482-491. DOI: 10.1038/onc.2009.356.
(51) Bose, R. N.; Maurmann, L.; Mishur, R. J.; Yasui, L.; Gupta, S.; Grayburn, W. S.; Hofstetter, H.; Salley, T. Non-DNA-Binding Platinum Anticancer Agents: Cytotoxic Activities of Platinum–Phosphato Complexes Towards Human Ovarian Cancer Cells. *Proceedings of the National Academy of Sciences* **2008,** *105* (47), 18314. DOI: 10.1073/pnas.0803094105.
(52) Kroemer, G.; El-Deiry, W. S.; Golstein, P.; Peter, M. E.; Vaux, D.; Vandenabeele, P.; Zhivotovsky, B.; Blagosklonny, M. V.; Malorni, W.; Knight, R. A.; Piacentini, M.; Nagata, S.; Melino, G. Classification of Cell Death: Recommendations of the Nomenclature Committee on Cell Death. *Cell Death Differ.* **2005,** *12* (2), 1463-1467. DOI: 10.1038/sj.cdd.4401724.
(53) Shader, R. I. Safety Versus Tolerability. *Clin. Ther.* **2018,** *40* (5), 672-673. DOI: 10.1016/j.clinthera.2018.04.003.
(54) Fox, J.; Barthold, S.; Davisson, M.; Newcomer, C.; Quimby, F.; Smith, A., *The Mouse in Biomedical Research*. UK: Academic Press: 2007. ISBN: 9780123694546.
(55) Miller, M. A.; Stabenow, J. M.; Parvathareddy, J.; Wodowski, A. J.; Fabrizio, T. P.; Bina, X. R.; Zalduondo, L.; Bina, J. E. Visualization of Murine Intranasal Dosing Efficiency Using Luminescent Francisella Tularensis: Effect of Instillation Volume and Form of Anesthesia. *PLoS One* **2012,** *7* (2), e31359. DOI: 10.1371/journal.pone.0031359.
(56) Kulkarni, S. A.; Feng, S.-S. Effects of Particle Size and Surface Modification on Cellular Uptake and Biodistribution of Polymeric Nanoparticles for Drug Delivery. *Pharm. Res.* **2013,** *30* (10), 2512-2522. DOI: 10.1007/s11095-012-0958-3.
(57) Oh, T.; Fakurnejad, S.; Sayegh, E. T.; Clark, A. J.; Ivan, M. E.; Sun, M. Z.; Safaee, M.; Bloch, O.; James, C. D.; Parsa, A. T. Immunocompetent Murine Models for the Study of Glioblastoma Immunotherapy. *J. Transl. Med.* **2014,** *12* (1), 107. DOI: 10.1186/1479-5876-12-107.

(58) Zeng, X.; Sun, J.; Li, S.; Shi, J.; Gao, H.; Sun Leong, W.; Wu, Y.; Li, M.; Liu, C.; Li, P.; Kong, J.; Wu, Y.-Z.; Nie, G.; Fu, Y.; Zhang, G. Blood-Triggered Generation of Platinum Nanoparticle Functions as an Anti-Cancer Agent. *Nat. Commun.* **2020,** *11* (1), 567. DOI: 10.1038/s41467-019-14131-z.
(59) Yin, P.; Li, H.; Ke, C.; Cao, G.; Xin, X.; Hu, J.; Cai, X.; Li, L.; Liu, X.; Du, B. Intranasal Delivery of Immunotherapeutic Nanoformulations for Treatment of Glioma through in Situ Activation of Immune Response. *Int J Nanomedicine* **2020,** *15*, 1499-1515. DOI: 10.2147/ijn.s240551.
(60) Owens, D. E.; Peppas, N. A. Opsonization, Biodistribution, and Pharmacokinetics of Polymeric Nanoparticles. *Int. J. Pharm.* **2006,** *307* (1), 93-102. DOI: 10.1016/j.ijpharm.2005.10.010.
(61) Li, S.-D.; Huang, L. Pharmacokinetics and Biodistribution of Nanoparticles. *Mol. Pharm.* **2008,** *5* (4), 496-504. DOI: 10.1021/mp800049w.
(62) Legendre, C.; Garcion, E. Iron Metabolism: A Double-Edged Sword in the Resistance of Glioblastoma to Therapies. *Trends Endocrinol. Metab.* **2015,** *26* (6), 322-331. DOI: 10.1016/j.tem.2015.03.008.
(63) Voth, B.; Nagasawa, D. T.; Pelargos, P. E.; Chung, L. K.; Ung, N.; Gopen, Q.; Tenn, S.; Kamei, D. T.; Yang, I. Transferrin Receptors and Glioblastoma Multiforme: Current Findings and Potential for Treatment. *J. Clin. Neurosci.* **2015,** *22* (7), 1071-1076. DOI: 10.1016/j.jocn.2015.02.002.
(64) Manz, D. H.; Blanchette, N. L.; Paul, B. T.; Torti, F. M.; Torti, S. V. Iron and Cancer: Recent Insights. *Ann. N. Y. Acad. Sci.* **2016,** *1368* (1), 149-161. DOI: 10.1111/nyas.13008.
(65) Behr, S. C.; Villanueva-Meyer, J. E.; Li, Y.; Wang, Y. H.; Wei, J.; Moroz, A.; Lee, J. K.; Hsiao, J. C.; Gao, K. T.; Ma, W.; Cha, S.; Wilson, D. M.; Seo, Y.; Nelson, S. J.; Chang, S. M.; Evans, M. J. Targeting Iron Metabolism in High-Grade Glioma with 68ga-Citrate Pet/Mr. *JCI insight* **2018,** *3* (21). DOI: 10.1172/jci.insight.93999.
(66) Garofalo, S.; D'Alessandro, G.; Chece, G.; Brau, F.; Maggi, L.; Rosa, A.; Porzia, A.; Mainiero, F.; Esposito, V.; Lauro, C.; Benigni, G.; Bernardini, G.; Santoni, A.; Limatola, C. Enriched Environment Reduces Glioma Growth through Immune and Non-Immune Mechanisms in Mice. *Nat. Commun.* **2015,** *6* (1), 6623. DOI: 10.1038/ncomms7623.
(67) Shuang, W. When Oncology Meets Immunology: Improving Gl261 Glioblastoma Treatment through Cancer-Related Immunity and Mrsi-Based Non-Invasive Follow-up of Response. Universitat Autònoma de Barcelona, 2020. ISBN: N/A.
(68) Ferrer-Font, L. Tuning Response to Therapy in Preclinical Gl261 Glioblastoma through Ck2 Targeting and Temozolomide Metronomic Approaches: Non-Invasive Assessment with Mri and Mrsi-Based Molecular Imaging Strategies. Universitat Autònoma de Barcelona, 2017. ISBN: 9788449069857.

Chapter 5

General conclusions

In this thesis, the rational design in Pt(IV) prodrug and novel nanoscale drug delivery systems have been stablished for the development and study of functional materials with potential biomedical applications, specifically for glioblastoma treatment. To achieve this challenging target, two types of nanocomposites were synthesized, fully characterized, and evaluated for their anti-GB potential *in vitro* and *in vivo* using intranasal administration as the administration route. The results were summarized as following:

1. Catechol-bearing Pt(IV) prodrug (PtBC) has been synthesized successfully starting from cisplatin with an overall yield of 25% and fully characterized with a range of techniques.

2. Two novel nanoscale drug delivery systems have been fabricated and characterized based on the Pt(IV) prodrug by forming a) coordination polymer nanoparticles (Pt-Fe NCPs) or b) polymeric nanoparticles (pPtBC NPs). In both cases the synthetic methodologies were based on one-pot simple and fast reactions.

3. Both nanodrug delivery systems have been fully characterized concerning their physicochemical properties and colloidal stability, while drug release profiles in different possible physiological conditions (different pH and in the presence/absence of GSH) have shown that both NPs are pH- and GSH-responsive which allows controlled drug release in tumor tissues, making them advantageous over cisplatin for *in vivo* biomedical applications.

4. Additionally, the *in vitro* relaxivity properties of Pt-Fe NCPs showed a high r_2 value, and the high ratio of r_2/r_1 implied that these nanoparticles could serve as a promising contrast agent for T_2 MRI. Although *in vivo* MRI was performed, no conclusive results were obtained due to the lack of contrast enhancement observed at experimental conditions used.

5. The cytotoxicity, cellular uptake and DNA-bound Pt were studied *in vitro*. The results demonstrated similar cytotoxicities of both NPs to cisplatin, although the DNA-bound Pt from both NPs was significantly lower than CDDP. The cellular uptake of Pt-Fe NCPs was significantly higher in comparison to the free

prodrug, cisplatin, or pPtBC NPs. Thus, Pt-Fe NCP system was selected as a candidate for further preclinical *in vivo* studies. Additionally, studies concerning ROS generation and cell morphology observation were performed. All indicated comparable *in vitro* anticancer effects of both NPs compared to CDDP.

6. The *in vivo* safety and biodistribution of these two nanoformulations have been studied in a preclinical murine model via intranasal administration, showing significantly higher Pt accumulation in the GB tumor. These results suggested the great benefit of IN route for drug delivery into brain and brain tumors as alternative to the classical administration routes.

7. Additionally, the *in vivo* efficacy of Pt-Fe NCPs has displayed a 20% of cure rate and a 20% of partial response rate with IMS administration schedule, encouraging the use of these drug delivery systems as potential new therapeutic platforms for GB treatment.

From these results, we can conclude that that the rational design of Pt-based nanoparticles (NCPs or polymeric NPs) are feasible and versatile nanoplatforms for drug delivery in the treatment of different cancers. Together with the utilization of nose-to-brain delivery and immune-enhancing metronomic schedule, the NCPs can address some existing challenges in GB chemotherapy, mainly reduction of side effects, improvement of drug bioavailability, and enhancement of chemotherapeutic efficacy of Pt agents.

Annex I

Cell morphological changes

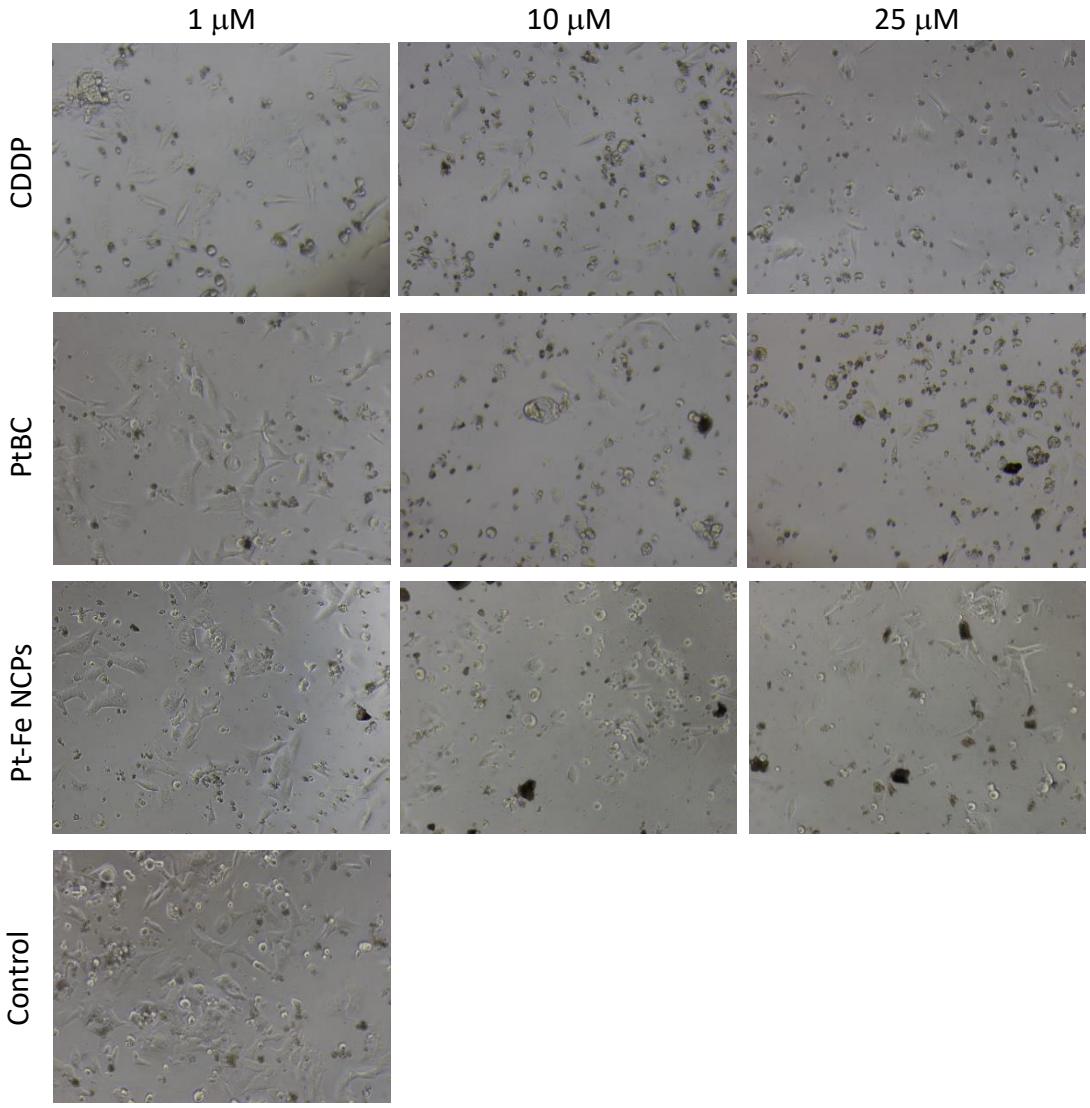

Figure I.1 Representative morphologies of GL261 cells with exposure to Pt-Fe NCPs and other Pt agents for 24 h.

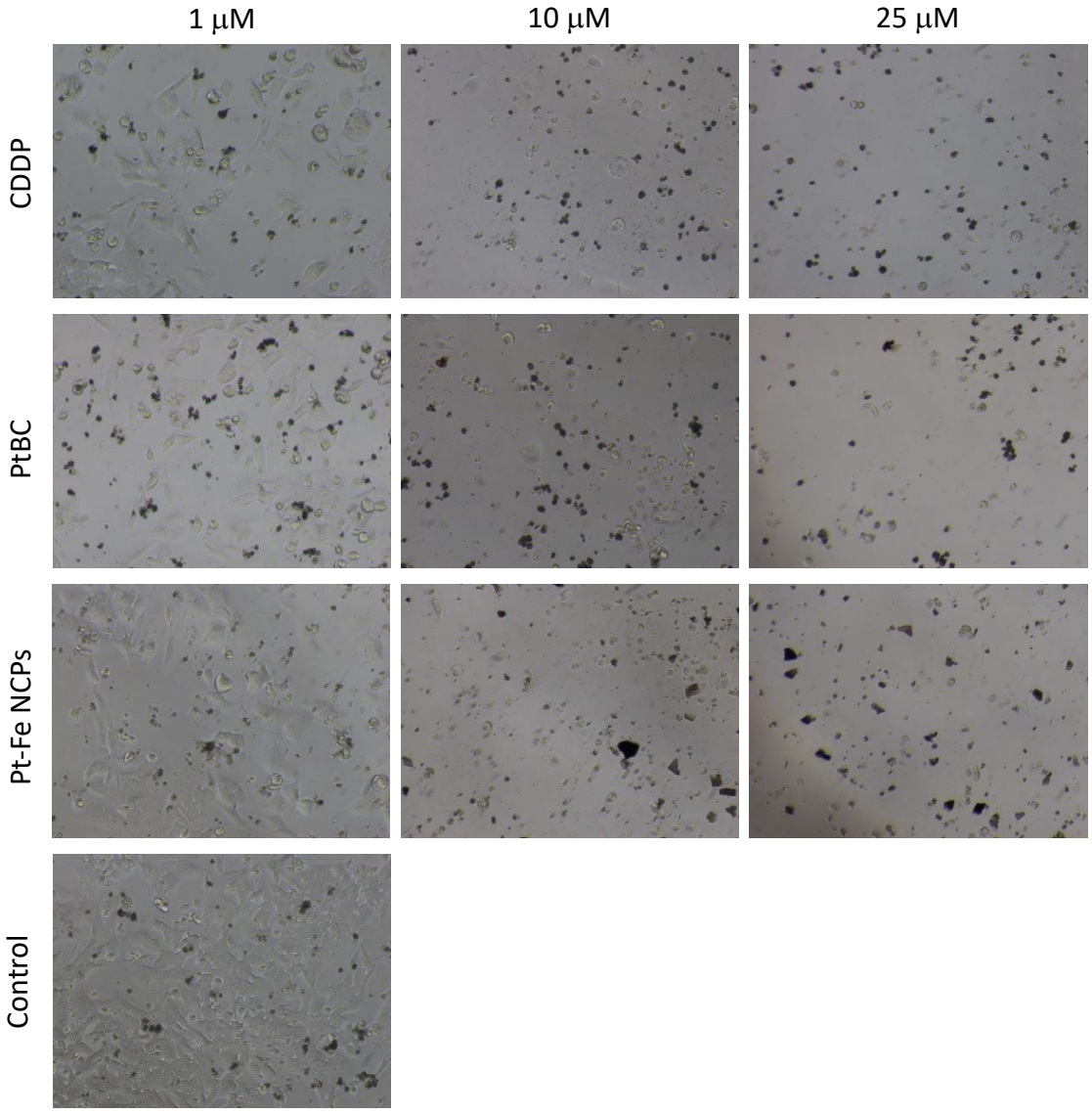

Figure I.2 Representative morphologies of GL261 cells with exposure to Pt-Fe NCPs and other Pt agents for 72 h.

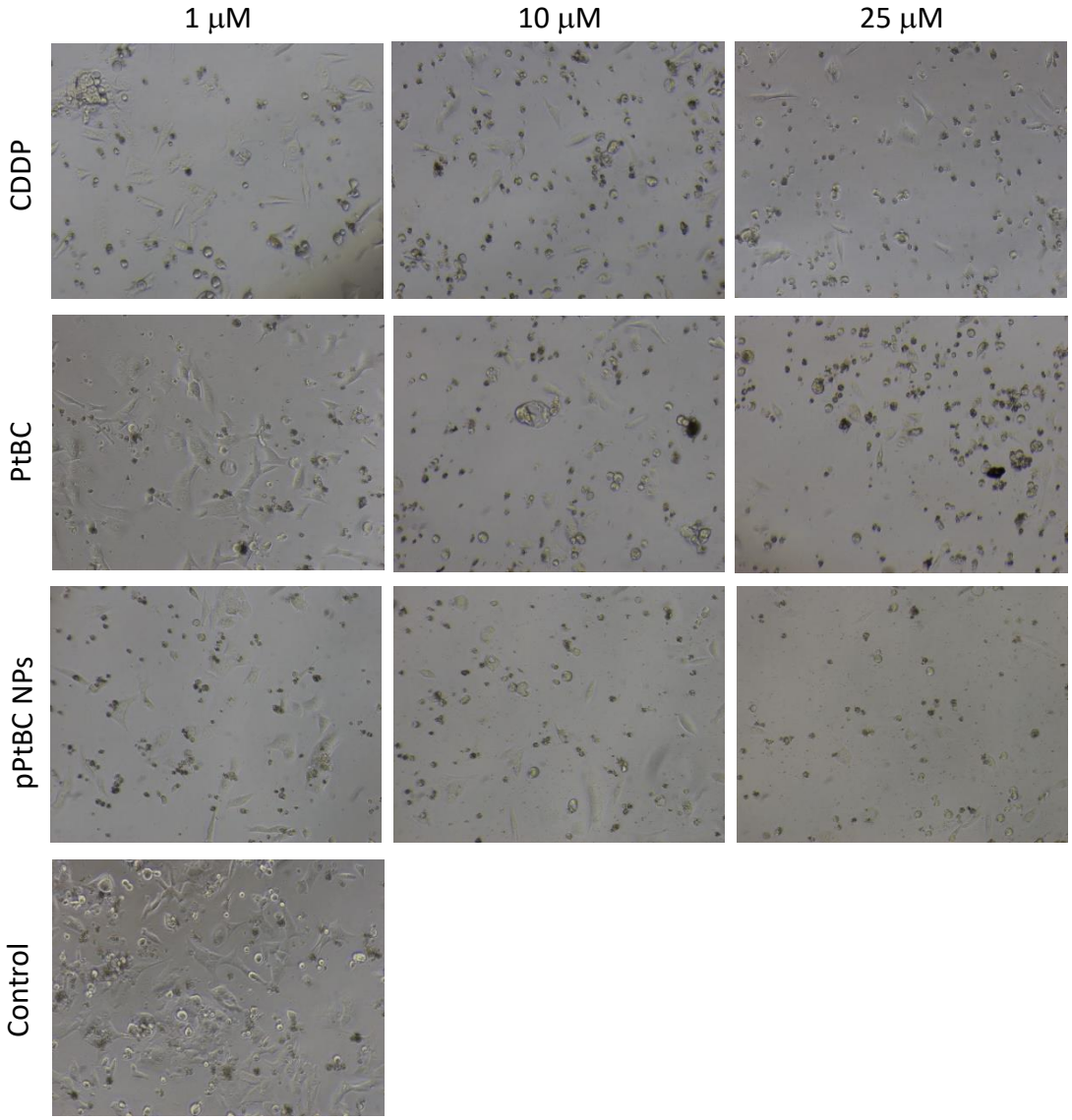

Figure I.3 Representative morphologies of GL261 cells with exposure to polymeric pPtBC NPs and other Pt agents for 24 h.

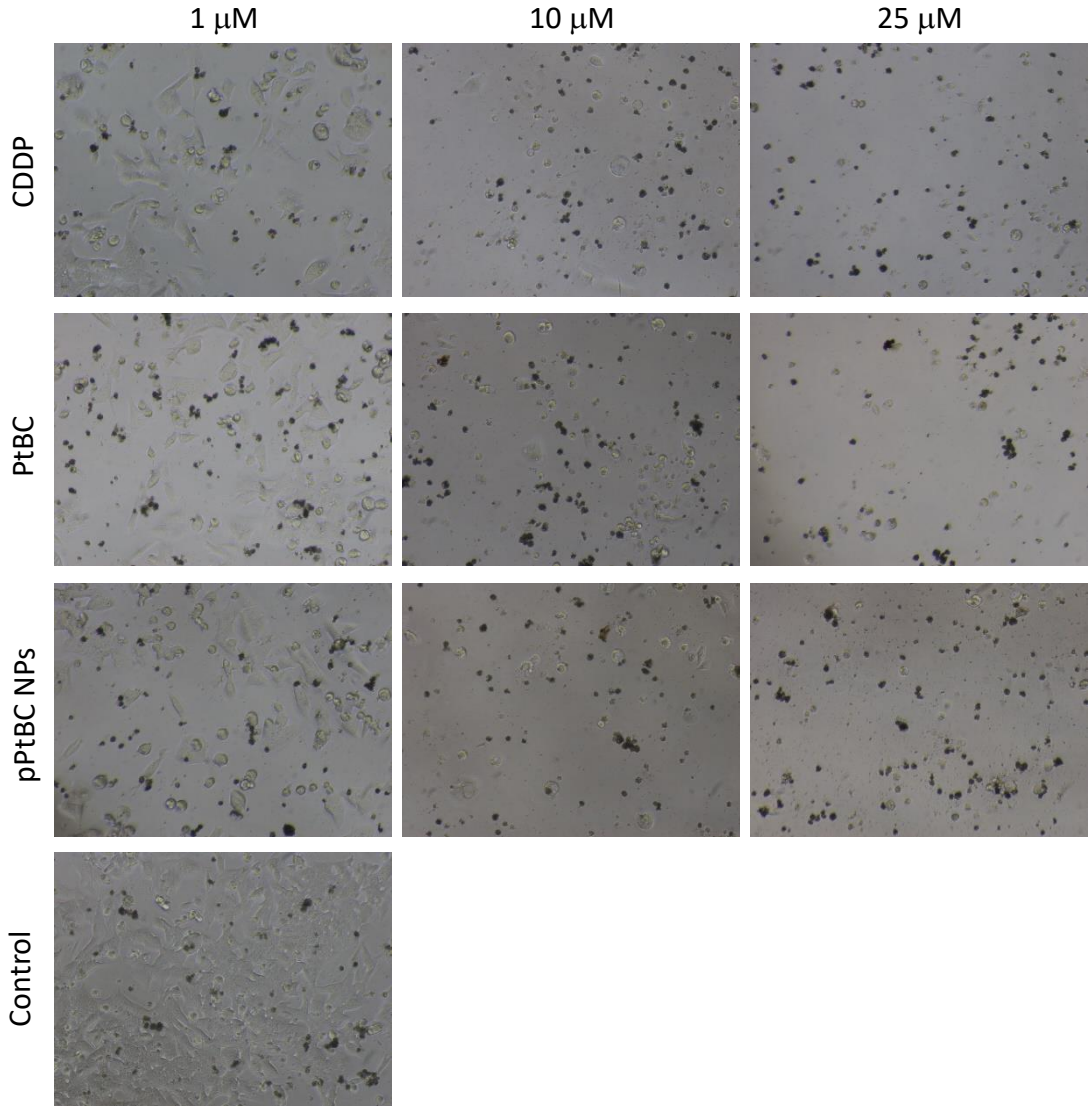

Figure I.3 Representative morphologies of GL261 cells with exposure to polymeric pPtBC NPs and other Pt agents for 72 h.

Annex II

Histological analyses of mice from tolerability

DENTIFICATION: C1506; C1508; C1512; C1513

SPECIES: Murine

SEX: Females

STEM: Not indicated

AGE: between 19 and 24 weeks

OWNERS: Julia Lorenzo IBB

APPLICANT: Julia Lorenzo IBB

PATHOLOGIST: Rosa M. Rabanal

ASSISTANT: Ester Blasco

HISTORY:

Animals treated intranasally: 2 with one type of nanoparticle and 4 with another experiment (2 with the Pt ligand and 2 with platinum nanoparticles).

UPM 117/20 (C1506) and UPM 118/20 (C1508): PtBC

UPM 119/20 (C1512) and UPM 120/20 (C1513): Pt-Fe NCPs

Euthanasia by cervical dislocation.

MACROSCOPIC INJURIES:

• UPM 117/20 (C1506): Focal hemorrhagic lesion in the oblong marrow. Massive hemorrhage in the thoracic cavity. Liver: has generalized pallor.

• UPM 118/20 (C1608): No apparent injuries. The thymus cannot be sampled.

• UPM 119/20 (C1512): Focal hemorrhagic lesion in the oblong marrow. Generalized pallor. Rest without apparent injuries.

• UPM 120/20 (C1513): Pale liver. Rest without apparent injuries.

A: brain; B: heart, lung, thymus, liver, spleen, pancreas and kidneys; C: stomach, intestines, ovaries, uterus, bladder; D: skin and skeletal muscle.

MICROSCOPIC INJURIES:

Central nervous system (CNS): scattered pycnosis of neural bodies, in the cerebellum, oblong marrow and cerebral cortex; focal hemorrhages associated with parenchymal rupture (tissue manipulation). No microscopic lesions were observed in the olfactory areas.

Liver: Blood vessels are empty of erythrocytes (corresponds to the pallor of the liver described macroscopically in some animals). Various degrees of cytoplasm disintegration are observed, which may correspond to the accumulation of physiological glycogen. In all the others isolated apoptosis of hepatocytes and formation of small dispersed granulomas is observed (spontaneous injury that can present/display in mice)

Lung: presence of a point-like material, more or less homogeneous in size, black in color, inside macrophages scattered by the alveolar, subpleural and perivascular septa (mild pneumoconiosis), more evident in the animal C1506 (UPM 117/20); it is a seemingly inert material that does not cause an inflammatory response. Focal perivascular hemorrhages in animal C1512 (UPM 119/20).

Kidneys: maintain normal characteristics. C1513 (UPM 120/20) shows dilation of some renal tubes with light hyaline cylinders (indicative of proteinuria), bilateral, focal and mild.

Spleen: Normal architecture is maintained in all animals. In C1506 (UPM 117/20) the red pulp is bloodless. In all animals, more or less deposits of ocher pigment in macrophages, compatible with hemosiderin, are observed.

The other organs evaluated: heart, thymus, digestive tract, pancreas, bladder, ovary, uterus, skeletal muscle and skin are uninjured and maintain normal architecture.

DIAGNOSIS:

No microscopic lesions indicative of acute or chronic disease are observed.

COMMENTS:

Pneumoconiosis refers to the presence of inhaled and accumulated dust in the lungs, which in large quantities can cause disease. In the animals studied, the amount observed is very small and it should be determined, by other methods, whether it is related to inhaled nanoparticles or other more common types of deposits such as coal (anthracosis).

The alterations described in the CNS are related to the opening of the skull and the manipulation of the brain. Bleeding from animals may explain the macroscopically observed hepatic and generalized pallor.

UPMiC
Unitat de Patologia Murina i Comparada

De UPM 117/20 a UPM 122/20

IDENTIFICACIÓ: C1506; C1508; C1512; C1513; C1583; C1584
ESPÈCIE: Murina
SEXE: Femelles
SOCA: No s'indica
EDAT: entre 19 i 24 setmanes

PROPIETARI: Julia Lorenzo IBB
SOLICITANT: Julia Lorenzo IBB
PATÒLEG: Rosa M. Rabanal
AJUDANT: Ester Blasco

HISTÒRIA:

Animals tractats intranasalment: 2 amb un tipus de nanopartícules i 4 que són d'un altre experiment (2 amb el lligand de Pt y 2 amb nanopartícules de platino).
UPM 117/20 (C1506) i UPM 118/20 (C1508): Pt-BC
UPM 119/20 (C1512) i UPM 120/20 (C1513): Pt-Fe
UPM 121/20 (C1583) i UPM 122/20 (C1584): Solumate
Eutanàsia mitjançant dislocació cervical.

LESIONS MACROSCÒPIQUES:

- UPM 117/20 (C1506): Lesió hemorràgica focal a la medul·la oblonga. Hemorràgia massiva a la cavitat toràcica. Fetge: presenta pal·lidesa generalitzada.
- UPM 118/20 (C1608): Sense lesions aparents. No es pot mostrejar el timus.
- UPM 119/20 (C1512): Lesió hemorràgica focal a la medul·la oblonga. Pal·lidesa generalitzada. Resta sense lesions aparents.
- UPM 120/20 (C1513): Fetge pàl·lid. Resta sense lesions aparents.
- UPM 121/20 (C1583): Pal·lidesa generalitzada de fetge i ronyons. Resta sense lesions aparents.
- UPM 122/20 (C1584): Cerebel trencat. No es pot mostrejar el timus. Resta sense lesions aparents.

A: encèfal; B: cor, pulmó, timus, fetge, melsa pàncrees i ronyons; C: estómac, intestins, ovaris, úter, bufeta de l'orina; D: pell i múscul esquelètic.

LESIONS MICROSCÒPIQUES:

Sistema nerviós central (SNC): picnosi dispersa de cossos neuronals, a cerebel, medul·la oblonga i còrtex cerebral; hemorràgies focals associades a trencament del parènquima (manipulació del teixit). No s'observen lesions microscòpiques a les àrees olfactòries.

Fetge: els vasos sanguinis estan buits d'eritròcit (es correspon amb la pal·lidesa del fetge descrita macroscòpicament en alguns animal). S'observen diversos graus de disgregació del citoplasma, que pot correspondre a l'acumulació de glicogen fisiològic. Excepte en l'animal C1583 (UPM 121/20), en tots els altres s'observa apoptosi aïllada d'hepatòcits i formació de petits granulomes dispersos (lesió espontània que poden presentar habitualment els ratolins)

Pulmó: presència d'un material puntiforme, més o menys homogeni en mida, de color negre, en el interior de macròfags dispersos pels septes alveolars, subpleural i perivascular (pneumoconiosi lleu), més evident en l'animal C1506 (UPM 117/20); es tracta d'un material aparentment inert que no provoca resposta inflamatòria. Hemorràgies focals perivasculars en l'animal C1512 (UPM 119/20) i alveolars a C1583 (UPM 121/20). L'animal C1584 (UPM 122/20) presenta focalment teixit limfoide peribronquial (BALT) una mica més evident.

Ronyons: mantenen les característiques normals. C1513 (UPM 120/20) presenta dilatació d'alguns tubs renal amb cilindres hialins a la llum (indicatiu de proteïnuria), bilateral, focal i lleu.

Melsa: es manté l'arquitectura normal en tots els animals. En C1506 (UPM 117/20) la polpa vermella està exsangüe. En tots els animals s'observen major o menor quantitat de dipòsits de pigment ocre en macròfags, compatible amb hemosiderina.

La resta d'òrgans avaluats: cor, timus, tracte digestiu, pàncrees, bufeta de l'orina, ovari, úter, múscul esquelètic i pell no presenten lesions i mantenen l'arquitectura normal.

DIAGNÒSTIC:

No s'observen lesions microscòpiques indicatives de malaltia aguda o crònica.

COMENTARIS:

La pneumoconiosi fa referència a la presència de pols inhalat i acumulat en els pulmons, que en grans quantitats pot provocar malaltia. En els animals estudiats la quantitat observada és molt escassa i s'hauria de determinar, mitjançant altres mètodes, si està relacionat amb les nanopartícules inhalades o altres tipus de dipòsits més comuns com per exemple carbó (antracosi).
Les alteracions descrites a SNC es relacionen amb l'obertura del crani i la manipulació de l'encèfal. El dessagnat dels animals pot explicar la pal·lidesa hepàtica i generalitzada observada macroscòpicament.

Firma:

Dra. Rosa M. Rabanal Prados
Bellaterra (Cerdanyola del vallès), a 3 d'octubre de 2020